

UCSF

UC San Francisco Electronic Theses and Dissertations

Title

Endoluminal Ultrasound Applicators for Thermal Therapy of Pancreatic Tumors

Permalink

<https://escholarship.org/uc/item/3sh509sd>

Author

Adams, Matthew

Publication Date

2017

Peer reviewed|Thesis/dissertation

**Endoluminal Ultrasound Applicators for Thermal Therapy of Pancreatic
Tumors**

by

Matthew Sean Adams

DISSERTATION

Submitted in partial satisfaction of the requirements for the degree of

DOCTOR OF PHILOSOPHY

in

Bioengineering

in the

GRADUATE DIVISION

of the

UNIVERSITY OF CALIFORNIA, SAN FRANCISCO

AND

UNIVERSITY OF CALIFORNIA, BERKELEY

To Star, Benji, and Spenser,
Proper dogs through and through

Acknowledgements

There are many individuals to thank for their direct involvement in or indirect support of my academic career, both of which instrumental towards the completion of my dissertation. First and foremost, I would like to extend my deepest gratitude towards my advisor, Chris Diederich. Chris has been an invaluable scientific mentor and personal advisor, whose close friendship contributed enormously to my overall happiness throughout graduate school. Along a similar vein, I thank all the fellow members of the TTRG group who helped make the lab an illuminating and enjoyable workplace. In particular, I thank Vasant Salgaonkar, Serena Scott, and Peter Jones, all of whom served as knowledgeable mentors when I first joined the lab and became close collaborators thereafter. I also thank Jessie Lee, Dong Liu, and Vishal Samboju, for their friendships and collaboration, and in helping me to develop as a mentor. I thank my other academic advisors, Steve Conolly, Viola Rieke, Dan Vigneron, John Kurhanewicz, and Peder Larson, who all provided me with invaluable feedback and guidance and directly helped me advance through graduate school by serving on my dissertation and qualifying exam committees. I also thank my many collaborators at Stanford – Graham Sommer, Juan Plata, Aurea Pascal, Donna Bouley, Kim Butts-Pauly – as well as the technicians who aided in the experimental MRI animal studies.

Lastly, I would like to thank my family and friends for their constant support. In particular, my parents have served as my role models throughout my entire life, and have undoubtedly been the root cause of my drive to pursue higher education. Similarly, my siblings Katrina, Chris, and Ryan, through their examples, continue to push me to improve myself. A big thanks to the many friends I made in the Joint Bioengineering Group, for making life in the Bay Area extremely fun and in sharing the incredible journey of graduate school together. Lastly (but not least!), an enormous thanks to Phoebe for her endless support, encouragement, and love.

Abstract

Endoluminal Ultrasound Applicators for Thermal Therapy of Pancreatic Tumors

by

Matthew Sean Adams

Doctor of Philosophy in Bioengineering

University of California, San Francisco and University of California, Berkeley

Chris Diederich, Ph.D., Dissertation Research Director and Chair

The goals of this work are to investigate the feasibility of endoluminal ultrasound for delivering thermal ablation and hyperthermia to pancreatic tumors, and to perform a comprehensive design analysis of both practical and more intricate ultrasound applicator configurations suitable for endoluminal thermal therapy.

A platform for modeling the 3D acoustic, temperature, and thermal dose distributions generated from endoluminal ultrasound applicators and applied to pancreatic tumors and surrounding anatomy was developed. Performance ranges of practical endoluminal applicator designs were determined through comprehensive parametric analyses of applicator design and expected tissue parameters. Modeling studies in patient specific anatomies highlighted the capability of endoluminal ultrasound applicators positioned in the duodenum or stomach to deliver conformal and volumetric ablation or hyperthermia of pancreatic tumors with boundaries within 3-4 cm of the luminal wall while mitigating thermal damage to surrounding sensitive tissues.

A family of MR-compatible endoluminal ultrasound applicators, with distinct transducer configurations (~3 MHz, planar or curvilinear-focused) were designed, fabricated, and

acoustically-characterized using bench-top methods. The capability of these applicators to be endogastrically delivered within the GI tract and to generate ablative temperature distributions in pancreatic tissue was evaluated in *ex vivo* and *in vivo* porcine studies, performed under MR navigation guidance and real-time treatment monitoring using MR temperature imaging. Preliminary acute studies in four *in vivo* pigs demonstrated the capabilities of the applicators to generate ablative temperature elevations of ~20-30 °C in pancreatic tissue at ~2-3 cm depths from the applicator, resulting in histologically-verified localized thermal lesions.

Novel endoluminal ultrasound applicator configurations that integrate deployable balloon-based acoustic reflector and fluid lens components were introduced and analyzed using theoretical modeling analysis and preliminary experimental validation. These applicators would be endoluminally delivered in a small profile, then expanded at the target luminal site to enhance the effective therapeutic aperture. A modeling framework, incorporating wave refraction and reflection at material interfaces was developed and used to perform comprehensive parametric studies for “end-firing” and “side-firing” design alternatives. Simulation studies illustrated the capability of these designs to achieve more localized thermal lesion formation and deeper penetration (up to 8-10 cm) as compared to conventional endoluminal ultrasound applicator designs.

Contents

Chapter 1	1
1 Introduction	1
1.1 Thermal therapy	1
1.1.1 Thermal ablation.....	2
1.1.2 Hyperthermia.....	3
1.1.3 Thermal dose	4
1.2 Therapeutic ultrasound.....	6
1.2.1 Basic physics ³⁵⁻⁴⁰	6
1.2.2 Generation of ultrasound	10
1.2.3 Acoustic field modeling.....	12
1.2.4 Ultrasound heating devices.....	16
1.2.5 Mechanical effects of ultrasound.....	20
1.3 MR temperature imaging	21
1.4 Biothermal modeling	25
1.5 Thermal therapy of pancreatic cancer.....	27
1.6 Research goals	29
1.6.1 Dissertation content	31
Chapter 2.....	34
2 Thermal therapy of pancreatic tumors using endoluminal ultrasound: parametric and patient-specific modeling	34
2.1 Abstract.....	34
2.2 Introduction.....	35
2.3 Materials and Methods.....	36
2.3.1 Endoluminal ultrasound applicator.....	36
2.3.2 Theory.....	39
2.3.3 Parametric studies.....	41

2.3.4	Patient anatomy models.....	44
2.4	Results.....	47
2.4.1	Parametric studies.....	47
2.4.2	Patient anatomy models:.....	53
2.5	Discussion.....	61
2.6	Conclusion.....	66
Chapter 3	67
3	Endoluminal ultrasound applicators for MR-guided thermal ablation of pancreatic tumors: preliminary design and evaluation in a porcine pancreas model.....	67
3.1	Abstract.....	67
3.2	Introduction.....	69
3.3	Materials and Methods:.....	71
3.3.1	Endoluminal ultrasound applicator fabrication.....	71
3.3.2	Acoustic characterization.....	74
3.3.3	MRI experimental setup and RTHawk software platform.....	75
3.3.4	MRTI thermometry validation.....	76
3.3.5	Heating characterization in MR guided ex vivo muscle tissues.....	77
3.3.6	Applicator delivery and heating characterization in MR guided ex vivo porcine cadaver experiments.....	77
3.3.7	MR guided in vivo porcine experiments.....	79
3.4	Results.....	81
3.4.1	Acoustic characterization:.....	81
3.4.2	MRTI experimental validation.....	83
3.4.3	Heating characterization in MR guided ex vivo muscle tissues.....	83
3.4.4	Applicator delivery and heating characterization in MR guided ex vivo porcine cadaver experiments.....	84
3.4.5	MR guided in vivo porcine experiments.....	88
3.5	Discussion.....	96
3.6	Conclusions.....	101
Chapter 4	102
4	Integration of deployable fluid lenses and reflectors with endoluminal ultrasound applicators: preliminary investigations of enhanced penetration depth and focal gain.....	102
4.1	Abstract.....	102
4.2	Introduction.....	104
4.3	Methods.....	109
4.3.1	Acoustic modeling theory.....	111
4.3.2	Fluid lens analysis.....	115
4.3.3	Influence of applicator design parameters on focal properties.....	116
4.3.4	Experimental validation.....	118
4.3.5	Biothermal modeling theory.....	119

4.3.6	Simulated temperature distributions from deployable assemblies	120
4.4	Results	122
4.4.1	Fluid lens analysis	122
4.4.2	Influence of applicator design parameters on focal properties.....	123
4.4.3	Experimental validation.....	131
4.4.4	Simulated temperature distributions from deployable assemblies	132
4.5	Discussion.....	137
4.6	Conclusions.....	144
Chapter 5	146
5	Conclusions and future work.....	146
5.1.1	Research summary.....	146
5.1.2	Future directions.....	149
Bibliography	153
Appendix A	171
A.1	Introduction	171
A.2	Design.....	172
A.2.1	Overview	172
A.2.2	Control handle	173
A.2.3	Pulley subassembly	175
A.2.4	Articulation rings.....	176
A.3	Fabricated prototypes	177
A.4	Discussion	179
Appendix B	180
B.1	Introduction	180
B.2	Volumetric end-fire/side-fire deployable assemblies.....	181
B.3	End-fire with 1D phased array and conical/paraboloid reflector	185

List of Tables

Table 2.1	Material properties used in acoustic and biothermal modeling.	41
Table 2.2	General anatomical characteristics of patient anatomy models of pancreatic tumors..	45
Table 2.3	Parameters and outcomes for patient anatomy ablation simulations.	54
Table 2.4	Parameters and outcomes for patient anatomy hyperthermia simulations.	56
Table 3.1	Transducer specifications for endoluminal ultrasound applicator configurations.	72
Table 3.2	Experimental details and MRTI $T > 15$ °C contour dimensions for ex vivo porcine cadaver heating trials of pancreatic tissue.	88
Table 3.3	Sonication parameters and details for in vivo porcine pancreas heating experiments.	89
Table 4.1	Acoustic properties of prospective lens fluids and water.	116
Table 4.2	Material properties of tissues used in biothermal modeling studies.	122

List of Figures

Figure 1.1 Reflection and transmission of an incident wave at an interface between two media with different acoustic properties.....	9
Figure 1.2 Simulated longitudinal intensity distribution in water for a 25.4 mm diameter, 1.5 MHz flat disk transducer.....	14
Figure 2.1 Schema and concepts of an endoluminal ultrasound applicator positioned in the GI tract for thermal therapy of pancreatic tumors.	37
Figure 2.2 Endoluminal ultrasound applicator transducer configurations.....	38
Figure 2.3 3D generalized pancreatic tumor model employed for parametric studies of endoluminal ultrasound thermal therapy.	42
Figure 2.4 Cross-sectional temperature distributions and 240 EM _{43°C} contours for ablation studies in the generalized tumor model.....	48
Figure 2.5 Effects of transducer configuration and operating frequency on ablation.	49
Figure 2.6 Effects of radius of curvature for curvilinear transducers on ablation.....	50
Figure 2.7 Effects of pancreatic tissue attenuation coefficient on ablation.	52
Figure 2.8 Effects of transducer configuration and operating frequency on hyperthermic temperature distributions.	53
Figure 2.9 3D model and temperature/thermal dose distributions generated for the Example 1 anatomy.....	55
Figure 2.10 3D model and temperature/thermal dose distributions generated for the Example 2 anatomy.....	57

Figure 2.11 3D model and temperature/thermal dose distributions generated for the Example 3 large pancreatic head tumor anatomy.	59
Figure 2.12 Maximum temperature distributions and 240 EM ₄₃ °C contours after ablation treatment for the Example 4 body tumor model.	60
Figure 3.1 Schema and concepts of an endoluminal ultrasound applicator positioned in the GI tract for thermal therapy of pancreatic tumors.....	71
Figure 3.2 Design schematics for the dual planar, dual lightly-focused curvilinear, dual strongly-focused curvilinear, and single strongly-focused curvilinear endoluminal ultrasound applicators..	72
Figure 3.3 Fabricated endoluminal ultrasound applicators.....	74
Figure 3.4 Normalized pressure-squared distributions in degassed water for each endoluminal applicator configuration.	82
Figure 3.5 Relative temperature change measurements during a heat in tissue-mimicking phantom using the dual planar applicator.	83
Figure 3.6 MRTI temperature distributions produced during sonications in <i>ex vivo</i> pork shoulder and pork sirloin meat slabs..	84
Figure 3.7 Active tracking coils localization using a Hadamard-encoded tracking sequence.....	85
Figure 3.8 Placement of the dual planar endoluminal ultrasound applicator in <i>ex vivo</i> porcine stomach lumen adjacent to pancreatic tissue..	86
Figure 3.9 MRTI slice prescription and temperature distributions generated in <i>ex vivo</i> pancreatic tissue using the dual planar applicator.	86
Figure 3.10 MRTI slice prescription and temperature distributions generated in <i>ex vivo</i> pancreatic tissue using the dual lightly-focused curvilinear applicator.	87
Figure 3.11 T2-weighted sagittal MRI images illustrating placement and visualization of the endoluminal ultrasound applicators in <i>in vivo</i> porcine experiments.....	90
Figure 3.12 Temperature distributions generated in pancreatic tissue <i>in vivo</i> in Fig 1 using the dual planar applicator.....	90
Figure 3.13 Temperature distributions generated in pancreatic tissue <i>in vivo</i> in Figs 2 and 3 using the dual planar and dual lightly-focused applicators.	92
Figure 3.14 Temperature distributions generated in pancreatic tissue <i>in vivo</i> in Fig 4 using the dual strongly-focused applicator.....	93
Figure 3.15 Contrast-enhanced T1w images depicting non-perfused volumes in the pancreas as verification of thermal lesion formation.	94

Figure 3.16	Gross appearance of thermal lesions on excised pancreatic tissues.....	95
Figure 3.17	Pancreatic histopathology.....	96
Figure 4.1	Schematics of two ultrasound applicator designs that each integrate a multi-compartment balloon that serves as a deployable acoustic reflector and fluid lens.	109
Figure 4.2	Simplified ray traces of acoustic propagation..	111
Figure 4.3	Proof-of-concept end-fire applicator assembly.	118
Figure 4.4	Generic tissue block model for thermal simulations of endoluminal ablation of liver or pancreatic tissue..	121
Figure 4.5	Normalized energy transmission through the convex interface of the fluid lens.	123
Figure 4.6	Simulated acoustic intensity gain distributions in water for the end-fire applicator assembly.....	124
Figure 4.7	Focal gain of the end-fire applicator assembly.....	126
Figure 4.8	Focal gain of the side-fire applicator assembly.....	127
Figure 4.9	Axial length of the focal zone for the end-fire applicator assembly.	128
Figure 4.10	Transverse width of the focal zone for the end-fire applicator assembly.....	129
Figure 4.11	Axial length of the focal zone for the side-fire applicator assembly.....	130
Figure 4.12	Transverse dimensions of the focal zone for the side-fire applicator assembly.....	130
Figure 4.13	Effects of transducer frequency, tissue attenuation, and focal depth on focal properties for the end-fire applicator assembly.	131
Figure 4.14	Normalized beam plots for the experimental end-fire test applicator assembly at increasing focal lengths or distensions of the fluid lens..	132
Figure 4.15	Simulated temperature distributions in pancreatic tissue using an end-fire applicator assembly.....	133
Figure 4.16	Simulated temperature distributions in pancreatic tissue using a side-fire applicator assembly.....	134
Figure 4.17	Results of thermal simulations using two select end-fire applicator assembly configurations and a side-fire applicator configuration in endoluminal ablation of pancreatic or liver tissue..	136
Figure A.1	CAD schematic of the MR-compatible endoluminal ultrasound applicator with articulated steering capabilities.....	173

Figure A.2 Control handle assembly.	174
Figure A.3 Pulley subassembly that controls pull-wire tension and tip articulation.	175
Figure A.4 Omnidirectional articulation assembly.	176
Figure A.5 Prototype endoluminal ultrasound applicator with endoscopic tip articulation capabilities..	177
Figure A.6 T2w MR image illustrating delivery of the prototype assembly through the porcine esophagus in vivo.....	178
Figure A.7 Prototype endoscopic tip articulation assembly with improved ring design.	178
Figure B.1 Schematic of the deployable ultrasound applicator assemblies with no distal fluid lens compartment.	181
Figure B.2 Simulated endoluminal hyperthermic temperature distributions in pancreatic tissue for end-fire applicator assemblies without focusing fluid lens compartments.....	183
Figure B.3 Simulated endoluminal hyperthermic temperature distributions in pancreatic tissue for the side-fire applicator assembly without a focusing fluid lens compartment.....	183
Figure B.4 Design schema for end-fire deployable assemblies with a tubular transducer phased-array source.....	186
Figure B.5 Cross-sectional view of the deployable end-fire assembly with a paraboloid balloon reflector.....	187
Figure B.6 Focal gain from paraboloid reflector geometries of varying geometric focal depths.	188
Figure B.7 Central axial intensity gain profile for a deployable applicator assembly consisting of a conical balloon reflector and a tubular phased-array.	190
Figure B.8 Central axial intensity gain profiles for deployable applicator assemblies with a tubular transducer phased-array and a conical or paraboloid reflector balloon.	191

Chapter 1

Introduction

1.1 Thermal therapy

Thermal therapy is a general term that encompasses the medical application of heat or cold to the body. As applied for cancer treatment, thermal therapy is typically subdivided into three distinct therapies that span different temperature ranges. Cryotherapy directly destroys cancerous tissues through exposure to lethal freezing temperatures of $< -50\text{ }^{\circ}\text{C}$.^{1,2} Hyperthermia encompasses mild temperature elevation to $39\text{-}45\text{ }^{\circ}\text{C}$, and is often used in conjunction with chemotherapy or radiation therapy.³⁻⁵ Thermal ablation destroys cancerous tissues through exposure to high temperatures above $50\text{ }^{\circ}\text{C}$.^{1,6} For each form of thermal therapy, cancer treatment revolves around the selective targeting and treatment of cancerous tissues while mitigating harmful exposure to normal tissues. To fulfill this overarching goal, a variety of electromagnetic (EM) and ultrasonic (US) energy sources have been adapted into therapeutic applicators to control the delivery and spatial application of thermal energy. Applicators have been developed for non-invasive (extracorporeal) application, as well as for minimally-invasive or invasive application.

1.1.1 Thermal ablation

Exposure of tissues to temperatures above 50 °C causes vascular disruption and a conglomerate of adverse cellular events, including protein denaturation, membrane rupturing, and mitochondrial degeneration, resulting in cell death and coagulative necrosis.^{1,6-8} At much higher extremes of temperature, cell death can be incurred by vaporization (> 100 °C) and by carbonization (> 300 °C).^{6,7} Most thermal ablation therapies are applied at maximum exposure temperatures between 50-95 °C.^{1,9}

Thermal ablation is primarily used in clinical oncology to produce localized and targeted destruction of tumors. Serving often as an alternative to surgical resection, particularly for patients who are not surgical candidates, thermal ablation offers the significant advantage of minimal or non-invasiveness, which can result in lower complication rates, patient morbidity, medical costs, and shorter hospital stays.^{8,9} As thermal ablative modalities utilize non-ionizing energy sources, multiple ablation treatments can be performed without concern for accumulative lifetime doses, as is an issue for radiation therapy. Compared to chemotherapy, thermal therapy can be applied in a much more localized and targeted fashion to mitigate undesirable systemic side-effects. Although the primary effect of thermal ablation treatments is highly localized, there is clinical evidence that thermal ablation can promote systemic anticancer stimulation of the immune system, with efficacy enhanced through combination with other immunomodulating drugs.¹⁰ Thermal ablation has also been combined in synergistic fashion with chemotherapy and radiation therapy, particularly to augment tumor destruction at the borders of the ablation zone where sub-lethal hyperthermic temperatures are generated.⁸

Thermal ablation has been clinically applied to treat cancer in a large variety of different sites, including, but not limited to, tumors in the liver, kidney, bone, lung, brain, prostate, breast,

and pancreas.¹¹⁻¹⁹ It has also been utilized for non-oncological treatments, including cardiac arrhythmia, uterine fibroids, benign prostatic hyperplasia, vision correction, and various cosmetic applications, among others.²⁰⁻²⁴

1.1.2 Hyperthermia

Hyperthermia involves a more moderate elevation of temperature to target tissues, typically within the 39-45 °C temperature range, at a sustained duration of 30-60 minutes or longer.^{3,25} At the upper ranges of this temperature range, cell death can be directly induced through a number of mechanisms, including protein denaturation, inhibition of DNA repair pathways, apoptosis, and/or mitotic catastrophe, among others.^{3,4,25,26} However, rather than its direct cytotoxic effects, hyperthermia is predominantly utilized for anti-tumor enhancement in combination with chemotherapy and/or radiation therapy.²⁵ Moderate hyperthermia enhances chemotherapy by augmenting local perfusion to targeted tumors, which increases intracellular drug accumulation, and by inhibiting DNA repair or drug resistance.^{5,25} Further, to increase targeting specificity of systemically administered chemotherapy, hyperthermia has been combined with chemotherapeutic drugs loaded into temperature-sensitive liposome carriers, which release their drug payload at the target site where hyperthermic temperature elevation is present.²⁷ Hyperthermia enhances radiation therapy by increasing oxygenation and free radical production in target tissues, and has greater inherent cytotoxicity in radio-resistant cells that are in the S-phase of the cell cycle or in hypoxic or acidified environments.²⁵

Hyperthermia has been applied in a variety of heating approaches, such as whole body heating, regional heating, superficial heating, or deep localized heating using interstitial/endocavitary/extracorporeal applicator delivery. A number of different cancer malignancies have been clinically treated with hyperthermia with or without adjuvant

chemotherapy and/or radiation, including head and neck tumors, melanoma, sarcoma, glioblastoma, and tumors in the GI track (esophagus, stomach, rectum), breast, head and neck, bladder, lung, cervix, and pancreas.^{3,25} Randomized trials comparing radiation with adjuvant hyperthermia to radiation alone have demonstrated significant improvements in overall survival (OS) in glioblastoma, complete response rates (CRR) and OS in head and neck cancer, CRR and local control rates (LCR) in breast cancer, LCR and CCR in pelvic cancers, and LCR and OS in skin cancer.²⁵ Combined hyperthermia with chemotherapy or chemoradiation have demonstrated improvements in local progression free survival in sarcoma, tumor recurrence rates in bladder cancer, overall survival in esophageal cancer, survival in prostate cancer, and have shown preliminary positive findings for melanoma and pancreatic cancers.²⁵

1.1.3 Thermal dose

In quantifying the biological effects of temperature on cells and tissue destruction, both the magnitude of temperature elevation and the duration of exposure are essential determinants. There is an exponential rate of cell death during exposure to heat, and as the temperature increases, the exposure duration necessary to produce an equivalent cytotoxic effect decreases exponentially.^{28,29} Arrhenius kinetic models, based on seminal skin burn studies by Henriques and Mortiz, are often used as the basis for modeling irreversible thermal alteration and protein denaturation processes in tissues, based on temperature, exposure time, and tissue-specific rate parameters.³⁰⁻³³ Sapareto and Dewey integrated temperature and exposure duration into a single metric of temperature-time history, known as thermal dose, which uses the units of equivalent minutes at 43 °C (EM_{43°C}) and can be related to cell death and other temperature-mediated tissue effects:³⁴

$$EM_{43^{\circ}C} = \sum_{t=0}^{t=final} R^{43-T} \Delta t \quad \text{Eq. 1.1}$$

where T is temperature (°C), t = time (minutes), and R is a constant of value 0.5 at T > 43 °C and 0.25 at T < 43 °C. This expression was derived from Arrhenius analyses of *in vitro* and *in vivo* cell survivability data across different temperatures, where 43 °C was recognized as an approximate breakpoint in the slope of the rate of cell death with temperature relationship.^{34,35} Practically, this expression means that above 43 °C, an increase in exposure temperature by degree results in an equivalent amount of thermally induced cell death at half the exposure time, while below 43 °C, decreasing the temperature by 1 °C requires a four-times longer exposure time for an equivalent effect. The slope breakpoint at 43 °C is thought to be related to the capability of cells to express heat-shock proteins at temperatures below ~43 °C, which can induce thermotolerance and resist temperature-mediated cell death.²⁹

While 240 EM_{43°C} is often employed as a general threshold for lethal thermal destruction of tissue (100% cell death) for thermal ablation treatments, it is important to note that thermal dose thresholds for tissue destruction can vary significantly between different tissue types.^{9,28,36} This is particularly important in determining appropriate thermal sparing of sensitive normal tissues adjacent to the target region. Further, while the thermal dose metric provides a practical means of relating and comparing different regimens of clinical temperature-time exposures, the metric alone is unsuitable as a prognostic of specific tissue damage. The absolute magnitude of temperature exposure, as well as the rate of temperature elevation, can both significantly impact the manifestation of thermal damage in the treated tissue, as well as the associated body healing response.^{29,37} For instance, heat fixation of tissue occurs in treatments with rapid tissue exposure to high temperatures (> 60 °C) and results in a fibrotic encapsulation or a foreign body wound

healing response, which is markedly different from resorption of tissue that underwent coagulative necrosis at lower temperature/thermal doses, despite both lesions having lethal or 100% cell death.^{7,37,38} For clinical adjuvant hyperthermia treatments with radiation or chemotherapy, a lower cumulative thermal dose of 6-10 EM_{43°C} over multiple treatments is targeted for the treatment volume.

1.2 Therapeutic ultrasound

1.2.1 Basic physics³⁹⁻⁴⁴

Ultrasound refers to mechanical pressure waves that are propagated by the motion of particles within a medium at frequencies above 20 kHz (20,000 cycles/s). In most soft tissues, akin to fluids or liquids, ultrasound energy propagates in the form of longitudinal waves, which cause oscillatory compressions and rarefactions of the particles in the tissue along the same axis of motion as the traveling wave. Shear or transverse waves can exist at soft tissue-bone interfaces, for which the direction of particle displacement and pressure oscillation is perpendicular to the direction of wave propagation. Wave propagation is governed by the wave equation, and varies both as a function of spatial position and time. For a simple longitudinal sinusoidal wave, the pressure at a fixed spatial position will oscillate at a temporal frequency f , while for a fixed time, the pressure will vary sinusoidally with a spatial frequency of $1/\lambda$, where λ is the wavelength. The speed at which ultrasound waves travel is known as the speed of sound c , which is a function of the medium's density and compressibility, and is related to the frequency f and wavelength λ of the wave by the expression:

$$c = \lambda f \qquad \text{Eq. 1.2}$$

When a wave propagates across materials with different speed of sounds, it is important to note that the frequency of the wave remains constant, while the wavelength changes. For longitudinal waves, the acoustic pressure p and particle velocity v (the derivative of particle displacement) can be related by:

$$p = Zv \quad \text{Eq. 1.3}$$

where Z the acoustic impedance of the material, and is equal to the product of the material density ρ and speed of sound. Ultrasound waves carry and impart energy to the medium in which they propagate, and the rate of energy flow through a unit area normal to the direction of wave propagation is known as the acoustic intensity I . The instantaneous intensity, assuming plane wave analysis, is:

$$I = \frac{|p|^2}{Z} \quad \text{Eq. 1.4}$$

It is important to note the difference between the particle velocity and speed of sound, as well as between particle displacement and wavelength, which are often mistakenly assumed equivalent. Particle displacement and velocity refers to the motion of the particles in the medium, as imparted by the propagating wave, whereas the speed of sound and wavelength refer to the wave itself. For example, considering a plane wave of 3 MHz propagating in soft tissue with a 1500 m/s speed of sound and density of 1000 kg/m³, the wavelength is 0.5 mm. At an instantaneous intensity of 1 W/cm², the pressure is 122 kPa, the particle velocity is 82 mm/sec, and the particle displacement is 4.3 nm. Doubling the intensity, the pressure, particle velocity, and particle displacement all increase by a factor of $\sim 1.41x$ to 173 kPa, 116 mm/sec, and 6.1 nm, respectively.

As ultrasound waves propagate through tissue (or any lossy medium), both the acoustic pressure and, by extension intensity, attenuate with distance (z):

$$p(z) = p_0 e^{-\mu z} \quad \text{Eq. 1.5}$$

$$I(z) = I_0 e^{-2\mu z} \quad \text{Eq. 1.6}$$

μ is the amplitude acoustic attenuation coefficient (units of Np/m), which combines the effects of absorption and scattering. Absorption of ultrasound is the primary mechanism by which ultrasound results in tissue heating, and occurs in part due to viscous forces and relaxation in the medium which act to oppose the oscillating motion of the particles, resulting in frictional and relaxation loss heat generation. Absorption (and attenuation) increases with higher frequencies, and is also a function of tissue composition and material properties. Scattering of ultrasound energy occurs as waves propagate across small (relative to the wavelength) reflectors or heterogeneities in the tissue, which disperse wave energy in all directions. This scattered energy is also absorbed and contributes to local heat generation, so typically the attenuation and absorption coefficients are approximated as equivalent when considering thermal effects of ultrasound in tissue.

When an ultrasound wave meets an interface between two media with different acoustic properties, it may be partially reflected and partially transmitted into the other medium. For plane interfaces, where the wavelength of the ultrasound plane wave is smaller than the dimensions of the interface, the reflected and transmitted waves are governed by Snell's law (as depicted in Figure 1.1), and follows similarly to the analogous situation in optics. The angle of reflection (θ_R) is equal to the angle of incidence (θ_i), both with respect to the normal of the interface, and the transmission angle is related to the angle of incidence and the speed of sounds of the two media by:

$$\frac{\sin(\theta_i)}{c_1} = \frac{\sin(\theta_T)}{c_2} \quad \text{Eq. 1.7}$$

The critical angle of incidence (θ_c), which exists for pairs of materials with speeds of sound c_1 and c_2 where $c_2 > c_1$, defines the incidence angle beyond which there is no transmission into the second media (the wave is completely reflected):

$$\theta_c = \sin^{-1} \left(\frac{c_1}{c_2} \right) \quad \text{Eq. 1.8}$$

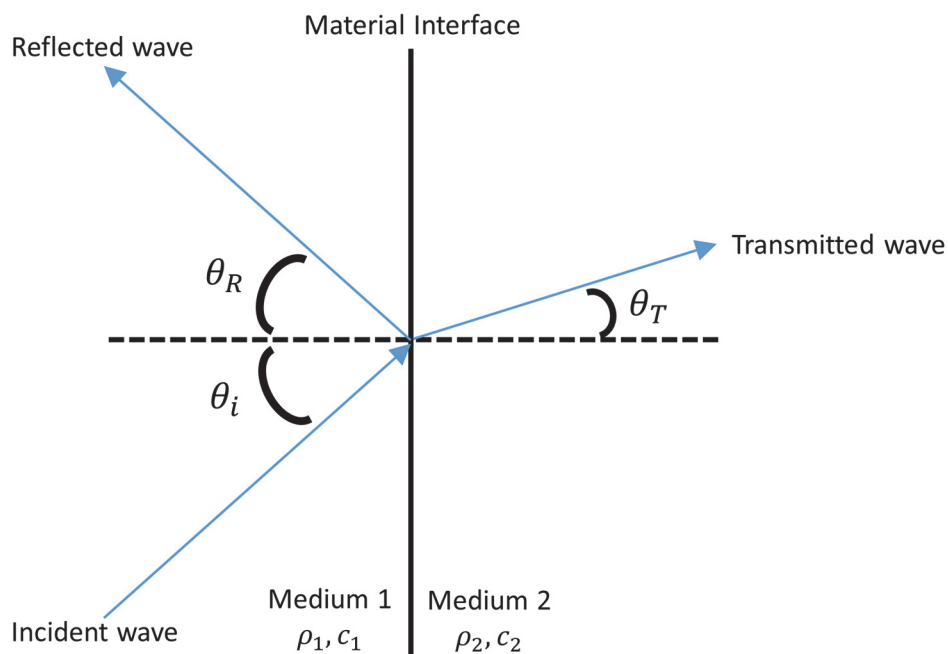


Figure 1.1 Reflection and transmission of an incident wave at an interface between two media with different acoustic properties.

The proportion of the wave which is reflected and transmitted can be described using reflectivity and transmittivity coefficients of the particle velocity, pressure, intensity, or power, all of which depend on difference in acoustic impedance Z between the two media as well as the angle of incidence of the incident wave. For example, the pressure reflectivity (R_p), which describes the ratio of reflected (p_r) to incident pressure (p_i), and the pressure transmittivity (T_p), which relates the ratio of transmitted pressure (p_t) to p_i , are given by:

$$R_p = \frac{p_R}{p_i} = \frac{Z_2 \cos \theta_i - Z_1 \cos \theta_T}{Z_2 \cos \theta_i + Z_1 \cos \theta_T} \quad \text{Eq. 1.9}$$

$$T_p = \frac{p_T}{p_i} = \frac{2Z_2 \cos \theta_i}{Z_2 \cos \theta_i + Z_1 \cos \theta_T} \quad \text{Eq. 1.10}$$

1.2.2 Generation of ultrasound

Ultrasound is typically produced by piezoelectric materials, such as quartz, or more commonly for medical applications, lead zirconate titanate (PZT). Piezoelectric materials are characterized by an asymmetric crystal lattice structure that changes its physical dimensions under the application of an electric field. When an alternating electrical field is applied across a piezoelectric material, displacements of positive and negative charged portions of the lattice result in physical expansion and contraction of the piezoelectric material at the same frequency, producing a mechanical pressure wave. Reciprocity also holds; as the piezoelectric crystal is deformed or stressed mechanically, as occurs when exposed to a pressure wave, displacements of positive and negative charges within the lattice result in voltage and electric field generation.

By varying the material composition and manufacturing processes, PZT materials with different vibrational properties can be produced. For therapeutic ultrasound, which relies on continuous-wave, high-intensity acoustic output for thermal generation, PZT formulations with high mechanical Q factors (e.g., PZT-4, PZT-8) are preferable. These materials result in minimal cyclical energy losses under continuous excitation, and as such operate within a narrow frequency band. The resonance frequency of the transducer is the frequency at which maximum displacement amplitudes can be generated at the transducer faces, and occurs when the half-wavelength of the frequency is equal to the thickness of the transducer PZT along the driving direction. In order to drive the PZT, an electrical sinusoidal excitation signal is applied across electrodes that are plated along the top and bottom surfaces of the PZT, thereby defining the direction of propagation for

output waves. Air is commonly used as the backing material when mounting therapeutic transducers onto applicator housing, as it maximizes reflection of acoustic waves from the back face of the transducer, and consequently allows maximum acoustic output from the front face to the load.

PZT can be machined and manufactured to produce ultrasound transducers of arbitrary geometries and dimensions. Commonly utilized transducer geometries include flat disks/rectangles/squares, cylindrical tubes, and curvilinear-planar or spherically-focused sections. Flat transducers produce a relatively collimated and directional spatial distribution of acoustic energy, or beam-pattern, whereas cylindrical tubes produce beam patterns that radially diverge from the outer face. Curvilinear and spherically-focused transducers focus the beam to produce a localized region of higher focal intensity, and the intensity gain at the focus, or focal gain, is a function of the aperture size, distance from the transducer surface to the focus (focal length), and wavelength. A larger aperture, shorter focal length, and/or shorter wavelength (higher frequency) all result in larger focal gains, assuming propagation in a non-attenuating medium.

Focusing of ultrasonic beams can also be accomplished using acoustic lenses, which are composed of materials with different speeds of sound from the coupling medium (typically water), causing refraction of the beam according to Snell's law as it traverses the material interface. In general, acoustic lenses offer the advantage of flexibility as compared to a static curved transducer geometry, as a single transducer could produce a variety of different beam patterns by switching lenses. Both solid and fluid lenses have been utilized in practice, with solid plastic-based lenses being the most common for thermal applications.³⁹ Solid lenses typically have a higher speed of sound as compared to water, and thus traditionally use a plano-concave geometry for focusing. Conversely, fluid lenses tend to have a lens fluid with a lower speed of sound, and thus use a

convex geometry to focus the beam as it crosses the lens-water interface. Solid lenses offer the advantage of precise manufacturing capabilities to create more complex geometries and resultant beam patterns⁴⁵⁻⁴⁷, but employ materials (e.g., polystyrene) with a higher absorption coefficient compared to lens fluids. Fluid lenses, which typically enclose the lens fluid using a distensible membrane, offer additional versatility through lens designs that permit real-time adjustment of the focal length by changing the lens' radius of curvature.⁴⁸

Ultrasound focusing can also be achieved using curved acoustic reflectors, akin to focusing light with mirrors, or by using phased array transducers with electronic steering. Phased arrays consist of 1D or 2D transducer arrays with each transducer element capable of being independently driven at a specified phase. Driving signals can be phased appropriately between the elements to produce constructive interference of all the output waves at the desired foci, which can be generated at arbitrary spatial positions in a two-dimensional space for a 1D array and in a three-dimensional space for a 2D array. Electronic focusing with phased arrays provides the most versatile means of steering an ultrasound beam in real-time, but also involves the most complexity in transducer design, manufacturing, and operation, and is much more expensive compared to the other focusing methods.

1.2.3 Acoustic field modeling

Various numerical models have been developed to simulate acoustic pressure distributions generated from single or multiple transducers of arbitrary geometry, dimensions, and operating frequency. The simulated beam pattern generated from an ideal, uniformly vibrated transducer is regarded as a suitable approximation for a real transducer of the same geometry/frequency. Some of the factors that contribute deviations between the real and simulated transducers may include manufacturing tolerances (e.g., non-uniform transducer thickness, PZT material inhomogeneities)

or effects of mechanical clamping from mounting transducers onto applicator devices, which lead to non-uniform surface vibration when powered.

Generally speaking, the beam patterns of all standard transducer geometries can be subdivided into two regions: the near-field and the far-field. The near-field region extends from the transducer face to the position of the last axial pressure maxima for flat transducer geometries, and is characterized by complex distributions of pressure peaks and valleys that decrease in spatial frequency as the distance from the transducer increases. The far-field extends beyond the last pressure maxima, and is characterized by smoothly decreasing pressure magnitude with depth and divergence of the beam in the transverse plane beyond the dimensions of the transducer. An example beam pattern, corresponding to acoustic intensity distribution in the longitudinal plane of a simulated 1.5 MHz flat disk transducer (25.4 mm aperture diameter) is shown in Figure 1.2. The distance from the transducer face to the near-field-far-field transition depth increases as the transducer aperture increases and the wavelength decreases (higher frequency). For focused transducers, the geometric focal region marks the near-far-field transition, and greater divergence is typically seen beyond the focus as compared to flat transducers, due to the greater geometric divergence angle of the transducer.

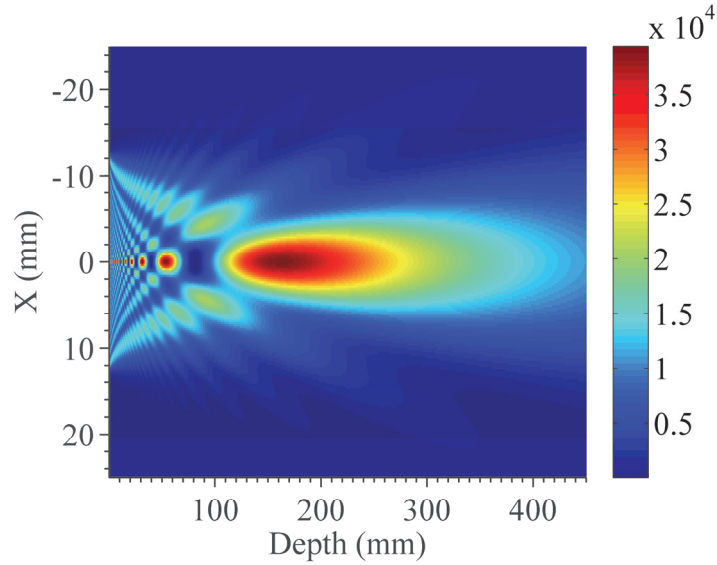


Figure 1.2 Simulated longitudinal intensity distribution (W/m^2) in water for a 25.4 mm diameter, 1.5 MHz flat disk transducer.

Linear propagation models are commonly employed to simulate the acoustic fields of ultrasound transducers that operate at sufficiently low intensities to preclude nonlinear propagation phenomena. Many of these models are based off the Rayleigh-Sommerfeld (RS) integral, which models wave diffraction effects by discretizing the transducer surface into infinitesimal baffled point sources that radiate spherically into an infinite half-space.⁴⁹ Pressure can be calculated at each field position by summing up the contribution of each point source, which is described by the Green's function:

$$\frac{e^{-jkr}}{2\pi r} \quad \text{Eq. 1.11}$$

j is $\sqrt{-1}$, k is the wave number [rad/m], and r [m] is the distance from the point source to the field position. While there is no general closed-form solution for the RS integral, it can be discretized and calculated numerically:

$$p(x, y, z) = \frac{j\rho ck}{2\pi} \sum_{n=1}^N u_n \frac{e^{-jkr_n}}{r_n} \Delta S_n \quad \text{Eq. 1.12}$$

where subscript n corresponds to the n th element of N total elements, ΔS_n is the area of the n th element, ρ is the density of the propagating medium, c is the speed of sound, and u_n [m/s] is the normal particle velocity of the n th element. This discretized expression is computationally intensive due to the small size requirements of the “point source” sub-elements relative to the wavelength.

The rectangular radiator method is an approximation of the discretized form of the RS integral, and involves subdividing the transducer surface into small rectangular elements of width Δw and height Δh .⁵⁰ The pressure contribution from each sub-element is calculated using the far-field approximation of a rectangular transducer, permitting larger element sizes, and thereby faster computation time, as the distance between the field position and the center of the sub-element increases. The rectangular radiation algorithm is shown below:

$$p(x, y, z) = \frac{j\rho c}{\lambda} \sum_{n=1}^N \frac{u_n}{r_n} e^{-jkr_n} \text{sinc}\left(\frac{kx_n \Delta w_n}{2r_n}\right) \text{sinc}\left(\frac{ky_n \Delta h_n}{2r_n}\right) \Delta w_n \Delta h_n \quad \text{Eq. 1.13}$$

where λ [m] is the wavelength, r_n [m] is the distance from the center of the n th element to the field point, Δw_n [m] and Δh_n [m] are the width and height of the n th element, and x_n [m] and y_n [m] are the difference in azimuthal and elevation coordinates between the tissue point and the element center. The size requirement of the rectangular sub-elements must fulfill the condition:

$$\Delta w, \Delta h \leq \sqrt{\frac{4\lambda z}{F}} \quad \text{Eq. 1.14}$$

where z is the axial distance from the transducer surface and F , representing the number of near-field-to-far-field transition distances from the source to the field point, is typically selected to be

≥ 20 for sufficient accuracy.⁵¹ Although the rectangular radiator method was originally developed for modeling flat rectangular transducers, it can be adapted to model arbitrary transducer geometries, including curved transducers, by discretizing the surface geometry into rectangular elements that are rotated and sufficiently small for close agreement with the original geometry. The rectangular radiator algorithm can be applied, making sure that the x_n and y_n distances are with respect to the local orientation of each rectangular subelement, which can be calculated using rotation matrices for simple geometries (e.g., tubular, curvilinear, spherically-focused).^{52,53} In order to account for attenuation of ultrasound waves as it propagates through lossy mediums, the complex wave number $k^c = k - j\mu$ is substituted for k in the exponential term, where μ is the pressure amplitude attenuation coefficient [Np/m] in the medium.

1.2.4 Ultrasound heating devices

Ultrasound energy is applied to heat body tissues using applicators that contain active transducer elements. Applicators have been developed for non-invasive, extracorporeal application as well as for minimally invasive insertion into the body through percutaneous, laparoscopic, or intracavitary delivery pathways.

Extracorporeal high intensity focused ultrasound (HIFU) uses large external focused transducers or phased arrays operating at ~ 0.5 -2 MHz to transmit acoustic energy up to ~ 10 -15 cm into the body and form tight foci and precise thermal lesions at the target tumor site.⁵⁴⁻⁵⁷ Acoustic intensities are low in tissues exposed to the pre-focal acoustic beam, but very high at the focus, permitting formation of localized small ‘cigar’ or ‘rice grain’ shaped thermal lesions ranging in size ~ 1 -3 mm width and 8-20 mm length.⁵⁴⁻⁵⁶ Each individual sonication duration is short, on the order of a few seconds, with rapid temperature elevation at the focus due to the very high focal intensities employed (up to $\sim 20,000$ + W/cm²).^{55,58} Such high intensities can augment heating by

nonlinear generation of higher harmonic emissions, which have higher tissue absorption, as well as by the formation of inertial cavitation in the tissue.⁵⁷

In order to treat a large tumor, the external transducer can be mechanically translated; or, if using a phased-array system, electronic steering can be used to change the position of the focal zone and sweep out the full volume. Due to the small size of each individual lesion, and the often requisite cooling period between sonications to prevent temperature build-up in sensitive tissues in the pre-focal or post-focal zones, total treatment times can extend hours, and increases for larger tumor volumes.^{58,59} Furthermore, anatomical targets need to have a clear acoustic window, unimpeded by bone or gaseous interfaces where ultrasound is preferentially absorbed or reflected, which makes treatment in tissues near the lungs, bowels, bones, or other sensitive anatomy challenging. Extracorporeal HIFU is compatible with and commonly paired with image-guidance, including ultrasound and MRI, for treatment planning and monitoring.^{60,61} It has been clinically applied for thermal ablation of tumors in many different sites, including the liver, breast, kidney, bladder, pancreas, prostate, and used for treating sarcoma, bone tumors, and uterine fibroids, among others.^{54,55,62}

Catheter-based ultrasound devices have been developed as a minimally-invasive alternative to generate thermal therapy within body tissues, and can be broadly classified into devices for interstitial/percutaneous delivery, and those for endoluminal/endocavity delivery and deployment.⁶³⁻⁶⁵ Interstitial ultrasound applicators are inserted directly inside or adjacent to the target tissue, and are either inserted stand-alone or with the applicator contained by a plastic delivery catheter that contains circulatory water flow for coupling of the acoustic energy to tissue and cooling of the transducers during operation.^{66,67} These applicators contain one to a few tubular or planar transducer elements (1.2-2 mm x 5-17 mm) along the device length, which can be

independently powered to tightly control the axial extent of heating.^{68,69} Tubular transducers, typically driven at resonance frequencies of 7-9 MHz, can also be sectored and powered independently for angular control over the heating expanse, allowing highly conformal thermal lesion formation.^{67,68,70} These applicators are capable of creating thermal lesions with up to 15-21 mm radial penetration in 5-10 minute treatment times, and have been evaluated in *in vivo* animal studies of the prostate, liver, brain, and other soft tissues.⁷⁰⁻⁷²

Endoluminal and endocavitary ultrasound applicators are delivered through and deployed within body lumens in order to target and treat adjacent tissue targets. These applicators tend to be larger than interstitial applicators, ranging from ~2 mm OD for endovascular and intraductal applications up to ~25 mm OD for endorectal applicators intended for transrectal prostate ablation.^{63,65} Simple applicator designs consist of an array (one to a few elements) of transducer elements situated at the distal end of a catheter assembly, surrounded by a balloon that contains circulatory water flow for acoustic coupling, cooling of the transducer, and cooling of the adjacent luminal wall if luminal sparing is desirable. Once positioned, energized transducers generate highly localized heating deposition, with spatial distribution and penetration determined by transducer geometry and operating frequency, and can conformally sweep out larger treatment volumes by mechanically translating or rotating the applicator assembly. Transducer configurations typically include an array of planar, tubular, curvilinear, or spherically-focused transducer elements situated along the length of the applicator, with independent power control to tailor heating extent. More complex designs have been developed, featuring phased array transducers, to mitigate the necessity for mechanical manipulation of the applicator to steer the energy deposition.^{73,74} Other more novel applicator designs incorporate deployable components,

such as an inflatable parabolic reflector balloon, to modulate the beam and heating pattern at the target site without impeding device delivery.⁷⁵

A large variety of different endoluminal applicator designs, each designed for a specific tissue target, delivery pathway, and clinical application, have been developed and evaluated in pre-clinical or clinical settings. Endogastric placement of endoluminal devices along the upper GI tract (esophagus, stomach, or small intestines) have been developed to deliver thermal ablation to esophageal⁷⁶, liver^{77,78}, or pancreatic tumors.⁷⁹ Prostate tumors or benign prostate hyperplasia have been ablated using ultrasound devices placed in the urethra⁸⁰⁻⁸³ or in the colorectal tract.^{84,85} Endovascular devices have been developed for renal denervation⁸⁶ and pulmonary vein isolation.^{75,87,88} Endocervical devices for hyperthermia in conjunction with high-dose rate brachytherapy for advanced cervical cancer have been investigated.⁸⁹ Similar applicator configurations have also been developed for laparoscopic abdominal cavity access and ablation of renal tissue.⁹⁰

Ultrasound-based thermal therapy offers significant advantages as compared to other clinically-utilized ablative modalities, including radiofrequency (RF), microwave (MW), cryotherapy, and laser ablation. Ultrasound permits much more precise and conformal control over the spatial deposition of heat, as afforded by choice of transducer geometry and frequency as well as the fundamentally smaller wavelength of therapeutic ultrasound relative to electromagnetic (EM)-based RF and MW radiation, which inherently permits tighter focusing capabilities and more precise energy deposition. Furthermore, at therapeutic frequencies (~0.5-10 MHz for ultrasound vs. 375-1000 kHz for RF vs. 900-2500 MHz for MW), the attenuation of ultrasound waves in tissue is less than for EM-based modalities, which permits deeper energy and thermal penetration for a set source aperture.⁹¹⁻⁹³ Furthermore, ultrasound applicators can be designed to be non-

magnetic, making them compatible with MRI image-guidance and MR temperature imaging (MRTI) for treatment monitoring.⁹ Disadvantage of ultrasound applicators relative to other modalities would include their higher complexity in design, fabrication, and operation relative to simpler modalities like RF. The preferential absorption of ultrasound energy in bone and high reflection at interfaces between soft tissue and lungs, bowel, or bones can also negatively impact treatment delivery depending on the application site.

Compared to external HIFU, catheter-based ultrasound is more invasive but provides better energy localization and more volumetric heat generation. This can lead to shorter treatment times, ranging from 10-30 minutes as compared to the order of hours.⁶³ Once positioned, applicator operation can be much simpler as compared to external HIFU, which often necessitates active tissue tracking and phase correction for beam steering in the presence of tissue motion (e.g., respiration or cardiac related motion) or changing acoustic windows.⁹⁴ Catheter-based ultrasound can also provide a means to target anatomical sites adjacent to bowel, lung, or bone tissues which would have challenging acoustic windows for access using extracorporeal ultrasound sources.

1.2.5 Mechanical effects of ultrasound

Beyond inducing direct thermal effects in tissue, ultrasound energy also interacts with tissue through non-thermal physical mechanisms, which can have clinical applications. All objects in an ultrasonic field experience a steady radiation force, caused by a transfer of momentum from the traveling wave to tissue contents.⁹⁵ Radiation force is closely related to radiation torque, which causes rotational motions in small (cellular and sub-cellular) particles, as well as acoustic streaming, which is a bulk fluid flow produced by ultrasound.⁹⁶ Tissue displacement, due to radiation force, is the primary mechanism behind ultrasound elastography, which has been clinically applied for imaging and staging of various tumor types based on their distinct mechanical

properties as compared to normal tissue.⁹⁷ Radiation force can also be measured with simple force balance setups, as is commonly utilized for calibration of ultrasonic fields and devices.⁹⁸

Cavitation stems from the interaction of ultrasound with gas bubbles, which can be generated at gaseous nucleation sites *in vivo*. Cavitation formation is promoted at lower frequencies and at higher magnitudes of the negative peak pressure. Non-inertial, or stable cavitation formation involves oscillatory expansion and contraction of gas bubbles over pressure cycles. At high enough pressure amplitudes, progressive growth of cavitation bubbles over pressure cycles can precipitate a violent collapse of the cavitation bubble, known as inertial or transient cavitation, which imparts tremendous thermal and mechanical stresses on the local tissue environment.⁹⁹ Inertial cavitation has been applied clinically both to augment thermal generation for ablation treatments (predominantly for extracorporeal HIFU⁵⁷) and as a predominant mechanism of lithotripsy, which generates ultrasonic mechanical shockwaves in tissue that have been clinically applied for the physical degradation of kidney stones.¹⁰⁰ Mechanical interactions of ultrasound with microbubbles, which can be injected locally or systemically into the body, have been utilized for therapeutic drug/gene delivery applications. Encapsulated microbubbles that contain drug/gene payloads can be triggered to release their contents at specific sites using ultrasound exposure.¹⁰¹ Interactions of ultrasound and microbubbles can also induce enhanced permeability of vasculature, including the blood-brain barrier, to enhance targeted therapeutic delivery.¹⁰²

1.3 MR temperature imaging

Thermal therapy procedures are typically paired with imaging modalities, such as x-ray/fluoroscopy, CT, diagnostic ultrasound, or MRI in order to guide applicator delivery and monitor or confirm therapeutic delivery. Of the aforementioned modalities, MRI currently

possesses the most developed and robust techniques for real-time temperature tomography, and offers the best soft-tissue contrast for anatomical imaging which aids in accurate target delineation and applicator delivery.¹⁰³ The capability to monitor treatment-related temperature evolution during thermal ablation or hyperthermia is invaluable, both in ensuring an effective therapeutic delivery as well as for preventing undesirable thermal damage to sensitive tissues adjacent to the target region.

There are a number of MR parameters that vary as a function of temperature, including the proton density, T₁ and T₂ relaxation times, magnetization transfer, the diffusion coefficient, and the proton resonance frequency (PRF).¹⁰⁴ While all of these parameters have been investigated for temperature mapping, methods based on the shift of the PRF with temperature change have many advantages over the others and as such have seen the most research development and clinical application.¹⁰³⁻¹⁰⁵ PRF-based methods are based on the change in the shielding constant for a water proton as temperature increases or decreases, due to the stretching or compression of hydrogen bonds as a function of temperature. The shielding constant affects the local magnetic field experienced by the water proton, which in turn determines the resonance or Larmor frequency that the proton will precess at after RF excitation in an MR pulse sequence. This effectively translates into a local phase shift between two images of the same anatomical imaging slice, one taken before and the other after the temperature change occurred. The phase-difference, evaluated on a per-voxel basis, between the before (“baseline” or “reference”) image and the after image can be derived as:¹⁰³⁻¹⁰⁵

$$\Delta\phi = 2\pi\gamma\alpha B_0 T E \Delta T \quad \text{Eq. 1.15}$$

where $\Delta\phi$ is the phase difference between the treatment image and baseline, γ is the gyromagnetic ratio (42.58 MHz/T), α is the temperature sensitivity coefficient (~ 0.01 ppm/°C), ΔT is the

temperature change ($^{\circ}\text{C}$), and TE is the echo time used in the gradient echo (GRE) image acquisition scheme. This expression can be simply re-arranged to calculate the change in temperature at each image voxel.

Thermometry using the PRF shift method has the significant advantage of near-independence of the temperature sensitivity coefficient across different soft-tissue types and its linearity over a wide temperature range of -15 - 100 $^{\circ}\text{C}$.^{104,105} Furthermore, GRE-based scanning sequences are relatively simple to implement and offer good spatial (~ 1 - 3 mm) and temporal (~ 3 s per slice) resolution, enabling real-time monitoring during a thermal ablation or hyperthermia treatment. One important caveat is that the tissues must be aqueous, as lipids possess a negligible change in resonance frequency with temperature change, and as such fat or tissues with lipid content are sources of artifact that compromise accurate thermometry.¹⁰⁵ Another important detail is that the signal-to-noise ratio of the temperature measurement is a function of the GRE signal intensity in the voxel.¹⁰⁴ This means that imaging sequence parameters need to be tailored based on the target tissue in order to maximize thermometry SNR therein, and that magnetic susceptibility artifacts, which create local signal loss and void artifacts in GRE images, also prevent accurate thermometry in affected voxels.

As the PRF method is primarily relies on subtraction of a baseline image to measure the relative temperature change, there are many sources of artifact stemming from baseline misregistration, which can happen due to motion and scanner phase-drift, among other means. Tissue displacement, caused by patient motion or more prevalently by respiration or cardiac-induced motion, results in misregistration between the treatment image and baseline, producing significant temperature artifacts.¹⁰⁴ Respiration-related motion affects many abdominal organs, especially those in the upper abdominal area, and tissues close to or adjacent to lungs have the

additional complication of the changing bulk susceptibility of the lungs during respiration, which can also fundamentally change the background phase of acquired images.¹⁰⁴ There are a number of strategies that can be employed to mitigate motion-related misregistration errors, however. One of the simplest techniques is to perform respiratory gating, which involves tracking the respiratory cycle and timing the acquisition of GRE thermometry sequence so that the image is consistently acquired during the same phase of respiration – ideally during expiration.¹⁰⁶⁻¹⁰⁸ This method works best under controlled respiration and anesthesia, but has been performed under free-breathing conditions.¹⁰⁶ Another method involves acquiring multiple-baseline images prior to treatment that adequately sample the respiratory cycle. During treatment, each thermometry image or acquisition is paired with the appropriate baseline using navigator echoes or intercorrelation coefficients between anatomical images.^{94,109} A technique that eliminates the need for baseline subtraction in PRF-based thermometry, known as referenceless thermometry, has also been developed, which works by mathematically modeling and isolating the background phase in the image from the temperature-induced phase.¹¹⁰ This technique relies on prior knowledge of where the temperature rise will occur in the image, in order to properly identify and fit the background phase, and also works best in imaging planes where the background phase is smoothly varying.¹¹⁰ As a result, this technique would be difficult to apply in imaging planes that contain excessive susceptibility differences between tissues, such as near lung or bowels. Background phase drift is another relevant complication in accurate PRF-based thermometry, particularly for longer duration thermal therapy procedures. Drift of the external magnetic field can be caused by intense driving of the gradient coils, among other things, and results in a changing background phase in thermometry images over time.¹¹⁰ This can result in erroneous temperature measurements for PRF methods that rely of baseline subtraction. Phase-drift can be corrected for by using standard reference phantoms

that remain at a fixed temperature throughout the treatment or are temperature insensitive (e.g., oils) and as such can be used to monitor and model the spatial distribution of background phase-drift in each image and separate it from temperature-induced phase change.¹¹⁰

1.4 Biothermal modeling

Numerical modeling can be applied to simulate thermal ablation and hyperthermia procedures, permitting calculation of resultant temperature and thermal dose distributions in various tissue models, as generated by an energy-based applicator source. As such, modeling serves as an imperative aid in the design and evaluation of applicators intended for thermal therapy, as well as for evaluating various thermal therapy treatment strategies and approaches.

Biothermal modeling, as applied to a biological system or tissue, is typically based upon Pennes bioheat equation, as shown below:¹¹¹

$$\rho C \frac{dT(x, y, z)}{dt} = \nabla[k \cdot \nabla T(x, y, z)] - \omega_b C_b [T(x, y, z) - T_b] + Q(x, y, z) \quad \text{Eq. 1.16}$$

where ρ (kg/m³) is tissue density, C (J/kg/°C) is the specific heat of tissue, T (°C) is tissue temperature, k (W/m/°C) is thermal conductivity, ω_b (kg/m³/s) is blood perfusion, C_b (J/kg/°C) is the specific heat of blood, and T_b (°C) is capillary blood temperature (37 °C). Q (W/m³) is the power or heat deposition in tissue, often used for metabolic heat generation. For modeling thermal ablation or hyperthermia-induced temperature elevation, this metabolic heat generation term is generally negligible and replaced with energy-based power deposition. For ultrasound-based energy sources, the power deposition can be derived from the acoustic pressure or intensity distribution in the modeled tissue, as below:

$$Q_{ac} = 2\alpha I_{SPTA} = \frac{\alpha |p|^2}{\rho c} \quad \text{Eq. 1.17}$$

where α is the acoustic absorption coefficient, p (Pa) is the pressure amplitude, ρ (kg/m³) is the tissue density, and c (m/s) is the tissue speed of sound. I_{SPTA} is the spatial-peak, temporal-average acoustic intensity, which for continuous wave excitation (assuming plane-wave analysis) is equal to:

$$I_{SPTA} = \frac{|p|^2}{2\rho c} \quad \text{Eq. 1.18}$$

As a partial-differential equation, Pennes equation can be numerically evaluated using finite-difference or finite-element methods (FEM). It incorporates terms of change in storage, heat conduction, blood perfusion, and power deposition, but contains many assumptions. In particular, the base equation only models capillary-level perfusion of tissues as a heat-sink, and assumes that it is isotropic and homogeneous for a given tissue type. As a result, the effects of large blood vessels, which can act as significant localized heat sinks in thermal therapy procedures, are ignored.¹¹² For models incorporating large blood vessels, significant improvements in accuracy can be made by incorporating their heat-sink effects, which can modeled using heat-flux boundary conditions at the vessel-tissue boundary.¹¹² Other modifications to the equation can be incorporated to augment their accuracy for thermal ablation modeling, as many tissue properties, including thermal conductivity, capillary perfusion, and acoustic attenuation and absorption coefficients, transiently vary as a function of temperature and thermal dose exposure.¹¹³

In order capture effects of complex patient anatomy, incorporating morphology of heterogenous organs and their proximity to other anatomical structures of interest, creating three-dimensional simulated geometries based on patient-specific anatomies can provide a more representative means of evaluating thermal therapy treatment strategies, as opposed to using simple, homogeneous tissue block models. These patient-specific geometries can be created using

segmentation of MRI/CT/ultrasound image data sets. With regards to the development of ultrasound applicators for thermal therapy, these models can directly provide the size, shape, and depth of necessary thermal coverage, which can inform transducer design choices as well as treatment parameters such as applicator positioning, applied powers and sonication durations. They can be used to estimate expected performance and therapeutic coverage in clinical applications, as well as to evaluate sparing techniques of sensitive tissues and structures adjacent to the target region.

1.5 Thermal therapy of pancreatic cancer

Pancreatic cancer causes the fourth highest number of cancer-related mortalities in the United States, and the current 5-year survival rate is 4%.¹¹⁴ At clinical presentation, over 80% of patients are diagnosed with locally advanced or metastatic disease, which precludes curative treatment in the form of surgical resection.¹¹⁴ The current standard clinical treatment for these patients involves gemcitabine-based chemotherapy with or without adjuvant radiation therapy, but these therapies have been shown to result in only modest survival and palliative benefit.¹¹⁵ To relieve pain-related symptoms, which affects over 90% of advanced-staged patients, oral analgesics are typically administered; however, these require around-the-clock dosing for suitable palliation and have debilitating side effects, such as constipation.^{116,117} Other current palliative techniques, such as alcohol ablation of the celiac plexus, have limited efficacy in some patients and may cause severe complications.¹¹⁷

Thermal ablation has been demonstrated to provide palliative relief in patients with advanced pancreatic cancer through tumor debulking and neurolysis/denervation mechanisms, even in cases where only partial tumor volume ablation is achieved.^{19,118-120} Ablation of locally advanced and metastatic pancreatic cancer can also potentially produce a survival advantage, as

highlighted by recent efforts integrating extracorporeal HIFU ablation with chemotherapy.¹²¹ Many ablative modalities, including radiofrequency ablation, cryoablation, microwave ablation, HIFU, photodynamic therapy, and irreversible electroporation are currently being developed or clinically investigated for treatment of pancreatic cancer.¹⁹ With the exception of HIFU, all of these methods rely on invasive percutaneous operation, which can be difficult to safely perform in the pancreas due to the close proximity of sensitive bowel tissues and major blood vessels, leading to many treatment-related complications.¹²² As a result, better treatment safety has been achieved by applying percutaneous applicators in a laparotomy setting, which is highly invasive.^{122,123} MRI or US guided extracorporeal HIFU offers a non-invasive means of ablating tumor tissue, but relies on clear acoustic transmission into the tumor site.⁶¹ This is often obstructed by intervening organs or gas-filled bowel in close proximity to the pancreas, particularly around the pancreatic head region.^{119,120}

In addition to thermal ablation, there is also potential clinical benefit in developing hyperthermia treatments for advanced pancreatic cancer. Pancreatic tumors are often characterized by hypovascularity, hypoxia, and desmoplastic stroma, which have been hypothesized to minimize the effectiveness of standard chemotherapy and radiation treatments.¹²⁴ By transiently increasing the perfusion and oxygenation of treated tissues, hyperthermia has been shown to be an effective adjuvant therapy for both chemotherapy and radiation treatments in many cancer models.^{25,125} Clinical studies evaluating the efficacy of combining regional hyperthermia and gemcitabine with or without cisplatin for patients with advanced pancreatic cancer have begun in both Europe and Japan.^{126,127} Hyperthermia may also enhance the delivery of encapsulated drugs into desmoplastic pancreatic tumors through increasing local perfusion and, in the case of thermally sensitive drug-containing liposomes, directly triggering the release of the drug at the target site.¹²⁸

1.6 Research goals

Endoluminal catheter-based ultrasound may serve as a promising minimally-invasive alternative for delivering localized and conformal thermal ablation or hyperthermia to pancreatic tumors. As the pancreas and surrounding region contain abundant sensitive anatomy, such as bowel, pancreatic/bile ducts, and major vasculature, the spatially-precise application of heat, as provided by ultrasound sources, could be invaluable to preclude undesirable thermal injury to non-target tissues. Further, an endoluminal approach, using the gastrointestinal (GI) tract as the delivery conduit and the stomach and duodenum as applicator placement sites adjacent to the pancreas, would obviate any physical intrusion and injury into the pancreas, as experienced in percutaneous approaches, while leveraging the enhanced penetration depth of ultrasound energy in tissue. It would also circumvent acoustic window challenges, as experienced in extracorporeal HIFU treatment of pancreatic cancer, and potentially lead to comparatively shorter treatment times. Further safety and monitoring of the applicator positioning and treatment delivery could be achieved using MR image-guidance and MRTI. As such, the first part of this dissertation will focus on developing MR-compatible endoluminal ultrasound applicators and approaches for thermal therapy of pancreatic cancer, spanning both theoretical modeling studies and experimental evaluations in a porcine animal model under MR-guidance.

The second part of this dissertation will focus on explorations and analyses of novel endoluminal ultrasound applicator designs that incorporate deployable reflector and fluid lens components that serve to modulate the beam pattern and enhance acoustic output. These proposed applicator designs will address issues with conventional ultrasound applicators, including the restricted acoustic aperture and limited flexibility in output acoustic/thermal distributions, without compromising applicator deliverability through anatomical passages. These designs are envisioned

to be applied for endogastric thermal therapy of pancreatic tumors, with related theoretical analyses performed, but could be adapted for many other endoluminal ultrasound applications.

The specific goals of this research project are outlined below:

1. To develop theoretical models of thermal ablation and hyperthermia of pancreatic tumors using endoluminal ultrasound applicators, and to use calculated temperature and thermal dose distributions to bracket expected ranges of performance through parametric studies of applicator design parameters and tissue properties.
2. To generate FEM-based patient-specific anatomies of pancreatic tumors and surrounding anatomy, and to employ them in numerical simulations to evaluate the general feasibility and expected performance of endoluminal ultrasound-based thermal ablation and hyperthermia across a range of disease states.
3. To design and fabricate prototype MR-compatible endoluminal ultrasound applicators, and to characterize them using benchtop acoustic measurements and MR-guided *ex vivo* tissue and porcine cadaver thermal ablation experiments.
4. To assess the general feasibility of using MR-compatible endoluminal ultrasound applicators to generate thermal ablation of pancreatic tissue from the GI lumen under MR-guidance using an *in vivo* porcine model, and to evaluate applicator tracking and motion compensation strategies for real-time MRTI.
5. To develop numerical methods that model ultrasound propagation in applicator assemblies containing transducers, acoustic reflectors, and acoustic lenses with arbitrary geometries, and to explore a variety of design alternatives for applicator configurations with deployable components that serve to increase achievable acoustic and thermal penetration, selectivity, or volumetric coverage.

6. To perform a comprehensive parametric analysis of select deployable applicator design in order to characterize expected acoustic and thermal performance based on design parameters, and to validate theoretical modeling through proof-of-concept experimental applicator development and characterization.

1.6.1 Dissertation content

This dissertation is divided into two sections. The first section focuses on theoretical and experimental investigations related to the development of an endoluminal ultrasound applicator for delivering thermal ablation and hyperthermia to pancreatic tumors. Herein practical applicator designs, with 1-2 active transducer elements that are surrounded by cooling water balloons at the distal tip of catheter assemblies, are considered. The second section focuses on novel design concepts for endoluminal ultrasound applicators with deployable acoustic reflector and fluid lens components that can be controllably expanded or collapsed as a means of increasing the effective therapeutic aperture and augmenting energy delivery. These designs are compatible with and evaluated for applications related to endogastric placement and treatment of tissues adjacent to the stomach, such as the pancreas, but could be applied for many other endoluminal applications as well.

Chapter 1 contains a background introduction on fundamental concepts of thermal therapy, therapeutic ultrasound, acoustic/biothermal modeling, treatment monitoring using MR temperature imaging, and clinical applications of thermal therapy for pancreatic cancer.

In Chapter 2, an acoustic/biothermal modeling analysis of thermal ablation and hyperthermia of pancreatic tumors using endoluminal ultrasound applicators is presented. Comprehensive parametric studies are performed to calculate power deposition, temperature, and thermal dose distributions as a function of transducer configuration, by varying the geometry

(planar, curvilinear-focused, and tubular radial-diverging) and frequency (1-5 MHz), across a range of expected tissue properties and anatomical conditions. 3D patient-specific anatomical geometries are generated using CT datasets of patients with pancreatic cancer, with cases chosen to bracket a wide range of disease severity. Endoluminal ultrasound thermal ablation and hyperthermia treatments are simulated in these patient-specific models to evaluate feasibility of the overall approach, evaluate treatment strategies, and determine projected efficacy in terms of therapeutic tumor coverage and sparing of adjacent sensitive tissues. The work presented in Chapter 2 is published in a journal article by Adams et al. in the *International Journal of Hyperthermia* and in a SPIE conference proceedings article by Adams et al.^{129,130}

Chapter 3 presents the design, fabrication, and evaluations of prototype endoluminal ultrasound applicators intended for delivering thermal therapy to pancreatic tumors from the GI tract (stomach/duodenum) lumen. A family of applicators, each made with a separate transducer configuration, are described and characterized using benchtop force-balance measurements, hydrophone beam-plots, and MRTI temperature measurements in phantom, *ex vivo* tissue, and *ex vivo* porcine cadaver heating trials. Evaluations of device deliverability/tracking, MRTI motion-compensation strategies, and ablative temperature generation using the prototype applicators for endoluminal ablation of pancreatic tissue under MR-guidance in *in vivo* porcine models are reported. The majority of the work presented in Chapter 3 is published in a journal article by Adams et al. in *Medical Physics* and in a SPIE conference proceedings article by Adams et al.^{130,131}

Chapter 4 explores concepts for novel designs of endoluminal ultrasound applicators that incorporate deployable, balloon-based acoustic reflector and fluid lens components – allowing for smaller insertion profile but improved localization of energy and therapy. An acoustic modeling methodology to simulate wave propagation, refraction, and reflection through the proposed

assembly is introduced, and used to analyze acoustic properties of individual components and complete applicator assemblies. Comprehensive parametric studies, spanning 3D acoustic and biothermal tissue heating simulations, are performed for two applicator assembly designs representing “end-firing” and “side-firing” configurations. Experimental proof-of-concept applicator assemblies were developed and characterized in order to validate theoretical analyses. The majority of the work presented in Chapter 4 is published in a journal article (currently under review) by Adams et al. in *Medical Physics*, and in a SPIE conference proceedings article by Adams et al.¹³²

Chapter 5 contains a summary of the findings from this dissertation, and a discussion of future directions for its constituent research projects.

Appendix A details the design of an MR-compatible endoluminal ultrasound applicator with endoscopic steering and articulation capabilities. Appendix B describes additional designs for deployable endoluminal ultrasound applicators that feature acoustic reflectors, fluid lenses, and/or phased arrays transducer sources, and presents preliminary theoretical analyses of each.

Chapter 2

Thermal therapy of pancreatic tumors using endoluminal ultrasound: parametric and patient-specific modeling

2.1 Abstract

Purpose: To investigate endoluminal ultrasound applicator configurations for volumetric thermal ablation and hyperthermia of pancreatic tumors using 3D acoustic and biothermal finite element models.

Materials and Methods: Parametric studies compared endoluminal heating performance for varying applicator transducer configurations (planar, curvilinear-focused, or tubular radial-diverging), frequencies (1-5 MHz), and anatomical conditions. Patient-specific pancreatic head and body tumor models were created and used to evaluate feasibility of generating hyperthermia and thermal ablation using an ultrasound applicator positioned in the duodenal or stomach lumen. Temperature and thermal dose were calculated to define ablation ($>240 \text{ EM}_{43^\circ\text{C}}$) and moderate

hyperthermia (40-45 °C) boundaries, and to assess sparing of sensitive tissues. Proportional-integral control over applied powers was incorporated to regulate maximum temperature to 70-80 °C for ablation and 45 °C for hyperthermia in target regions.

Results: Parametric studies indicated that 1-3 MHz planar transducers are most suitable for volumetric ablation, producing 5-8 cm³ lesion volumes for a stationary 5 minute sonication. Curvilinear-focused geometries produce more localized ablation to 20-45mm depth from the GI tract and enhance thermal sparing ($T_{\max} < 42$ °C) of the luminal wall. Patient anatomy simulations show feasibility in ablating 60.1-92.9% of head/body tumor volumes (4.3-37.2 cm³) with <15 EM_{43°C} in the luminal wall for 18-48 min treatment durations, using 1-3 applicator placements in GI lumen. For hyperthermia, planar and radial-diverging transducers could maintain up to 8 cm³ and 15 cm³ of tissue, respectively, between 40-45 °C for a single applicator placement.

Conclusions: Modeling studies indicate the feasibility of endoluminal ultrasound for volumetric thermal ablation or hyperthermia treatment of pancreatic tumor tissue.

2.2 Introduction

Endoluminal and intracavitary catheter-based ultrasound applicators can provide a minimally-invasive solution for delivery of thermal ablation or hyperthermia to tumors accessible from body lumens. Significant advantages of this ultrasound-based approach for thermal therapy include the high degree of control over the spatial distribution of energy as compared to other modalities, direct localization of the energy source and therapy adjacent to the target zone, as well as compatibility with diagnostic ultrasound or MR guidance techniques for possible real-time treatment monitoring and feedback control.⁶³ Specific applicator configurations for placement in the upper gastrointestinal (GI) tract have been applied clinically for endoluminal ablation of esophageal and biliary tumors.^{76,133} An endoscope with a miniature spherically-focused transducer

at the tip has also been developed and experimentally validated to create ablation lesions in porcine pancreas and liver under endoscopic ultrasound guidance.^{79,134}

Simulation studies incorporating parametric analysis and patient specific anatomical models have been applied for device design and performance evaluations of endoluminal and interstitial ultrasound technologies for thermal therapy (e.g.,^{83,135-140}). The objectives of this study are to investigate the feasibility and to characterize the performance of delivering volumetric thermal therapy to target regions within the pancreas using an endoluminal ultrasound applicator positioned within the GI tract. 3D acoustic and biothermal finite element models were developed to calculate power deposition patterns and resulting temperature and thermal dose distributions for both ablation and hyperthermia treatment paradigms. Full 3D multi-component models were used to perform parametric studies across applicator design parameters and anatomical variations to determine favorable designs and establish ranges of expected performance. Comprehensive patient-specific models, based on segmentation of CT images of pancreatic tumors and surrounding anatomy, were developed to serve as generalized anatomy models that bracket a range of representative geometries and potential target volumes. Using specific device configurations, as informed by the parametric studies, both thermal ablation and hyperthermia treatments were independently simulated in these models to evaluate delivery strategies and capabilities for achieving volumetric coverage of pancreatic tumor tissue while minimizing exposure to surrounding/intervening normal tissues.

2.3 Materials and Methods

2.3.1 Endoluminal ultrasound applicator

As shown in Figure 2.1, the endoluminal applicator would be inserted orally through the esophagus, and, akin to an endoscope, positioned in the stomach or duodenal lumen adjacent to

the tumor-bearing region of the pancreas. Acoustic energy would be directed through the GI luminal wall into the tumor by an ultrasound transducer array on the distal tip of the applicator. A balloon covering the transducers, containing circulating cooled water, would provide coupling of the acoustic energy into the adjacent tissue and cool the wall tissue to protect it from thermal injury.

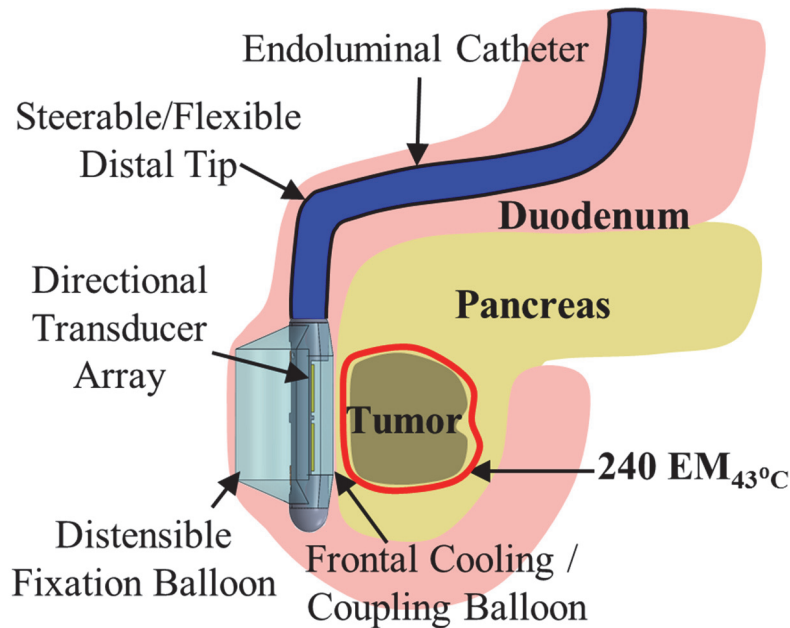


Figure 2.1 Schema and concepts of an endoluminal ultrasound applicator positioned in the GI tract for thermal therapy of pancreatic tumors. The applicator is illustrated as positioned in the duodenum for sonication of tumors in the head of the pancreas, following placement and insertion strategies common in endoscopy. Transducer arrays are configured for focused or diffuse patterns to provide a high degree of spatial control and volumetric heating.

The dimensions of the applicator and transducer assembly were conservatively chosen to be within a 15 mm diameter limit, following general constraints of the gastrointestinal anatomy on dimensions of endoscopic devices.¹⁴¹ As illustrated in Figure 2.2, four separate transducer configurations were considered for this study: planar, tubular section, curvilinear along the azimuthal axis of the applicator (lightly focused), and curvilinear along the elevation axis (strongly focused). The dimensions of the planar and curvilinear transducers were modeled as 10 mm width x 20 mm length, and the tubular transducer was modeled with a 20 mm length, 80° active acoustic

sector angle, and 6 mm radius of curvature. These geometries were chosen both due to their practical implementation and to examine diffuse vs. focal acoustic distributions. The distal tip of the applicator transducer assembly was modeled as a 12 mm diameter x 50 mm length cylinder with a single central transducer and the cooling balloon boundary situated 6.5 mm from the transducer surface, based off existing devices developed by our group.

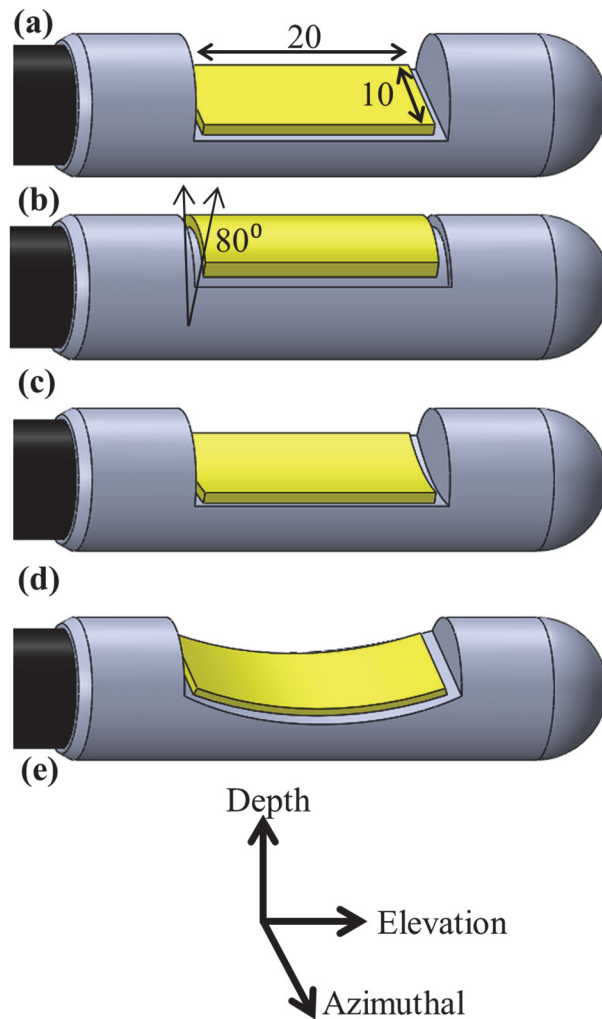


Figure 2.2 Considered transducer (yellow) configurations: (a) planar, (b) tubular section, (c) lightly focused curvilinear along the azimuthal direction, and (d) strongly focused curvilinear along the elevation direction, with respect to the (e) transducer coordinate system. The planar and curvilinear transducers are 20 x 10 mm along the elevation and azimuthal directions, and the tubular section is an 80° sector with a 6 mm radius of curvature and a 20 mm length.

2.3.2 Theory

3D acoustic and bioheat transfer models were implemented to calculate the acoustic intensity patterns and resulting transient temperature and thermal dose profiles produced by ultrasound applicators in an endoluminal anatomical setting. The preliminary modeling framework for endoluminal ablation of pancreatic tumors was developed by Prakash et al., and expanded upon herein.¹⁴² Temperature distributions were simulated using an implicit finite element method (FEM) solver (COMSOL Multiphysics 4.3, COMSOL, Inc.) and the Pennes bioheat transfer equation (Eq. 1.16).¹¹¹ The acoustic absorption coefficient was approximated as equal to the acoustic attenuation coefficient μ (Np m^{-1}) for each tissue, as all scattered energy was assumed to be absorbed locally. The acoustic pressure field was calculated for all considered transducer configurations using the Rayleigh-Sommerfeld diffraction integral, through a MATLAB (MathWorks, Inc.) implementation of the rectangular radiator approximation (Eq. 1.14).⁵⁰ Uniform excitation and vibration across the surface of the transducer was assumed, and as such the surface velocity u_n for all N elements was calculated using the plane-wave analysis expression below (Eq. 2.1):

$$u_n = \sqrt{\frac{2I_s}{\rho c}} \quad \text{Eq. 2.1}$$

where I_s is the transducer surface intensity, which is equal to the electrical power applied to the transducer multiplied by the acoustic efficiency divided by the transducer surface area.

Temperature distributions were calculated using a direct implicit stationary solver (PARDISO) in COMSOL. Dirichlet boundary conditions constrained the outer boundaries of the tissue to 37°C , and a convective heat flux boundary condition was imposed at the balloon-tissue interface, with a heat transfer coefficient of $h = 500$ ($\text{W m}^{-2} \text{ }^\circ\text{C}^{-1}$).⁸⁹ The range of temperatures for the cooling water flow was $7\text{-}25$ $^\circ\text{C}$, based on practical ranges typically used for ablation and

hyperthermia devices. 7-10 °C cooling temperature was used for the ablation simulations to more efficiently reduce heating of the luminal wall. 20-25 °C water-cooling was applied in the hyperthermia simulations, with inherently lower applied power levels and resulting temperature and thermal dose, to avoid over-cooling and to extend therapeutic temperatures to tissue regions close to the luminal wall. Heterogenous tissue properties and perfusion values for stomach wall, duodenal wall, pancreas, tumor, and surrounding soft tissues were incorporated and are shown in Table 2.1.¹⁴³⁻¹⁴⁸ The material properties of pancreatic tumor tissue were assumed to be the same as pancreatic tissue, except for the attenuation coefficient where values equal to and slightly (1.25 times) higher than normal pancreatic tissue were included. This estimated higher value was used to account for the higher collagen content and fibrotic nature of the pancreatic tumor stroma, as collagen density has been shown to correlate with acoustic attenuation in other soft tissues.^{115,149,150} While a range of attenuation values for pancreatic tissue was extracted from literature, and is specifically examined along with the corresponding tumor attenuation value in the parametric studies, all other modeling incorporated the highest values of these ranges, as shown in Table 2.1, to give the most conservative estimates of achievable thermal lesion volumes and heating penetration. Proportional-integral (PI) feedback control of the applied power was integrated into the transient thermal solver, with the set-point evaluated between 70-80 °C to control the maximum temperature in the tumor. This controller was implemented to provide a standard point of comparison between simulations and to simulate a feasible feedback control scheme for treatment monitoring under either invasive thermometry or MR temperature imaging guidance.¹⁵¹ Thermal dose distributions were calculated using the Sapareto-Dewey formulation (Eq. 1.1).³⁴ The thermally destroyed or ablated tissue region was defined as the tissue in which the dose exceeded 240 EM₄₃ °C, which has been shown to correspond to an approximate threshold for coagulative

necrosis in many soft tissues^{28,36,152}. In order to simulate the dynamic cessation of perfusion during ablation, a binary switch was implemented to reduce tissue perfusion from nominal to $0 \text{ kg m}^{-3}\text{s}^{-1}$ during heating when tissue temperature exceeded $52 \text{ }^\circ\text{C}$ or thermal dose exceeded $300 \text{ EM}_{43^\circ\text{C}}$.¹¹³

Tissue	Density (kg/m^3)	Attenuation (Np/m)	Thermal Conductivity ($\text{W/m}^\circ\text{C}$)	Specific Heat ($\text{J/kg}^\circ\text{C}$)	Perfusion Rate ($\text{kg/m}^3/\text{s}$)
Pancreas	1045 [24]	$11.9f^{0.78}$ [24]	0.51 [25]	3164 [25]	10 [24]
Pancreatic Tumor	1045	$1.25 \times 11.9f^{0.78}$	0.51	3164	4.5 [26,28,29]
Stomach Wall	1045 [25]	$5f$ *	0.53 [25]	3698 [25]	6.75 [24,27]
Duodenal Wall	1045 [25]	$5f$ *	0.53 [25]	3698 [25]	16.67 [24]
Soft Tissue	1045 [24]	$6.4f$ [24]	0.49 [25]	3421 [25]	3 [24]
Blood	1050 [25]	$1.6f^{1.21}$ [24]	0.52 [25]	3617 [25]	-

Table 2.1 Material properties used in acoustic and biothermal modeling. f: frequency (MHz). *Estimated from lab attenuation measurements in porcine stomach tissue.

2.3.3 Parametric studies

A simplified 3D model of a pancreatic head tumor, with surrounding normal pancreas and intervening tissue regions adjacent to the duodenum, was created (Figure 2.3) to provide the framework for parametric studies of general applicator design and performance. The applicator was positioned with the transducer off-set 6.5 mm from the duodenal wall, with water-cooling of the luminal wall surface adjacent to the applicator cooled by $10 \text{ }^\circ\text{C}$ or $25 \text{ }^\circ\text{C}$ water for ablation and

hyperthermia treatments, respectively. The proximal edge of the pancreatic tumor tissue was 5 mm deep from the inner duodenal wall, and the overall dimensions of the tissue block were 50 x 50 x 73.5 mm. The duodenal luminal wall was modeled as distended with a 2 mm thickness.¹⁵³ Tissue thermal domains closer to the transducer were meshed at a finer resolution (equivalent to the acoustic wavelength) to appropriately capture the steep heating gradients near the applicator. The mesh size gradually increased to a maximum of 4 mm at the peripheral edges of the model. The acoustic calculations to obtain Q_{ac} were performed on a finer mesh (quarter-wavelength element length), which was then decimated to fit the thermal solver mesh. Convergence studies for both acoustic and bioheat transfer modeling were performed to ensure that the mesh element sizes were sufficiently small for accuracy and solution stability.

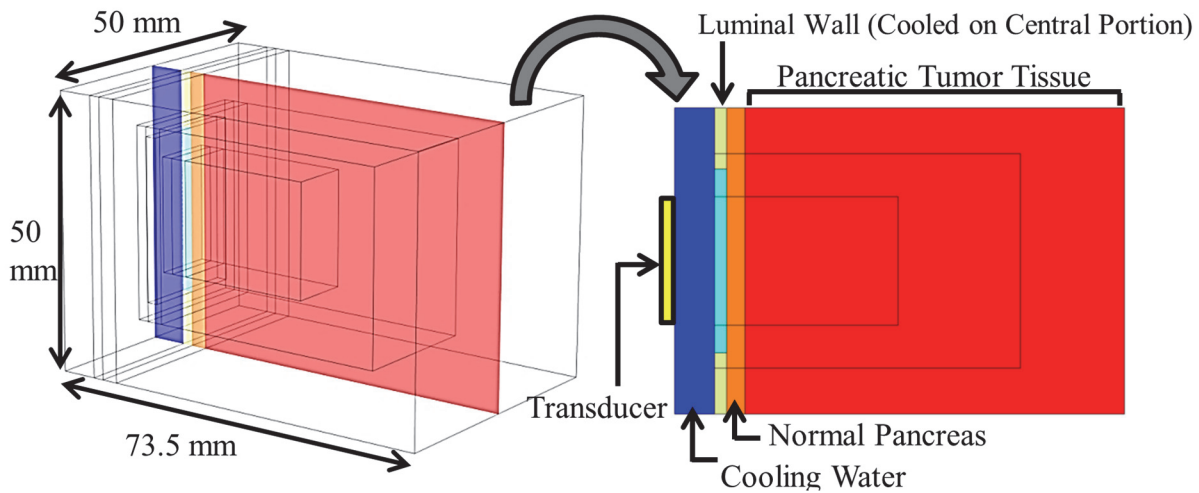


Figure 2.3 3D generalized pancreatic tumor model employed for parametric studies of endoluminal ultrasound thermal therapy.

For parametric studies of ablation, the feedback controller was set to limit maximum tumor temperature to 80 °C. The following transducer design parameters were varied: the transducer configuration (planar, tubular section, lightly focused curvilinear, or strongly focused curvilinear), frequency (1-5 MHz), and the radius of curvature (ROC) for curvilinear geometries (15-100 mm).

In order to capture the range of anatomical variation in adults, the duodenal wall thickness was varied between 1 and 5 mm. A range of values for the attenuation coefficient of pancreatic and tumor tissues, based off values reported in literature, was also incorporated. The range for pancreatic tissue was $4.37f^{1.2}$ Np/m – $11.9f^{0.78}$ Np/m, and the tumor attenuation was varied between 1-1.25 times greater than the corresponding pancreatic value.^{143,154} The effects of all of these parameters on the penetration depth of the thermal lesion, the total thermal lesion volume, and the maximum luminal wall temperature and thermal dose were evaluated. For each study, transient temperature solutions at a single applicator orientation were obtained with a variable time-stepping scheme for 5 minutes of total power application and heating time, followed by three minutes of cool-down with continued accrual of thermal dose and thermal spread of temperature contours. The PI controller proportional gain (K_p) and integral gain (K_i) parameters were adjusted for each case (K_p : 0.11-0.28 W °C⁻¹, K_i : 0.0012-0.005 W °C⁻¹ s⁻¹) to achieve a 5 minute rise time to the maximum set-point temperature. This scheme was selected empirically to minimize power requirements and to set an appropriate time frame for image-guided control such as MRTI. It also resulted in minimal temperature overshoot and reduced thermal exposure of the luminal wall relative to shorter duration, high power schemes.

For parametric studies of hyperthermia, only the planar and tubular transducer configurations were considered, due to their larger volumetric coverage of heating. The frequency was varied between 1-4 MHz for both configurations, and the volumes and dimensions of the 40 °C and 43 °C contours were measured as endpoints. Simulations were designed to approach pseudo-steady state during 10 minute long transient solutions. The controller parameters, K_p and K_i , were chosen to elevate the max temperature to 45 °C within 2-3 minutes and sustain it for 7-8

additional minutes. These final isothermal contours approximate the steady-state hyperthermia distributions that could be maintained for desired treatment lengths.

2.3.4 Patient anatomy models

3D patient anatomy models were created based on axial CT imaging studies of patients with pancreatic cancer. Four geometries were incorporated, with details of each shown in Table 2.2. These examples, while limited in representing the full scope of disease manifestation, were chosen to capture a range of distinct geometries, in terms of tumor size, location, and proximity to sensitive structures. Example 1 included a ~2 cm diameter pancreatic head tumor with boundaries immediately adjacent to the duodenum. Example 2 represents a ~2 cm diameter pancreatic head tumor located deeper (~5 mm from inner duodenal wall to closest proximity) in the pancreas and adjacent to the superior mesenteric artery (SMA), pancreatic duct, and bile duct. A strategy of preserving the bile duct during ablation treatment by using a simulated cooling balloon catheter was evaluated in this model. Example 3 represents a very advanced case, consisting of a large (~5 cm diameter) pancreatic head tumor close in proximity to the aorta, vena cava, portal vein, SMA, and superior mesenteric vein (SMV). While its size and proximity to vasculature may limit its candidacy for thermal therapy treatment, this model is incorporated in the analysis to investigate generalized heating performance and potential strategies that may be applicable in extreme cases. As such, multiple large position changes of the applicator along the duodenum were considered in this model to extend coverage of the tumor. Example 4 included a ~4 cm diameter pancreatic body tumor peripheral to the stomach, portal vein, SMV, splenic artery, splenic vein, hepatic artery, and the right gastroepiploic vein. In this model sonication from the stomach lumen was simulated with a longer (10 x 30 mm) transducer geometry at two discrete applicator positions. For all cases, the

applicator was rotated about the long (elevation) axis during therapy by discrete amounts in order to extend treatment coverage.

Case	Tumor location	Applicator placement	Tumor vol. (cm ³)	Tumor dim. (mm)	Nearest distance of tumor to inner luminal wall (mm)	Distances from tumor to sensitive anatomical structures (mm)
1	Head	Duodenum	4.3	21 x 19 x 18	2	PD – 1.5
2	Head	Duodenum	4.3	17 x 22 x 24	5	PD – 3 BD – 0 SMA – 0
3	Head	Duodenum	37.2	50 x 44 x 25	2.5	PD – 0 VC – 3 Aorta – 2 PV – 6 SMV – 0 SMA – 1.5
4	Body	Stomach	17.5	45 x 25 x 25	4.5	PD – 0 PV – 0.5 SMV – 1 SV – 1 RGV – 1 HA – 4 SA – 1

Table 2.2 General anatomical characteristics of patient anatomy models of pancreatic tumors. PD: pancreatic duct, BD: bile duct, SMA: superior mesenteric artery, VC: vena cava, PV: portal vein, SMV: superior mesenteric vein, SV: splenic vein, RGV: right gastroepiolic vein, HA: hepatic artery, SA: splenic artery.

Mimics (Mimics Innovation Suite, Materialise) was used to segment the CT images and generate 3D surface meshes of nearby and relevant anatomical structures, including the tumor, pancreas, duodenum/stomach, luminal wall, ducts, and nearby significant vasculature in each model. Using 3-matic (Mimics Innovation Suite, Materialise), models of the applicator within a 2 cm diameter cooling balloon were positioned in either the duodenum or stomach lumen adjacent to the target volume, and the 3D object contours were converted into finite element meshes. Applicators were empirically positioned into a section of lumen close in proximity to the targeted

region, such that large volumetric coverage of tissue could be achieved by rotation or minute translation of the applicator, and such that there were not sensitive structures (such as ducts, vessels) along the beam path. For models with multiple applicator positions, these placements were selected with the additional criteria that they should afford minimal overlap of thermal coverage. Interior luminal surfaces adjacent to the applicator were modeled as smooth, under the assumption that the cooling balloon provides distension of luminal folds with no trapped gas present at the interface. Convergence studies of mesh size were performed to ensure solution stability and accuracy, with a maximum mesh size of .75 mm in the region adjacent to the transducer surface extending 3-4 cm over the tumor volume, gradually transitioning to a maximum mesh size of 5-8 mm at the outer peripheries of the models. Each model consisted of 1.5-3 million elements, and Example 3 had three separate meshes which corresponded to the three distinct positions of the applicator.

Specific transducer configurations, empirically selected according to the model geometry and informed by the general performance characteristics revealed from the parametric studies, were chosen for ablation and hyperthermia simulations for each patient anatomy model. Each finite element mesh was imported into MATLAB for calculation of the acoustic intensity field using the rectangular radiator method, and all biothermal simulations were performed in COMSOL 4.3. Heterogeneous tissue properties, as shown in Table 2.1, were incorporated. The attenuation coefficients of pancreatic and pancreatic tumor tissue were selected as the highest value in the aforementioned range ($11.9f^{0.78}$ and $1.25 \times 11.9f^{0.78}$, respectively). When visibly distended, ducts were modeled with the properties of static water. Localized cooling effects of major blood vessels were modeled using heat flux boundary conditions at the inner surface of the blood vessels, with an ambient blood temperature of 37 °C, and the heat transfer coefficient h value was calculated

using the method detailed by Haemmerich et al., with vasculature parameters obtained from literature.^{112,155-159} The duodenal and stomach walls were modeled as 2 mm and 3 mm thick, respectively.^{153,160,161} Feedback control over the maximum tumor temperature was applied for the ablation simulations and transient temperature solutions were obtained. For hyperthermia studies, a single applicator position was considered. A constant input power to the transducer was applied to obtain temperature distributions at steady-state. Thermal treatment parameters, including cooling water temperature, maximum set-point temperature for the feedback controller, heating time lengths, and applicator orientations underwent minor iteration for each case to limit thermal exposure to luminal and other sensitive tissues, and to extend volumetric coverage of tumor tissue, but were not rigorously optimized.

2.4 Results

2.4.1 Parametric studies

The characteristic temperature and thermal dose contours produced by each transducer configuration for ablation treatment simulations are shown in Figure 2.4, for the frequency and curvatures specified in the caption. The effects of transducer configuration and frequency on ablation volume, penetration depth, and maximum luminal wall temperature/thermal dose are shown in Figure 2.5. The ablation volume for these five minute sonications ranged from 2.2-11.6 cm³, and the penetration depth from the inner luminal wall into the targeted tumor tissue ranged from 18.6-43.4 mm depending on which configuration and frequency was used. Both frequency and transducer configuration had a significant effect on the sparing of the luminal wall, with the maximum temperature ranging from 37.3-44.5 °C at 1 MHz and 46.2-51.9 °C at 5 MHz across configurations. Maximum thermal dose exposure of the luminal wall exceeded 15 EM₄₃ °C for

tubular transducers (at all frequencies), for planar and lightly curvilinear transducers operating at or above 4 MHz, and for strongly focused curvilinear transducers at 5 MHz.

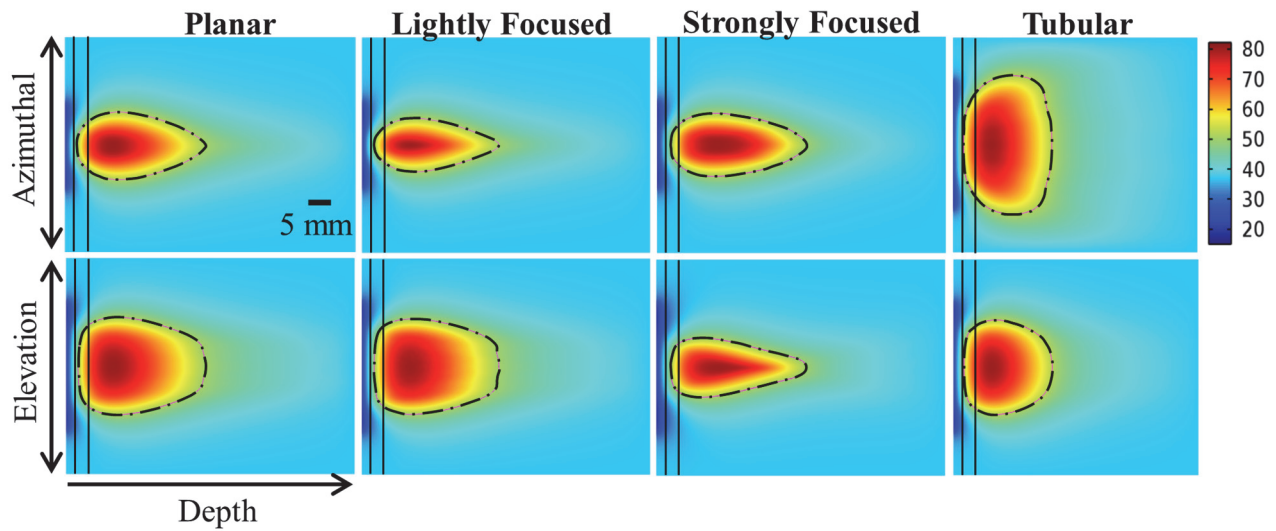


Figure 2.4 Cross-sectional temperature distributions and 240 EM₄₃°C contours (black dashes) for ablation studies in the generalized tumor model for 10 x 20 mm planar, lightly focused, strongly focused, and 80° tubular transducer configurations operating at 2 MHz, after 5 minutes of active sonication.

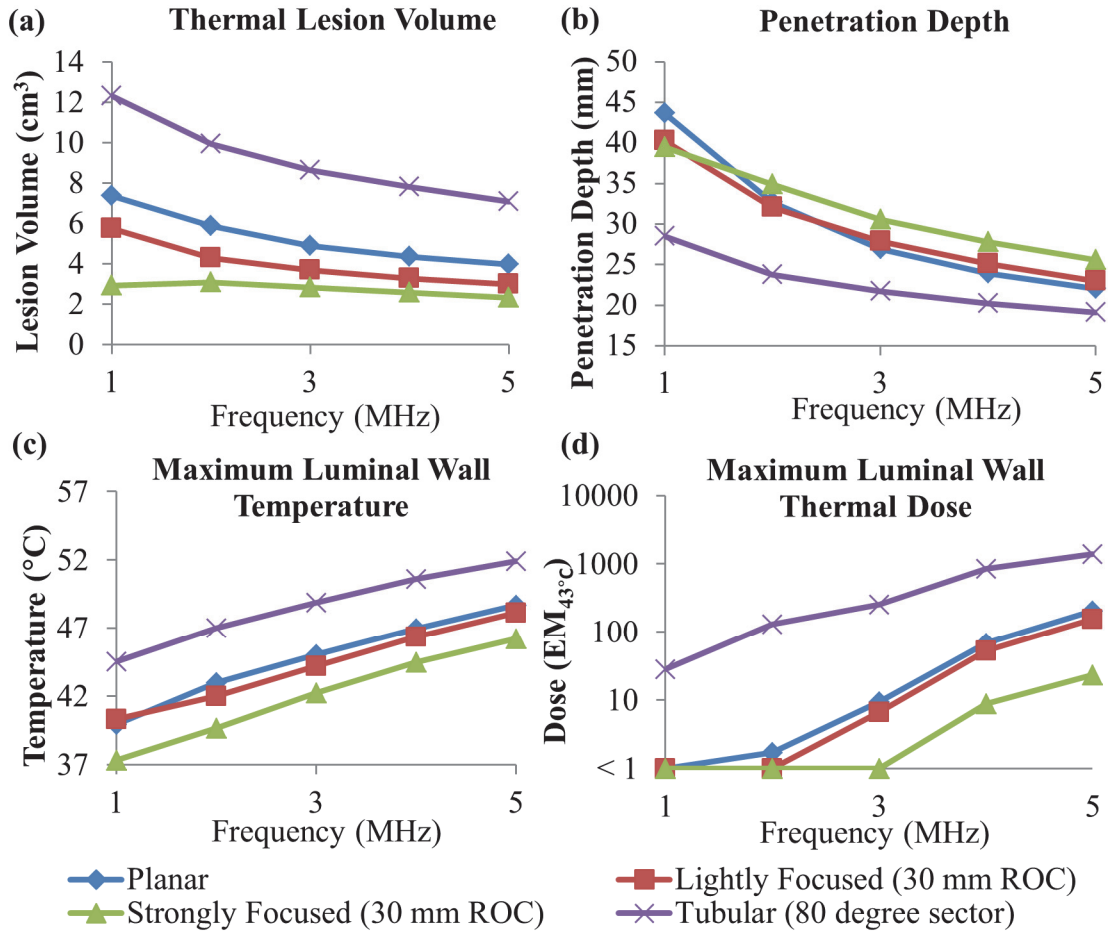


Figure 2.5 Effects of transducer configuration and operating frequency on (a) tumor ablation volume (thermal dose > 240 EM₄₃ °C), (b) penetration depth (measured from inner luminal wall) of thermal lesion, and maximum (c) temperature and (d) thermal dose of luminal wall tissue, after a single 5 minute sonication with a temperature set-point of 80 °C and 3 minutes of post-sonication cooling.

For curvilinear transducer geometries, the effect of the degree of focusing on thermal lesions was examined by varying the radius of curvature (ROC) at a set frequency of 2 MHz, as shown by Figure 2.6. The influence of this parameter on the resulting lesion parameters was more pronounced with the strongly focused design. Increasing the radius curvature resulted in larger lesion volumes, ranging from 1.1-5.1 cm³ as the ROC varied from 15-100 mm. A maximum penetration depth of 44.2 and 33.6 mm were obtained for the strongly focused and lightly focused transducers, respectively, at a 60 mm ROC. Sparring of the luminal wall was improved with lower

ROCs down to approximately 20 mm, until the geometric focus of the transducer was within 10 mm of the luminal tissue.

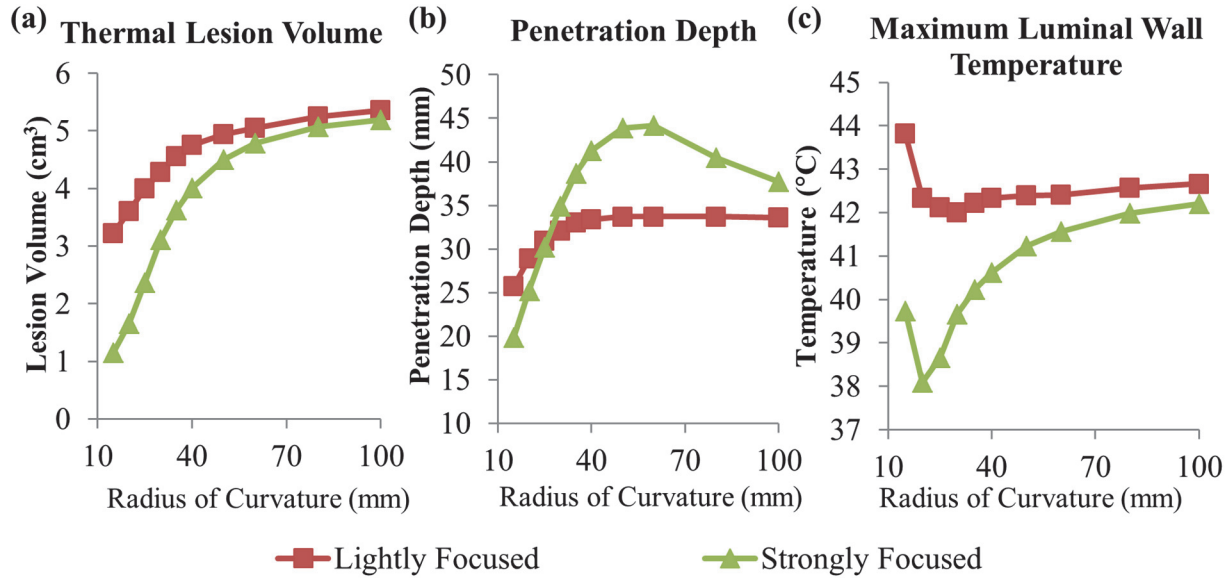


Figure 2.6 Effects of radius of curvature for 2 MHz curvilinear transducers on (a) tumor ablation volume (dose > 240 EM₄₃ °C), (b) penetration depth (measured from inner luminal wall) of thermal lesion, and (c) maximum temperature of luminal wall tissue, after a single 5 minute sonication with a temperature set-point of 80 °C and 3 minute post-sonication cooling.

As the luminal wall thickness increased from 1-5 mm, the maximal luminal wall temperature varied from 37.0-56.3 °C for planar, 37.0-54.8 °C for lightly focused curvilinear (30 mm ROC), 37.0-51.8 °C for strongly focused curvilinear (30 mm ROC), and 38.6-61.8 °C for tubular section transducers, all operating at 2 MHz. The relationship between luminal wall thickness and maximum wall temperature was approximately linear for all transducer configurations.

Sensitivity of the thermal lesion parameters to pancreatic and tumor attenuation coefficients varied with transducer configuration, as shown in Figure 2.7. For 2 MHz planar transducers, the lesion volume decreased 8.4-5.0 cm³, the penetration depth decreased 50.5-34.5 mm, and the maximum luminal wall temperature increased 41.7-43 °C as pancreatic attenuation

increased from $4.37f^{1.2}$ Np/m – $11.9f^{0.78}$ Np/m, with tumor attenuation 1.25x greater. When tumor attenuation was equal to pancreatic attenuation, the penetration depth and thermal lesion volume increased, by up to ~5 mm and 1 cm³, respectively. The strongly focused transducer was insensitive to attenuation changes with regard to lesion volume, and the tubular section was relatively insensitive in terms of luminal heating. The penetration depths of both configurations were less sensitive to attenuation compared to the planar and lightly focused transducers.

Parametric studies for hyperthermia treatments investigated the temperature distributions at steady-state, with maximum temperature set to 45 °C, and revealed similar trends as the ablation cases above. Tissue volumes elevated above 40 and 43 °C for the tubular section and planar transducers across 1-4 MHz frequencies are shown in Figure 2.8, in addition to the penetration depth of each temperature contour. The azimuthal extent of tubular section 40 and 43 °C contours were an average of 34.3 and 22.1 cm³ across frequencies, while the same for the planar transducer were 14.2 and 7.4 cm³, respectively. The contours' extents in the elevation direction were approximately equal (22.2 cm³ and 15.1 cm³ for tubular 40 and 43 °C contours vs. 21.8 cm³ and 15.3 cm³ for planar), and frequency independent. Maximum luminal temperatures for all tested configurations were below 39.5 °C, with maximum temperatures occurring with the 4 MHz tubular section configuration.

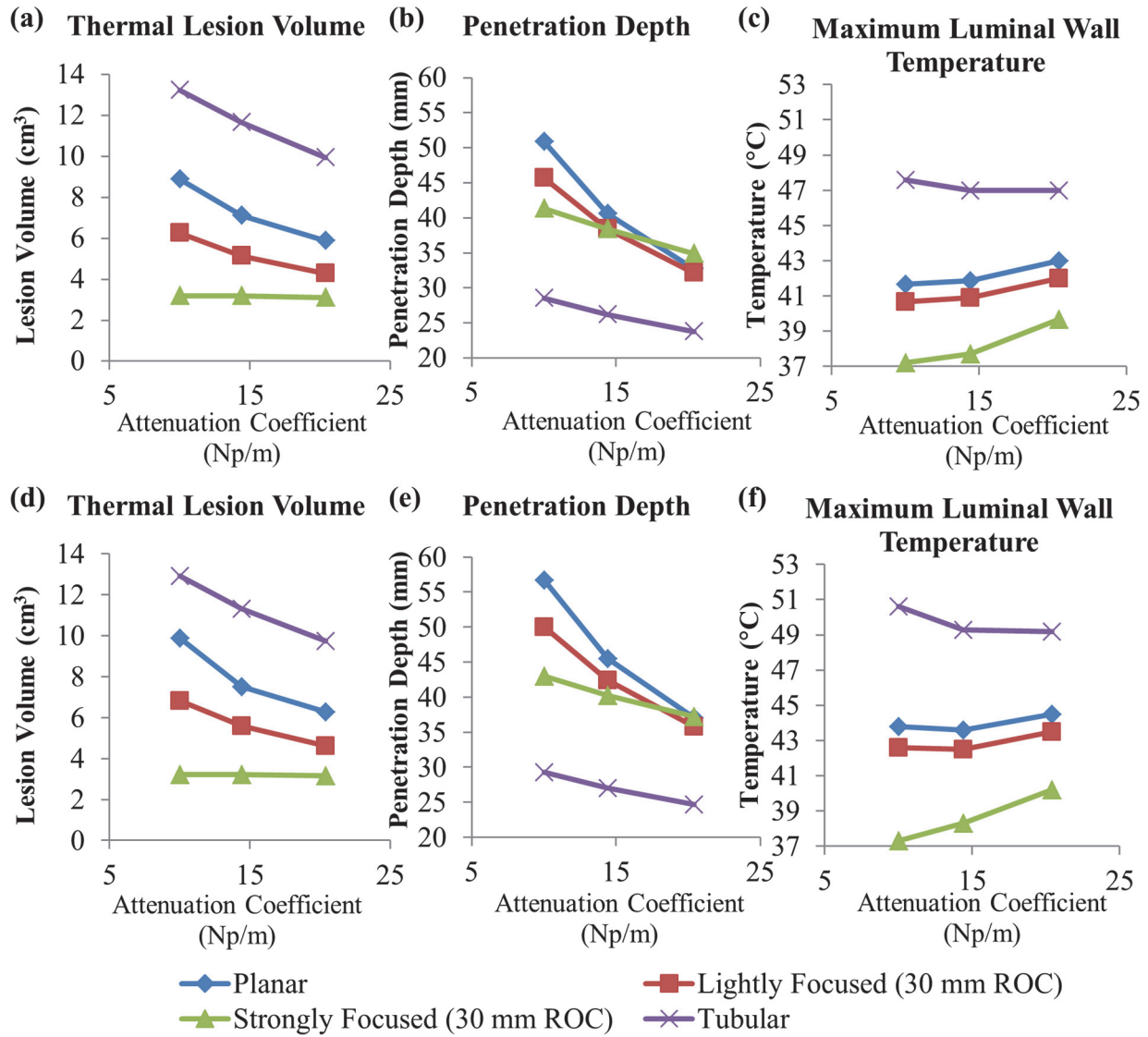


Figure 2.7 Effects of pancreatic tissue attenuation coefficient on (a,d) tumor ablation volume (dose > 240 EM₄₃ °C), (b,e) penetration depth (measured from inner luminal wall) of thermal lesion, and (c,f) maximum temperature of luminal wall tissue, after a single 5 minute sonication at 2 MHz operating frequency, with a maximum temperature set-point of 80 °C and 3 minute post-sonication cooling period. The tumor attenuation coefficient is 1.25x the corresponding pancreatic tissue attenuation in (a)-(c), and equivalent to the pancreatic tissue attenuation in (d)-(f).

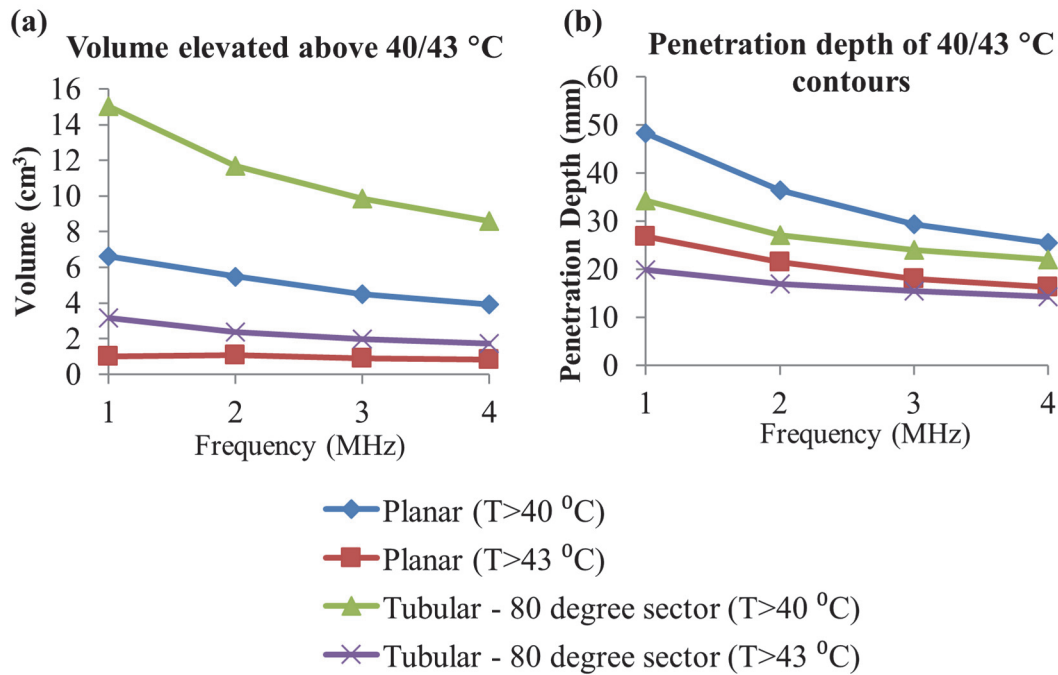


Figure 2.8 Effects of transducer configuration and operating frequency on (a) tumor volume elevated above 40 and 43 °C, and penetration depth (measured from inner luminal wall) of 40 and 43 °C temperature contours, at steady-state with a maximum temperature set-point of 45 °C for generation of moderate hyperthermia.

2.4.2 Patient anatomy models:

Example 1 – small head tumor: Ablation studies for this geometry (Figure 2.9) were simulated using an applicator placed in the duodenal lumen for two separate transducer configurations: a 2 MHz planar transducer and a 2 MHz lightly focused curvilinear transducer with an ROC of 25 mm. These were chosen due to the near proximity of the tumor boundary to the duodenal lumen and their capability to cover the majority of the tumor volume solely through rotation of the applicator. As shown in Table 2.3, which details ablation treatment delivery parameters and results for all four cases, use of either configuration demonstrated ablation of over 90% of the tumor volume under twenty-five minutes without exceeding a duodenal wall thermal dose of 5 EM₄₃ °C. More (5 vs. 3) discrete rotations of the applicator were necessary using the curvilinear transducer

to extend tumor coverage. The curvilinear transducer resulted in a lower maximal thermal dose exposure of luminal tissue and the distal pancreatic duct.

Case	Transducer Configuration	Freq. (MHz)	Max set-point temp. (°C)	Cooling water temp. (°C)	Total time (min)	% Tumor ablated	Max Temperature / Dose on Sensitive Anatomy
1	Planar	2	70	10	20	92.9%	DW – 44.3 °C, 5 EM PD – 46.8 °C, 30 EM
1	Lightly Focused 25 mm ROC	2	70	10	24	90.3%	DW – 41.8 °C, 0.4 EM PD – 46.2 °C, 16 EM
2	Strongly Focused 32.5 mm ROC	2	75	10	18	86.3%	DW – 39.3 °C, .02 EM PD – 44.1 °C, 3.9 EM BD – 58.3 °C, 6x10 ⁴ EM BV – 45.7 °C, 17.1 EM
2	Strongly Focused 32.5 mm ROC *Cooled bile duct	2	75	10	18	81.3%	DW – 39.6 °C, .03 EM PD – 45.7 °C, 6.7 EM BD – 44.4 °C, 16.2 EM BV – 45.9 °C, 18.9 EM
3	Planar	2	75	10	48	60.1%	DW – 44.1 °C, 11.8 EM PD – 43.2 °C, 2.33 EM BV – 42.9 °C, 1.95 EM
4	Planar	2	75	7	29	79.8%	SW – 44.4 °C, 13.3 EM PD – 44.6 °C, 4.0 EM BV – 43.0 °C, 0.9 EM

Table 2.3 Parameters and outcomes for patient anatomy ablation simulations. DW: duodenal wall, PD: pancreatic duct, BD: bile duct, BV: blood vessels, SW: stomach wall.

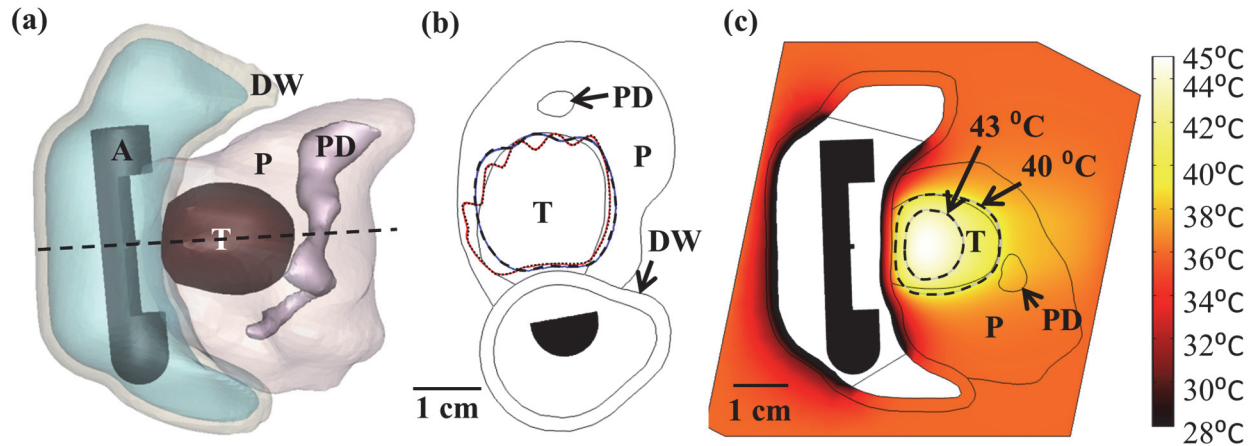


Figure 2.9 (a) 3D model of the Example 1 anatomy, consisting of a small pancreatic head tumor directly adjacent to the duodenal lumen and positioned applicator. (b) 240 $EM_{43}^{\circ C}$ contours for ablation simulations using a 2 MHz planar (blue with dashes) and 2 MHz lightly focused curvilinear transducer with a 25 mm ROC (red with dots) across the central transverse slice through the applicator. (c) Temperature distributions and 40 and 43 $^{\circ C}$ contours (grey with dashes) are given for a hyperthermia simulation using a 1 MHz tubular section transducer. A: applicator, T: tumor, P: pancreas, DW: duodenal wall, PD: pancreatic duct.

Details of hyperthermia treatment simulations for all four geometries are shown in Table 2.4. A 1 MHz tubular transducer (80° active sector) was chosen for this geometry due to the relatively short depth of the tumor boundaries from the duodenum. With a constant applied surface intensity of 2.8 W/cm^2 , 95% of the tumor volume could be elevated above $40^{\circ C}$, as shown in Figure 2.9 (c). No rotation or translation of the applicator was necessary for full tumor coverage.

Case	Transducer Configuration	Freq. (MHz)	Applied intensity (W/cm ²)	Max tumor temp. (°C)	Cooling water temp. (°C)	Volume, % tumor > 40/43°C
1	Tubular (80° sector)	1	2.8	45.0	25	4.1 cm ³ , 95.0% / 1.4 cm ³ , 32.8%
2	Planar	1.5	1.5	45.0	20	3.7 cm ³ , 86.5% / 0.9 cm ³ , 20.4%
3	Planar	1.5	1.7	45.0	25	7.6 cm ³ , 20.4% / 1.4 cm ³ , 3.8%
4	Planar	1.5	1.6	45.0	25	11.6 cm ³ , 66.6% / 2.4 cm ³ , 13.7%

Table 2.4 Parameters and outcomes for patient anatomy hyperthermia simulations.

Example 2 – small head tumor: The ablation study was simulated using an applicator placed in the duodenal lumen with a 2 MHz strongly focused curvilinear transducer (ROC of 32.5 mm) to more effectively target the deeper tumor depth and limit exposure to the adjacent sensitive tissues. Both rotation and minor translation (< 1 cm) of the applicator were necessary to increase tumor coverage. Over 80% of the tumor volume could be ablated in less than 20 min, with minimal thermal exposure to the SMA and pancreatic duct, as shown in Table 2.3 and Figure 2.10. Intraductal cooling of the bile duct using a simulated balloon catheter, with circulating coolant at 33 °C, was necessary to achieve adequate sparing of the bile duct, as shown in Figure 2.10 (b), for the simulated applicator placements. Hyperthermia was performed with the applicator in a single position by rotating a 1.5 MHz planar transducer to cover the extent of the tumor, and could elevate 86.5% of the tumor volume above 40 °C at steady state, as shown in Figure 2.10 (c).

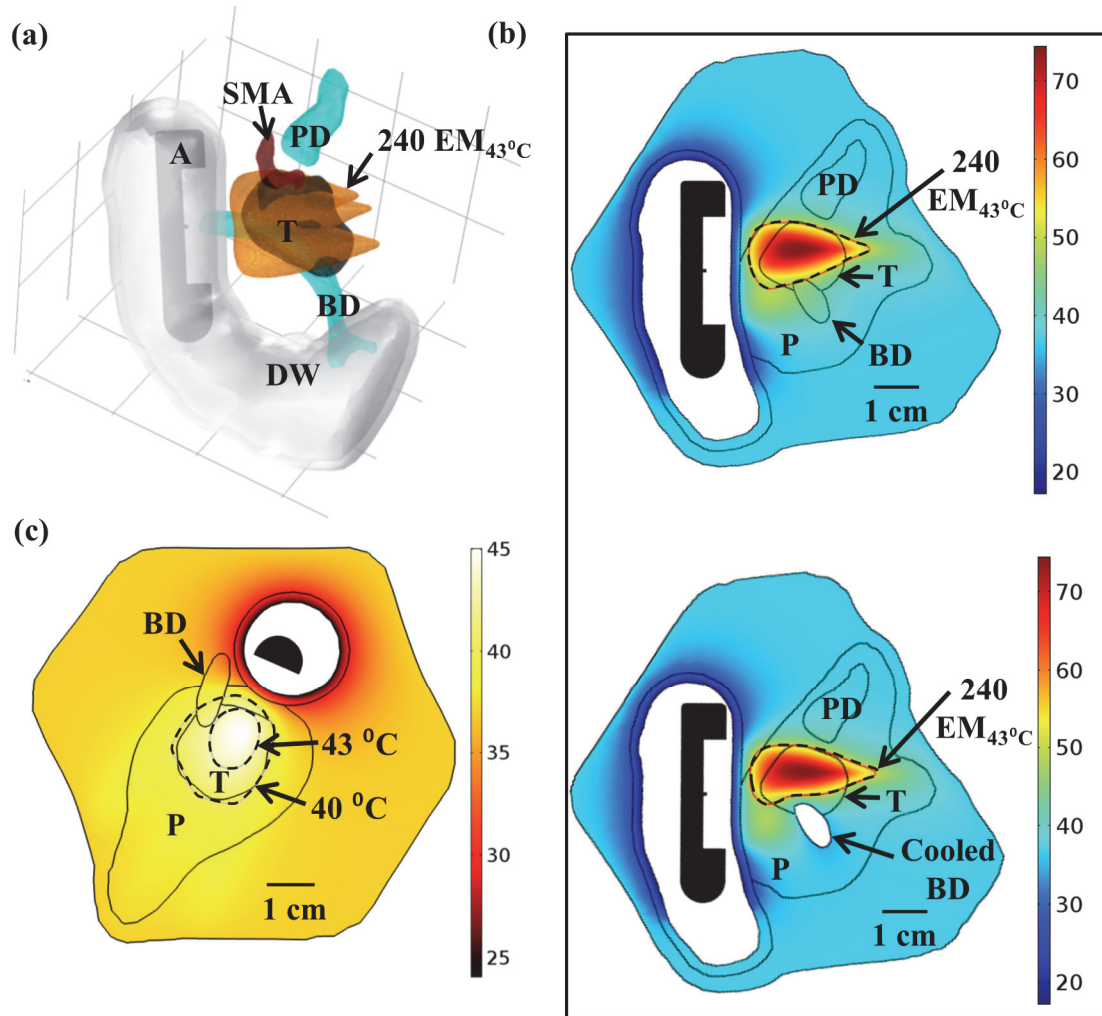


Figure 2.10 (a) Ablated lesion volume (dose $> 240 \text{ EM}_{43^\circ\text{C}}$) overlaid with the Example 2 model anatomy, consisting of a small head tumor surrounded by the SMA, PD, and BD, using a 2 MHz strongly focused curvilinear transducer. (b) Maximum temperatures and $240 \text{ EM}_{43^\circ\text{C}}$ contours across a sagittal plane for two ablation simulations: without (top) and with (bottom) simulated cooling of the bile duct, all other treatment parameters being identical. Sparing of the bile duct (BD) could be achieved by perfusing it with cooling water during the duration of the ablation treatment. (c) Temperature distributions and 40 and 43°C contours (grey with dashes) for hyperthermia produced by rotating a 1.5 MHz planar applicator. A: applicator, T: tumor, P: pancreas, DW: duodenal wall, PD: pancreatic duct, BD: bile duct, SMA: superior mesenteric artery.

Example 3 – large head tumor: Three discrete positions of the applicator along the length of the duodenum were used for the ablation study, as shown in Figure 2.11, with multiple rotations of the applicator at each position to increase tumor coverage. A planar 2 MHz transducer was chosen due to its large volumetric capabilities. Using this approach, about 60% of the 37 cm^3 volume

could be ablated within 50 minutes of cumulative heating and cooling time. The maximal thermal doses applied to the adjacent vasculature, pancreatic duct, and duodenal wall were all less than 15 $EM_{43}^{\circ C}$. Within this same model, hyperthermia was simulated using a 1.5 MHz transducer at a single position shown in Figure 2.11 (c). With rotation of the applicator, 7.6 cm^3 (20.4%) of the tumor volume could be elevated above 40 $^{\circ}C$ at steady state.

Example 4 – body tumor: The applicator was positioned at two discrete locations in the stomach, and minutely translated and rotated at each to increase tumor coverage. For ablation, a 2 MHz planar transducer was chosen for volumetric capabilities, and generated ablation of 79.8% of the tumor volume in a 29 min total treatment time, as shown in Figure 2.12. Thermal damage to the 3 mm thick stomach wall was minimized ($< 15 EM_{43}^{\circ C}$) by using a lower cooling water temperature of 7 $^{\circ}C$, and there was no substantial heating of the surrounding major blood vessels in the region (all $< 1 EM_{43}^{\circ C}$) or the pancreatic duct ($< 5 EM_{43}^{\circ C}$). For hyperthermia, a 1.5 MHz planar transducer was used at a single applicator position, and could elevate 66.6% of the tumor volume above 40 $^{\circ}C$ at steady state by rotating the applicator to cover the tumor extent, as shown in Figure 2.12 (c).

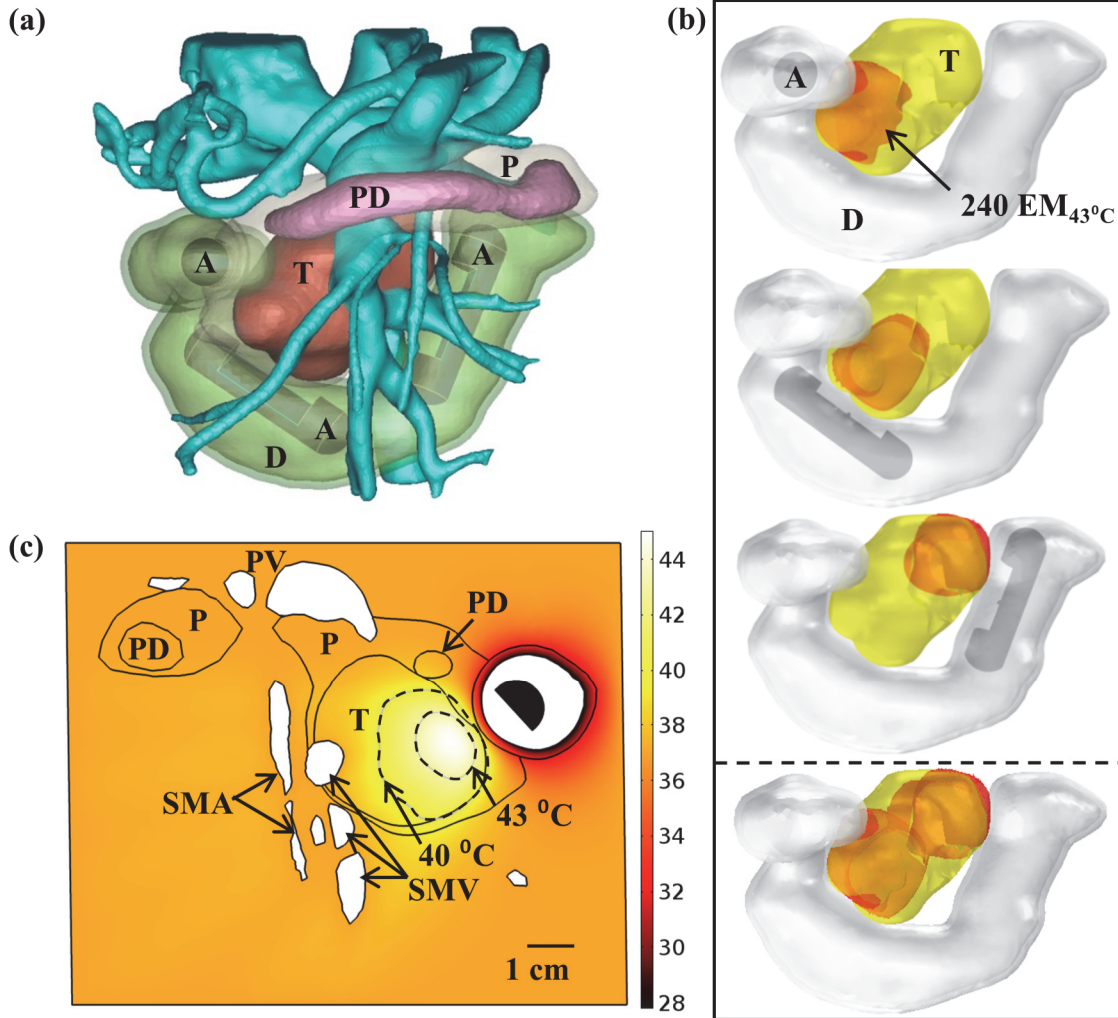


Figure 2.11 (a) 3D model of the Example 3 large pancreatic head tumor and surrounding anatomy, illustrating proximity of tumor to significant vasculature. (b) Ablated lesions (orange) were produced in the tumor by translating an applicator with a 2 MHz planar transducer to three individual positions along the length of the duodenum, with the cumulative thermal lesion shown at the bottom. (c) Temperature distribution and 40 and 43 °C contours (grey with dashes) across an axial plane for hyperthermia simulation using a 1.5 MHz planar transducer, rotated at a single position in the duodenum. A: applicator, T: tumor, P: pancreas, D: duodenum, PD: pancreatic duct, PV: portal vein, SMV: superior mesenteric vein, SMA: superior mesenteric artery.

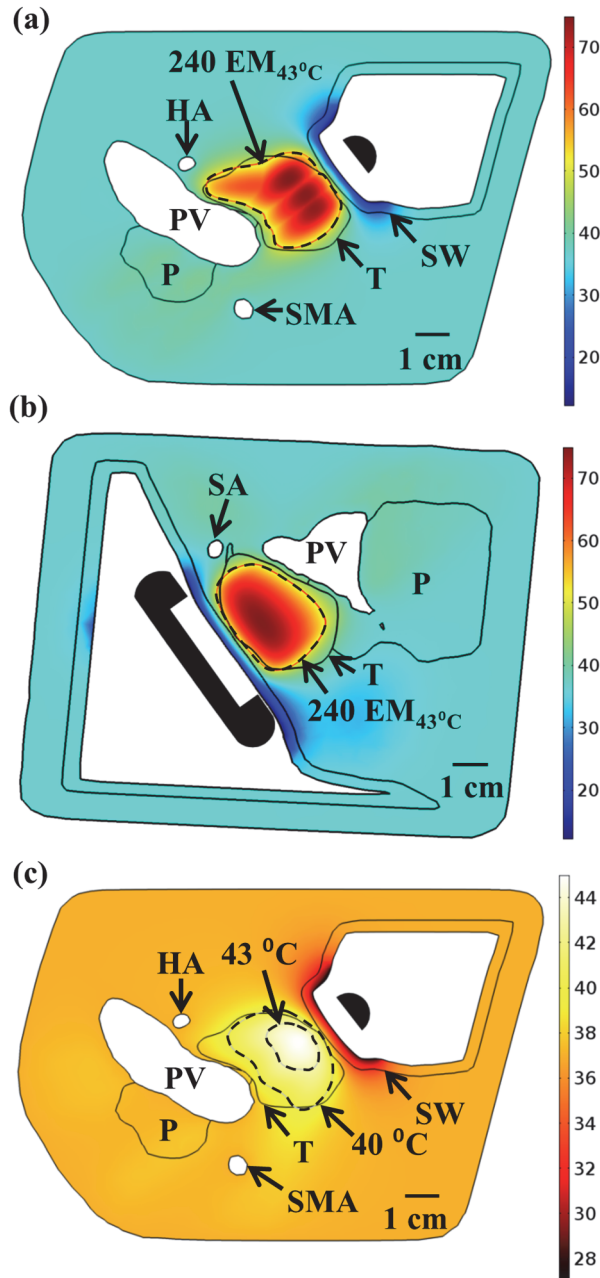


Figure 2.12 Maximum temperature distributions and 240 EM_{43 °C} contours (dashed) across (a) axial and (b) sagittal planes after ablation treatment for the Example 4 body tumor model, as treated with an applicator positioned in the stomach lumen with a 30x10 mm 2 MHz planar transducer. (c) Temperature distribution and 40 and 43 °C contours (grey) across an axial slice for hyperthermia by rotating a 1.5 MHz planar applicator. T: tumor, SW: stomach wall, P: pancreas, PV: portal vein, SMA: superior mesenteric artery, HA: hepatic artery, SA: splenic artery.

2.5 Discussion

This study has applied preliminary parametric and patient-specific acoustic and biothermal models to demonstrate the feasibility of generating ultrasound-based volumetric thermal ablation and hyperthermia within pancreatic tumors through the GI wall using an endoluminal delivery approach. Applicator transducer designs were investigated by evaluating four configurations (planar, lightly focused curvilinear, strongly focused curvilinear, and tubular section) across ranges of operating frequency and degree of focusing, with regard to heating capabilities and sparing of the luminal wall. Sweeps across transducer frequency for all configurations indicated that lower frequencies (1-3 MHz) were generally advantageous compared to higher frequencies (4-5 MHz), as they produced larger thermal lesion volumes and deeper penetration, while retaining the luminal wall at lower temperatures and thermal doses (Figure 2.5). In consideration of increased applied power requirements due to decreased absorption, cavitation thresholds within the applicator cooling fluid and tissue, and possibly excessive penetration of energy toward distal tissues and interfaces at frequencies at or below 1 MHz, a nominal low frequency of 2 MHz was selected for ablation simulations of the generalized patient anatomy models (Table 2.3). With regards to heating characteristics of each transducer configuration, parametric studies revealed that the planar transducer has the most favorable general-performance profile: deep (~30-35 mm) penetration, high lesion volume capability (up to 6 cm³ for a single position and 5 minute application), and suitable sparing ($T < 45$ °C, dose < 10 EM₄₃ °C) of the luminal wall at frequencies below 3 MHz (Figure 2.5). The strongly focused curvilinear transducer offers significantly superior sparing (3-4 °C lower max temperature, ~tenfold less thermal dose) of luminal tissue and the capability of tailoring the penetration and thermal lesion volume through *a priori* selection of the ROC (Figures 2.5, 2.6). These properties would make it appropriate as a more specialized design option, suitable

for selective targeting of smaller target regions deeper from the GI tract or sonication through thicker (> 3 mm) luminal walls. Lightly curvilinear transducers represent an intermediate between the planar and strongly focused designs, allowing some control over heating depth and volumetric coverage (Figures 2.5, 2.6), but without a distinct significant advantage. Ablation studies across varying normal pancreatic and tumor tissue attenuation coefficients revealed that heating characteristics of focused transducers were less influenced by tissue attenuation as compared to the more diffuse configurations (Figure 2.7). Thus, in the absence of quantitative tissue property measurements, focused transducer designs could be advantageous due to their more predictable and consistent performance. Tubular sector transducers, in contrast, were demonstrably the least suitable for ablation due to shallow heat penetration and comparably higher thermal exposure (4-7 °C higher max temperature) of the luminal wall relative to other configurations (Figure 2.5). However, low-frequency tubular transducers could be appropriate for delivering hyperthermia to small target volumes within 3 cm of the luminal wall (Figure 2.9). Planar transducer devices would require rotation to cover equivalent azimuthal extent, but could be advantageous for generating hyperthermia within larger/deeper targets due to greater penetration and potential volumetric coverage. As an alternative to having an assortment of these fixed transducer configurations available for a procedure, it may be possible to incorporate a more complex phased array transducer capable of dynamically producing variations of these focused and diffuse beam patterns, thereby permitting more flexibility from a single device in treatment delivery.^{73,162,163}

One of the primary safety requisites for endoluminal ultrasound delivery of thermal ablation to pancreatic targets is precluding thermal damage to the stomach or duodenal wall. This concern is relatively minimal for hyperthermia delivery, due to the much lower temperature elevation requirements, as shown by the parametric studies. While specific thermal dose thresholds

of thermal damage for human duodenal or stomach wall tissues have not been distinctly established, approximate damage thresholds can be inferred from experimental investigations in porcine GI tract (esophagus, small intestine, rectum).^{29,164,165} These studies indicate that significant acute and chronic damage, including degenerative necrosis of the tissue or thromboses of blood vessels, occur at thermal dose levels greater than 80-120 EM₄₃ °C and temperatures greater than 45-47 °C.^{29,165} As such, the maximum luminal temperatures and doses obtained in the ablation simulations for the patient anatomy model studies (< 45 °C and < 15 EM₄₃ °C) were considered to be within the safe limit to avoid significant thermal injury. As shown by the parametric studies, maximum luminal wall thermal exposures were strongly dependent on the luminal wall thickness. As such, sonicating through the stomach wall would likely have a higher risk of thermal injury as compared to through the duodenal wall, due to its greater thickness. However, there are many treatment parameters that could be adjusted to compensate for the increased risk of sonication through thicker GI luminal walls, including lowering the maximum set-point temperature or decreasing the cooling water flow temperature, as shown in the body tumor model (Figure 2.12). Using more focused transducer configurations, tailoring the ROC, and/or using lower frequency transducers could also improve sparing of the luminal wall (Figures 2.5, 2.6). In practice, it could be beneficial to distend the stomach or duodenum lumen to stretch and thin the luminal wall. This would be particularly important in the presence of folds or rugae, which could cause an increase in effective wall thickness or harbor air bubbles that could impact acoustic transmission and increase localized heating.⁷⁹ Distension of the lumens may be achievable either through filling the stomach or small intestines with water, through endoscopic manipulation, or by incorporating large distensible balloons onto the applicator that would be inflated once the applicator was positioned.¹⁶⁶

Simulations of these applicators incorporating patient anatomy models of pancreatic tumors and surrounding tissues illustrated feasibility of safely generating conformal ablation or hyperthermia across a range of tumor positions, sizes, and applicator positioning. Positioning the applicator within the duodenum provided the most access to tumors in the head of the pancreas (Figures 2.9-2.11), whereas the body tumor was most accessible to an applicator placed in the stomach lumen (Figure 2.12). All models necessitated sequential rotation and/or repositioning of the applicator to extend coverage of tumor volumes, leading to slightly scalloped or irregular outer boundaries of the lesions, as typical for heating with discretely rotating planar and curvilinear devices.¹⁶⁷ Substantial portions (> 80% of total volume) of head tumors under 3 cm diameter could be targeted for ablative or hyperthermic temperature exposures in short (< 30 minutes) heating times without any major applicator repositions (Figures 2.9, 2.10). Furthermore, fewer manipulations were needed for applicators with a planar transducer as compared to lightly or strongly focused transducer configurations, due to its greater volumetric coverage (Figure 2.9 (b)). However, tailoring the ROC of focused transducers to the target anatomy provided more preferential heating of the tumor and enhanced sparing of normal tissues proximal/distal to the tumor, as compared to the non-focused geometry (Table 2.3, Figure 2.9 (b)). Obtaining suitable volumetric ablation of large pancreatic tumors (> 4 cm diameter) places additional demands on applicator positioning and manipulation to access different portions of the tumor, as shown in Figure 2.11. These large target volumes and re-positional requirements could increase technical and time demands, and may be impractical for extended hyperthermia delivery, depending upon temperature range and time regimen required. In addition to size, the proximity of pancreatic tumors to sensitive anatomy, such as ducts, bowel, or significant vasculature, limits volumetric tumor coverage for ablation and imposes the need for highly accurate placement and manipulation

of the applicator to ensure that energy is directed precisely towards target tissues. Integrating the applicator with an endoscope may provide sufficient control for positional accuracy⁷⁹. Image-guidance techniques, incorporating MRI or ultrasound guidance, could also be employed to verify positioning, monitor treatments, and permit feedback control.^{60,79,104} While the PI feedback control scheme employed herein permitted conformal lesion formation, more advanced schemes incorporating pilot/boundary-control points or model predictive control could further improve targeting and reduce undesirable thermal exposure.^{113,168} Additional strategies to preserve sensitive tissues, such as internal cooling of major ducts using a cooling catheter, as shown in Figure 2.10 (b), may be considered. Further optimization of designs and delivery strategies can be achieved with more extensive modeling inclusive of additional and broader ranges of patient anatomy cases.

In principle, this endoluminal ultrasound approach may offer significant advantages over existing techniques for delivering thermal therapy to the pancreas. It can provide an attractive alternative to percutaneous RF or microwave ablation by minimizing complication risk through much more selective and targeted heating, and would not require major open surgery for its application.^{19,122,123} Compared to extracorporeal HIFU, endoluminal ultrasound could provide overall shorter ablation treatment times or enhanced hyperthermia coverage due to its local volumetric heating capability (Tables 2.3, 2.4). It could also provide easier access to tumors near or invading the duodenum or bowels that are often acoustically inaccessible from extracorporeal sources.¹¹⁸⁻¹²⁰ Further, although not investigated herein, application of these devices from within the body also suggests that in terms of energy delivery, compensating for respiratory or other sources of motion may be less challenging as compared to extracorporeal HIFU due to tissue and applicator motion being constrained together through endoscopic fixation. However, integrating the endoluminal approach with image-guidance treatment monitoring and feedback, e.g., by using

MR thermometry, could still require respiratory gating or other motion-compensatory techniques.¹⁰⁴

2.6 Conclusion

3D acoustic and biothermal models illustrate the feasibility of generating ultrasound-based thermal therapy within pancreatic tumors using an endoluminal applicator placed in the duodenal or stomach lumen. Four specific applicator transducer configurations, ranging from curvilinear-focused to planar or radial-diverging, were demonstrated to provide appreciable volumetric coverage for thermal ablation of pancreatic tumors or the delivery of moderate hyperthermia. Planar and curvilinear configurations could produce ablative temperatures and lethal thermal doses for tissue volumes of up to 8 cm³ for a single applicator placement and 5 minute sonication length, and for larger tumors additional rotations or translations of the applicator could be used to extend coverage. For moderate hyperthermia delivery, non-focused transducer geometries could sustain up to 16 cm³ of target tissue between a temperature range of 40-45 °C. Thermal simulations provide preliminary guidelines for appropriate frequency, transducer geometry, positioning, and treatment parameters to deliver conformal thermal therapy to pancreatic head or body target regions ranging from 20-45 mm deep from the GI wall while minimizing thermal exposures (dose < 15 EM_{43°C}) to the intervening stomach or duodenal tissues. Additional modeling in the form of parametric studies and patient anatomy models can be applied for further optimization of device designs and delivery approaches.

Chapter 3

Endoluminal ultrasound applicators for MR-guided thermal ablation of pancreatic tumors: preliminary design and evaluation in a porcine pancreas model.

3.1 Abstract

Purpose: Endoluminal ultrasound may serve as a minimally invasive option for delivering thermal ablation to pancreatic tumors adjacent to the stomach or duodenum. The objective of this study was to explore the basic feasibility of this treatment strategy through the design, characterization, and evaluation of proof-of-concept endoluminal ultrasound applicators capable of placement in the gastrointestinal (GI) lumen for volumetric pancreas ablation under MR guidance.

Methods: Four variants of the endoluminal applicator, each containing a distinct array of 1-2 independently-powered planar or curvilinear-focused transducers at the distal end of a meter long flexible catheter assembly, were designed and fabricated. Transducers and circulatory water flow

for acoustic coupling and luminal cooling were contained by a low-profile polyester balloon covering the transducer assembly fixture. Each applicator incorporated miniature spiral MR coils and mechanical features (guiding tips, hinge) to facilitate tracking and insertion through the GI tract under MRI guidance. Characterization of each device was performed using radiation force balance measurements, hydrophone measurements, and heating studies in *ex vivo* muscle tissue. Device delivery into the upper GI tract, adjacent to the pancreas, and heating characteristics for treatment of pancreatic tissue were evaluated in MR-guided *ex vivo* and *in vivo* porcine experiments. MR-guidance was utilized for anatomical target identification, tracking/positioning of the applicator, and MR temperature imaging (MRTI) for PRF-based multi-slice thermometry, implemented in the real-time RTHawk software environment.

Results: Acoustic efficiencies ranged between 48.8%-65.5% for the four applicator configurations. *Ex vivo* studies in whole-porcine carcasses revealed capabilities of producing ablative temperature rise ($\Delta T > 15\text{ }^{\circ}\text{C}$) contours in pancreatic tissue 4-40 mm long and 4-28 mm wide for the dual planar transducer applicator (1-13 minute sonication duration, $\sim 4\text{ W/cm}^2$ applied acoustic intensity). An applicator with dual lightly-focused curvilinear transducer produced more selective heating, with a narrower $\Delta T > 15\text{ }^{\circ}\text{C}$ contour length and width of up to 1-24 mm and 2-7 mm, respectively (1-7 minute sonication duration, $\sim 4\text{ W/cm}^2$ applied acoustic intensity). Active tracking of the miniature spiral coils was achieved using a Hadamard encoding tracking sequence, enabling real-time determination of each coil's coordinates and automated prescription of imaging planes for thermometry. *In vivo* MRTI-guided heating trials in four pigs demonstrated capability of $\sim 20\text{-}30\text{ }^{\circ}\text{C}$ temperature elevation in pancreatic tissue at 2 cm depths from the applicator, with 5-7 W/cm^2 applied intensity and 3-16 min sonication duration. Higher temperatures and more selective lesion formation was achieved using strongly-focused curvilinear transducer configurations. Dimensions

of thermal lesions in the pancreas ranged from 7-28 mm, 3-10 mm, and 5-12 mm in length, width, and depth, respectively, as verified through histological analysis of tissue sections. Multiple-baseline reconstruction and respiratory-gated acquisition were demonstrated to be effective strategies in suppressing motion artifacts for clear evolution of temperature profiles during MRTI in the *in vivo* studies.

Conclusions: This study demonstrates the technical feasibility of generating volumetric ablation in pancreatic tissue using endoluminal ultrasound applicators positioned in the stomach lumen. MR-guidance facilitates target identification, device tracking/positioning, and treatment monitoring through real-time multi-slice PRF-based thermometry.

3.2 Introduction

Endoluminal and intracavitary catheter-based ultrasound applicators can potentially provide a minimally invasive and effective means of ablating tumors adjacent to the gastrointestinal tract. Catheter-based ultrasound possesses many advantages compared to other ablative technologies, including the high degree of control over the spatial deposition of acoustic energy through transducer design, direct localization of energy delivery to the target region, and compatibility with imaging modalities, such as ultrasound or MRI, for direct treatment feedback.⁶³ In consideration of treating pancreatic adenocarcinoma (PDAC), endoluminal ultrasound could serve as a less invasive and inherently safer alternative to traditional radiofrequency and microwave interstitial ablation techniques, and may also circumvent accessibility issues associated with extracorporeal HIFU, in particular for target regions close to the GI tract. Specific configurations of endoluminal ultrasound applicators have been developed for delivering ablation to GI-accessible sites, including the biliary tract,¹³³ esophagus,⁷⁶ and liver.^{77,78} For ablating pancreas and liver tissue from the stomach lumen, an endoscope with an integrated miniature spherically-focused HIFU

transducer (12 mm diameter, 35 mm radius of curvature (ROC), 3.73 MHz) has been developed and experimentally verified in *in vivo* porcine studies.⁷⁹ This device demonstrated feasibility of creating small (~3 x 10 mm) lesions beyond the stomach wall that were sequentially delivered with ~30s sonication durations, and illustrated the utility of integrated endoscopic ultrasound to guide positioning and monitor bubble formation as an indicator for ablation.⁷⁹

Ultrasound¹⁶⁹ and MRI^{170,171} can be used to guide and monitor thermal therapy treatments in real-time, and provide a means to enhance the accuracy of energy deposition and directly verify the efficacy of treatment delivery. Advantages of MR guidance include improved targeting due to enhanced soft-tissue contrast, and generation of multiple tomographic temperature maps across arbitrary planes using MR temperature imaging (MRTI), thereby providing direct and volumetric feedback to treatment progress. MRTI has been paired with many ablative modalities, and recently has been used in conjunction with extracorporeal HIFU for ablation of pancreatic body tumors in patients with locally advanced PDAC.¹¹⁹

The principal aim of this study is to assess the general feasibility of using an MR-compatible endoluminal ultrasound applicator to generate thermal ablation of pancreatic tissue from the GI lumen under MR guidance, as shown in Figure 3.1. In contrast to spherically- or highly-focused ultrasound, emphasis was placed on designing applicators capable of volumetric thermal coverage, as appropriate for the large size of advanced primary pancreatic tumors,¹⁷² and in order to minimize repositioning requirements and take advantage of MRTI multi-slice capabilities. Here we report the technical design of the proof-of-concept (POC) applicators, results of acoustic and thermal characterizations, and preliminary delivery and performance assessments in exploratory MR-guided *ex vivo* and *in vivo* heating trials in porcine animal models.

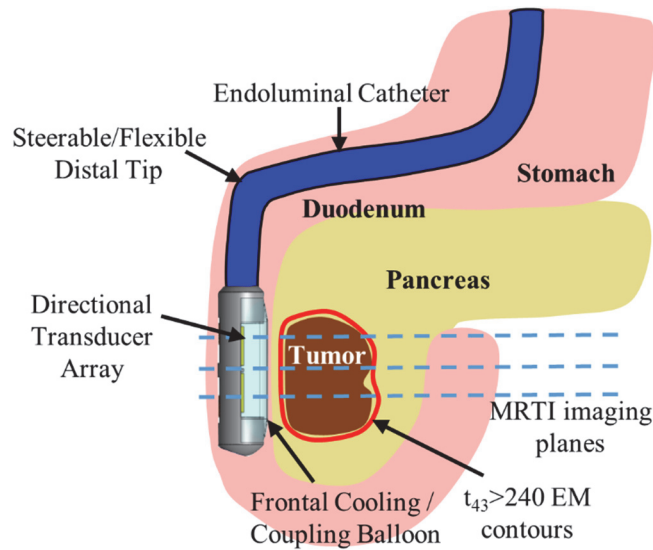


Figure 3.1 Schema and concepts of an endoluminal ultrasound applicator positioned in the GI tract for thermal therapy of pancreatic tumors. The applicator is illustrated as positioned in the duodenum for sonication of tumors in the head of the pancreas, following placement and insertion strategies common in endoscopy. Transducer arrays are configured for lightly focused or diffuse patterns to provide a high degree of spatial control and volumetric heating.

3.3 Materials and Methods:

3.3.1 Endoluminal ultrasound applicator fabrication

Four configurations of endoluminal applicators, incorporating different transducer geometries, were designed and fabricated. Transducer specifications for each applicator configuration are shown below in Table 3.1. All transducers were gold-plated PZT (EBL #1/#4, EBL Products, Inc.). Transducer assembly fixtures for the distal tip of the applicator were designed for each configuration in SolidWorks, as shown in Figure 3.2. The fixtures contain rectangular channels for seating each transducer, ports for wiring, internal channels for circulatory water flow, and attachment ports to the body and tip of the applicator. The dimensions of the cylindrical fixtures were 12 mm OD and 45 mm length, conservatively chosen to accommodate passage through gastrointestinal anatomy.

Applicator configuration	# of elements	Operating frequency (MHz)	PZT Material	Dimensions (width x length mm)	Radius of curvature (mm)
Dual planar	2	3.2	EBL #1	10 x 10	N/A
Dual lightly-focused curvilinear	2	3.3	EBL #1	8 x 10	20 along width
Dual strongly-focused curvilinear	2	3.1	EBL#4	9.3 x 11.4	25 along length
Single strongly-focused curvilinear	1	3.3	EBL#4	9.3 x 22	37 along length

Table 3.1 Transducer specifications for each endoluminal ultrasound applicator configuration.

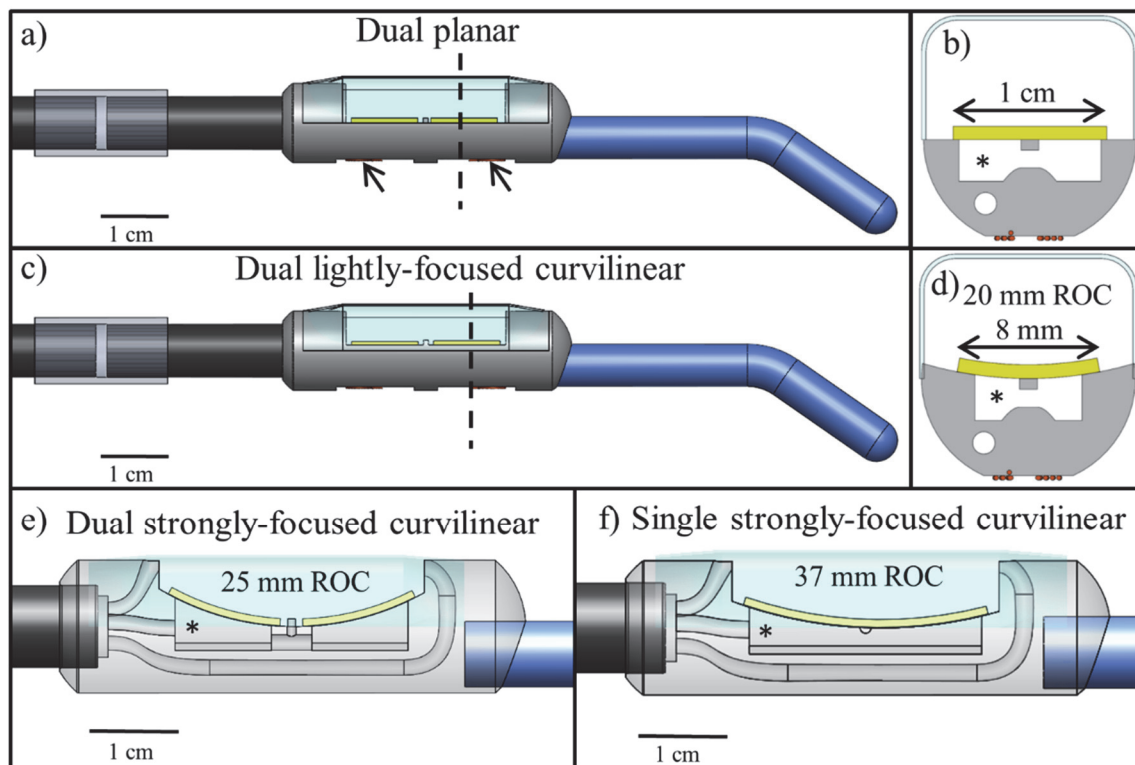


Figure 3.2 Design schematics for the (a,b) dual planar, (c,d) dual lightly-focused curvilinear, (e) dual strongly-focused curvilinear, and (f) single strongly-focused curvilinear endoluminal ultrasound applicators. Each design features the transducer assembly fixture, which consists of a 1-2 element

transducer array (yellow) seated along the device length covered by a thin-walled PET balloon, and active MR tracking coils on the fixture underside (arrows). Maneuverability and tracking into the GI tract are enhanced by the distal polyurethane tip (blue) and proximal silicone hinge (grey). Cross-sections along the dashed line through the assembly fixture are shown for the (b) dual planar and (c) dual lightly-focused curvilinear configurations, showing transducer dimensions and seating over the air-backed channels (asterisks). The internal structure of the housing fixtures, containing channels for electrical wiring and circulatory water flow, are shown in e,f).

The transducer fixtures were 3D printed in Veroclear material using an Objet260 Connex (Stratasys, Ltd.). Transducers were secured using Stycast 2651 epoxy (Henkel Electronics Materials) over the corresponding channels of the fixture for air-backing. A fixed-shape low profile (radius = 7 mm) balloon made from .025 mm thick polyethylene terephthalate (PET) (Advanced Polymers, Inc.) was secured to the top of the fixture to cover the transducers and contain circulatory water flow. Approximately 1 meter of nylon tubing (8 mm OD x 6 mm ID, McMaster-Carr) was used for the body of the applicator. Polyethylene tubing (1.4 mm ID, Becton, Dickinson, and Company) and coaxial cabling (Molex, Inc.) served for circulatory water flow and power transmission to the transducers, respectively, and were routed within the nylon body. On the proximal end of the applicator, Redel RF power connectors (Lemo S.A.) and luer connectors (Quosina Corporation) for water flow were attached. Active MR tracking coils, based off a spiral surface coil design¹⁷³ with 4 turns, ID ~ 1-1.5 mm, and OD ~ 4 mm, were fabricated using silver wire (.1 mm OD, California Fine Wire Company) and secured to the two platforms on the underside of each transducer fixture. Coaxial cables (Molex, Inc.) terminating with BNC connectors were attached to the coils. To improve maneuverability through the GI tract, a pre-shaped 6-8 cm long polyurethane (6.4 mm OD, Cole-Parmer) tip was secured to the distal end of the applicator, and a flexible pivot point made from silicone tubing (9.5 mm OD, HelixMark) was incorporated 3 cm proximal of the transducer stage fixture. Photos of the POC endoluminal ultrasound applicators are shown in Figure 3.3.

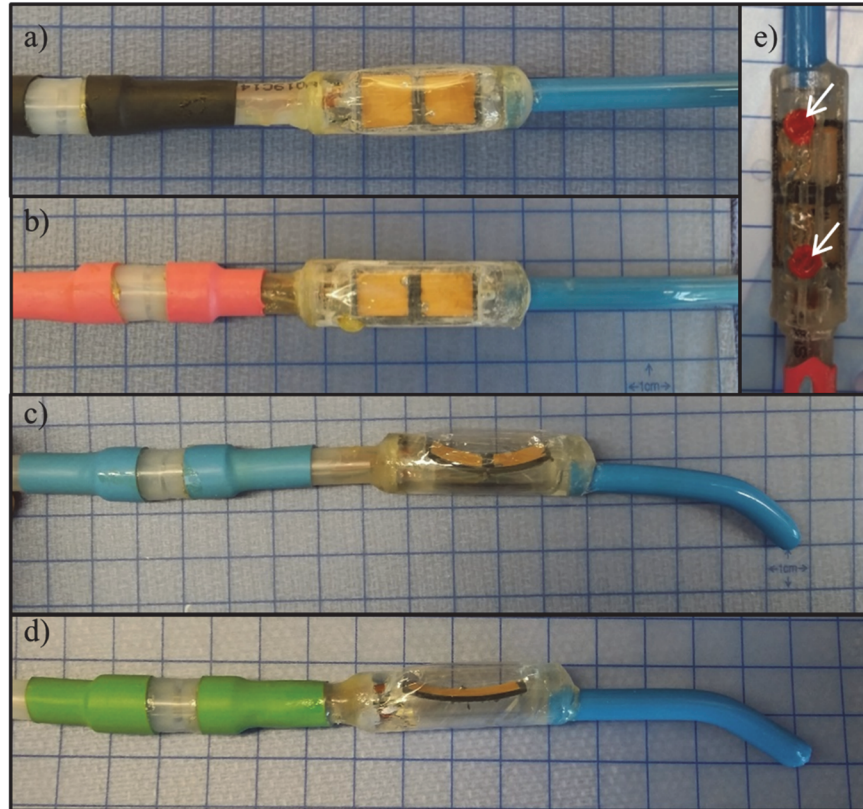


Figure 3.3 Fabricated (a) dual planar, (b) dual lightly-focused curvilinear, (c) dual strongly-focused curvilinear, and (d) single strongly-focused curvilinear endoluminal ultrasound applicators. (e) Two spiral tracking coils (arrows) for active MR tracking were integrated on the backside of each transducer assembly fixture.

3.3.2 Acoustic characterization

The mounted transducers on the fully assembled endoluminal ultrasound applicators were characterized using (1) force balance measurements⁹⁸ to determine acoustic output power and efficiencies, and (2) hydrophone measurements to map acoustic beam profiles across axial and sagittal planes relative to the mounted transducers. Force balance was performed using a bottom-loading mass balance (BP2100S, Sartorius AG) setup, with the applicator under test submerged in deionized and degassed water, directing acoustic energy into acoustic absorbers on the balance. The acoustic output power was calculated using the mass displacement, and the acoustic efficiency was calculated as the ratio of acoustic power to net electrical power (range: 5-25 W) delivered to

both transducers, as measured using a power meter (438A, Hewlett-Packard). Beam intensity distributions were characterized by placing the applicator under test in a tank filled with deionized, degassed water and scanning a needle-type hydrophone (Onda HNP-0400, Onda Corp.) under motor control along the X-Z (axial) and Y-Z (sagittal) planes. Step sizes were .25 mm for the X and Y axes, and .5 mm along the Z (depth) axis. The pulse repetition rate for sonication was 1 ms, and burst count was 250 cycles. The peak-to-peak voltage measurements from the hydrophone were measured using an oscilloscope (AFG3022C, Tektronix, Inc.) and squared to obtain pressure-squared distributions, which were then normalized to maximum value and represent normalized beam intensity distributions.

3.3.3 MRI experimental setup and RTHawk software platform

A 3T GE Discovery MRI scanner was used for all MR-guided experiments. Electronics for delivering RF power and cooling water flow were kept in the control room outside the MR suite. A function generator (HP Agilent 33220A) and RF amplifier (E&I Model 240L, Electronics & Innovation) were used to drive the transducers, with forward and reflected power monitored using an inline power meter (4391A, Bird Technologies). To reduce interference noise in the MRI images from the driving electronics, high power low pass filters (Model YA-1, Bencher, Inc.) and custom-built isolation transformers were integrated along the power lines to the shielded penetration panel of the MR suite. Shielded RF cabling was used to connect RF power lines to the applicator in the MR suite. Circulatory water flow was driven through the applicator PET balloon using a peristaltic pump (Masterflex, Cole-Palmer). Direct cooling of the water flow was achieved using an in-line copper tubing heat exchanger that was submerged in an ice-bath immediately proximal to the applicator input. Imaging was performed either with a phased-array cardiac coil (GE), or with two or three 13 cm or 20 cm surface coils connected to the scanner using a custom

5-channel adapter and hardware. This second configuration enabled connections and active tracking capabilities of the two miniature RF coils integrated onto the underside of the applicator transducer fixture using a Hadamard encoding tracking sequence (TE = 2 ms, TR = 4 ms, FOV = 30cm, sample = 512),¹⁷⁴ which incorporated dithering along 6 orthogonal directions to reduce bulk noise.¹⁷⁵

The RTHawk software environment (HeartVista, Inc.) was integrated with the GE scanner to provide real-time multi-slice continuous imaging and reconstruction capabilities, while allowing instant changes to pulse sequence parameters and imaging plane position and orientation. For thermometry purposes, a PRF-based GRE sequence (TE = 8 ms, TR = 23 ms, flip angle = 15, FOV = 30 cm, 128 X 128 acquisition matrix, slice thickness = 5 mm) was implemented in RTHawk and provided multi-slice temperature monitoring at an update time of ~3s per slice. Baseline images were acquired immediately after circulating flow was initiated (to incorporate any positional or flow-related artifact into the baseline) and prior to power delivery, and used to subtract baseline phase for temperature reconstruction during the course of heating. Background temporal phase drift was monitored in an ROI outside of the heated region and used to correct temperature calculations.¹⁷⁶ For improved target contrast, an IR-FSE sequence (TI = 729 ms, TE = 120 ms, TR = 1285.7 ms, flip angle = 90, echo train length = 24, FOV = 30 cm, 256 x 256 acquisition matrix, slice thickness = 7 mm, NEX = 1) was also implemented in the RTHawk environment, and used to confirm final positioning of the device and prescription of thermometry slices before the start of sonication.

3.3.4 MRTI thermometry validation

An experiment was performed to validate the accuracy of the temperature measurements produced by the PRF GRE thermometry sequence and reconstruction scheme. A 12 cm OD cylindrical slab

of tissue-mimicking phantom¹⁷⁷ was placed into the MR scanner bore, with the dual-planar applicator inserted into the phantom through a central bore. A fiber-optic based thermocouple was inserted adjacent to the central bore at a depth of 15 mm from the applicator, just adjacent to the projected beam path. A sonication was performed at ~ 3.8 W/cm² transducer surface intensity for a duration of 3 minutes, during which concomitant thermometry sequences along a sagittal plane (visualizing the lengths of the inserted applicator and thermocouple) were ran, along with fiber-optic measurements. Temperature measurements were continued for ~ 3 minutes following the end of sonication. Following the sonication, temperature measurements from the thermometry images were extracted at the portion of the image corresponding to the thermocouple tip location, and compared to the thermocouple measurements.

3.3.5 Heating characterization in MR guided ex vivo muscle tissues

Sonications were performed in store-bought meat slabs (pork shoulder/pork loin sirloin) under MR guidance in order to characterize the heating patterns of each applicator. Each applicator was placed in the middle of two slabs of meat, with ultrasound gel used to couple the applicator balloon to the tissue. Sonications were performed during single or multi-slice MRTI monitoring, with slices oriented along the length of the applicator (sagittal) and perpendicular to the applicator through the transducer stage (axial). Sonications were performed for up to 5 min durations, at ~ 1.5 - 4 W/cm² applied acoustic surface intensities.

3.3.6 Applicator delivery and heating characterization in MR guided ex vivo porcine cadaver experiments

In order to validate applicator delivery strategies and characterize heating performance within the GI tract, six heating experiments were performed with six ~ 40 kg whole pig cadavers (euthanized

from previous experiments within 12-24 hours and kept in cold storage prior to study) within a 3T GE MRI scanner. Given the onset of rigor mortis, and hence the lack of access through the mouth, the esophagus was surgically accessed prior to each experiment. The POC endoluminal applicator under test was introduced into the esophagus and directed into the stomach. High resolution T2-weighted FRFSE sequences (TE = 103 ms, TR = 3000-9000 ms, flip angle = 111, echo train length = 15, FOV = 30 cm, 512 X 512 acquisition matrix, slice thickness = 3 mm, NEX = 2) were used to delineate the anatomy, the position of the device, and to identify the target region of the pancreas. Under guidance of the real-time imaging capabilities of the RTHawk platform, fine manual manipulation (translation, rotation) of the endoluminal applicator to the target position in the stomach adjacent to pancreatic tissue was performed. If targets within the pancreatic tissue could not be defined, the liver adjacent to the stomach was used as a surrogate target tissue instead. Temperature monitoring slices were prescribed using two approaches: manually, using a scout scan in the RTHawk interface to localize the applicator and determine alignment; or automatically using the coordinates of the two active tracking coils.¹⁷⁸ One thermometry slice was positioned sagittal to the applicator transducer fixture to visualize the longitudinal extent of heating, and one to three were prescribed along the axial plane through the transducer stage. All slices were 5 mm thickness with 1 mm gap between parallel slices, chosen to capture planes through the center of each transducer and the transducer assembly fixture. Sonications were performed for 5-13 min duration, at 3.8-5 W/cm² applied acoustic surface intensity. The heat-exchanger was placed in ice slurry to cool circulating water temperature during sonication, and circulatory water flow was set at a rate of 50-70 ml/min, resulting in a cooling water temperature of ~4.5 °C in the applicator. Due to the low baseline core temperature of the cadavers, which would preclude representative

thermal lesion formation for the achieved temperature elevations, no excision or gross inspection of treated tissues following each study was performed.

3.3.7 MR guided *in vivo* porcine experiments

Preliminary investigations of applicator placement strategy, heating generation, and thermometry motion-compensation techniques were performed with *in vivo* heating trials within four adult female White York porcines (weight: 43-51 kg). All animal experiments and procedures were approved by Stanford IACUC. For each experiment, the animal was anesthetized with Atropine (.05 mg/kg) and Telazol (5 mg/kg), and maintained on isoflurane gas inhalation and controlled respiration for the duration of the experiment. Vital signs were continuously monitored. The animal was placed in the MRI scanner in dorsal or left lateral recumbency to facilitate device delivery into the stomach. The cardiac phased array coil (chosen to obtain high SNR for image guidance and thermometry) was positioned around the proximal abdomen of the animal, closely centered to the region of the pancreas. The endoluminal applicator under test was inserted through the oral cavity into the esophagus to the stomach. Scout and T2 weighted anatomical scans were used for initial localization of the applicator and pancreas. Real-time imaging feedback (< 1s update time) with RTHawk was used for fine manual manipulation to positions within the stomach adjacent to the splenic lobe of the pancreas. Once the applicator was in position, imaging planes thermometry were prescribed and ice cooled water flow was set to a rate of 70 ml/min just prior to the start of sonication.

Two different strategies for performing thermometry in the presence of respiratory motion were implemented and evaluated. The first scheme integrated single or multi-slice MRTI (with one slice sagittal and up to three axial with respect to the device) acquired continuously during the course of heating with a multiple-baseline¹⁰⁹ reconstruction strategy. A library of ~15-30 reference

baseline images were acquired prior to the onset of heating. Matching of temperature phase maps with the appropriate baseline was performed by determining the maximum intercorrelation coefficient between the target region of the corresponding anatomical image and the set of baseline images.⁹⁴ Breath-holds (30-60 s duration) were induced just prior to heating to obtain baselines (30 s with flow off and 30 s with flow on) and every subsequent 2-4 minutes following the start of heating in order to further minimize baseline misregistration and validate the reconstruction. The second thermometry scheme consisted of a single-slice with gated acquisition, using pressure bellows wrapped around the chest of the animal and connected to the MRI scanner. No breath-holds were induced, and while the GRE thermometry sequence was continuously prescribed so steady-state was achieved, data for a temperature image was only acquired and saved at the onset of expiration for each respiratory cycle. All MRTI images were thresholded to remove temperature measurements for the pixels with lowest (1-10%) signal intensity magnitude, and rectangular spatial filters, centered on the applicator and target region, were used to isolate device-related heating.

After the sonications were complete, the applicator was withdrawn and the animal was removed from the MRI scanner and euthanized following protocol procedures. The pancreas and stomach were removed in necropsy and sectioned in order to measure and photograph dimensions of the gross lesions, defined by hyperemic border or tissue blanching. Transverse and longitudinal sections through the pancreatic lesions were harvested, fixed in formalin, routinely processed for paraffin embedding, and 4 micron-thick sections were adhered to glass slides and stained using hematoxylin and eosin (H&E) for histological analysis of tissue structure. In the fourth *in vivo* porcine studies, prior to applicator removal and euthanasia, a 5.5 mL bolus of Gadovist (1.0 mmol/mL) contrast agent was injected intravenously following the final ablation, and a T1w

LAVA ARC sequence (TE = 1.7 ms, TR = 3.7 ms, TI = 5 ms, flip angle = 15, echo train length = 1, FOV = 44 cm, 512 X 512 acquisition matrix, slice thickness = 3 mm, NEX = 2) was acquired before and after the bolus to obtain contrast-enhanced images of the treatment area.

3.4 Results

3.4.1 Acoustic characterization:

The acoustic efficiencies of the combined transducers were $48.8\% \pm 1.9\%$ for the dual planar applicator, $47.8\% \pm 0.5\%$ for the dual lightly-focused curvilinear applicator, $65.5\% \pm 0.9\%$ for the dual strongly-focused curvilinear applicator, and $60.9\% \pm 1.2\%$ for the single strongly-focused curvilinear applicator. The normalized acoustic beam pressure-squared distributions for each applicator are shown in Figure 3.4 for longitudinal and transverse planes. Pressure-squared distributions were smoothed using a 3 x 3 pixel Gaussian filter, with a sigma value of 0.8. For the dual lightly-focused curvilinear applicator, the dimensions of the -3 dB beam-width is 1.2 mm along the focused dimension and extends 25 mm in depth, while for the dual planar applicator the -3 dB contour beam-width extends 3.2 mm. The dimensions of the -3 dB focal zone for the dual strongly-focused curvilinear applicator is 0.4 x 2.9 x 4.0 mm (length x width x depth), and the focal zone for the single strongly-focused curvilinear applicator is 0.8 x 2.7 x 9.3 mm.

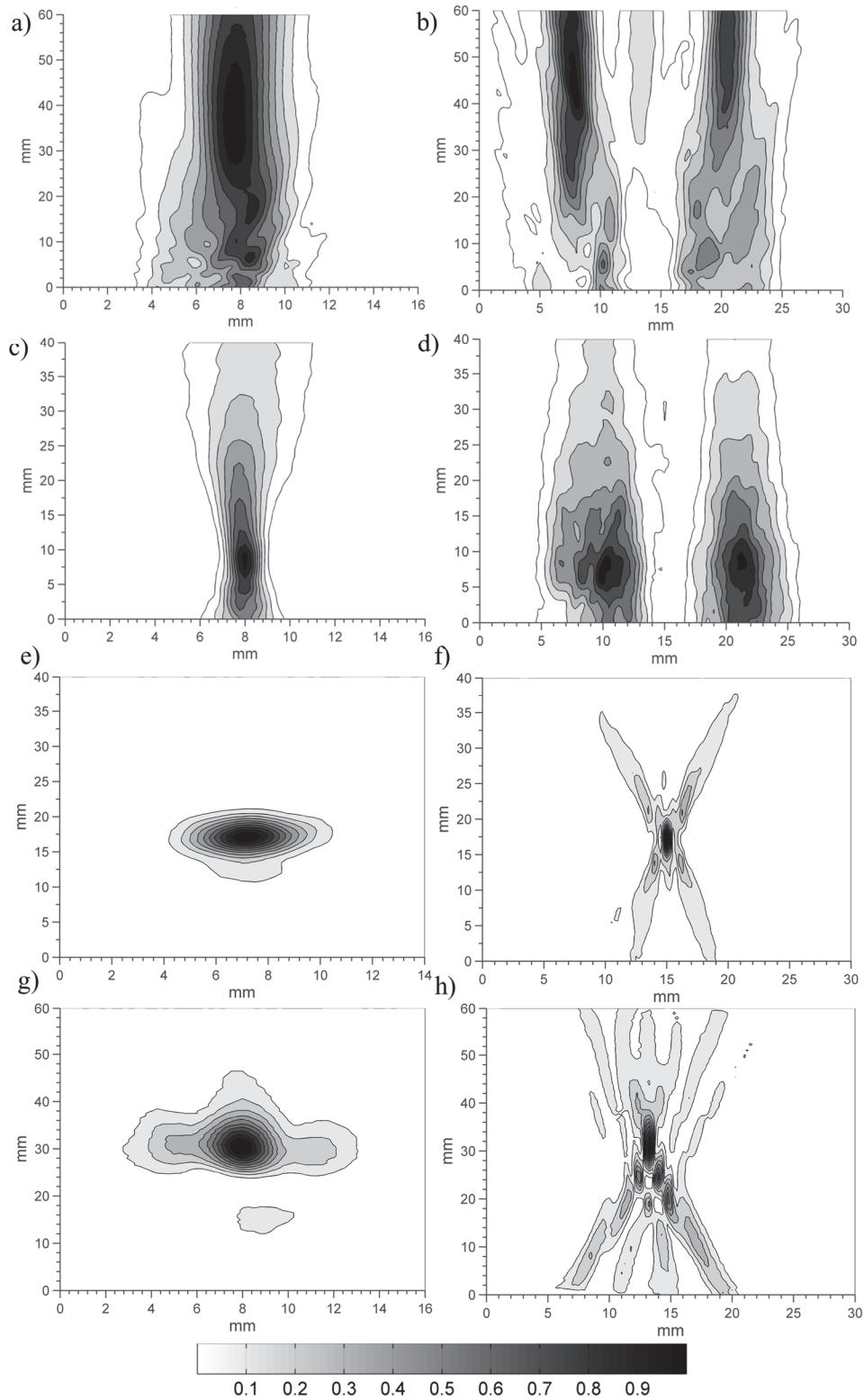


Figure 3.4 Normalized pressure-squared distributions in degassed water for the (a,b) dual planar, (c,d) dual lightly-focused curvilinear, (e,f) dual strongly-focused, and (g,h) single strongly-focused applicators across the (a,c,e,g) axial and (b,d,f,h) sagittal planes, as measured using a hydrophone.

3.4.2 MRTI experimental validation

Agreement between the temperature measurements extracted from the PRF GRE sequence and the fiber optic thermocouples can be visualized below in Figure 3.5. The average absolute magnitude of difference between the two measurements over the entire measurement time-course was 0.5 °C.

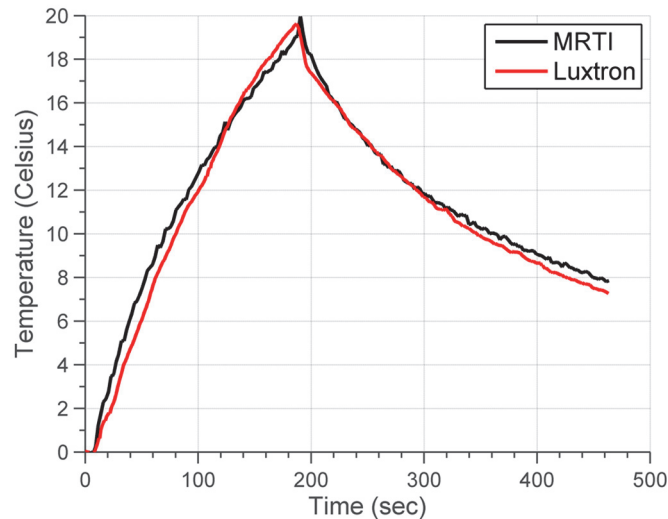


Figure 3.5 Relative temperature change measurements during a heat in tissue-mimicking phantom using the dual planar applicator. Temperature change was measured using a fiber optic thermocouple (“Luxtron”) and the PRF thermometry sequence (“MRTI”) for comparison and validation of the PRF sequence and temperature reconstruction scheme. Baseline temperature was 22 °C.

3.4.3 Heating characterization in MR guided ex vivo muscle tissues

Figure 3.6 shows representative temperature distributions produced by each applicator in pork shoulder (dual planar / dual lightly-focused curvilinear) and pork loin sirloin (dual strongly-focused curvilinear and single strongly-focused curvilinear). Applied surface intensities were ~4 W/cm² for the a-b) dual planar and c-d) dual lightly-focused curvilinear configurations, and ~2.5 W/cm² for the e) dual strongly-focused curvilinear applicator, with the depicted temperature distributions for each taken at 1 minute following the start of sonication. For the f) single strongly-focused curvilinear, the applied surface intensity was ~1.5 W/cm², and the temperature distribution corresponds to a 3 minute heating duration.

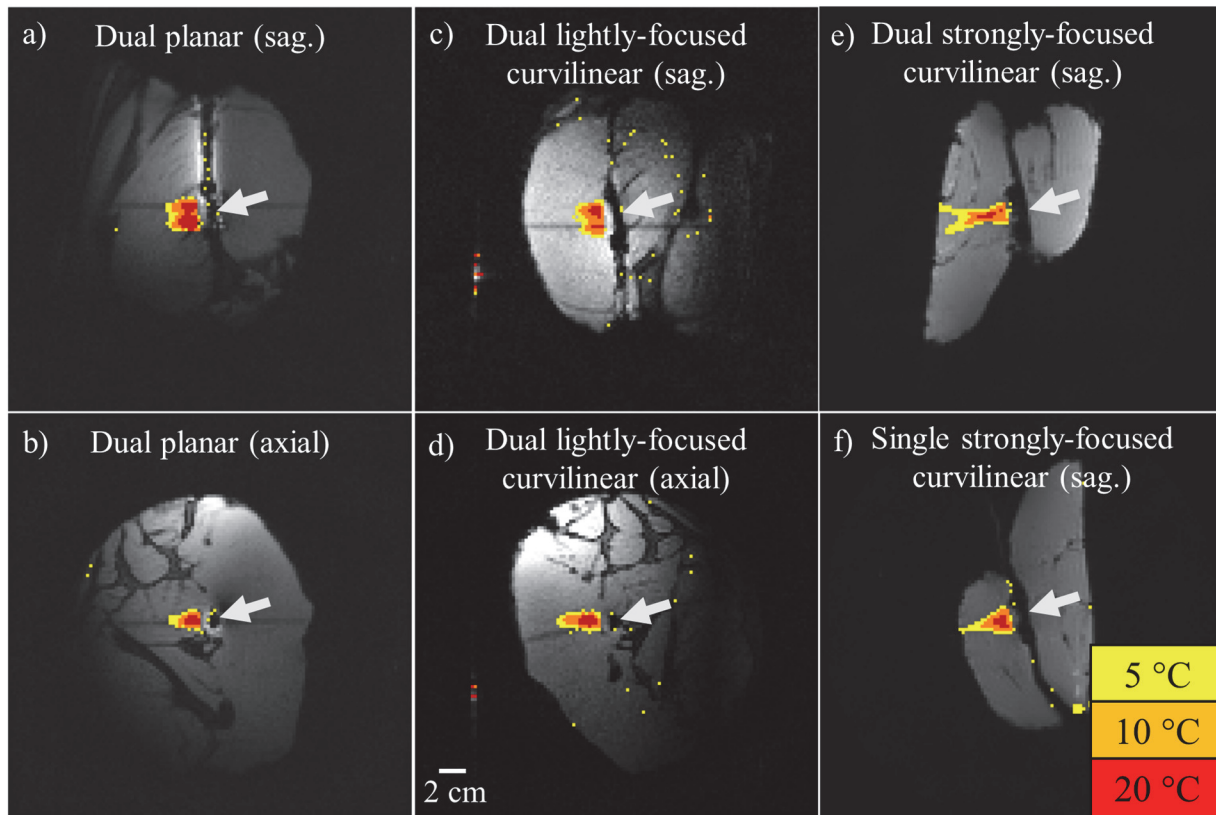


Figure 3.6 MRTI temperature distributions produced during sonications in *ex vivo* pork shoulder and pork sirloin meat slabs. Applicator placement for (a,c,e,f) sagittal and (b,d) axial temperature monitoring planes are indicated by the white arrow. Sonication durations were 1 minute for (a)-(e) and 3 minutes for (f), with applied surface intensities between $\sim 1.5\text{-}4\text{ W/cm}^2$.

3.4.4 Applicator delivery and heating characterization in MR guided *ex vivo* porcine cadaver experiments

As shown in Figure 3.7, the Hadamard encoded tracking sequence enabled determination of each coil's 3D coordinates in the scanner, permitting automatic prescription of imaging planes through the transducer stage for monitoring thermometry. The tracking coils could also be directly visualized with a GRE sequence, and used to determine the orientation of the applicator. Alternatively, when using the phased-array cardiac coil, the device position and orientation could be determined from the characteristic hypointense profile of the transducer assembly fixture.

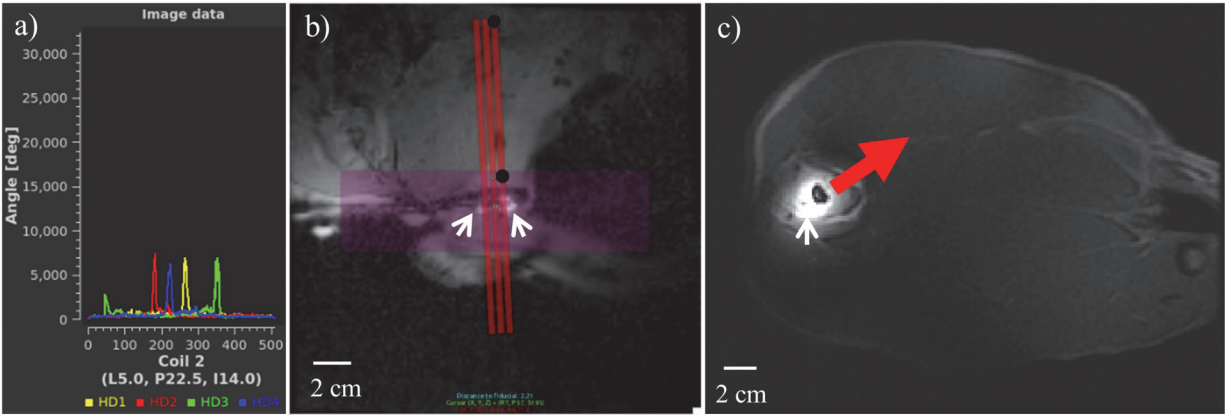


Figure 3.7 (a) The 3D coordinates of the tracking coils were localized using a Hadamard-encoded tracking sequence to obtain four projections of the coil signal. (b) Tracking coils (white arrows) could be visualized on the fixture and used to automatically prescribe imaging planes through the transducer stage. (c) Orientation of the applicator and direction of sonication (red arrow) could be determined by the relation between the hyperintense coil signal (white arrow) and hypointense applicator body.

Applicator insertion into the stomach and placement against the stomach wall for treatment of adjacent pancreatic tissue, as demonstrated in Figure 3.8, was achieved in 5 out of 6 total porcine cadaver experiments. Multi-slice temperature profiles for endoluminal sonications of pancreatic tissue using the dual planar and dual lightly-focused curvilinear applicators in separate experiments are shown in Figures 3.9 and 3.10, respectively. Treatment parameters and MRTI measurements are shown for each carcass heating trial in Table 3.2. For the planar applicator, potentially ablative ($\Delta T > 15\text{ }^{\circ}\text{C}$) contour dimensions increased from 4-40 mm in length and 4-28 mm in width as sonication time increased from 1-13 minutes, for applied surface intensities around 4 W/cm^2 (range: $3.8\text{-}5\text{ W/cm}^2$). For the dual lightly-focused curvilinear applicator at 4 W/cm^2 , $\Delta T > 15\text{ }^{\circ}\text{C}$ contours extended approximately 1-24 mm in length and 2-7 mm in width as heating time increased from 1-6 minutes. Temperature standard deviation using the phased array coil and surface coils varied between $0.2\text{-}0.3\text{ }^{\circ}\text{C}$ and $2.2\text{-}4.0\text{ }^{\circ}\text{C}$, respectively.

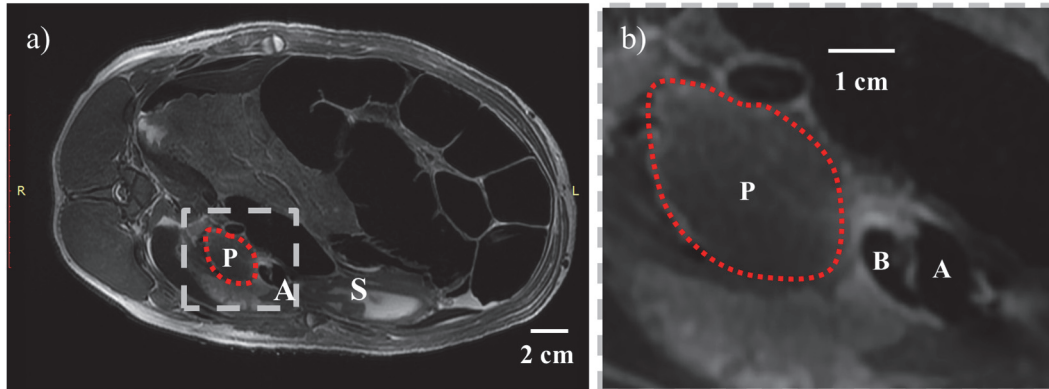


Figure 3.8 (a) Placement of the dual-planar endoluminal ultrasound applicator **A** in *ex vivo* porcine stomach lumen **S** adjacent to pancreatic tissue **P** (bordered by red dotted line). (b) $\sim 3.5\times$ magnified image showing axial cross-section of the transducer assembly fixture **A** with frontal coupling balloon **B** aligned with and facing pancreatic tissue **P**.

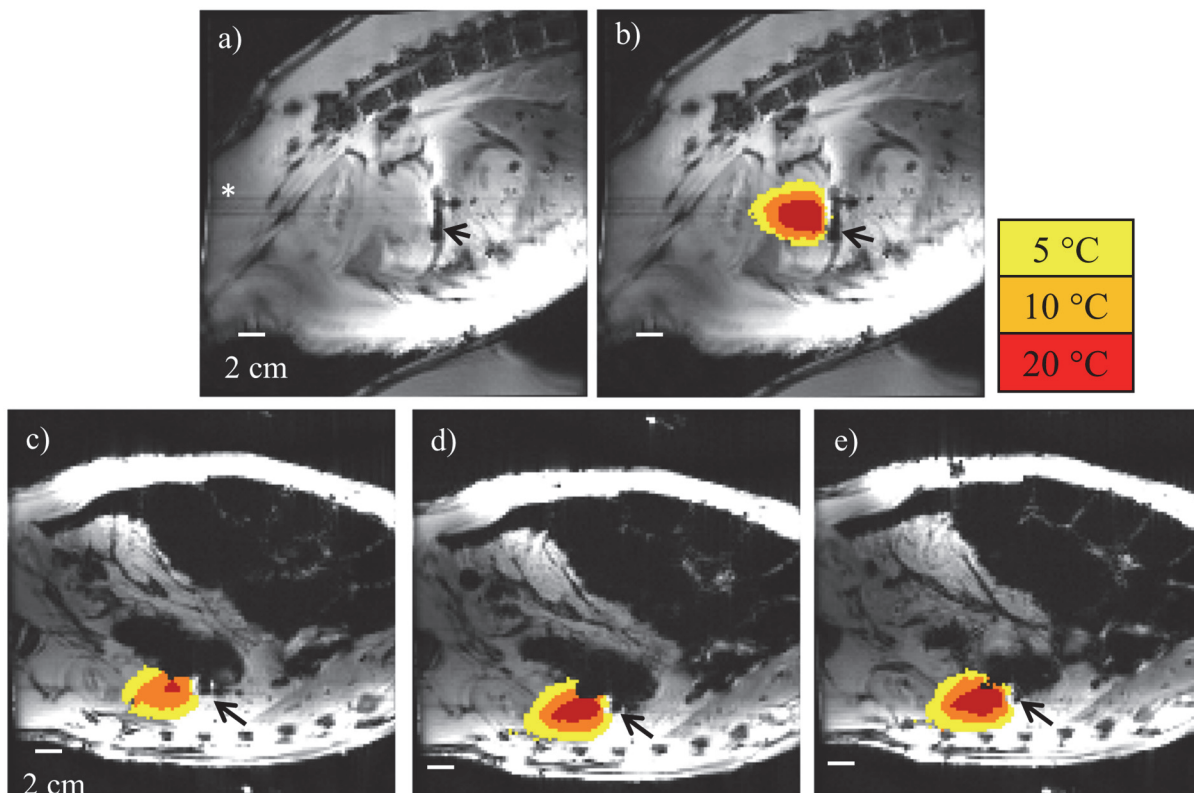


Figure 3.9 (a) Following dual-planar applicator placement in *ex vivo* stomach lumen for sonication of pancreatic tissue (Figure 3.8), an oblique imaging slice was prescribed through the central axis of the applicator (black arrow) and used to prescribe three additional axial monitoring planes through the transducer stage, with slice placement shown by the saturation bands (asterisk). Temperature distributions for each monitoring slice (b)-(e) are shown at the end of the 13 minute heat (4 W/cm^2 applied intensity), with a maximum temperature rise of $\sim 40\text{ }^\circ\text{C}$.

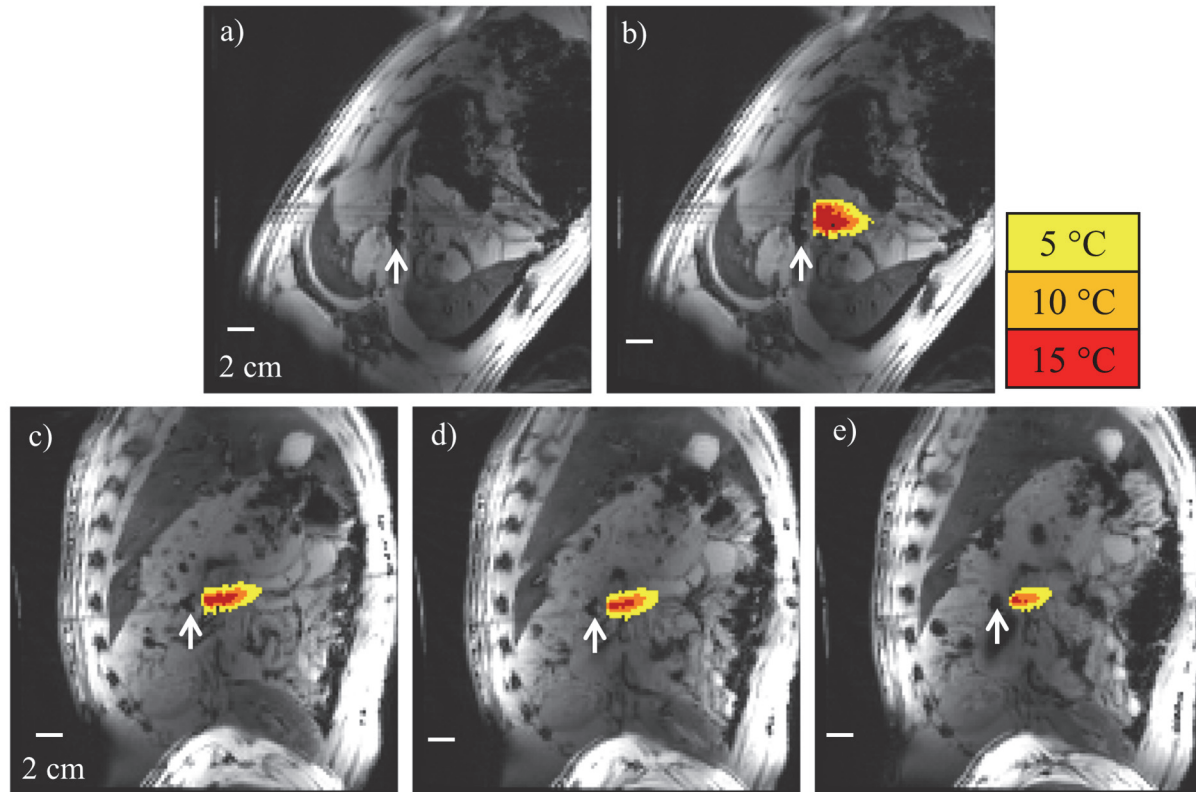


Figure 3.10 (a) Placement of the dual lightly-focused curvilinear endoluminal applicator (white arrow) in *ex vivo* pig carcass stomach and sonication of adjacent pancreatic tissue. Real-time thermometry was monitored in a (b) sagittal slice through the applicator and (c)-(e) three axial slices orthogonal to the transducer stage. Sonication duration was 6 minutes at 4 W/cm^2 applied acoustic intensity, and produced a maximum temperature elevation of $24 \text{ }^\circ\text{C}$.

Exp. #	Device	Freq. (MHz)	Coil	Acoustic intensity (W/cm ²)	Time (min)	Max Temp. (° C)	Temp. Std. Dev. (° C)	Long. extent [5 min/ t _{final}] (mm)	Transverse extent at 1 cm depth [5 min/ t _{final}] (mm)
1	Dual LF Curv.	3.3	Phased-array	4.0	6	22	0.3	[23 / 25]	[6 / 6]
2	Planar	3.2	Phased-array	4.0	13	40	0.2	[24 / 42]	[12 / 27]
3	Planar	3.2	Phased-array	3.8	5	25	0.3	23	11
4	Planar	3.2	Phased-array	4.5	10	40	0.2	[20 / 20]	[13 / 15]
5†	Planar	3.2	Surface/tracking	4.5	5	30	4.0	18	14
6	Planar	3.2	Surface/tracking	5	5	28	2.2	20	12

Table 3.2 Experimental details and MRTI T > 15 °C contour dimensions for *ex vivo* porcine cadaver heating trials of pancreatic tissue. † liver tissue targeted through the stomach was used as surrogate transgastric target similar to pancreas.

3.4.5 MR guided *in vivo* porcine experiments

Table 3.3 lists details for each *in vivo* animal experiment, including device under test, sonication parameters, MRTI scheme, and MRTI/gross lesion measures. Oral, intraesophageal delivery of the dual planar, dual lightly-focused curvilinear, and dual strongly-focused applicators under MR guidance into the stomach and positioning adjacent to the splenic lobe of the porcine pancreas was achieved in all experiments, as demonstrated in Figure 3.11. Better success in mitigating susceptibility artifacts caused by bowel gas adjacent to the treatment site for clearer thermometry was achieved with the animal in dorsal recumbency as compared to left-lateral recumbency.

Pig	Device	Freq. (MHz)	MRTI scheme	Son. site	Animal position	Acoustic intensity (W/cm ²)	Time (min)	Max Temp. (° C)	Temp. Std. Dev. (° C)	T > 15 °C dimensions (mm)*	Lesion dimensions (mm)*
1	Planar	3.2	Multi-slice / multi-baseline	1	Left lateral	5.5	10	NA	NA	NA	17 x 4 x 9
				2	Dorsal	5.5	16	20	3.0	15 x 7 x 8	16 x 4 x 10
2	Planar	3.2	Single-slice w/ resp. gating	1	Dorsal	5.4	12	18	2.0	19 x NA x 7	22 x 10 x 6
				2	Dorsal	6.2	12	20	2.3	19 x NA x 9	28 x 8 x 5
3	Dual LF Curv.	3.3	Single-slice w/ resp. gating	1	Dorsal	6.2	9	17	0.8	12 x 3 x 6	NA
						6.9	6	16	0.8		
4	Dual SF Curv.	3.14	Single-slice w/ multi-baseline	1	Dorsal	5.9	5	31	3.3	10 x NA x 14	11 x 8 x 12
				2		5.9	2.75	29	2.1	6 x NA x 10	7 x 6 x 9

Table 3.3 Sonication parameters and details for *in vivo* porcine pancreas heating experiments. *Dimensions reported in Length x Width x Depth. NA: not available

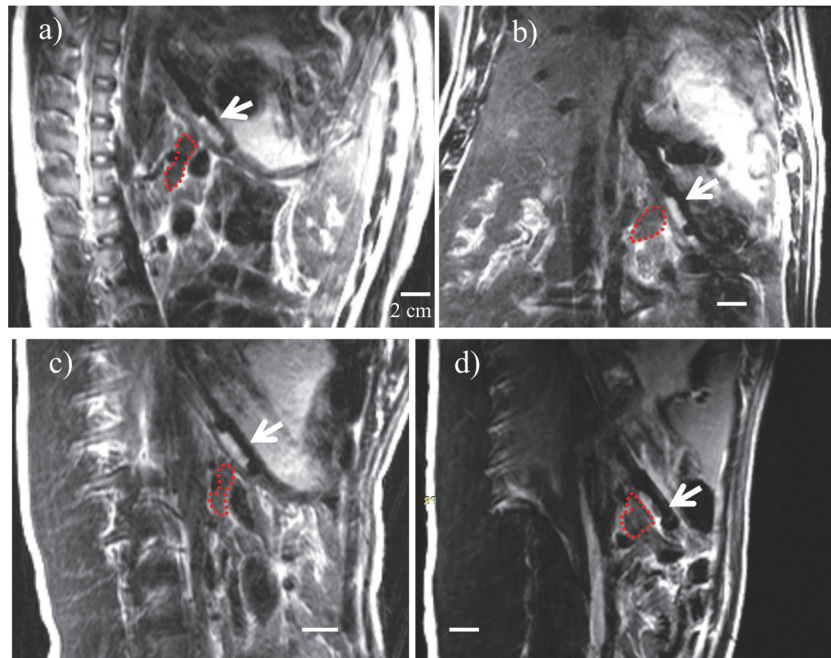


Figure 3.11 T2-weighted sagittal MRI images illustrating placement and visualization of the (a,b) dual planar, (c) dual lightly-focused curvilinear, and (d) dual strongly-focused curvilinear endoluminal applicators (white arrow) in the stomach lumen adjacent to the splenic lobe of the pancreas (red dotted outline) in the four *in vivo* porcine experiments.

Figure 3.12 illustrates MRTI temperature images from the second sonication in pancreatic tissue in Fig 1. A maximum temperature elevation of ~ 20 °C was generated in pancreatic tissue at a depth of about 17 mm from the transducer surface. This temperature maximum was reached and sustained after ~ 4 min of heating. Using the multiple-baselines reconstruction approach permitted recovery of temperature data for the entire treatment as shown in Figure 3.12 (e), by reducing motion-associated misregistration artifacts. There was general agreement in the temperature measurements recorded during breath-holds (where baseline misregistration would be minimal) and interim time-points. The temperature standard deviation was 3.0 °C using the multiple-baseline reconstruction, as compared to 4.5 °C using a single-baseline reconstruction.

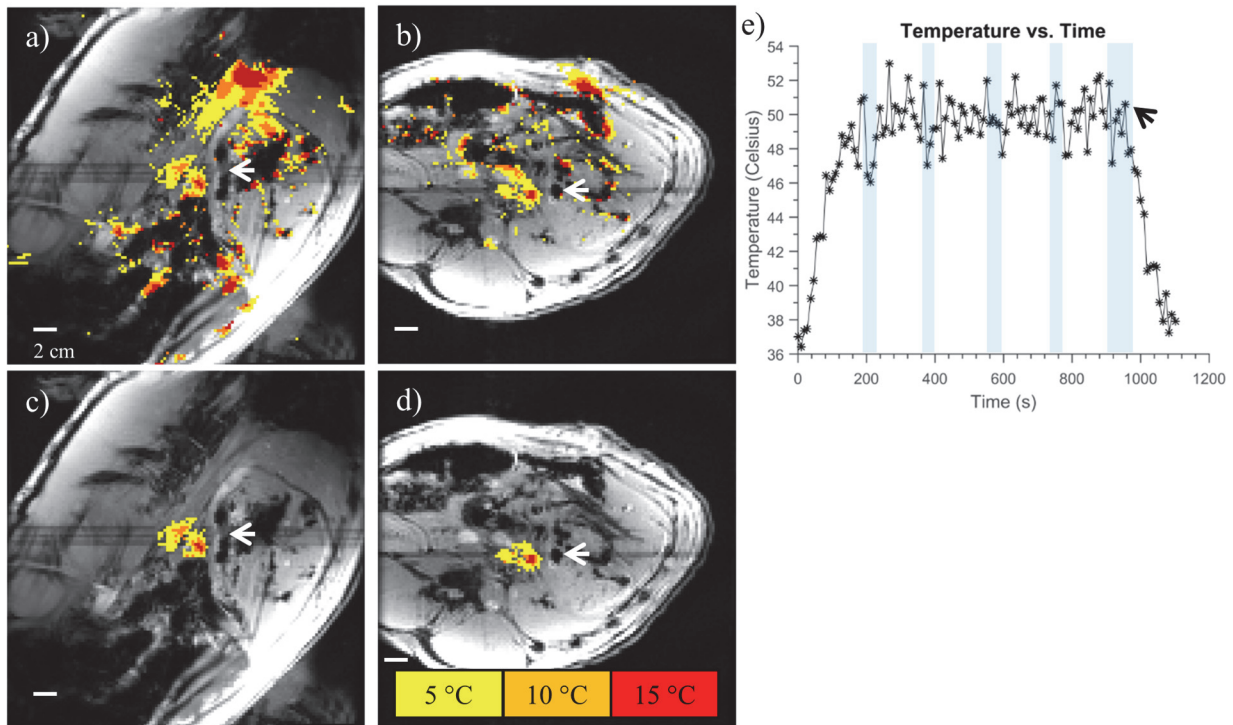


Figure 3.12 (a) Sagittal and (b) axial temperature monitoring planes generated using a multiple baseline reconstruction, for endoluminal sonication of pancreatic tissue *in vivo* in Fig 1 after 6 minutes of heating,

at $\sim 5.5 \text{ W/cm}^2$ applied to each transducer of the dual-planar applicator (white arrow). (c,d) For clarity, rectangular spatial-masks were applied to each image to isolate sonication-induced temperature change. (e) The temperature profile over time in a small (3 x 3 pixels) ROI in the heated region using the multiple baseline reconstruction, illustrating prolonged temperature elevation of target tissue to around $50 \text{ }^\circ\text{C}$, with the end of sonication indicated by the black arrow. Temperature measurements taken during breath-holds are contained within the shaded boxes.

Temperature profiles for heating trials using the dual planar applicator in Fig 2 and the dual lightly- focused curvilinear applicator in Fig 3 are illustrated in Figure 3.13. MRTI in both experiments was performed using a single thermometry plane, with respiratory gating to minimize misregistration. This scheme permitted visualization of the entire course of heating during the treatment, with minimal motion-related artifacts. For the first treatment site in Fig 2, the maximum temperature elevation was $\sim 18 \text{ }^\circ\text{C}$ at a depth of 20 mm from the transducer surface, and the temperature magnitude was responsive to increases in applied input power to the transducers, as shown in Figure 3.13 (b). For Fig 3, using the dual-curvilinear applicator, a maximum temperature elevation was $\sim 17 \text{ }^\circ\text{C}$ was reached 16 mm from the transducer, and the temperature near the splenic vein immediately distal to the target region was reduced to $\sim 5 \text{ }^\circ\text{C}$. The temperature standard deviations for the thermometry in Fig 2 and 3 were $2.0\text{-}2.3 \text{ }^\circ\text{C}$ and $0.8 \text{ }^\circ\text{C}$, respectively, as measured in the target region prior to the onset of heating. The greater temperature uncertainty in Fig 2 can likely be attributed to closer proximity of the target region to bowel tissue with large susceptibility artifacts. MRTI revealed moderate temperature penetration ($\Delta T_{\text{max}} > 10 \text{ }^\circ\text{C}$) beyond the pancreas boundaries for treatment site #2 for Fig 2, with preferential heating of spine tissue within 4 cm of and directly aligned with the applicator.

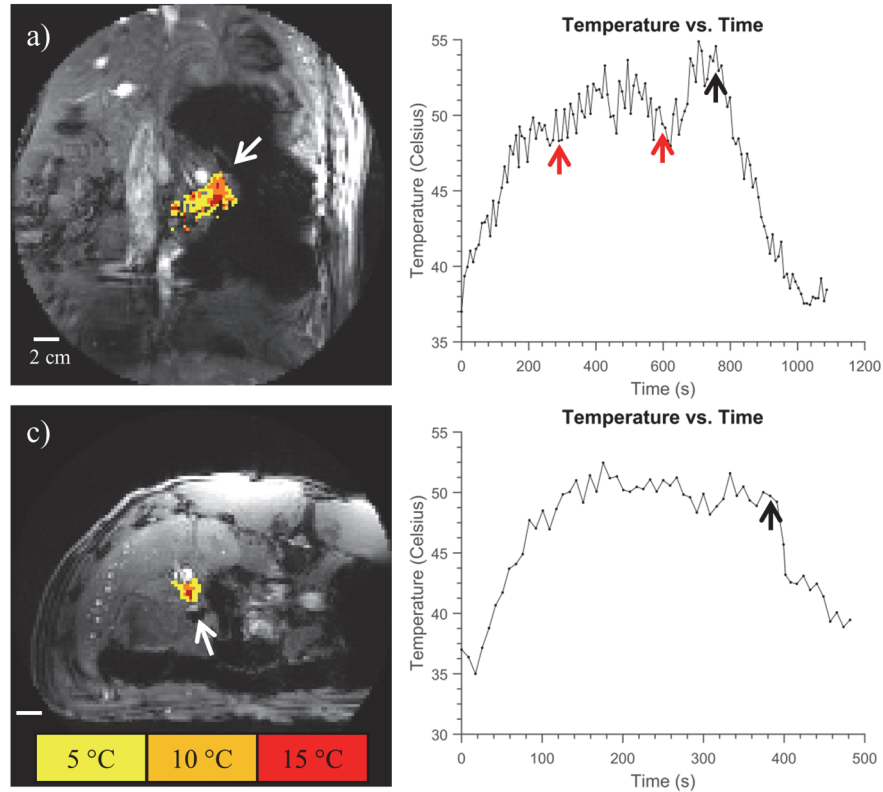


Figure 3.13 End-sonication temperature distributions are shown for endoluminal heating of pancreatic tissue through the stomach lumen for (a) a sagittal monitoring slice of the dual planar applicator in sonication site #1 for Fig 2 , and (c) an axial monitoring slice of the dual lightly-focused curvilinear applicator in Fig 3. For both experiments, MRTI was performed with a single monitoring slice and respiratory-gated acquisition. Temperature-time curves for small (3 x 3 pixels) ROIs in the heated region are shown in (b,d) for the dual planar and dual lightly-focused curvilinear heats, respectively. The transducers were driven at an average of 5.4 W/cm^2 for (a,b) and 6.9 W/cm^2 for (c,d). Time-points at which the applied power to the transducers were increased from 4.8 W/cm^2 to 5.5 W/cm^2 , then from 5.5 W/cm^2 to 6 W/cm^2 for Fig 2 are shown by the red arrows in (b), and the points at which power was switched off are indicated by the black arrows for both experiments.

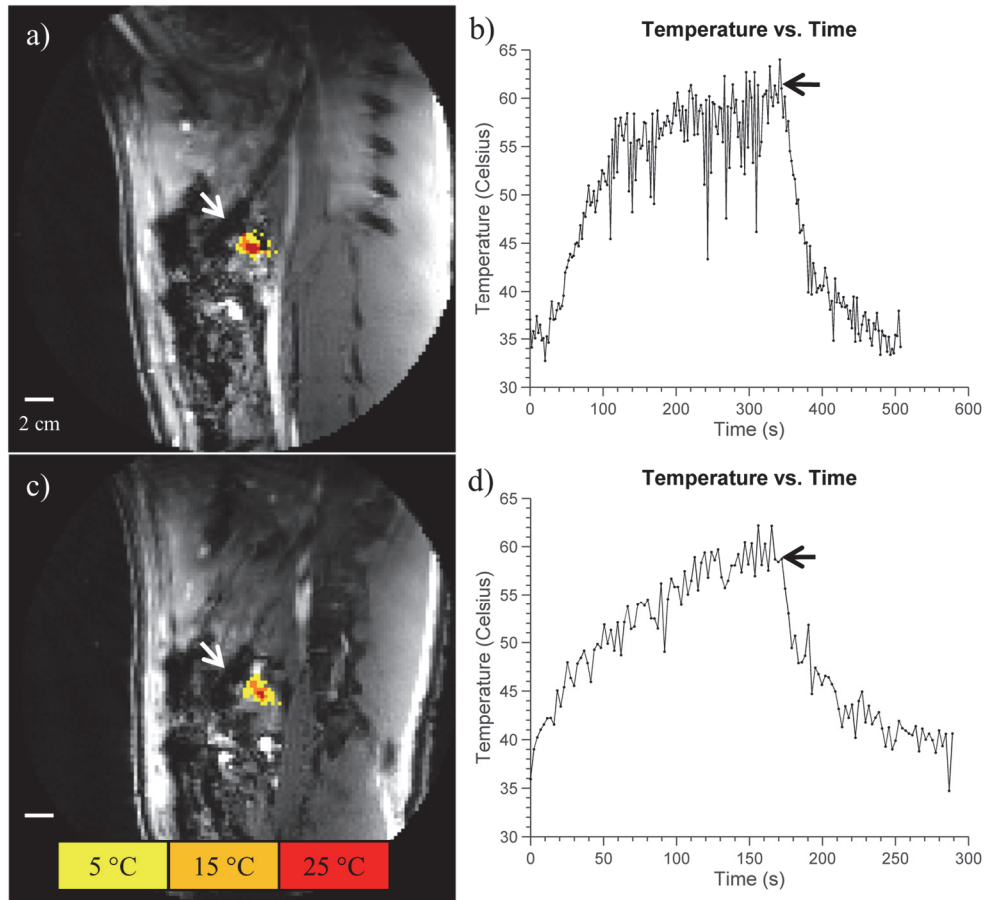


Figure 3.14 End-sonication temperature distributions are shown for endoluminal heating of two different sites in pancreatic tissue through the stomach lumen using the dual strongly-focused curvilinear applicator. A single sagittal temperature monitoring plane was prescribed and continuously acquired during both heating trials, with intermittent breath-holds used to mitigate motion-associated artifacts. Applied surface intensities were 5.9 W/cm^2 for both trials, with a (a,b) 5 min sonication duration for the first heating trial, and (c,d) 2.75 min sonication duration for the second. Time-points at which power was ceased are indicated by the black arrows for both trials.

Two heating trials in Fig 4 were performed using the dual strongly-focused curvilinear applicator, with resulting temperature distributions and temperature time-courses shown in Figure 3.14. MRTI was performed using a single thermometry monitoring plane (sagittal with respect to the applicator) with continuous acquisition (no respiratory gating), allowing an effective temporal resolution of $\sim 2.3 \text{ s}$. Breath-holds were used prior to and after the onset of heating, and applied every 2-3 minutes during the heats. A baseline library of 15-30 images were acquired prior to the start of heating, and were used for a multibaseline thermometry reconstruction. The maximum

temperature at the end of the first heating trial (5 min sonication duration) was 31 °C, which occurred at a depth of 18 mm from the transducer. The maximum temperature at the end of the second heating trial (2 min 45 s sonication duration) was 29 °C, and also occurred 18 mm from the transducer. The standard deviations of temperature for the two trials were 3.3 °C and 2.2 °C, respectively, with the lower value of the second trial potentially attributable to the larger number of baseline images used in the multibaseline reconstruction (30 vs. 15). After the sonications were completed in Fig 4, contrast-enhanced T1w images were taken to confirm lesion formation, as shown in Figure 3.15.

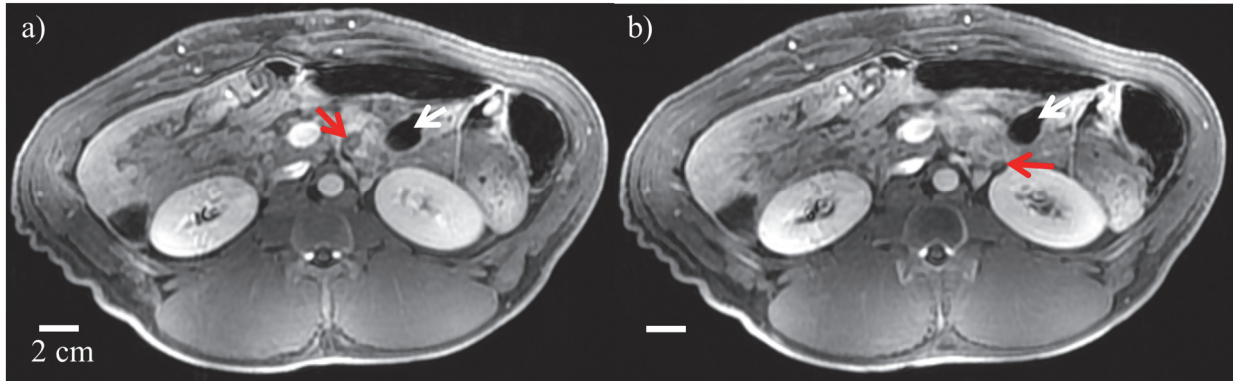


Figure 3.15 Contrast-enhanced T1w images depicting non-perfused volumes (NPV) in the pancreas as verification of thermal lesion formation. The NPVs are labelled by the red arrows, corresponding to the (a) first and (b) second heating trials in Fig 4. The applicator is depicted by the white arrows.

Following animal euthanasia and excision of the pancreas and adjacent stomach tissue, the presence of thermal lesions in the splenic lobe of the pancreas were confirmed for each animal. Figure 3.16 depicts representative images of the gross appearance of the thermal lesions, as taken from Fig 1 and Fig 4. A section of each lesion was taken and stained with H&E to visualize and verify the contiguous volumetric zone of coagulative necrosis, which appeared paler in comparison to undamaged or normal tissue, as shown in Figure 3.17. Dimensions of the thermal lesions for each pig and sonication site, based on gross inspection, are given in Table 3.3. For Pig 3, thermal

lesions dimensions were not available from gross measurements, and instead were estimated by $\Delta T > 15\text{ }^{\circ}\text{C}$ contours from MRTI. The length, width, and depth of the lesions from the surface of the pancreas ranged from 7-28 mm, 3-10 mm, and 5-12 mm, respectively. The width of the transition zone, forming the boundary between complete coagulation and normal tissue, was less than 2 mm for all cases. Inspection of excised stomach tissue revealed that samples from Pigs 1 and 3 possessed a slight discoloration on the exterior surface adjacent to the treated pancreas, and histological analysis confirmed areas of acute, sublethal thermal damage to portions of the outer muscular and serosal layers. In Pig 4, one of the thermal lesions extended to the superficial surface of the kidney. Otherwise, there was no observed lesion formation in tissues other than the stomach and pancreas during gross inspection at necropsy.

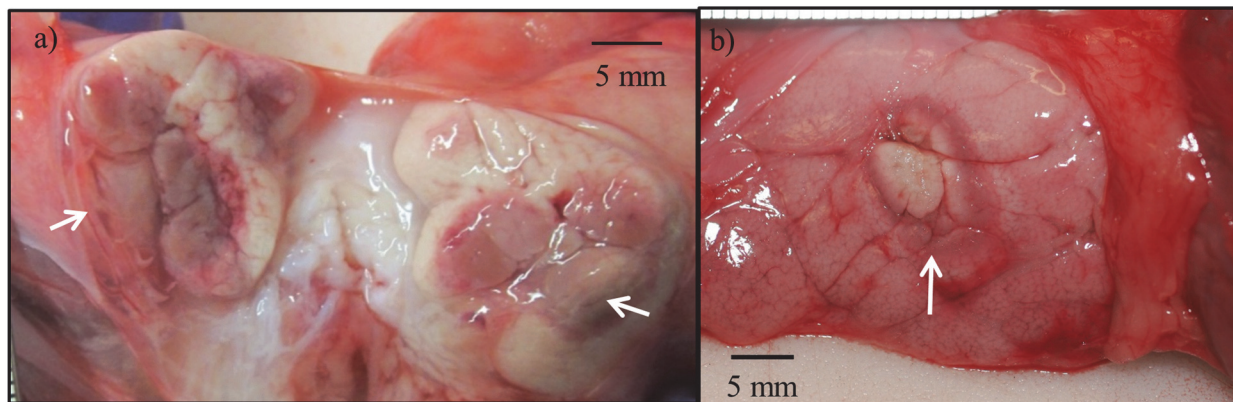


Figure 3.16 (a) Longitudinal section through a thermal lesion on the splenic lobe of the excised pancreas from the first *in vivo* porcine study, revealing ablative penetration to a depth of ~ 1 cm from the pancreas surface, with direction of applied ultrasound shown by the white arrows. (b) Surface view of a thermal lesion generated on the pancreas from the fourth *in vivo* porcine study, with conspicuous tissue blanching and hyperemic rim defining the lesion boundaries.

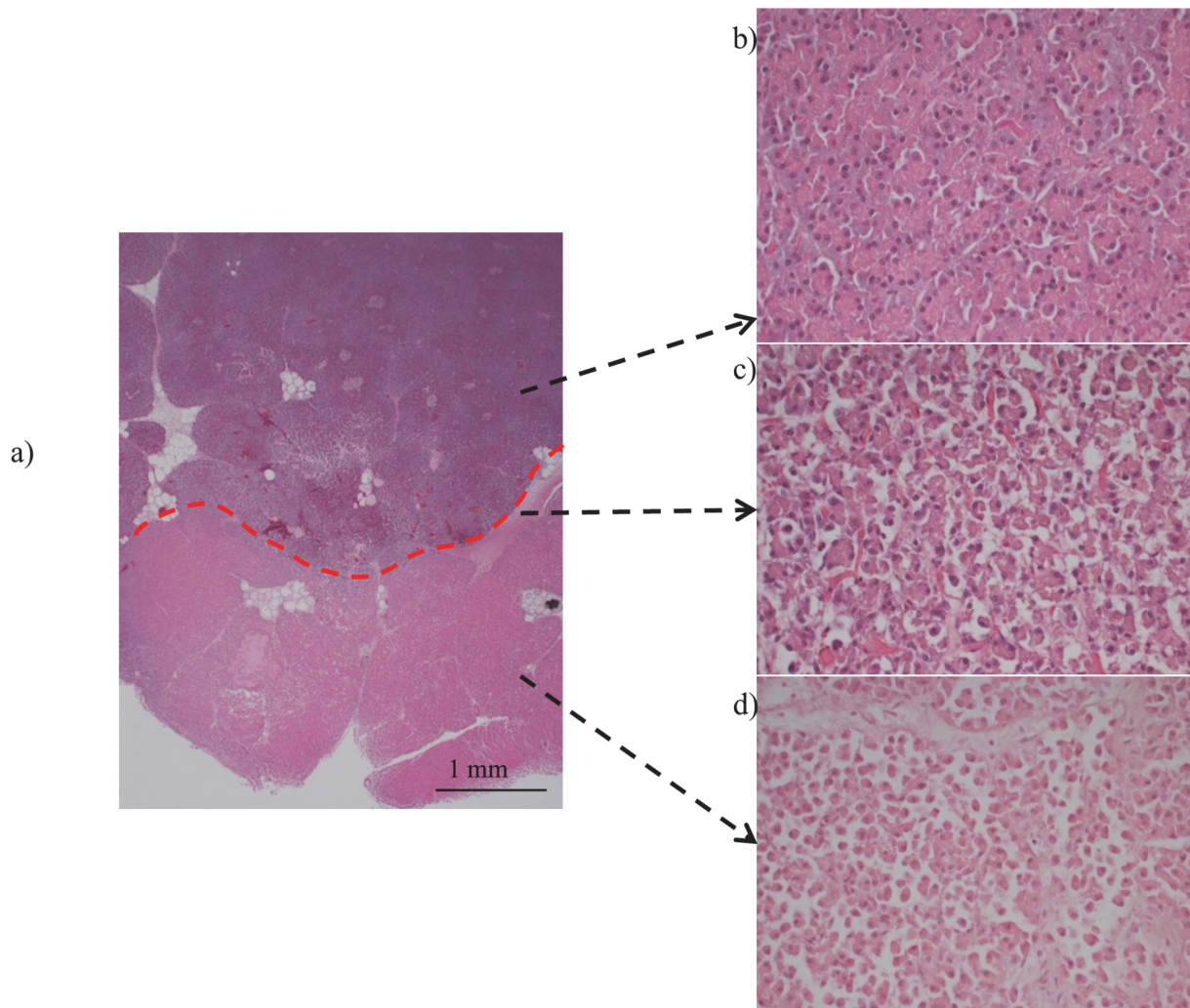


Figure 3.17 (a) Pancreatic histopathology illustrates the sub gross or macroscopic histology of the pancreas and clearly depicts the boundaries of the thermal lesion (delineated by red dashed line). Histological analysis of the pancreas was characterized by (b) untreated, normal pancreatic acini, (c) sublethally damaged lesion borders or transition zone, and (d) thermally ablated tissue that resulted in diffuse coagulation necrosis. (b = 2.5x, c-e = 40x. All slides stained with H&E.)

3.5 Discussion

This study has demonstrated the basic feasibility of generating ablative temperature elevations and thermal lesions in the porcine pancreas through the stomach wall using an endoluminal ultrasound applicator under MR guidance. These POC MR-compatible applicators could be positioned under real-time MR guidance, through the GI tract and immediately adjacent to the pancreas target

region. The feasibility of using MRTI techniques to permit multi-slice and real-time monitoring of temperature evolution during treatments was demonstrated. The planar and lightly-focused curvilinear transducer designs were able to achieve ablative temperature elevation ($>15\text{ }^{\circ}\text{C}$) in pancreatic tissue at depths of 2-4 cm from the luminal wall in *ex vivo* porcine carcass models. As shown by MRTI (Figures 3.6, 3.9-3.10; Table 3.2, 3.3) and the acoustic beam profiles (Figure 3.4), curvilinear transducer configurations resulted in more spatially-selective heating profiles that were narrower along the curved dimension relative to the planar applicator, as expected.¹⁶⁷ In the *in vivo* experiments, the maximum temperatures and extents of effective temperature elevations extended $\sim 30\text{ }^{\circ}\text{C}$ at depths up to 2 cm from the transducer surface, but were reduced compared to *ex vivo* studies for the dual planar and lightly-focused curvilinear designs. One likely cause for these discrepancies is the heat sink effect caused by general perfusion and the proximity of nearby major vasculature, i.e the splenic vein and artery, which run along the length of the splenic lobe and were evident at a depth of 1.5-2 cm in the pancreas (Figure 3.11). In the face of perfusion effects, greater applied powers could be utilized to increase heat generation. Utilizing more strongly-focused transducer designs could also increase exposure temperatures, as demonstrated in Fig 4 using the dual strongly-focused curvilinear applicator (maximum temperature of $\sim 30\text{ }^{\circ}\text{C}$ as opposed to $\sim 20\text{ }^{\circ}\text{C}$ for the planar/lightly-focused curvilinear designs). Coupling and positional alignment between the applicator, stomach lumen, and pancreatic tissue may also be inconsistent in the presence of respiratory motion, resulting in the dispersion of acoustic energy over a larger volume of tissue. Applicator fixation methods could alleviate this coupling issue, with potential strategies including distensible back balloons, clip fixation, or vacuum suction of the applicator against the stomach lumen. Incorporation of flexibility, steering, and placement strategies common to endoscopes into the flexible distal end of the device may also improve positioning and reduce movement. Further,

variation in the lesion dimensions and shapes in the *ex vivo* and *in vivo* experiments may be attributed to the distinct anatomical conditions in each animal, as access to pancreatic tissue and the overall size of targetable tissue varied between animals (Figure 3.11).

A primary safety concern affiliated with this endoluminal delivery of thermal ablation approach is the preservation of the luminal wall from thermal injury, which could cause formation of gastric fistula.¹¹⁸ While MRTI in the *ex vivo* and *in vivo* studies illustrated that the water cooling was effectively pushing the maximum temperatures deeper into the tissue, there was some histological evidence of acute thermal damage to the outer muscular and serosal layers of excised stomach tissues from the *in vivo* studies. One likely cause for this is the large measured thickness (~8 mm) of the porcine stomach wall near the esophagus, where the sonications for treating the splenic lobe of the pancreas were performed. In theoretical simulations of endoluminal ultrasound ablation of human pancreatic cancer, while pertaining to different anatomical conditions and tissue properties compared to porcine anatomy, it was demonstrated that endoluminal sonication through thinner luminal walls results in lower temperatures within the wall and minimizes the risk of thermal injuries.¹²⁹ As such, the risk of thermal damage would be reduced in humans due to the lower anticipated luminal wall thicknesses (2-3 mm). Similarly, in the experimental porcine setting there was likely an increased effective acoustic attenuation and absorption in the wall tissue due to the presence of food particles and/or gas bubbles in the mucosal layers, which could be reduced by flushing the interior stomach or GI lumen via lavage prior to treatment.⁷⁹ Transducer designs that incorporate tighter focusing, with the focus depth at least 1 cm beyond the wall tissue, should also improve stomach sparing, as verified in Fig 4.¹²⁹ Improving coupling between the applicator cooling balloon and luminal wall through tip steering, compression, or fixation mechanisms may also provide for consistent or enhanced luminal sparing.

While the porcine represents a close animal model to humans in terms of digestive anatomy, key differences exist which present unique challenges as compared to the application of this technique in humans. In humans, the head of the pancreas is the largest region of the organ and the most common site for tumor genesis as compared to tail/body regions.¹¹⁵ Treatment of tumors in the pancreatic head would ideally be performed with the endoluminal applicator positioned in the duodenal lumen (see Figure 3.1), which is intimately attached to the head and would facilitate luminal sparing due to the thinner thickness of the duodenal wall (2 mm distended) as compared to stomach wall (3-5 mm) in humans.^{153,160,161} In the porcine model, the head of the pancreas (the duodenal lobe) is the smallest volumetric portion of the pancreas,¹⁷⁹ and is separated from the medial duodenum by mesentery, leaving potential gaps between the two organs.¹⁶⁴ Further, the pyloric region that connects the stomach and duodenum contains a mucosal protuberance called the torus pyloricus, which results in much more constriction in the porcine model than in humans, impeding endoluminal access. As such, the splenic lobe of the porcine pancreas (analogous to the tail of the human pancreas) was chosen as the target region, due to its larger comparative volume and relative ease of access from the stomach lumen. Tradeoffs associated with this target choice include the greater susceptibility to respiratory motion in the tail region,¹⁸⁰ the thicker luminal walls adjacent to the tail relative to the stomach antrum or duodenum, and proximity to major vasculature and the left kidney, which act as heat sinks.

The endoluminal ultrasound applicators were designed for compatibility with MR-guidance, which permitted target identification, device localization and positioning, as well as direct treatment monitoring through PRF-based MRTI. Inclusion of the active tracking coils provided quick localization of the applicator and automated prescription of thermometry planes through the transducers, thereby reducing overall procedural times for a single device placement

and sonication by approximately 5-10 minutes, as compared to manual methods. Hardware limitations of the MRI system in our current setup required that they could only be implemented with up to three individual surface coils for deep abdominal imaging, which suffered from poorer imaging quality and lower thermometry fidelity as compared to what could be achieved with the phased array coil (Table 3.2), and hence were unsuitable for the *in vivo* studies. With additional hardware to integrate the tracking coils with phased array coil imaging, they could be valuable in reducing procedural times as well as further developed to track applicator motion *in vivo*, as a means of evaluating different fixation strategies, or for gating sonications in the presence of significant motion.

Due to the relatively long durations (3-15 min) of active sonications associated with this volumetric heating strategy, multi-slice MRTI is a valuable and appropriate tool for monitoring the complete extent of heating over time. MRTI performed in the *ex vivo* studies using the phased array coil permitted real-time and clear demarcation of temperature contour evolution, with the only significant noise source being susceptibility artifacts caused by gas in nearby bowel tissue. As anticipated, MRTI in the *in vivo* study suffered from additional respiratory motion artifacts, as well as flow artifacts from nearby major vasculature. While there was general agreement between the gross lesion measurements and MRTI ($\Delta T > 15\text{ }^{\circ}\text{C}$) measurements (Table 3.3), discrepancies were expected due to limited thermometry precision as well as the inherent difficulty in registering the temperature monitoring planes and lesion cutting planes, particularly as the orientation, shape, and position of the inspected tissues shift during excision. Both multiple-baseline reconstruction (Figures 3.12, 3.14) and respiratory gating (Figure 3.13), using controlled respiration and pressure bellow input signal, were demonstrated to reduce motion artifacts for clearer real-time monitoring of thermometry during treatments. Compared to multiple-baseline reconstruction, the respiratory

gated acquisition scheme permitted more precise thermometry (Table 3.3), and could be similarly adapted for multiple-plane monitoring at the cost of temporal resolution.^{181,182} The multiple-baseline reconstruction methods as applied also have errors in temperature measurements immediately adjacent to the applicator, due to either different circulatory flow conditions or the development of temperature gradients caused by cooling water circulation throughout the duration of baseline collection. Besides motion compensation, other sources of significant artifacts, such as excessive gas in the stomach/bowels and peristalsis motion, could be reduced in future studies by flushing and filling the stomach with degassed water prior to treatment,⁷⁹ and by administration of anticholinergic drugs, such as dicyclomine,¹⁸³ respectively. Although not demonstrated in this study, a substantial benefit of MRTI-based thermometry that could be applied in future studies is the real-time calculation of thermal dose accumulation in tissues, and inclusion of feedback control schemes based on temperature/dose levels in target or sensitive tissues to modulate applied power levels and/or applicator positioning.^{94,184-186}

3.6 Conclusions

The results of this study demonstrate preliminary feasibility that MR-guided endoluminal ultrasound applicators can generate volumetric thermal therapy in pancreatic tissues from within the GI tract. MR guidance provides an effective means of localizing and positioning the applicator in the GI tract for targeting pancreatic tissues, and has the potential to enable conformal therapies through monitoring volumetric temperature elevation. Further development of this approach, including treatment control, validation, and refinement to applicator design and MR thermometry techniques, is warranted for preclinical evaluation.

Chapter 4

Integration of deployable fluid lenses and reflectors with endoluminal ultrasound applicators: preliminary investigations of enhanced penetration depth and focal gain

4.1 Abstract

Purpose: Catheter-based ultrasound applicators can generate thermal ablation of tissues adjacent to body lumens, but have limited focusing and penetration capabilities due to the small profile of integrated transducers required for the applicator to traverse anatomical passages. This study investigates two designs for an endoluminal or laparoscopic ultrasound applicator with deployable acoustic reflector and fluid lens components, which can be expanded after device delivery to increase the effective acoustic aperture and allow for deeper and dynamically adjustable target

depths. Acoustic and biothermal theoretical studies, along with benchtop proof-of-concept measurements, were performed to investigate the general concept and proposed designs.

Methods: Two distinct applicator designs, one an “end-firing” configuration and the other “side-firing”, were conceived. The design schema for the end-fire configuration consists of an array of tubular transducer(s) situated at the end of a catheter assembly, surrounded by an expandable water-filled conical balloon with a secondary reflective compartment that redirects acoustic energy distally through a plano-convex fluid lens. The side-fire configuration integrates three planar transducer arrays arranged in an equilateral triangle geometry along the tip of the catheter assembly, with planar reflectors and plano-convex fluid lens compartments arranged to output energy adjacent to the transducer assembly. By controlling the lens fluid volume, the convex surface of the fluid lens can be altered to adjust the focal length or collapsed for device insertion or removal. Acoustic output of the expanded applicator assemblies was modeled using the rectangular radiator method and secondary sources, accounting for reflection and refraction at interfaces. Parametric studies of transducer fixture radius (1-6 mm), transducer length (3-30 mm), frequency (1.5-3 MHz), expanded balloon diameter (10-50 mm), lens focal length (10-100 mm), lens fluid (silicone oil, perfluorocarbon), and tissue attenuation (0-10 Np/m/MHz) on beam distributions and focal gain were performed. A proof-of-concept end-fire applicator assembly was fabricated and characterized using hydrophone-based intensity profile measurements. Biothermal simulations of endoluminal ablation in liver and pancreatic tissue were performed for target depths between 2-10 cm.

Results: Simulations indicate that focal gain and penetration depth scale with the expanded reflector-lens balloon diameter for the end-fire design, and with transducer size for the side-fire configuration, with greater achievable fluid lens transmission using perfluorocarbon lens fluid.

Simulations of a 50 mm balloon OD, 10 mm transducer OD, 1.5 MHz end-fire assembly in water resulted in maximum intensity gain of ~170 (focal dimensions: ~12 mm length x 1.4 mm width) at ~5 cm focal depth and focal gains above 100 between 24-84 mm depths. The largest side-fire configuration (12 mm fixture OD, 30 mm transducer length, ~40 mm balloon aperture diameter) produced a maximum gain of 250 (focal dimensions: ~8 mm length x 1.1 mm width) at ~28 mm focal depth and focal gains above 100 between 12-66 mm depths. Compared to a conventional applicator with a fixed spherically-focused transducer of 12 mm diameter, focal gain was enhanced at depths beyond 20 mm for assembly configurations with expanded balloon diameters ≥ 20 mm. Hydrophone characterizations of the experimental end-fire assembly (31 mm reflector/lens diameter, 4.75 mm transducer radius, 1.7 MHz) illustrated focusing at variable depths between 10-70 mm with a maximum gain of ~60 and demonstrated agreement with theoretical simulations. Biothermal simulations (30 s sonication, 75°C maximum) indicate that investigated applicator assembly configurations could create localized ellipsoidal thermal lesions increasing in size from 10-46 mm length x 4-8 mm width in pancreatic tissue as target depth increased from 2-8 cm.

Conclusions: Preliminary theoretical and experimental investigations demonstrate that combining endoluminal ultrasound with an expandable acoustic reflector and fluid lens assembly can significantly enhance acoustic focal gain and penetration from inherently smaller diameter catheter-based applicators.

4.2 Introduction

Endoluminal catheter-based ultrasound applicators provide a minimally invasive option for delivering localized and spatially-precise thermal therapy to tissue targets that are adjacent to body cavities or lumens. Compared to other commonly used energy sources for thermal ablation, such

as RF, laser, or microwave, ultrasound provides a high degree of control over the spatial deposition of energy and heating, and improved penetration for targeting deeper tissues.⁶³ Extracorporeal high intensity focused ultrasound (HIFU) uses large focused transducer arrays (0.5-1.5 MHz) to target depths of 10-15 cm and is completely non-invasive, but requires a clear acoustic window from the transducer to the target location for safe and effective treatments, which is challenging in treating sites near in proximity to bone or gaseous interfaces such as the bowels or lungs.⁵⁴ Catheter-based ultrasound, while more invasive than external HIFU, can be used to target sites with limited external acoustic access and provides better volumetric energy localization.⁶³

Despite its advantages, there are physical limitations to current endoluminal ultrasound technology which impose practical constraints on achievable energy and thermal penetration depths. By necessity, these catheter-based devices need to have a small size profile (i.e., overall diameter) and high flexibility in order to navigate through narrow luminal passages to reach the target site. Similarly, laparoscopic-based ultrasound devices are restricted in diameter to minimize the incision or port size for access to the abdominal cavity. These requirements constrain the physical size of the integrated transducer assembly (fixed or phased array) and its effective aperture, thereby limiting acoustic output and depth of penetration typically to within a few centimeters of the device. While this limited penetration may be appropriate for sites with shallow and small targets, greater penetration and control of the focal depth could expand the utility of endoluminal ultrasound for treating sites with larger and/or deeper targets, such as for advanced stages of liver or pancreatic cancer. Beyond simply extending the length of produced lesions, a valuable capability would be target depth specificity, whereby localized lesions could be generated at specified depths without substantial near-field heating. This would be essential for targeting tissues with deep borders ($>\sim 3$ cm) from the luminal wall, without inducing thermal injury to the

luminal wall or intervening tissues. Accomplishing such specificity requires high focal gain at target depths, which is typically precluded at focal depths beyond a few centimeters due to the small effective aperture of mounted focused transducers.

One means of enhancing the effective aperture of radiating acoustic energy in endoluminal ultrasound, without compromising the device's ease of placement or delivery, is to integrate an expandable multi-compartment balloon around the transducers that serves as an acoustic reflector. The concept of combining endoluminal ultrasound with expandable balloon reflectors was introduced by Nakagawa et al., where it was used to re-direct and focus acoustic energy from a tubular transducer source to create annular ring lesions for pulmonary vein isolation.⁷⁵ Their design featured a multi-compartment balloon that was collapsed during device delivery and removal, and expanded at the treatment site up to a diameter of 35 mm, with the inner coupling compartment of the balloon filled with water and the outer compartment filled with CO₂ gas to form the reflective interface.⁸⁷ Whereas the Nakagawa et al. device used a highly-precise and fixed parabolic surface geometry to create the annular ring focus, a simpler balloon geometry, such as a conical surface profile, could be combined with tubular transducer sources to redirect all energy in the forward direction of the applicator, without focusing. Reflected energy would be dispersed over a larger surface area (as a function of the reflector geometry) relative to the source, resulting in an increased effective aperture of the acoustic emission. While focusing could also be directly achieved using the reflector, as demonstrated by Nakagawa et al., it requires a more complex and geometrically-precise surface profile upon inflation, which is not practically amenable to dynamic and fine adjustment in order to vary the size or depth of the focal region.

Rather than use the deployable reflector to both augment the aperture and focus the acoustic energy, focusing can be achieved using an acoustic fluid lens. Fluid lenses incorporating

perfluorocarbon or silicone oil solutions have been integrated with therapeutic ultrasound sources for extracorporeal hyperthermia applications by Yoon et al.^{53,187} The lens is composed of a liquid that has a different speed of sound relative to water or tissue contained by a distensible membrane, and by varying the fluid volume, the spherical radius-of-curvature (ROC) of the convex membrane and resulting focal length of the lens can be adjusted. This distensible spherical lens allows for dynamic adjustment of the focal depth, and serves as a simpler, albeit more limited, means of achieving dynamic focusing capabilities as compared to a 2D phased array source which, while permitting dynamic 3D focusing, is significantly more expensive and technically complex to fabricate and operate.

Based upon the above concepts, the core design concept explored herein is to combine deployable acoustic reflectors and fluid lenses within an endoluminal ultrasound applicator, as a means to increase focusing and penetration depth, while maintaining a small insertion profile. Figure 4.1 shows concept drawings of two distinct “end-firing” and “side-firing” deployable applicator configurations, each of which featuring an expandable multi-compartment balloon that functionally serves as an acoustic reflector and lens in order to disperse acoustic energy across a larger surface area and focus it. The proposed “end-fire” design, as shown in Figure 4.1 (a), consists of a central tubular transducer source surrounded by a conical balloon filled with water in the interior compartment and gas or reflective components in the external compartment to form a reflective surface. At the distal tip, a separate balloon compartment would serve as a plano-convex fluid lens, with a distensible distal membrane to permit dynamic adjustment of the focal depth by changing the volume of lens fluid. The “side-fire” design (Figure 4.1 (b)) utilizes three planar transducer arrays geometrically arranged in an equilateral triangle configuration along the long axis of the applicator, with deployable reflector and distensible fluid lens compartments spatially-

configured to direct and focus all acoustic energy adjacent to the applicator. Both configurations would emulate a larger diameter spherically-focused device with the focal region in line with or adjacent to the longitudinal axis of the device, for the end-fire and side-fire designs, respectively. For both configurations, the entire reflector-lens assembly would be collapsible during device insertion and removal, and could be deployed at the target site, such as the stomach or GI tract, for treatment.

The objective of this study is to evaluate the capabilities of the proposed designs and characterize their performance as a function of various design parameters, applying both theoretical and experimental approaches. Models of acoustic propagation through both assemblies, incorporating the rectangular radiator method and the method of secondary sources to incorporate acoustic reflection and refraction at material interfaces, were implemented. An extensive set of parametric studies over transducer, reflector, lens, and tissue properties were performed to investigate their effects on resulting acoustic pressure and intensity distributions for each applicator design. In order to validate the acoustic modeling methodology and core concepts explored in this study, a modular proof-of-concept “end-fire” applicator assembly was designed, fabricated, and characterized using hydrophone measurements for comparative purposes. Finally, a series of three-dimensional biothermal simulations were performed to investigate the heating characteristics produced by each proposed design for endoluminal ultrasound ablation in pancreas and liver tissue targets.

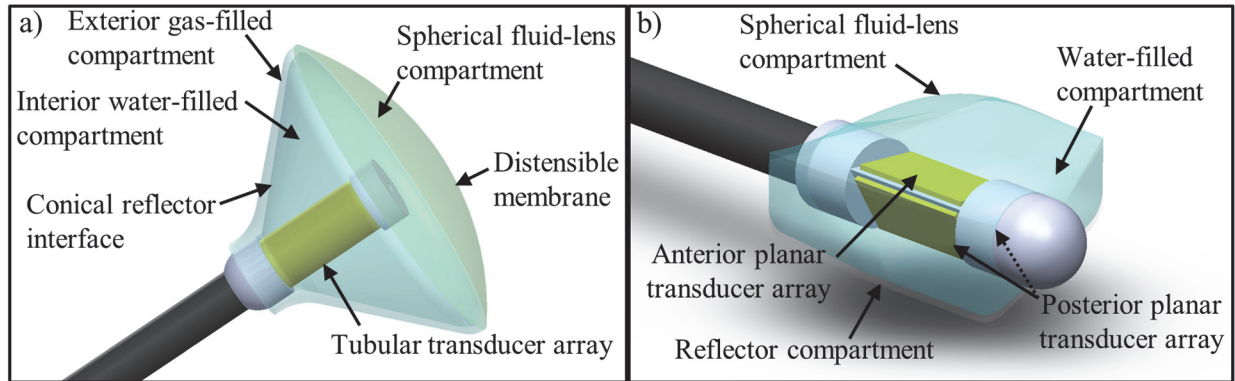


Figure 4.1 Schematics of two ultrasound applicator designs that each integrate a multi-compartment balloon that serves as a deployable acoustic reflector and fluid lens. The multi-compartment balloons are illustrated in their expanded or deployed states. For the (a) end-fire configuration, acoustic energy would be emitted by the central tubular transducer, reflected off the conical reflector interface, and focused by the convex interface of the fluid lens in line with the long axis of the device. The (b) side-fire configuration consists of three planar transducers arranged in triangular geometry, and the reflector is used to collimate energy from the posterior elements in line with the anterior element for focusing energy adjacent to the applicator.

4.3 Methods

Acoustic modeling of the wave propagation within and through multiple material interfaces is complex, and requires incorporation of wave reflection and refraction. Figure 2 (a)-(b) shows side-profile and transverse section schematics of the proposed applicator assemblies, with ray traces to approximate how the acoustic energy propagates through each compartment of the expanded balloons. For the end-fire design, acoustic energy would be generated by the central tubular transducer array, and emitted radially through the water-filled interior compartment. Complete reflection would occur at the interface to the outer gas-filled compartment, which has a 45° angle relative to the long axis of the device in order to collimate all reflecting acoustic energy along the long central axis of the device. At the interface between the water-filled compartment and the fluid lens, partial reflection would occur due to the impedance mismatch between the two fluids. Partial reflection and refraction of the acoustic waves would occur at the distal interface of the fluid lens due to its convex surface, which focuses the beam. For the side-fire, acoustic energy would be

generated by the posterior and anterior planar transducer arrays, which are arranged in an equilateral triangular cross-sectional geometry. The acoustic output of the posterior elements would be completely reflected by the posterior gas-filled compartment with planar surface profiles that are angled to collimate energy along the direction of the anterior transducer element. Akin to the end-fire design, partial reflection/transmission would occur at the interface of the water-filled compartment and fluid lens, and then partial reflection and refraction at the convex boundary of the fluid lens. Due to the different distance travelled by the acoustic waves outputted by the posterior planar elements relative to the anterior element, a phase difference in the driving signals may be necessary to ensure the waves are all in phase at the focus. A thorough description of the theory and methodology employed to model acoustic propagation through the applicator assemblies is given below:

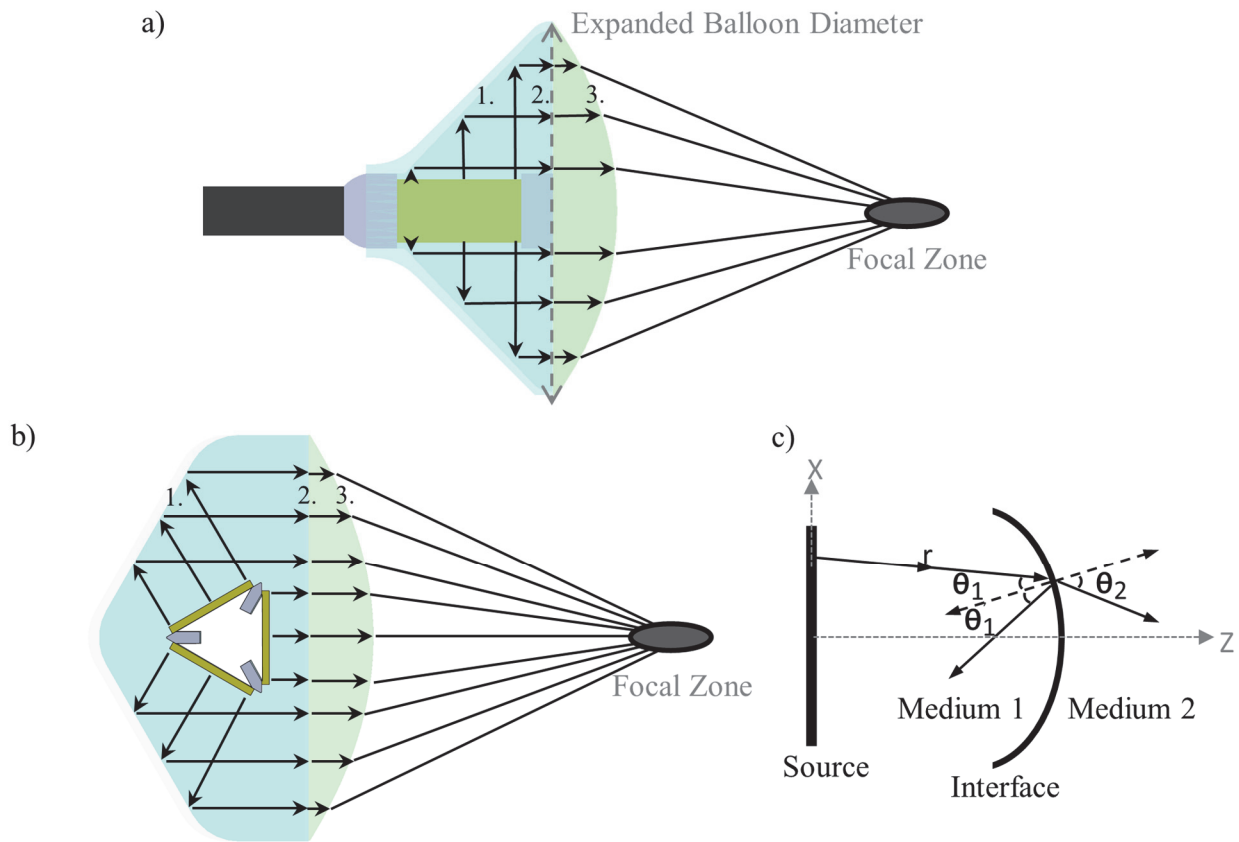


Figure 4.2 Simplified ray traces of acoustic propagation for the (a) end-fire and (b) side-fire configurations, highlighting reflection/refraction at each material interface of the applicator assembly, as numbered. Complete reflection occurs at interface 1., partial reflection at interface 2., and partial reflection and refraction at interface 3.. Materials comprising each interface: 1. Water-gas (CO₂); 2. Water-lens fluid; 3. Lens fluid-field medium (water, tissue). (c) Diagram for theoretical modeling of reflection and refraction at each material interface.

4.3.1 Acoustic modeling theory

In a homogeneous medium, the acoustic velocity potential (ψ) due to a radiating transducer source in an infinite rigid baffle can be determined using the Rayleigh-Sommerfeld diffraction integral:

$$\psi(x, y, z) = \frac{1}{2\pi} \int_S u \frac{e^{-(\mu+jk)r}}{r} dS \quad \text{Eq. 4.1}$$

where integration is over the entirety of the radiating surface S , u [m/s] is the normal particle velocity on the radiating surface, μ [Np/m] is the acoustic attenuation coefficient of the medium, $j = \sqrt{-1}$, k [radians/m] is the wave number, and r [m] is the distance between the field point and an infinitesimal source element of area dS . By discretizing the radiating surface into N elements of small enough area ΔS to be considered point sources, and summing the contributions from each element to the field point of interest, the expression can be evaluated as:

$$\psi(x, y, z) = \frac{1}{2\pi} \sum_{n=1}^N u_n \frac{e^{-(\mu+jk)r_n}}{r_n} \Delta S_n \quad \text{Eq. 4.2}$$

where subscript n corresponds to the n th element. The resulting acoustic pressure on a field point is:

$$p(x, y, z) = j\rho ck\psi(x, y, z) \quad \text{Eq. 4.3}$$

where ρ [kg/m³] is the density and c [m/s] is the speed of sound of the medium. If the radiating source is divided into N rectangular elements, then the rectangular radiator method⁵⁰ (Eq. 1.13) can be used to calculate the field point pressure.

In order to model wave refraction and reflection at material interfaces, the secondary source approach as applied by Fan and Hynynen¹⁸⁸ and expanded by Moros et al.¹⁸⁹ was employed, whereby each interface was treated as a new radiator source of a complex wave front that reflects energy back into the original medium or transmits (refracts) energy into the second medium. This method assumes plane wave theory, which was regarded as an acceptable approximation for our analysis as the distances between interfaces typically exceeded several wavelengths.

As shown in Figure 4.2 (b), consider a ray from the n th small point source of the radiating surface traveling along r_n to an infinitesimal area of the interface between two mediums at an angle of incidence θ_1 relative to the interface surface normal. By definition, the particle velocity along r_n can be calculated by taking the derivative of the velocity potential of the small source:

$$\Delta v = -\frac{\delta\psi}{\delta r_n} = \frac{1}{2\pi} u_n \frac{e^{-(\mu + jk_1)r_n} [1 + (\mu + jk_1)r_n]}{r_n^2} \Delta S_n \quad \text{Eq. 4.4}$$

where k_1 [radians/m] is the wave number of the first medium. The reflected particle velocity from the interface due to the incident ray can be calculated as the particle velocity at the interface in the first medium multiplied by the velocity reflectivity R_v , and is defined along a new direction θ'_1 . Hence, the normal reflected particle velocity on the interface (Δv^R) is the component of the reflected particle velocity along the normal of the interface:

$$\Delta v^R = R_v \cdot \Delta v \cdot \cos(\theta'_1) \quad \text{Eq. 4.5}$$

where the velocity reflectivity R_v can be calculated as:

$$R_v = \frac{\rho_2 c_2 \cos(\theta_1) - \rho_1 c_1 \cos(\theta_2)}{\rho_2 c_2 \cos(\theta_1) + \rho_1 c_1 \cos(\theta_2)} \quad \text{Eq. 4.6}$$

Similarly, the transmitted or refracted particle velocity in the second medium is equal to the particle velocity at the interface in the first medium multiplied by the velocity transmittivity T_v , and is

defined along the direction θ_2 . The normal transmitted particle velocity on the interface (Δv^T) is the component of the transmitted particle velocity in the second medium along the normal to the interface:

$$\Delta v^T = T_v \cdot \Delta v \cdot \cos(\theta_2) \quad \text{Eq. 4.7}$$

Where the velocity transmittivity T_v can be calculated as defined in Fan and Hynynen¹⁸⁸ (rather than the approximation employed in Moros et al.¹⁸⁹):

$$T_v = \frac{2\rho_1 c_1 \cos(\theta_1)}{\rho_2 c_2 \cos(\theta_1) + \rho_1 c_1 \cos(\theta_2)} \quad \text{Eq. 4.8}$$

Note that the angles of incidence (θ_1), reflection (θ'_1), and refraction (θ_2) are related by Snell's Law:

$$\theta_1 = \theta'_1 \text{ and } c_1 \sin(\theta_2) = c_2 \sin(\theta_1) \quad \text{Eq. 4.9}$$

The reflected and transmitted normal particle velocities on the interface due to the entire radiating surface source are calculated by summing the contributions from each source element:

$$v^R = \frac{1}{2\pi} \sum_{n=1}^N u_n \frac{e^{-(\mu+jk_1)r_n} [1 + (\mu + jk_1)r_n]}{r_n^2} \Delta S_n R_v(\theta_1^n) \cos(\theta_1'^n) \quad \text{Eq. 4.10}$$

$$v^T = \frac{1}{2\pi} \sum_{n=1}^N u_n \frac{e^{-(\mu+jk_1)r_n} [1 + (\mu + jk_1)r_n]}{r_n^2} \Delta S_n T_v(\theta_1^n) \cos(\theta_2^n) \quad \text{Eq. 4.11}$$

By discretizing the entire interface surface into M sub-elements, and using Eqs. (11, 12) to calculate the reflected and transmitted normal particle velocities for each element, the interface can be treated as a new radiating source. The resultant pressures in the second (or transmitted) medium can be calculated using Eqs. 4.2, 4.3 or Eq. 1.13, by summing over the M interface elements where n is replaced by m , the index of the m th interface element, and u_n is replaced by

v_m^T , representing the transmitted normal velocity of the m th element. Similarly, the pressures in the first medium from interface reflections can be calculated using v_m^R , the reflected normal velocity of the m th interface element. Further, successive material interfaces can be each regarded as secondary sources, whereby the normal velocity distributions on each interface are calculated using Eqs. 4.10, 4.11 using the reflected or transmitted normal velocity distributions of the prior interface or radiating source as the input.

Acoustic propagation through each applicator assembly was modeled by separately considering each interface as secondary sources. The interfaces, as shown and numbered in Figure 4.2 (a)-(b), consist of 1 – the water-gas interface between the internal and reflector compartments; 2 – the water-lens fluid interface between the internal and lens compartments; and 3 – the interface between the lens fluid and the adjacent medium in the computational field. For interface 1, the central tubular transducer is used as the radiating source in the end-fire configuration, whereas the posterior transducers are the sources in the side-fire. The reflected normal particle velocity distribution on the conical and planar interfaces are calculated for the end-fire and side-fire assemblies, respectively. These interfaces are approximated as an ideal reflector, with a velocity reflectivity R of 1 and no acoustic transmission into the adjacent gas compartment. The contributions of each element of the transducer source were constrained to affect only the elements of the interface that were in front of the source element tangent plane. For interface 2, the reflected normal velocity distribution on interface 1 was used to calculate the transmitted normal particle velocities on the planar interface. For the side-fire, the normal velocity distribution on the anterior planar transducer was also used. Contributions from source-interface element pairs were nullified if the ray trace between the two elements intersected with the central transducer structure. For interface 3, the transmitted normal velocity distribution of interface 2 was used to calculate the

transmitted normal velocities on the convex lens surface. Following, the pressure field in the adjacent medium was calculated by discretizing the lens surface into rectangular subelements and using the transmitted normal velocity distribution as the input for the rectangular radiator method (Eq. 1.13). The surface geometry of the convex lens was modeled as a spherical section, which is an appropriate approximation of the more complex paraboloid geometry that characterizes fluid lenses made in practice.¹⁹⁰

4.3.2 Fluid lens analysis

A theoretical analysis was used to characterize acoustic performance of the fluid lens and to compare two candidate lens fluids: perfluorocarbon solution and silicone oil. The acoustic properties each of these fluids were taken from formulations in Yoon et al.¹⁸⁷, and are shown in Table 4.1. The lens focal length, aperture diameter, and constituent fluid were all varied to investigate their impact on energy transmission across the convex lens interface. The focal length of the lens was approximated using the optical analogy for a plano-convex lens⁵³:

$$f = \frac{ROC}{\left(\frac{c_2}{c_1} - 1\right)} \quad \text{Eq. 4.12}$$

where ROC [m] is the radius-of-curvature of the lens, and c_1 and c_2 are the speed of sound of the lens fluid and water, respectively. Eq. 13 was used to determine the ROC associated with each lens focal length.

For the analysis, a 2D central cross-section of the spherical lens was considered. Energy transmission across the lens was determined by calculating and summing the power transmission coefficient T_{pow} across the 2D section:

$$T_{pow} = \frac{4\rho_1 c_1 \rho_2 c_2 \cos(\theta_1) \cos(\theta_2)}{(\rho_2 c_2 \cos(\theta_1) + \rho_1 c_1 \cos(\theta_2))^2} \quad \text{Eq. 4.13}$$

Snell’s law (Eq. 4.9) was used to calculate the relationship between angle of incidence and angle of refraction. At each point along the 2D section, the power transmission coefficient was calculated assuming a uniform and collimated energy source, such that the angle of incidence varied along the section according to:

$$\theta_1(x) = \text{asin}\left(\frac{x}{ROC}\right) \quad \text{Eq. 4.14}$$

where x is the x-coordinate of the point along the 2D section, and defined as zero at the center of the lens. The maximum absolute x-coordinate along the lens was constrained by the aperture diameter, and could not exceed the lens ROC. The sum of the power transmission coefficient across the 2D section was used to approximate the total energy transmission.

Liquid	Density (kg/m ³)	Speed of Sound (m/s)	Attenuation (Np/m/MHz)
Silicone Oil	980	1002	0.055
Perfluorocarbon	1820	610	0.006
Water	1050	1484	~ 0

Table 4.1 Acoustic properties of prospective lens fluids and water.

4.3.3 Influence of applicator design parameters on focal properties

Using the theory and methodology presented in the prior section, parametric studies were performed to characterize acoustic output of both applicator assembly designs. Parameters varied for the end-fire design include the expanded balloon aperture diameter (as illustrated in Figure 4.2

(a)) between 10-50 mm, the transducer radius (1-6 mm), and lens focal length (1-100 mm). For each distinct configuration, the height of the tubular transducer was set by the expanded balloon diameter, matching the height of the conical reflector compartment (varying accordingly between ~3-25 mm). For the side-fire design, the radius of the transducer housing fixture and the length of the transducers were adjusted between 2-6 mm and 10-30 mm, respectively. The width of each transducer segment was equal to $0.866 * (2 * \text{Fixture radius}) - 1$ mm, where the 1 mm is to ensure a 0.5 mm gap between the transducer sides from the edge of the housing fixture. All simulations were performed using a perfluorocarbon lens fluid and the resulting acoustic pressure and time-averaged intensity distributions were calculated in a water medium.

Simulations were also performed for a single spherical bowl transducer (without incorporating the reflector-lens assembly) in a water medium, to serve as a comparison. The spherical transducer aperture radius was varied between 1-6 mm, and the ROC adjusted between 1-100 mm. In both cases, the transducer operating frequency was 1.5 MHz. 6 mm was chosen as the upper limit of the transducer radius in both sets of simulations as a conservative size constraint on the non-collapsible overall device profile. This upper limit would be appropriate for endogastric access, based on diameters of currently available endoscopes on the market.¹⁴¹

A second series of parametric studies, utilizing only the end-fire applicator configuration, investigated the effects of transducer frequency and attenuation of the field medium on achievable focal gain as a function of focal depth. A single end-fire configuration was used (50 mm expanded balloon diameter, 5 mm transducer radius), while the transducer frequency was varied between 1.5 and 3 MHz, and the medium attenuation varied between 0-10 Np/m/MHz, assuming a linear frequency dependence.

4.3.4 Experimental validation

In order to validate the methodology and acoustic simulations presented herein, a proof-of-concept end-fire test applicator assembly was designed, fabricated, and characterized using hydrophone measurements of the beam profiles. The assembly, as shown in Figure 4.3, consists of a 9.5 mm OD x 9.5 mm height 1.70 MHz tubular transducer mounted on a 3D printed housing fixture (Form 1+, Formlabs Inc.), centered in a conical brass reflector fixture. The fluid lens was made from a 3D printed fixture (Form 1+, Formlabs Inc.), with a latex sheet (.006" thick, McMaster-Carr) serving as the distal distensible lens membrane, and a stiff polyimide sheet (.005" thick, McMaster-Carr) as the proximal boundary. Fluid inlet and outlet ports were used to inject the perfluorocarbon solution (Fluorinert FC-43, Synquest Lab Inc.) into the lens, and the radius of curvature of the latex membrane could be manually adjusted by varying the volume of perfluorocarbon in the fixture. The aperture diameter of the lens and the diameter of the brass reflector opening were 31 mm. The fluid lens fixture was centered over the applicator-brass reflector assembly using a 3D printed adapter (M200, Zortax).

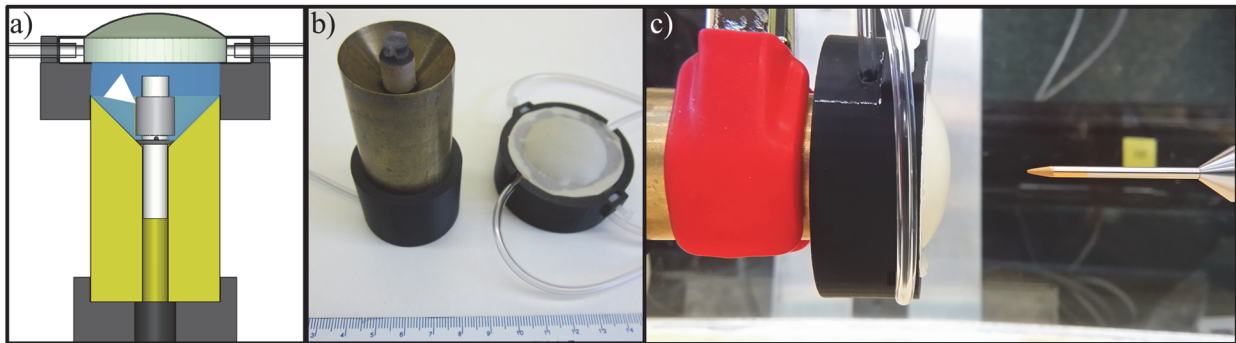


Figure 4.3 (a) Cross-sectional schematic of the proof-of-concept end-fire applicator assembly, consisting of a tubular transducer applicator (1.70 MHz, 4.75 mm radius x 9.5 mm height, white arrow) mounted in a brass conical reflector fixture, a fluid lens fixture filled with perfluorocarbon solution, and 3D printed adapters for mounting and alignment. (b) The applicator, brass reflector and lens fixture subassemblies are shown. (c) Acoustic characterization was performed using hydrophone scanning in a water tank, and the focal length of the lens was varied between measurements by adjusting the fluid volume in the lens fixture.

Measurements of the intensity profiles of the modular POC assembly were performed in deionized, degassed water by scanning a needle-type hydrophone (Onda HNP-0400, Onda Corp.) under computerized motor control and acquisition. Longitudinal scanning planes through the applicator center and extending up to 90 mm in depth were obtained for a range of lens focal length, which was varied by adjusting the volume of fluid in the lens between scans. The step sizes were 0.5 mm in the transverse dimension and 1 mm in the axial dimension, and the pulse repetition period and burst count were 1 ms and 230 cycles, respectively. Peak-to-peak voltage measurements from the hydrophone were taken using an oscilloscope (AFG3022C, Tektronic, Inc.), and converted into time-averaged intensity values using the acoustic efficiency of the transducer. The transducer efficiency was determined through force balance measurements⁹⁸ using a bottom-loading mass balance (AE200, Mettler-Toledo Ltd.), with the applicator-reflector subassembly submerged in deionized and degassed water, directing acoustic energy into absorbers suspended from the balance. Acoustic simulations that modeled the POC assembly were performed for comparative purposes, but did not incorporate modeling of the thin latex or polyimide lens membranes.

4.3.5 Biothermal modeling theory

In order to investigate the utility of the proposed applicator assemblies for thermal ablation of tissue, three-dimensional bioheat transfer models of endoluminal tissue heating in liver and pancreatic tissue were employed. Transient temperature distributions resulting from the incident acoustic pressure field were simulated using an implicit finite element method solver (COMSOL Multiphysics 4.3, Burlington, MA) and the Pennes bioheat transfer equation¹¹¹ (Eq. 1.16).

The acoustic heat deposition in tissue was derived from the acoustic pressure field using Eq. 1.17. The acoustic absorption coefficient was approximated as equal to the acoustic attenuation coefficient μ (Np m^{-1}) for each tissue, as all scattered energy was assumed to be absorbed locally.

4.3.6 Simulated temperature distributions from deployable assemblies

A three-dimensional model of endoluminal ablation of either liver or pancreatic tissue through the stomach wall, as shown in Figure 4.4, was used. The deployable applicator assembly was situated in the stomach lumen, with the rest of the lumen filled with cooling and coupling water (25 °C). In order to constrain the parametric space, two select configurations of the end-fire applicator assembly were modeled: configuration 1 was for 30 mm expanded balloon diameter, 3 mm transducer radius x 12 mm height, sonicating at 1.5 MHz; configuration 2 was for 50 mm expanded balloon diameter, 5 mm transducer radius x 20 mm height, sonicating at 1.5 MHz. One configuration of the side-fire applicator assembly was modeled, incorporating a fixture radius of 6 mm and transducer height of 30 mm, resulting in an effective balloon diameter of ~40 mm. Short duration (30 s) sonications were simulated, with a constant transducer input power that was empirically adjusted to produce a maximum tissue temperature of 75 °C by the end of sonication. The maximum value of the input power was constrained so as not to exceed a transducer surface intensity of 20 W/cm^2 .¹⁹¹ The lens focal length was varied between simulations to evaluate the capability of producing selective heating at specific depths up to 10 cm.

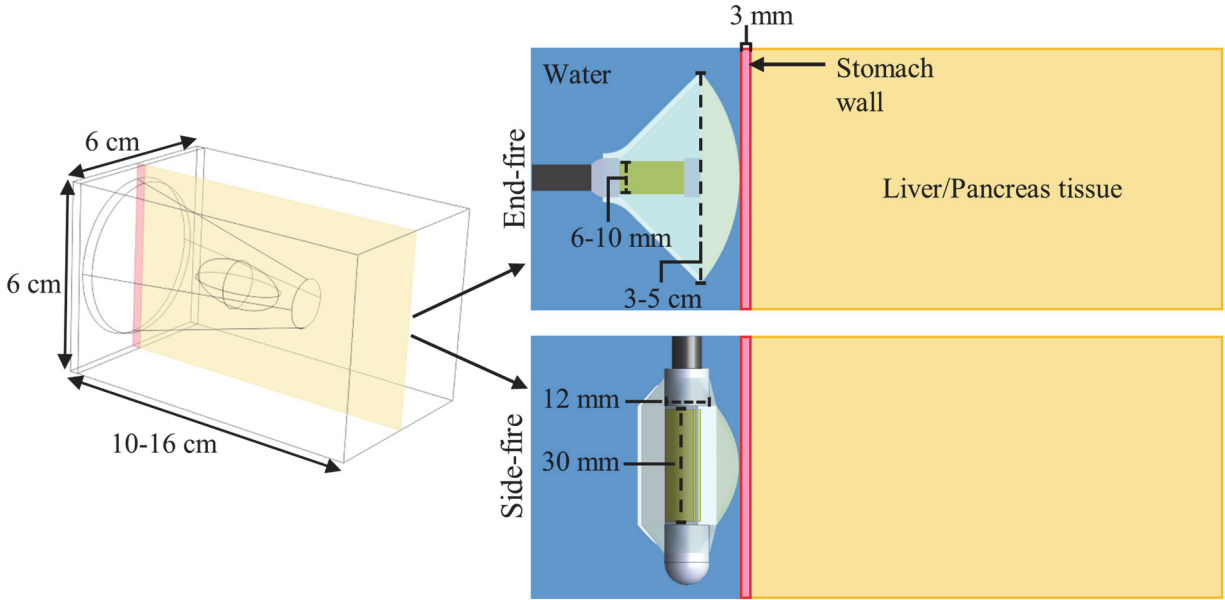


Figure 4.4 Generic tissue block model for thermal simulations of endoluminal ablation of liver or pancreatic tissue using the proposed ultrasound applicator assemblies. Ranges for the dimensions for the tissue block and constituent features (transducer dimensions, expanded balloon diameter) of the applicator assembly are shown. The transducer frequency was 1.5 MHz, and the radius-of-curvature of the lens was adjusted to target focal depths of 2-10 cm in the tissue.

For comparative purposes, simulations were also performed for a more conventional endoluminal ultrasound applicator design that contained a single 1.5 MHz, 12 mm diameter spherically focused transducer. The ROC of the transducer was varied to adjust the treatment focal depth.

The acoustic and thermal material properties of each tissue that were incorporated in the simulations are listed in Table 4.2.^{129,143,144} Water cooling (25 °C) was modeled on the interior of the stomach luminal surface, by using a convective heat flux boundary equation with a heat transfer coefficient of $h = 500 \text{ W/m}^2/\text{°C}$.¹²⁹ The stomach wall was modeled as 3 mm thick.¹⁶⁰ Dirichlet boundary conditions constrained the outer borders of the tissue boundary to 37 °C. In order to simulate the dynamic cessation of perfusion during ablation, tissue perfusion was reduced from its nominal value to zero when the temperature exceeded 52 °C, which closely tracks the boundary

of lethal thermal dose in these simulations.¹¹³ Borders of coagulative necrosis or thermal lesion formation by the end of the sonication were approximated by the $T > 52$ °C contour.

Tissue	Density (kg/m ³)	Attenuation (Np/m)	Thermal conductivity (W/m/°C)	Specific heat (J/kg/°C)	Perfusion rate (kg/m ³ /s)
Pancreas	1045	$11.9f^{0.78}$	0.51	3164	10
Liver	1050	$6.9f$	0.51	3639	15.8
Stomach Wall	1045	$5f$	0.53	3698	6.75
Blood	1050	-	0.52	3617	-

Table 4.2 Material properties of tissues used in biothermal modeling studies.

4.4 Results

4.4.1 Fluid lens analysis

Figure 4.5 illustrates how acoustic energy transmission across a fluid lens with a spherical curvature changes as a function of lens fluid, aperture diameter, and focal length. Energy transmission rises with increasing focal length up to a saturation level, and increasing the aperture size yields a greater saturation level at a higher focal length. At each focal length, there is a maximum limit of energy transmission that cannot be raised by increasing the aperture size, and that scales in magnitude with focal length. Figure 4.5 also shows that at all focal lengths, the perfluorocarbon fluid lens permits greater energy transmission as compared to silicone oil. The difference in transmission is relatively minimal beyond the saturation focal length for each aperture size, but is more significant prior to saturation. Hence, these results formed the basis for employing perfluorocarbon as the lens fluid in the remaining modeling and experimental work presented in this study.

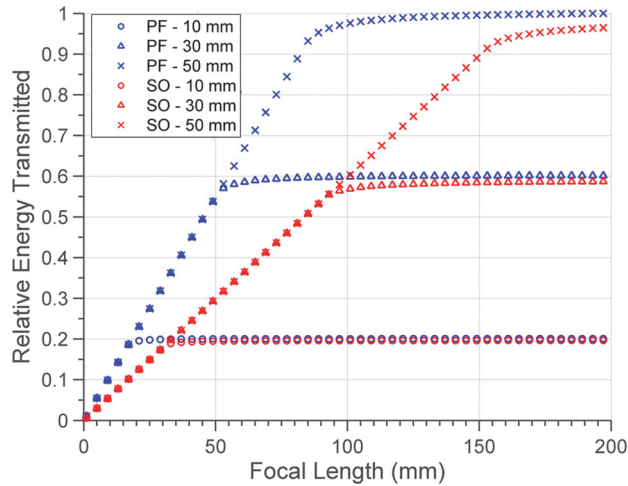


Figure 4.5 Normalized energy transmission through the convex interface of the fluid lens as a function of lens focal length, lens fluid (PF – perfluorocarbon, SO – silicone oil), and aperture diameter (10, 30, or 50 mm).

4.4.2 Influence of applicator design parameters on focal properties

Figures 4.6 (a)-(c) show three 2D planes of simulated longitudinal intensity distributions, corresponding to a single end-fire applicator assembly configuration (50 mm expanded balloon diameter, 5 mm transducer radius x 20 mm length, 1.5 MHz) at three focal depths of ~20, 40, and 60 mm in water. The scale is normalized to the input surface intensity of the tubular transducer, thus representing effective intensity gain. For each assembly configuration, a series of central axial intensity profiles were simulated, as demonstrated in Figure 4.6 (d) for the 50 mm balloon diameter, 5 mm transducer radius x 20 mm length configuration. Each individual intensity vs. depth profile corresponds to a specific lens focal length, and interpolation of the maximum gains and corresponding depths across all profiles was used to generate a general “performance envelope”. This envelope approximates the maximum achievable focal gain at each depth that could be realized by adjusting the lens curvature, and was generated for each applicator configuration.

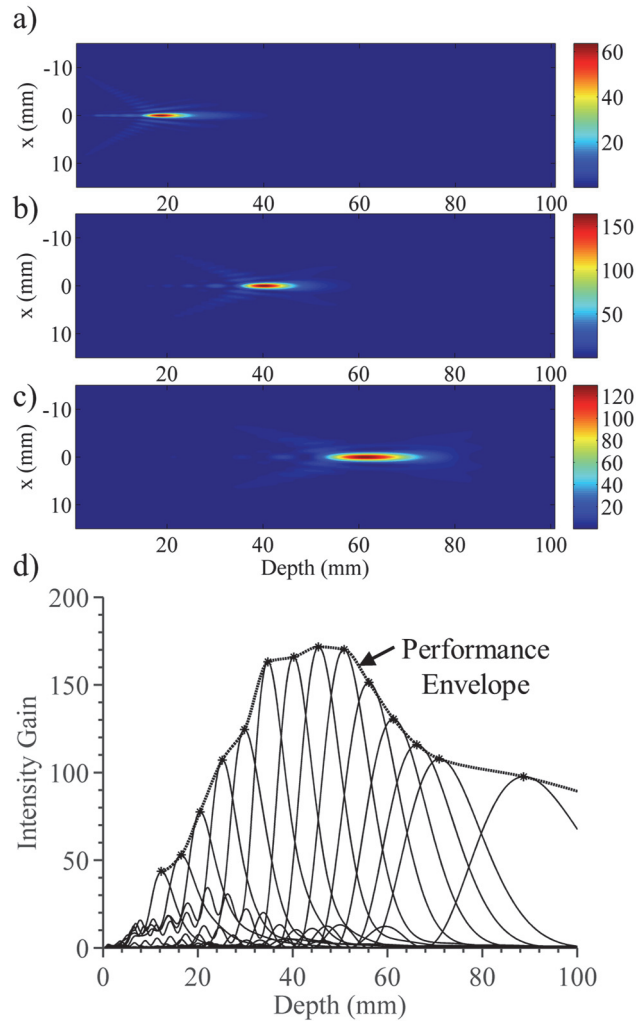


Figure 4.6 Simulated acoustic intensity gain distributions in water for the end-fire applicator assembly (1.5 MHz, 50 mm expanded balloon diameter, 5 mm transducer radius) for three separate lens focal lengths of (a) ~ 20 mm, (b) ~ 40 mm, and (c) ~ 60 mm. (d) A series of intensity profiles along the central axial axis (solid lines) are created by varying the lens focal length. Depth is measured as the axial distance from the lens membrane. By compiling the maximum intensity and corresponding depth of each profile, an interpolated envelope (dotted line with stars) or “performance envelope” that approximates the achievable focal gain at each depth can be determined.

A series of performance envelopes for 1.5 MHz end-fire configurations are shown in Figure 4.7, with expanded balloon diameter (10-50 mm) varied between panels and transducer radius (1-6 mm radius) varied between curves. In the last panel (Figure 4.7 (f)), a series of simulations corresponding to a single spherically focused transducer, with varying aperture radius and ROC, is shown for comparison. It can be seen that as the balloon diameter of the applicator assembly

increases, both the magnitude and the depth of the maximum focal gain increase. For all configurations, the achievable focal gain generally increases as a function of focal depth up to a maximum value, then tapers down gradually. In varying the transducer radius for each balloon size, the maximum focal gain is achieved by an intermediate transducer radius value. As the balloon aperture increases, then the transducer radius that corresponds to the curve with the highest maximum gain increases as well. Comparing the end-fire applicator assembly configurations to the spherical transducer, it is evident that at very short focal depths (<15 mm) the largest spherical transducer is capable of higher focal gains than any of the assembly configurations. However, beyond 20 mm, many assembly configurations with balloon diameters of 2 cm or greater achieve higher focal gain, with an increasing discrepancy in magnitude as the balloon size and focal depth increase. As a quantitative comparison, whereas the 6 mm radius spherical bowl transducer cannot effectively produce a focus beyond 30 mm, the assembly configuration with a 50 mm balloon diameter and 5 mm transducer radius achieves its peak focal gain of ~170 around 45 mm depth and tapers off gradually, retaining a gain of ~90 at 100 mm depth. Smaller configurations with a 10 mm balloon diameter show a maximum potential focal gains of ~6 and cannot focus beyond 2 cm.

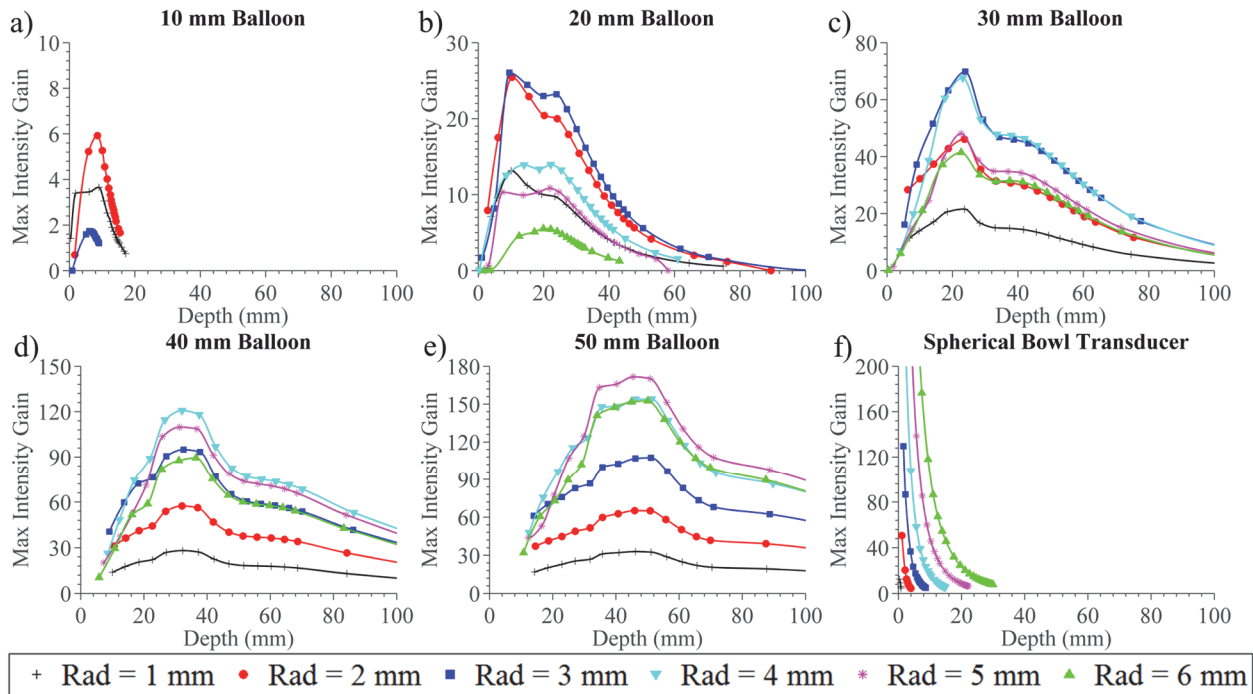


Figure 4.7 (a)-(e) Approximate maximum focal gain of the end-fire applicator assembly at 1.5 MHz operating frequency, as a function of focal depth, transducer radius (“Rad”), and expanded balloon diameter. (f) A comparative case, consisting of a 1.5 MHz spherically focused transducer of various aperture radii with curves generated by varying the radius-of-curvature, is shown.

The performance envelopes for the side-fire applicator configurations are shown in Figure 4.8. Achievable intensity gain increases as a function of larger transducer height and fixture width, as both parameters also corresponded to larger expanded balloon dimensions. The absolute maximum of the achievable focal gain is greater for the side-fire configuration compared to the end-fire, but the gain also exhibits steeper fall-off as the focal depth increases. For example, the maximum gain of the largest side-fire configuration (6 mm fixture radius, 30 mm transducer height, ~40 mm effective balloon aperture) is ~250 at a depth of ~28 mm, whereas the maximum gain of the optimal end-fire configuration (5 mm transducer radius, 20mm transducer height, 50 mm balloon aperture) is ~170 at ~46 mm. At 50 and 60 mm depths, the gain of the largest side-fire configuration drops down to ~160 and ~115, respectively, while at the same depths the end-fire configuration gains are ~170 and ~135, respectively.

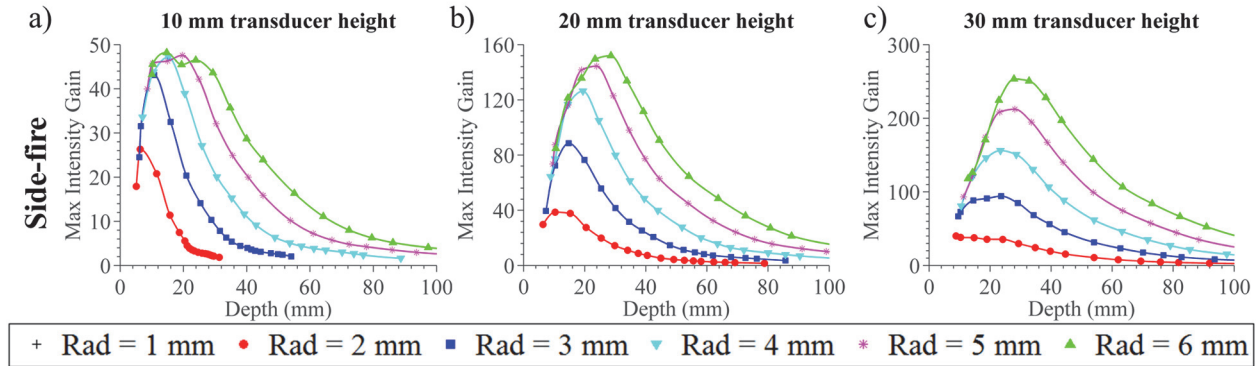


Figure 4.8 Approximate maximum focal gain of the side-fire applicator assembly at 1.5 MHz operating frequency, as a function of focal depth, fixture radius (“Rad”), and transducer heights, ranging from (a) 10 mm, (b) 20 mm, and (c) 30 mm.

The approximate sizes of the focal zones produced by the end-fire configurations in terms of the full-width-half-max (FWHM) across the axial and transverse dimensions, corresponding to the extents of the -3 dB intensity contours, are shown in Figures 4.9 and 4.10, respectively. As expected, the axial length of the focal zone generally increases with rising focal depth, though for configurations with larger balloon apertures there is an inflection point, where the axial length only starts to increase significantly after a specific focal depth. As the balloon size increases, this inflection point translates to higher focal depths, and the overall magnitude of axial length decreases significantly (e.g., for 50 mm focal depth, the axial length is ~50 mm for configurations with 20 mm balloon diameter, and ~10 mm for 50 mm diameter). Within each balloon size, the axial length of the focal zone correlates with transducer radius, with smaller transducers producing tighter foci; this is opposite the behavior for the spherical bowl transducer. The spherical bowl transducer, compared to the tubular applicator assembly configurations, generally produces larger focal zones beyond a ~15 mm depth. The transverse width of the focal zone increases as a function of focal depth and decreases as balloon size increases, though to a lesser extent as compared to the

axial length. In contrast with the axial length, the width decreases as transducer radius increases, though to a relatively minimal degree (~ 0.5 mm as transducer radius increases from 1 to 6 mm).

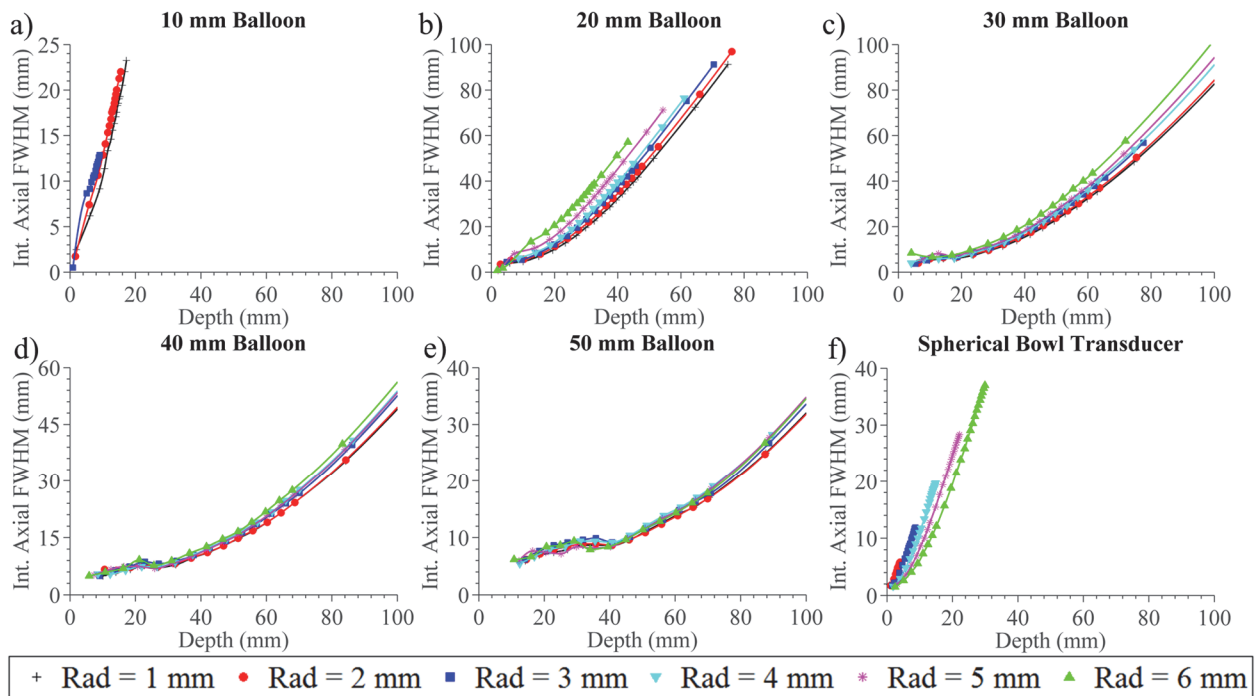


Figure 4.9 (a)-(e) Axial length of the focal zone as defined by the -3 dB intensity extents or FWHM for the end-fire applicator assembly, as a function of focal depth, transducer radius (“Rad”), and expanded balloon diameter. (f) Focal zone length for a spherically focused transducer with varying radius and radius-of-curvature.

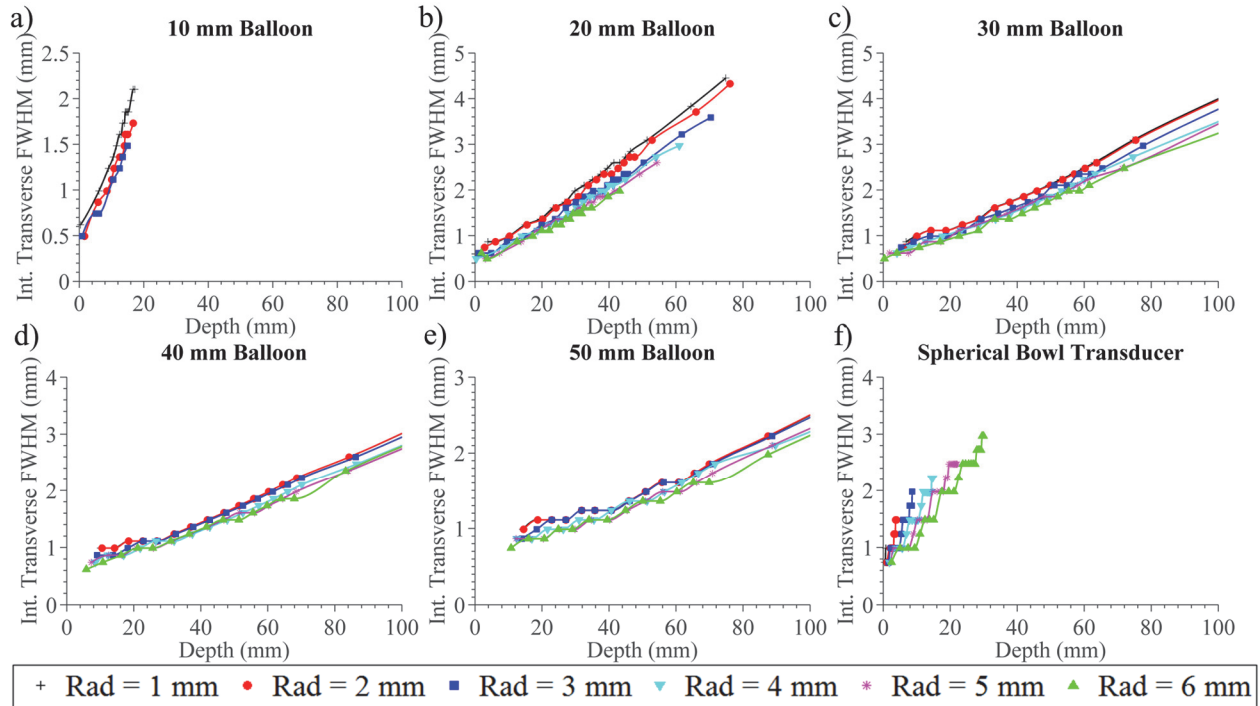


Figure 4.10 (a)-(e) Transverse width of the focal zone as defined by the -3 dB intensity contours or FWHM for the end-fire applicator assembly, as a function of focal depth, transducer radius (“Rad”), and expanded balloon diameter. (f) Focal zone width for a spherically focused transducer with varying radius and radius-of-curvature.

The axial and transverse FWHM dimensions of the focal zones produced by the side-fire applicator configurations are shown by Figure 4.11 and Figure 4.12, respectively. It can be seen that increasing the fixture radius and transducer height increases in tighter foci, and that the fixture radius has a greater impact on the focal zone dimensions compared to the end-fire design. This is likely because the fixture radius is intrinsically linked to the overall size of the reflector-lens balloon for the side-fire design. Also, unlike the end-fire design, the focal zone is not symmetric around the central longitudinal axis, due to different dimensions of the balloon aperture along the X and Y dimensions, where Y is the dimension along the transducer height, and X the transducer width. As such, the transverse FWHM measures are shown along the X (Figure 4.12 (a)-(c)) and Y (Figure 4.12 (d)-(f)) profiles as well.

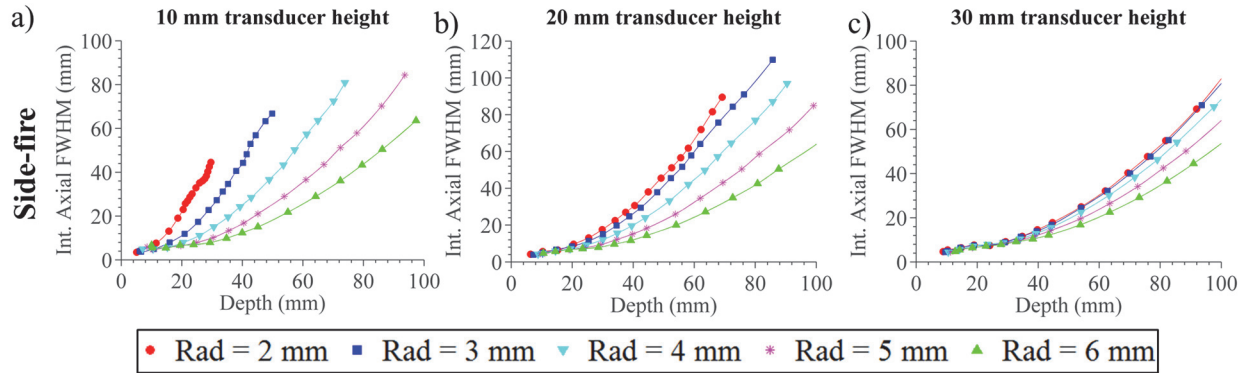


Figure 4.11 Axial length of the focal zone as defined by the -3 dB intensity extents or FWHM for the side-fire applicator assembly, as a function of focal depth, fixture radius (“Rad”), and transducer heights ranging from (a) 10 mm, (b) 20 mm, and (c) 30 mm.

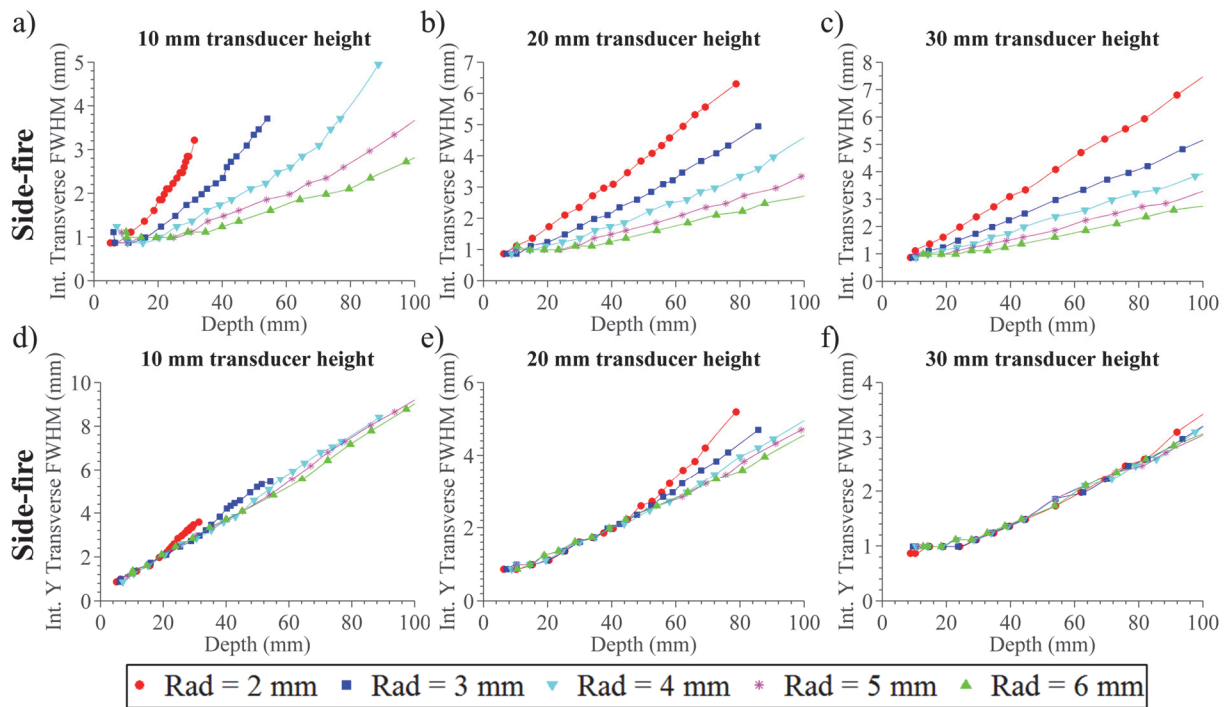


Figure 4.12 Transverse dimensions of the focal zone as defined by the -3 dB intensity extents or FWHM for the side-fire applicator assembly, as a function of focal depth, fixture radius (“Rad”), and transducer heights. Dimensions along the X axis are shown in (a)-(c), and the Y axis shown in (d)-(f).

Figure 4.13 shows the results for the second series of parametric studies for a single end-fire deployable configuration (50 mm balloon diameter, 5 mm transducer radius x 20 mm height), with the transducer frequency and attenuation of the medium varied. As expected, increasing the

frequency results in tighter foci, with shorter -3dB axial and transverse extents and greater focal gains in non-attenuating mediums. As the medium attenuation increases, then the lower frequency assembly is capable of producing greater gain at longer focal depths, whereas the higher frequency provides greater gain at shorter depths.

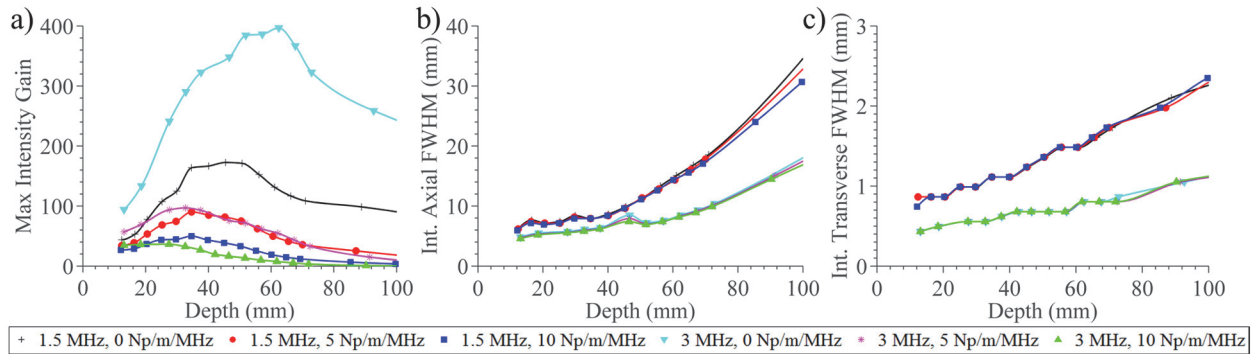


Figure 4.13 Effects of transducer frequency, tissue attenuation, and focal depth on the maximum (a) focal gain, (b) axial length, and (c) transverse width of the focal zone for an end-fire applicator assembly with a 50 mm expanded balloon diameter and 5 mm transducer radius.

4.4.3 Experimental validation

Figure 4.14 (a) shows beam-plots created from scanning hydrophone measurements of the test end-fire applicator assembly in a water tank. Each contour plot shows the normalized pressure-squared distributions along longitudinal scanning planes along the central axis, with the transverse origin at the center of the fluid lens and the depth origin situated ~ 1 mm axial from the lens membrane. Four distributions are shown, each obtained using a different volume of lens fluid injected into the fluid lens to alter its distal curvature and effective focal length. These plots (a-d) show focal depths between ~ 1 cm and ~ 5 cm, and illustrate broadening of the axial length of the focal zone as the lens volume is reduced and focal depth increases.

A series of central axial intensity profiles were measured for the test applicator assembly across eleven distinct focal depths by varying the lens fluid volume. The measured profiles are shown in Figure 4.14 (e) and the corresponding simulated intensity gain profiles that model the

test assembly in Figure 4.14 (f). Overall agreement between the experimental and theoretical profiles and trends is good, though discrepancies are present, particularly at the near or far limits of the focal depth.

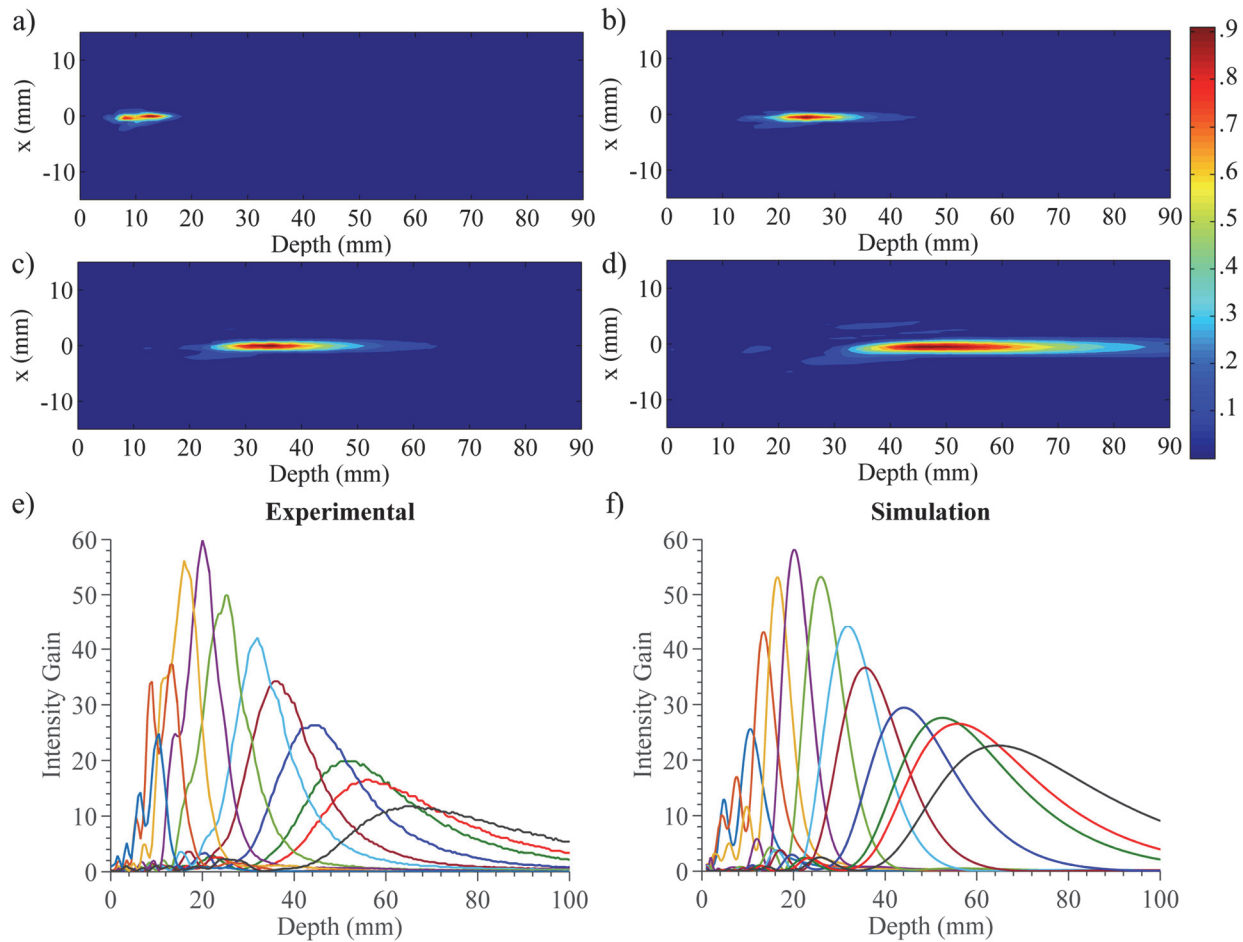


Figure 4.14 (a)-(d) Normalized beam plots (pressure-squared distributions) measured by hydrophone in water for the experimental end-fire test applicator assembly at increasing focal lengths or distensions of the fluid lens. (e) Measured and (f) simulated central axial intensity gain profiles at a range of focal lengths.

4.4.4 Simulated temperature distributions from deployable assemblies

Figure 4.15 shows simulated temperature distributions in pancreatic tissue after 30 s sonication using the larger end-fire applicator assembly (50 mm balloon diameter, 5 mm transducer radius x 20 mm height, 1.5 MHz) at four distinct lens focal depths of ~20, 40, 60, and 80 mm (Figure 4.15 (a)-(d) respectively). The analogous temperature distributions for the side-fire applicator

configuration (fixture radius of 6 mm and transducer height of 30 mm) are shown in Figure 4.16. Contours that approximate ablation boundaries of $T = 52\text{ }^{\circ}\text{C}$ and a safety margin of $T = 43\text{ }^{\circ}\text{C}$ are included. These plots illustrate that the end-fire applicator configuration is capable of selective and localized temperature rise up to the set-point temperature ($75\text{ }^{\circ}\text{C}$) at the each of the target depths with minimal pre-focal heating. The side-fire applicator configuration generates substantial pre-focal heating at focal depths beyond 60 mm, as seen in Figure 4.16 (c)-(d).

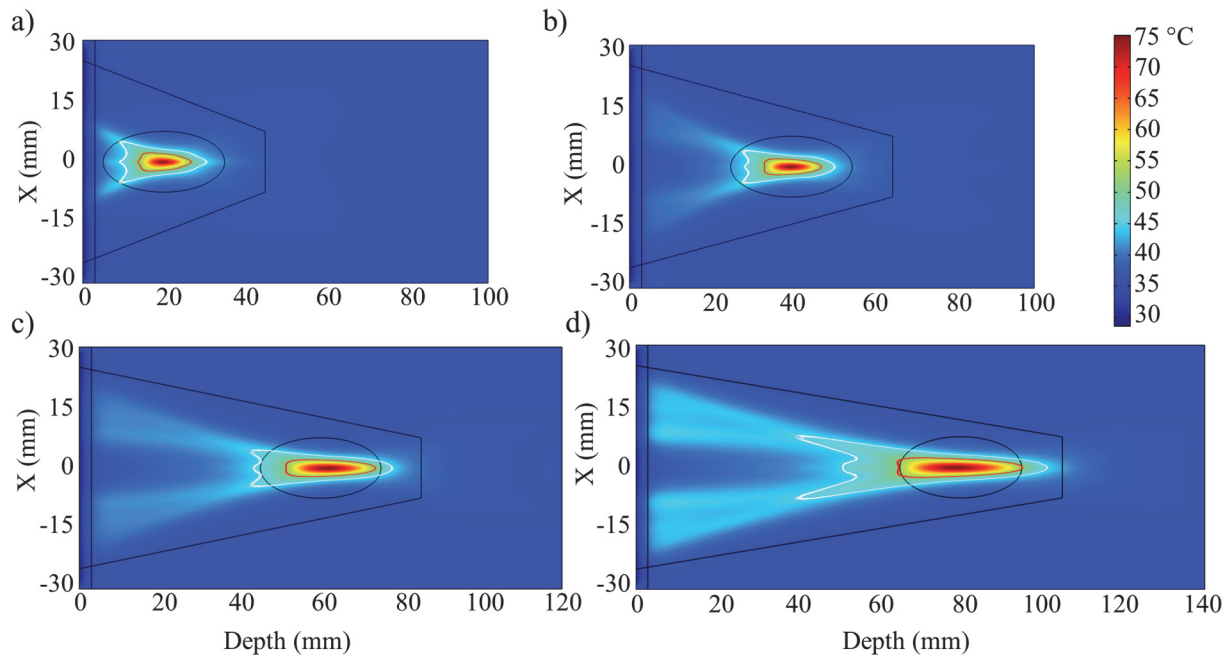


Figure 4.15 Simulated temperature distributions after 30 s sonication durations in pancreas tissue using an end-fire applicator assembly (1.5 MHz, 50 mm expanded balloon diameter, 5 mm transducer radius), for four separate treatment target depths of (a) 2 cm, (b) 4 cm, (c) 6 cm, and (d) 8 cm. The red contour ($T = 52\text{ }^{\circ}\text{C}$) approximates the ablated lesion borders, while the white line demarcates a $T = 43\text{ }^{\circ}\text{C}$ safety margin.

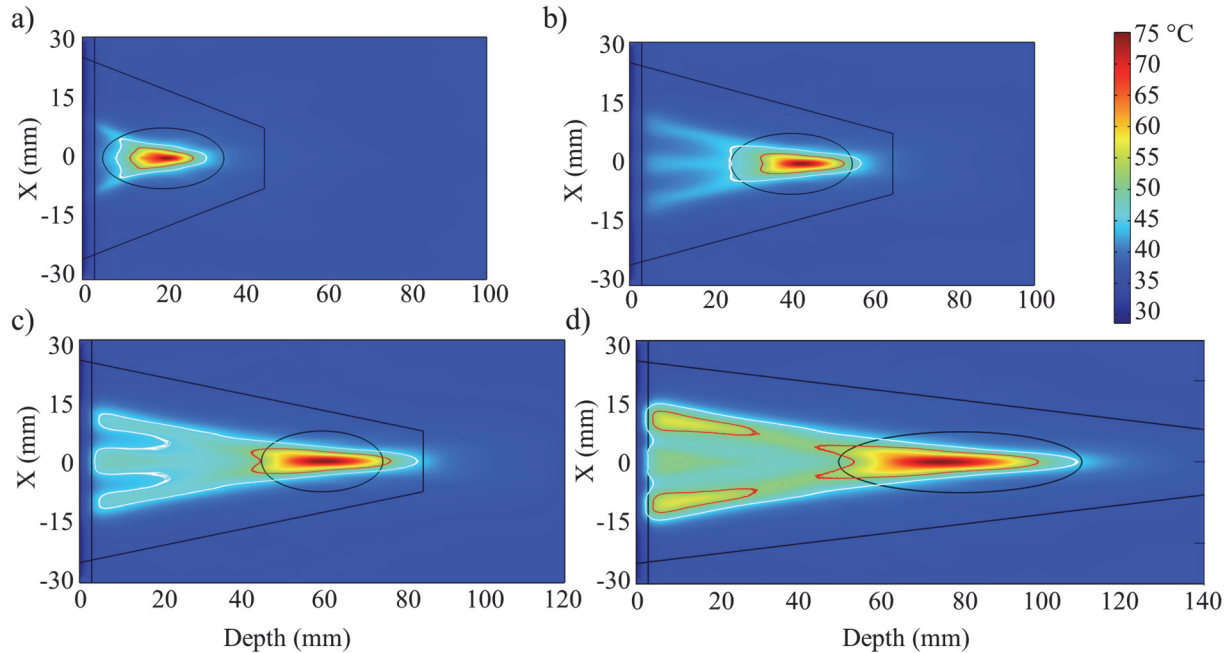


Figure 4.16 Simulated temperature distributions after 30 s sonication durations in pancreas tissue using a side-fire applicator assembly (1.5 MHz, 6 mm fixture radius, 30 mm transducer height), for four separate treatment target depths of (a) 2 cm, (b) 4 cm, (c) 6 cm, and (d) 8 cm. The red contour ($T = 52\text{ }^{\circ}\text{C}$) approximates the ablated lesion borders, while the white line demarcates a $T = 43\text{ }^{\circ}\text{C}$ safety margin.

Figure 4.17 compiles thermal simulation data regarding the dimensions and position of the ablation zones ($T > 52\text{ }^{\circ}\text{C}$) in pancreatic and liver tissues as a function of target depth for each applicator assembly configuration, and compared with a 12 mm diameter spherically focused transducer. Comparing the two end-fire assembly configurations, the larger (50 mm balloon) configuration produces deeper and more localized lesions compared to the 30 mm balloon configuration. In liver tissue, the ablation volume increases from $\sim 90\text{-}480\text{ mm}^3$ as target depth increases from $\sim 20\text{-}100\text{ mm}$, and from $\sim 75\text{-}910\text{ mm}^3$ over $\sim 20\text{-}70\text{ mm}$ target depths, for the larger and smaller assembly configurations, respectively. These volume increases primarily correspond to lengthening of the axial extents of the lesion from $\sim 12\text{-}42\text{ mm}$ and $\sim 12\text{-}56\text{ mm}$, whereas the transverse widths increase from $\sim 3.5\text{-}4.5\text{ mm}$ and $\sim 3.3\text{-}5.6\text{ mm}$, respectively, over the corresponding depth ranges. The nearest border of the ablated region, marking the depth in tissue

to the lesion boundary, increases from ~15-83 mm as target depth increases from 20-100 mm for the larger configuration, and from ~15-48 mm over a target depth range of ~20-70 mm for the smaller configuration, with the differences from the target depth increasing at deeper depths. The maximum target depth for the smaller configuration was limited to 70 mm due to insufficient focal gain to reach a maximum temperature of 75 °C within the time/power constraints at deeper depths. Similar trends can be seen for ablation in pancreatic tissue, which primarily represents a more attenuating medium (16.3 Np/m for pancreas vs 10.3 Np/m for liver at 1.5 MHz). This translates to more pre-focal heating at deeper targets and shallower lesion depths; nearest lesion borders are up to ~3 mm shallower at an 80 mm target depth for the larger configuration, and up to ~10 mm shallower at a 50 mm target depth for the smaller configuration. The lesion volumes in pancreas are also greater by ~20-100 mm³ over 20-80 mm target depths and by ~25-140 mm³ over 20-50 mm depths for the larger and smaller configurations, respectively. For the larger configuration, significant pre-focal heating occurs and creates a much larger ablation volume of ~2000 mm³ with near lesion borders at 5 mm at 100 mm target depth, while similar heating behavior and an ablation volume of ~3000 mm³ was observed for the smaller configuration at 60 mm target depth. As such, 100 mm and 60 mm approximate the focal depth limits at which the two assembly configurations can no longer create localized thermal lesions in pancreatic tissue.

The side-fire configuration has intermediate performance, lying between the smaller and larger end-fire configurations in terms of selective lesion formation and penetration depth. Maximum penetration depths in pancreatic and liver tissue without significant pre-focal heating are ~6 and ~8 cm, respectively. Primary thermal lesion length and width increase from ~20-50 mm and 5-8 mm, respectively, in pancreas over target depths of 2-8 cm, and increase from 15-45 mm and 4.5-6 mm in liver over the same depth range.

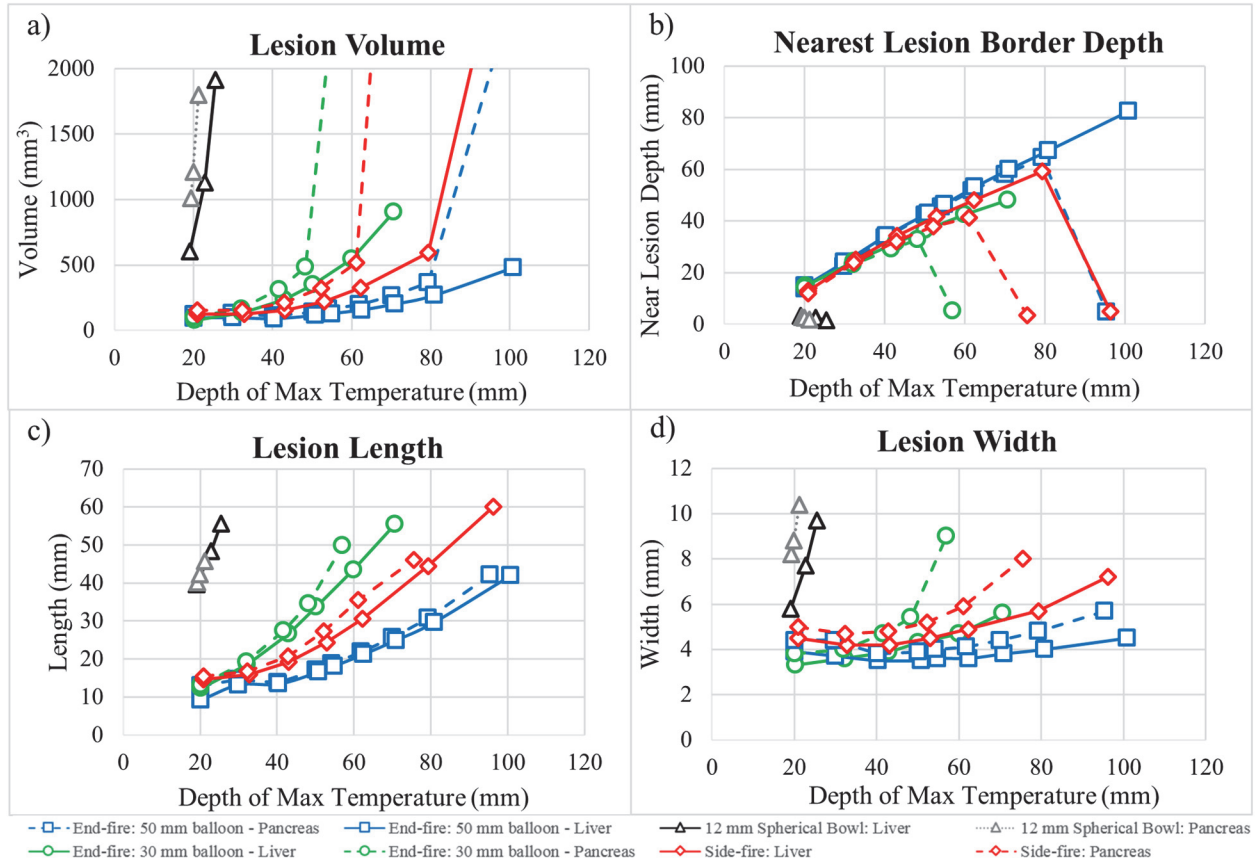


Figure 4.17 Results of thermal simulations using two select end-fire applicator assembly configurations (1.5 MHz, 30/50 mm expanded balloon diameter, 3/5 mm transducer radius) and a side-fire applicator configuration (1.5 MHz, 6 mm fixture diameter, 30 mm transducer length, ~40 mm balloon aperture diameter) in endoluminal ablation of pancreatic or liver tissue across a range of target depths. Sonications were 30 seconds long with a maximum temperature of 75 °C, and lesion boundaries were approximated by the 52 °C boundaries. Comparison cases using a single 12 mm diameter spherically focused bowl transducer in liver and pancreatic tissue are also shown.

Figure 4.17 also includes comparative biothermal simulations of a spherical transducer with a 6 mm aperture radius and 1.5 MHz operating frequency. In liver tissue the depth of maximum temperature, which approximates the focal depth, could not exceed ~25 mm. Due to the much more limited focusing capabilities at depth, the resultant ablation volumes were larger (up to ~1900 mm³ at a 25 mm target depth). At this largest limit the axial length of the lesion extended up to 55 mm, and its nearest border depth was 1.6 mm, which was within the stomach wall layer. Similar volumetric performance was seen in ablation of pancreatic tissue; however, the axial length

of the lesion peaked at 45 mm due to the higher attenuation, and correspondingly the depth of maximum temperature could not exceed ~22 mm. Greater heating in the transverse extents was observed, along with very shallow (< 3 mm) depths to nearest borders of the thermal ablation zone.

4.5 Discussion

This study has introduced and investigated design concepts for a catheter-based ultrasound applicator assembly that incorporates deployable acoustic reflector and fluid lens components within an expandable multi-compartment balloon, with potential to increase the therapeutic aperture and enhance focal gain and penetration depth. Specific designs for a “forward- or end-firing” applicator and a “side-firing” applicator have been presented and acoustic simulations were employed to characterize and assess the capabilities of the proposed applicators and to determine the influence of key design parameters. The acoustic modeling methodology and simulations were in part validated by constructing a test end-fire applicator assembly and comparing hydrophone measurements of beam distributions to simulations. Finally, a series of biothermal simulations were performed and demonstrated capabilities of select assembly configurations to create selective and localized temperature rise at a range of depths (2-10 cm), for endoluminal ablation applications in either pancreas or liver tissue targets, while sparing the intervening luminal wall.

The trends seen in the theoretical model for energy transmission across a convex fluid lens interface offer insight towards optimal design practices concerning the fluid lens. As seen in Figure 4.5, the energy transmission increases as the lens focal length increases due to the lessening of the radius of curvature of the lens surface; this results in smaller angles of incidence for the incident acoustic rays, and therefore lower reflection. This property also explains the saturation of energy transmission for a particular aperture size at long focal lengths, as the lens asymptotically flattens, leading to normal incidence of all incoming rays across the surface. Furthermore, the maximum

transmission of energy at each lens focal length can be attributed to the critical angle. Once the angles of incidence for acoustic rays at the lens' periphery exceed the critical angle, then no additional energy transmission can be realized by increasing the aperture. Instead, increasing the aperture beyond that threshold would decrease transmission due to the higher profile and subsequent greater attenuation of the fluid lens. In terms of constituent lens fluids, the perfluorocarbon solution was shown to achieve better transmission compared to the silicone oil (Figure 4.5), especially at lower lens focal lengths (before saturation). This performance difference can be primarily attributed to the much lower speed of sound of perfluorocarbon relative to silicone oil (610 m/s vs. 1002 m/s), as this translates into a significantly larger radius of curvature for each focal length, permitting greater transmission due to the smaller angles of incidence. At very high focal lengths, where both lens fluids converge towards flat interfaces, the transmission difference is minimal, and solely due to the relatively small difference in acoustic impedance between the two fluids. Other studies^{187,190} involving acoustic fluid lenses have indicated preference of silicone oil over perfluorocarbon due to its lower density, which is close to water. In those studies the high density of perfluorocarbon was predicted to cause buckling or distortion of the lens profile due to gravitational forces acting on the lens fluid volume; however, the lens sizes were much larger (> 10 cm diameters) and would be more susceptible to that issue. For the experimental lens evaluated in this study, which was about ~3 cm in diameter, no significant distortion of the lens due to buoyancy forces was observed. Additionally, the membranes which make up the lens boundary can be made from less compliant materials to better maintain shape. Other desirable qualities for the lens fluid would include low acoustic attenuation, which again favors perfluorocarbon over silicone oil, as well as biocompatibility and high temperature stability.

Both the acoustic simulations and preliminary experimental investigations performed within this study illustrate that there is a complex relationship between the achievable focal gain and target focal depth for the proposed applicator designs. The general trend shows that as target depth increases, the focal gain generally rises to a maximum then decreases beyond that corresponding depth (Figures 4.6-4.8, 4.14). The explanation for this trend is that there is a fundamental tradeoff between increasing the energy transmission through the fluid lens, or equivalently the effective aperture of the lens, and the inherent loss in focal gain, both caused by increasing the focal depth. At short focal depths, the increase in energy transmission or effective aperture of the lens outweighs the losses caused by increasing the focal depth, causing an upward slope in gain vs. depth. The maximum gain and corresponding depth mark the transition point, beyond which the losses exceed the increase in lens energy transmission as focal depth increases further. Whereas Figure 4.5 predicts smooth increases in energy transmission as the focal length increases, the changes in achievable focal gain with depth (Figures 4.6-4.8, 4.14) appear to be more irregular and erratic. One possible reason for this discrepancy is that the modeling used in the energy transmission analysis (Figure 4.5) assumes a uniform acoustic source, whereas the actual distribution of acoustic energy reflecting off of the conical interface is nonuniform. As such, the increase in energy transmission would be expected to fluctuate more with increasing focal length, and varies based on the transducer size and frequency, as shown in Figures 4.7, 4.8 and 4.13. The end-fire acoustic simulations were compared to hydrophone measurements of the experimental test fixture, and demonstrated good agreement in terms of the relationship between intensity gain and focal depth, as described above. The differences between the experimental assembly beam plots and theoretical simulations, while relatively minimal near the apex of focal gain, were more substantial at the low and high focal depth extremes. Discrepancies at the low

focal length limit can likely in part be attributed to the extreme distension of the lens at the short depths, which would break the validity of assuming a spherical geometry. At the upper focal depth limits, the progressive thickening of the lens membrane and corresponding increase in attenuation due to reduced distension at lower fluid volumes may have contributed to the more rapid decrease in focal gain magnitude observed experimentally.

The expanded balloon size, transducer dimensions, and transducer operating frequency all have significant impact on the predicted achievable focal gain (Figures 4.7 – 4.8). For the end-fire applicator, increasing the balloon size, and correspondingly, the transducer lengths, resulted in greater focal gains, with large increases primarily at greater focal depths. Larger transducer diameters, conversely, did not always result in more focal gain. This is because for a set balloon diameter, increasing the transducer diameter results in a smaller effective aperture, since the transverse footprint of the transducer on the lens surface is blocked. This is particularly consequential since the footprint covers the center of the lens, which has the greatest transmission, particularly at shallow focal depths. As such, there is a tradeoff between the amount of energy emitted by the transducer, which increases with larger transducer diameters, and the effective aperture size, which increases with smaller transducers. In order to offset the blocking issue and increase gain at smaller focal depths, it may be possible to incorporate a flat disk transducer on top of the tubular transducer at the distal tip of the housing fixture, though this would add complexity and potentially increase near-field heating. An alternative means of increasing gain, as shown by Figure 13, would include increasing the transducer frequency, though medium attenuation must be accounted for in choosing the optimal frequency for a specific target depth. For the side-fire applicator design, increasing both the fixture diameter, which constrained the width of the planar transducer arrays, and the transducer length resulted in greater focal gains. When comparing a

side-fire applicator configuration to an end-fire configuration with an equivalent transducer array profile (length and fixture diameter), the balloon size needed to cover the acoustic output of the transducers was smaller for a given transducer footprint relative to the end-fire design, meaning that the energy was dispersed over a smaller effective aperture. Furthermore, the effective surface area of the radiating transducer array is smaller for the side-fire design as compared the end-fire, as the tubular transducer has a larger surface area relative to the three planar transducers. As a result, the side-fire design produces lower gains at deeper depths when compared to an end-fire design with a similar transducer array profile. However, since the side-fire design incorporated an anterior transducer element that transmitted through the central portion of the fluid lens, much higher gains were possible at closer depths compared to comparable end-fire designs.

Both deployable applicator designs are capable of generating ablative temperature distributions in a localized and selective fashion across a large range of target depths (Figures 4.15-4.17). In comparing the heating performances of the two end-fire assembly configurations, the larger configuration (50 mm balloon diameter, 5 mm transducer radius) is capable of creating more selective lesions across a greater range of ~20-100 mm treatment depths in liver, as compared to the smaller configuration (30 mm balloon diameter, 3 mm transducer radius) which could produce focal heating at depths up to ~70 mm. For both assemblies, maximum penetration depth of the produced thermal lesions (~125 mm and 104 mm, respectively) extended approximately twice as far as is possible using the 12 mm diameter spherically focused transducer, while circumventing significant luminal heating and volumetric lesion formation. Furthermore, comparisons between simulations in pancreatic and liver tissue indicate that the applicator assembly configurations provide greater consistency across tissues with different material properties, particularly at moderate tissue depths (~20-80 mm and ~20-50 mm for the larger and smaller configurations,

respectively). The performance in “liver” and “pancreas” can also be generalized as possible in other similar target tissues. It is important to note that the scope of the biothermal simulations performed in this preliminary study emphasized demonstrating the generation of localized heating at target depths, and hence treatment parameters, including power, sonication duration, and set-point temperature, were tailored for this purpose. More volumetric heating could possibly be achieved with the applicator assemblies than demonstrated, by adjusting the sonication parameters (lower power, longer duration). More extensive biothermal modeling analysis that incorporates additional assembly configurations, operating frequencies, and tissue dimensions and properties could also be performed to further evaluate the design and determine optimal configurations for specific target applications.

The demonstrated capabilities of the deployable reflector – lens applicator assembly could enable tissue targets that were previously untreatable with catheter-based ultrasound intervention. This fundamental design lends itself towards particular endoluminal or laparoscopic sites and delivery pathways. Endogastric placement of the applicator into the stomach or upper GI tract is particularly appropriate due to the large luminal volume once positioned within these structures, permitting insertion diameters as large as 15 mm for initial placement and deployment of the expandable balloon assembly up to and potentially beyond a 5 cm diameter. Fine positioning and manipulation of the applicator assembly could be achieved by incorporating articulation and positional control mechanisms commonly employed in endoscopic devices. From these sites tumor targets in the liver or pancreas would be most accessible; however, tumors in the gall bladder or biliary tract, kidneys or spleen, while less common and farther in anatomical proximity, could also potentially be targeted. This applicator assembly could also be suitable for laparoscopic access and ablation of tumors (such as for targets in the kidney), permitting a minimal access port (incision)

diameter and large balloon expansion within the abdominal cavity. Besides tumor ablation, another potential application could be nerve ablation for pain palliation, with the celiac plexus bundle serving as one candidate target. Other potential delivery pathways beyond endogastric or laparoscopic routes include colorectal, bronchial, and endovascular lumens. For more constricted lumens, assembly configurations with smaller profiles (~3-6 mm transducer/catheter diameter) and potentially higher operating frequencies that expand up to 10-20 mm may be particularly suited for targeting shallow (1-3 cm) treatment depths.

In realizing the proposed deployable assemblies in practice, both the interior balloon, whose boundary serves as the reflector, as well as the distensible lens compartment may require high precision requirements in terms of the surface geometries and mounted orientations relative to the ultrasound source. These requirements and associated manufacturing tolerances could be potentially elucidated in simulation studies that explore varying degrees of “non-ideal” surface geometries or lens aberrations. With regards to the balloons comprising the reflector, precisely pre-shaped non-compliant medical balloons have been demonstrated and used in a variety of catheter-based medical applications, such as stent/heart valve delivery or angioplasty, with many different balloon shapes and materials (PET, Nylon, etc.) possible.¹⁹² Further, precisely shaped non-compliant balloons with a reflective multi-lumen compartment or coating have been demonstrated and integrated with ultrasonic and fiber optic sources, respectively.^{87,193} Greater technical difficulty may be associated with the integration and controlled distension of the convex lens. Bonding the distensible membrane to the non-compliant balloon could potentially be achieved using thermoplastic welding techniques (e.g., laser, RF) or with flexible medical-grade adhesives to preserve compact collapse.^{194,195} Material selection and thickness tolerance for the lens membrane will be important to ensure bonding compatibility and predictable distension

behavior. As a simpler design alternative to the separate distal fluid lens compartment, the interior balloon could be filled with lens fluid rather than water and its distal boundary modified to a fixed-shaped spherically-convex geometry. This design would preserve effective aperture and focal gain enhancement for a set focal length, as defined by the convex boundary curvature, at the loss of dynamic adjustment to the target depth.

Lastly, it is important to note that the core concepts introduced in this study – integrating endoluminal ultrasound sources with expandable acoustic reflector and lens components – could be combined into different applicator configurations besides the specific end-fire and side-fire designs evaluated herein. Furthermore, while the fluid lens compartment was highlighted to provide dynamic adjustment to the focal length by using a distensible membrane, a membrane that inflates to a fixed-shape could be applied to generate a fixed distance focus. Beyond a simple spherical convex profile, a fixed-shape lens membrane could be molded to a custom shape or profile to create more complex beam patterns that are tailored for specific target sites or various thermal (i.e., ablation, hyperthermia) or mechanical (e.g., drug delivery) therapeutic applications. Finally, as with other catheter-based ultrasound devices, these conceived applicator assemblies could also be made compatible with ultrasound or MR-based imaging guidance for navigation and treatment monitoring, as well as targeting sequential sonications similar to extracorporeal and endorectal HIFU systems.

4.6 Conclusions

Concepts and designs for integrating catheter-based endoluminal ultrasound devices with deployable acoustic reflectors and fluid lenses, in order to enhance acoustic output and penetration depth from small diameter devices, have been introduced. Acoustic simulations that incorporate acoustic transmission and reflection at material interfaces were performed, and show good

agreement with experimental characterization of a test applicator assembly. Parametric modeling studies demonstrates capability of the proposed applicator designs to achieve high focal gain and localized ablative temperature elevation at target depths between 10-100 mm. Based upon these positive findings, future studies will be directed towards further theoretical analysis and construction of complete prototypes of the proposed applicator for experimental evaluations.

Chapter 5

Conclusions and future work

5.1.1 Research summary

The overarching goal of this research project was to develop catheter-based therapeutic ultrasound delivery systems capable of targeting tissues adjacent to the gastrointestinal tract. The primary focus was on generating thermal ablation or hyperthermia within pancreatic tumors using ultrasound applicators placed in the stomach or duodenal lumens. However, many of the explored device configurations could be adapted for alternative luminal sites and tissue targets. The first part of this dissertation focused on developing and evaluating practical endoluminal ultrasound applicator device designs, spanning both theoretical and experimental investigations. The second part of this dissertation served as a preliminary exploration and theoretical analysis of more complex applicator configurations that contain deployable reflector and fluid lens components to enhance therapeutic energy delivery capabilities.

In Chapter 2, numerical models of ultrasound-based thermal ablation or hyperthermia generation in pancreatic tumor targets were developed and used to evaluate applicator designs with

different transducer configurations. Parametric studies revealed that select transducer geometries operating within a lower frequency range (1-3 MHz) were capable of greater volumetric thermal ablation of tissue while retaining sufficient thermal sparing ($T_{\max} < 45$ °C) of the luminal wall. Planar transducer designs were most suitable for volumetric ablations, generating 5-8 cm³ lesion volumes for a stationary 5 min sonication, while curvilinear transducer designs could produce more localized ablations to 20-45 mm depths from the luminal wall and enhance luminal sparing. Simulations in patient-specific anatomies showed that applicators with planar or curvilinear were capable of ablating >80% of the tumor volume for small (<5 cm³) tumors in the pancreatic head within 25 min and a single applicator placement. For larger tumors (17-38 cm³) in the pancreatic head and body, 2-3 applicator placements and longer treatments (up to ~50 min) would be necessary to cover appreciable portions (60-80%) of the tumor. For hyperthermia treatments, either planar or tubular section transducer configurations could be used for volumetric tissue coverage (8, 15 cm³ within 40-45 °C, respectively), with the planar providing deeper penetration as compared to the larger transverse coverage of the tubular section. These findings confirmed the theoretical feasibility of utilizing endoluminal ultrasound for volumetric thermal ablation or hyperthermia of pancreatic tumor targets, illustrating favored performance for treating smaller tumor targets near the luminal boundaries, with lower frequency planar and curvilinear transducers favored for ablative lesion formation while retaining luminal sparing.

In Chapter 3, based on the results of the theoretical modeling analysis, a family of endoluminal applicators with different transducer configurations (~3 MHz, planar or curvilinear-focused geometries) were designed and fabricated. These applicators were designed to be MR-compatible, with embedded tracking coils to facilitate *in vivo* placement under MR guidance and treatment monitoring using PRF-based MRTI. The applicators were characterized through force

balance efficiency measurements (ranging between ~50-65%), and the spatial distribution of energy deposition for each unique transducer configuration was characterized through hydrophone beam plots and MRTI-guided *ex vivo* tissue heating experiments. To assess the capabilities of the applicators to be endogastrically delivered and positioned within the GI tract and generate heating in targets within the pancreas, a porcine animal model was used due to their high similarities to humans with respect to GI anatomy. *Ex vivo* evaluations in a porcine cadaver confirmed capabilities of positioning the endoluminal applicators in the stomach under MR-guidance and generating and monitoring temperature elevations within pancreatic tissue. Maximum ablative temperature elevations extended up to 4 cm deep and 28 mm wide. Preliminary investigations in *in vivo* studies were performed using 4 animals, and demonstrated the capabilities of the applicators to generate temperature elevations of ~20-30 °C in pancreatic tissue at ~2 cm depths from the applicator, using 5-7 W/cm² applied acoustic intensity and sonication durations ranging from 3-16 minutes. Localized thermal lesions were generated in the pancreas, as verified through histological assessment, with dimensions ranging from 7-28 mm in length, 3-10 mm in width, and 5-12 mm in depth. Different strategies for mitigating motion artifacts during temperature monitoring *in vivo* were evaluated, and both multiple-baseline reconstruction and respiratory-gated acquisitions were shown to improve thermometry accuracy and mitigate artifacts for clear real-time thermometry measurements. Overall, these preliminary experimental investigations confirmed the technical feasibility of the endoluminal ultrasound approach to generating thermal ablation within pancreatic tissue targets under MRI and MRTI-guidance.

In Chapter 4, novel endoluminal ultrasound applicator configurations that integrate deployable balloon-based acoustic reflector and lens components were introduced and analyzed using theoretical modeling analysis and preliminary experimental validation. The core concept

behind these applicators is that they would be inserted and delivered in a small profile, then expanded at the target luminal site to enhance potential focal gain and penetration depth, permitting deeper and more selective treatment targets. By incorporating a fluid lens compartment bound by a distensible membrane, the lens' focal length could be adjusted to dynamically change the target depth. Two specific designs, representing alternatives with “end-firing” or “side-firing” capabilities, were proposed, and an acoustic modeling methodology that accounts for wave reflection/refraction was employed to model acoustic propagation through the applicator assemblies. Comprehensive parametric studies across design parameters for both applicator configurations were performed and demonstrated significant enhancement of focal gain, selective lesion formation, and penetration depth for the proposed assemblies as compared to conventional applicator designs with focused transducer configurations. Preliminary experimental investigations, using a proof-of-concept “end-fire” applicator assembly, validated the modeling analysis. Biothermal simulations demonstrated the capability of the proposed applicator assembly configurations to produce localized ellipsoidal thermal lesions increasing in size from 10-46 mm length x 4-8 mm width in pancreatic tissue as target depth increased from 2-8 cm. As such, these proposed designs possess significant improvements over conventional ultrasound applicator designs that could permit deeper targets and more selective heating while being fundamentally adaptable to other luminal sites and delivery strategies beyond the GI tract, such as for laparoscopy.

5.1.2 Future directions

One of the limitations of the modeling analysis performed in Chapter 2 is the uncertainty in the acoustic and thermal properties of pancreatic tumor tissue. Many of these material properties were approximated from values reported for pancreatic tissue, with modifications based on reported physiological differences in tissue composition between them. However, even for normal

pancreatic tissue, there was a wide range of values reported in literature, such as for the acoustic attenuation coefficient. While this entire range was taken into account to bracket expected performance of the explored applicator configurations, more precise and accurate modeling results could potentially be determined if large numbers of samples of human pancreatic adenocarcinoma were obtained and characterized in terms of their material properties. In addition, significant future efforts could be directed into converting the modeling platform developed and used herein into a full treatment planning platform with inverse planning algorithms that automatically optimize over various treatment parameters to maximize tumor coverage while maintaining sufficient sparing of adjacent normal tissues. Parameters that could be potentially optimized over could include design parameters of the applicators themselves (transducer frequency, geometry), positioning or placement of the applicator along the GI tract, as well as applied powers and durations of sonications. In order to be clinically useful for treatment planning purposes, full patient-specific model creation and simulations would have to be greatly accelerated in terms of total run-times. Automated segmentation techniques could potentially be developed to rapidly decrease the time requisite to segment patient image sets and generate 3D FEM models of the relevant anatomy. Superposition-based thermal solutions, based on lookup tables, could also significantly decrease simulation computation time, though would need to be verified in terms of retaining sufficient modelling accuracy. As much of the total simulation time in the patient-specific models performed in this work could be attributed to the iterative approach in determining appropriate treatment parameters, inverse planning algorithms could mitigate the iterative demands and substantially decrease overall computational times.

With respect to the experimental applicator development and evaluations in Chapter 3, the primary outcome of this preliminary investigation was demonstration of the basic feasibility of

placement, targeting and generating ablation in the pancreas under endoluminal device placement and MR/MRTI guidance. Further refinement to the positional control over the applicator can be made by incorporating and refining the articulation steering assembly highlighted in Appendix A. Improvements to the animal study protocol, such as including a lavage of the stomach prior to applicator insertion and treatment, could also reduce variability between animal studies, improve coupling of the applicator to tissue, and enhance sparing of the luminal wall. Due to the substantial experimental variations and challenges that were encountered in each animal study, it was difficult to clearly define relationships between sonication parameters (durations, powers, transducer geometries) and resulting lesion formation. Future validation studies can be applied to more clearly assess the safety and efficacy of this endoluminal approach using additional acute and chronic in vivo porcine studies. Further development and refinement of applicator designs and experimental methods should permit more reproducible experimental conditions and characterization studies to elucidate clearer relationships between sonication parameters, resulting temperature/thermal dose distributions, and lesion dimensions. These studies should permit formation of a consistent set of treatment parameters and methods, which can be evaluated in comprehensive safety studies to assess any acute and long-term complications resulting from the endoluminal ablation, as well as to evaluate thermal damage to the stomach and other tissues adjacent to the pancreas. Furthermore, as an alternative to ablation, further development of this approach could also be directed towards delivering moderate (40-45 °C) hyperthermia in the pancreas, which would benefit from the volumetric nature of heating and MR temperature monitoring, and could potentially enhance drug delivery, chemotherapy, or radiation therapies in patients with pancreatic adenocarcinoma.

For all the work investigating endoluminal applicators with deployable reflector and/or fluid lenses, as presented in Chapter 4 and Appendix B, natural next steps are towards complete

prototype fabrication and experimental evaluations. More comprehensive theoretical analyses of the proposed applicator configurations in Appendix B would be instructive in evaluating their capabilities and promise. Further explorations could also be directed towards investigating balloon profiles with more intricate surface geometries that permit complex beamforming, as may be preferred for specific anatomical targets or therapeutic applications.

Bibliography

- 1 P. Stauffer and S. Goldberg, "Introduction: thermal ablation therapy," *International Journal of Hyperthermia* **20**, 671-677 (2004).
- 2 D. Theodorescu, "Cancer cryotherapy: evolution and biology," *Rev.Urol.* **6 Suppl 4**, S9-S19 (2004).
- 3 P. Wust, B. Hildebrandt, G. Sreenivasa, B. Rau, J. Gellermann, H. Riess, R. Felix and P. Schlag, "Hyperthermia in combined treatment of cancer," *The lancet oncology* **3**, 487-497 (2002).
- 4 B. Hildebrandt, P. Wust, O. Ahlers, A. Dieing, G. Sreenivasa, T. Kerner, R. Felix and H. Riess, "The cellular and molecular basis of hyperthermia," *Crit.Rev.Oncol.* **43**, 33-56 (2002).
- 5 R.D. Issels, "Hyperthermia adds to chemotherapy," *Eur.J.Cancer* **44**, 2546-2554 (2008).
- 6 R.W. Habash, R. Bansal, D. Krewski and H.T. Alhafid, "Thermal therapy, part 1: an introduction to thermal therapy," *Critical Reviews™ in Biomedical Engineering* **34**, (2006).
- 7 S. Thomsen and J.A. Pearce, "Thermal damage and rate processes in biologic tissues", in *Optical-thermal response of laser-irradiated tissue* (Springer, 2010), pp. 487-549.
- 8 K.F. Chu and D.E. Dupuy, "Thermal ablation of tumours: biological mechanisms and advances in therapy," *Nature Reviews Cancer* **14**, 199-208 (2014).
- 9 C.J. Diederich, "Thermal ablation and high-temperature thermal therapy: overview of technology and clinical implementation," *Int J Hyperthermia* **21**, 745-753 (2005).
- 10 S.P. Haen, P.L. Pereira, H.R. Salih, H.G. Rammensee and C. Gouttefangeas, "More than just tumor destruction: immunomodulation by thermal ablation of cancer," *Clin.Dev.Immunol.* **2011**, 160250 (2011).

- 11 M. Ahmed and S.N. Goldberg, "Thermal ablation therapy for hepatocellular carcinoma," *Journal of vascular and interventional radiology* **13**, S231-S243 (2002).
- 12 C. Erce and R. Parks, "Interstitial ablative techniques for hepatic tumours," *Br.J.Surg.* **90**, 272-289 (2003).
- 13 D.P. Murphy and I.S. Gill, "Energy-based renal tumor ablation: a review," *Semin.Urol.Oncol.* **19**, 133-140 (2001).
- 14 C.J. Simon and D.E. Dupuy, in Seminars in musculoskeletal radiology, (Copyright© 2006 by Thieme Medical Publishers, Inc., 333 Seventh Avenue, New York, NY 10001, USA., 2006) pp. 137-144.
- 15 J.C. Zhu, T.D. Yan and D.L. Morris, "A systematic review of radiofrequency ablation for lung tumors," *Annals of surgical oncology* **15**, 1765-1774 (2008).
- 16 Y. Anzai, R. Lufkin, A. DeSalles, D.R. Hamilton, K. Farahani and K.L. Black, "Preliminary experience with MR-guided thermal ablation of brain tumors," *AJNR Am.J.Neuroradiol.* **16**, 39-48; discussion 49-52 (1995).
- 17 I. Meiers, D.J. Waters and D.G. Bostwick, "Preoperative prediction of multifocal prostate cancer and application of focal therapy: review 2007," *Urology* **70**, S3-S8 (2007).
- 18 Z. Zhao and F. Wu, "Minimally-invasive thermal ablation of early-stage breast cancer: a systemic review," *European Journal of Surgical Oncology (EJSO)* **36**, 1149-1155 (2010).
- 19 M.G. Keane, K. Bramis, S.P. Pereira and G.K. Fusai, "Systematic review of novel ablative methods in locally advanced pancreatic cancer," *World J. Gastroenterol.* **20**, 2267 (2014).
- 20 I.D. McRury and D.E. Haines, "Ablation for the treatment of arrhythmias," *Proc IEEE* **84**, 404-416 (1996).
- 21 C. Bouza, T. López, A. Magro, L. Navalpotro and J.M. Amate, "Systematic review and meta-analysis of transurethral needle ablation in symptomatic benign prostatic hyperplasia," *BMC urology* **6**, 14 (2006).
- 22 T. Lourenco, R. Pickard, L. Vale, A. Grant, C. Fraser, G. MacLennan, J. N'Dow and Benign Prostatic Enlargement team, "Minimally invasive treatments for benign prostatic enlargement: systematic review of randomised controlled trials," *BMJ* **337**, a1662 (2008).
- 23 S. Taneri, J.D. Zieske and D.T. Azar, "Evolution, techniques, clinical outcomes, and pathophysiology of LASEK: review of the literature," *Surv.Ophthalmol.* **49**, 576-602 (2004).

- 24 Z. Rahman, H. MacFalls, K. Jiang, K.F. Chan, K. Kelly, J. Tournas, O.F. Stumpp, V. Bedi and C. Zachary, "Fractional deep dermal ablation induces tissue tightening," *Lasers Surg.Med.* **41**, 78-86 (2009).
- 25 M. Hurwitz and P. Stauffer, in *Seminars in oncology*, (Elsevier, 2014) pp. 714-729.
- 26 J.L. Roti Roti, "Cellular responses to hyperthermia (40–46 C): Cell killing and molecular events," *International Journal of hyperthermia* **24**, 3-15 (2008).
- 27 C.D. Landon, J.Y. Park, D. Needham and M.W. Dewhirst, "Nanoscale Drug Delivery and Hyperthermia: The Materials Design and Preclinical and Clinical Testing of Low Temperature-Sensitive Liposomes Used in Combination with Mild Hyperthermia in the Treatment of Local Cancer," *Open Nanomed J.* **3**, 38-64 (2011).
- 28 W.C. Dewey, "Arrhenius relationships from the molecule and cell to the clinic*," *Int J Hyperthermia* **25**, 3-20 (2009).
- 29 M. Dewhirst, B. Viglianti, M. Lora-Michiels, M. Hanson and P. Hoopes, "Basic principles of thermal dosimetry and thermal thresholds for tissue damage from hyperthermia," *Int J Hyperthermia* **19**, 267-294 (2003).
- 30 F.C. Henriques and A.R. Moritz, "Studies of Thermal Injury: I. The Conduction of Heat to and through Skin and the Temperatures Attained Therein. A Theoretical and an Experimental Investigation," *Am.J.Pathol.* **23**, 530-549 (1947).
- 31 A.R. Moritz and F.C. Henriques, "Studies of Thermal Injury: II. The Relative Importance of Time and Surface Temperature in the Causation of Cutaneous Burns," *Am.J.Pathol.* **23**, 695-720 (1947).
- 32 A.R. Moritz, "Studies of Thermal Injury: III. The Pathology and Pathogenesis of Cutaneous Burns. An Experimental Study," *Am.J.Pathol.* **23**, 915-941 (1947).
- 33 J.A. Pearce, in *SPIE BiOS: Biomedical Optics*, (International Society for Optics and Photonics, 2009) pp. 718104-718104-15.
- 34 S.A. Sapareto and W.C. Dewey, "Thermal dose determination in cancer therapy," *Int J Radiat Oncol Biol Phys* **10**, 787-800 (1984).
- 35 L. Roizin-Towle and J.P. Pirro, "The response of human and rodent cells to hyperthermia," *International Journal of Radiation Oncology* Biology* Physics* **20**, 751-756 (1991).

- 36 P.S. Yarmolenko, E.J. Moon, C. Landon, A. Manzoor, D.W. Hochman, B.L. Viglianti and M.W. Dewhurst, "Thresholds for thermal damage to normal tissues: an update," *Int J Hyperthermia* **27**, 320-343 (2011).
- 37 J.E. Coad, in SPIE BiOS, (International Society for Optics and Photonics, 2011) pp. 790103-790103-12.
- 38 J.E. Coad, in Biomedical Optics 2005, (International Society for Optics and Photonics, 2005) pp. 15-22.
- 39 K. Hynynen, "Biophysics and technology of ultrasound hyperthermia", in *Methods of external hyperthermic heating* (Springer, 1990), pp. 61-115.
- 40 P.N.T. Wells, Biomedical ultrasonics, (Academic Pr, 1977).
- 41 J.L. Prince and J.M. Links, Medical imaging signals and systems, (Pearson Prentice Hall Upper Saddle River, New Jersey, 2006).
- 42 V. Bull and G.R. ter Haar, "The physics of ultrasound energy sources", in *Physics of Thermal Therapy: Fundamentals and Clinical Applications* (Taylor & Francis, 2012), pp. 75-94.
- 43 D.L. Hykes, W.R. Hedrick and D.E. Starchman, Ultrasound physics and instrumentation, (Mosby, 1992).
- 44 R.S. Cobbold, Foundations of biomedical ultrasound, (Oxford University Press, 2006).
- 45 R.J. Lalonde, A. Worthington and J.W. Hunt, "Field conjugate acoustic lenses for ultrasound hyperthermia," *IEEE Trans.Ultrason.Ferroelectr.Freq.Control* **40**, 592-602 (1993).
- 46 T. Fjield, V. Sorrentino, H. Cline and K. Hynynen, "Design and experimental verification of thin acoustic lenses for the coagulation of large tissue volumes," *Phys.Med.Biol.* **42**, 2341 (1997).
- 47 T. Fjield, C.E. Silcox and K. Hynynen, "Low-profile lenses for ultrasound surgery," *Phys.Med.Biol.* **44**, 1803 (1999).
- 48 F. Foster and J. Hunt, "The focussing of ultrasound beams through human tissue", in *Acoustical imaging* (Springer, 1980), pp. 709-718.
- 49 E. Neufeld, M.M. Paulides, G.C. van Rhooon and N. Kuster, "Numerical modeling for simulation and treatment planning of thermal therapy", in *Physics of Thermal Therapy: Fundamentals and Clinical Applications* (Taylor & Francis, 2012), pp. 119-136.
- 50 K.B. Ocheltree and L. Frizzel, "Sound field calculation for rectangular sources," *IEEE Trans. Ultrason. Ferroelectr. Freq. Control* **36**, 242-248 (1989).

- 51 E.G. Moros, R.J. Myerson and W.L. Straube, "Aperture size to therapeutic volume relation for a multielement ultrasound system: Determination of applicator adequacy for superficial hyperthermia," *Med.Phys.* **20**, 1399-1409 (1993).
- 52 C. Lee and P.J. Benkeser, "A computationally efficient method for the calculation of the transient field of acoustic radiators," *J.Acoust.Soc.Am.* **96**, 545-551 (1994).
- 53 Y.J. Yoon and P.J. Benkeser, "Sound field calculations for an ultrasonic linear phased array with a spherical liquid lens," *IEEE Trans. Ultrason. Ferroelectr. Freq. Control* **39**, 268-272 (1992).
- 54 J.E. Kennedy, "High-intensity focused ultrasound in the treatment of solid tumours," *Nature reviews cancer* **5**, 321-327 (2005).
- 55 J. Kennedy, G. Ter Haar and D. Cranston, "High intensity focused ultrasound: surgery of the future?" *Br.J.Radiol.*, (2014).
- 56 Y.S. Kim, H. Rhim, M.J. Choi, H.K. Lim and D. Choi, "High-intensity focused ultrasound therapy: an overview for radiologists," *Korean J.Radiol.* **9**, 291-302 (2008).
- 57 >.G. ter Haar and C. Coussios, "High intensity focused ultrasound: physical principles and devices," *International Journal of Hyperthermia* **23**, 89-104 (2007).
- 58 F. Wu, Z. Wang, W. Chen, H. Zhu, J. Bai, J. Zou, K. Li, C. Jin, F. Xie and H. Su, "Extracorporeal high intensity focused ultrasound ablation in the treatment of patients with large hepatocellular carcinoma," *Annals of surgical oncology* **11**, 1061 (2004).
- 59 R. Illing, J. Kennedy, F. Wu, G. Ter Haar, A. Protheroe, P. Friend, F. Gleeson, D. Cranston, R. Phillips and M. Middleton, "The safety and feasibility of extracorporeal high-intensity focused ultrasound (HIFU) for the treatment of liver and kidney tumours in a Western population," *Br.J.Cancer* **93**, 890-895 (2005).
- 60 E.S. Ebbini and G. Ter Haar, "Ultrasound-guided therapeutic focused ultrasound: current status and future directions," *International Journal of Hyperthermia* **31**, 77-89 (2015).
- 61 Y. Kim, "Advances in MR image-guided high-intensity focused ultrasound therapy," *International Journal of Hyperthermia* **31**, 225-232 (2015).
- 62 L. Chen, F. Li, F. Wu and E.G. Moros, "Clinical External Ultrasonic Treatment Devices", in *Physics of Thermal Therapy: Fundamentals and Clinical Applications* (Taylor & Francis, 2012), pp. 177-188.

- 63 V.A. Salgaonkar and C.J. Diederich, "Catheter-based ultrasound technology for image-guided thermal therapy: Current technology and applications," *International Journal of Hyperthermia* **31**, 203-215 (2015).
- 64 C.J. Diederich and K. Hynynen, "Ultrasound technology for hyperthermia," *Ultrasound Med.Biol.* **25**, 871-887 (1999).
- 65 C.J. Diederich, "Endocavity and catheter-based ultrasound devices", in *Physics of Thermal Therapy: Fundamentals and Clinical Applications* (Taylor & Francis, 2012), pp. 189-200.
- 66 C. Diederich, "Ultrasound applicators with integrated catheter-cooling for interstitial hyperthermia: theory and preliminary experiments," *International journal of hyperthermia* **12**, 279-297 (1996).
- 67 W. Nau, C. Diederich and P. Stauffer, "Directional power deposition from direct-coupled and catheter-cooled interstitial ultrasound applicators," *International journal of hyperthermia* **16**, 129-144 (2000).
- 68 W. Nau, C. Diederich and E. Burdette, "Evaluation of multielement catheter-cooled interstitial ultrasound applicators for high-temperature thermal therapy," *Med.Phys.* **28**, 1525-1534 (2001).
- 69 R. Chopra, C. Luginbuhl, A.J. Weymouth, F.S. Foster and M.J. Bronskill, "Interstitial ultrasound heating applicator for MR-guided thermal therapy," *Phys.Med.Biol.* **46**, 3133 (2001).
- 70 D.L. Deardorff and C.J. Diederich, "Axial control of thermal coagulation using a multi-element interstitial ultrasound applicator with internal cooling," *IEEE Trans.Ultrason.Ferroelectr.Freq.Control* **47**, 170-178 (2000).
- 71 W.H. Nau, C.J. Diederich, A.B. Ross, K. Butts, V. Rieke, D.M. Bouley, H. Gill, B. Daniel and G. Sommer, "MRI-guided interstitial ultrasound thermal therapy of the prostate: A feasibility study in the canine model," *Med.Phys.* **32**, 733-743 (2005).
- 72 M. Kangasniemi, C.J. Diederich, D. Price, E. Roger, R.J. Stafford, D.F. Schomer, L.E. Olsson, P.D. Tyreus, W.H. Nau and J.D. Hazle, "Multiplanar MR temperature-sensitive imaging of cerebral thermal treatment using interstitial ultrasound applicators in a canine model," *Journal of Magnetic Resonance Imaging* **16**, 522-531 (2002).

- 73 D. Melodelima, R. Salomir, C. Mougenot, C. Moonen and D. Cathignol, "64-element intraluminal ultrasound cylindrical phased array for transesophageal thermal ablation under fast MR temperature mapping: An ex vivo study," *Med.Phys.* **33**, 2926-2934 (2006).
- 74 U. Lindner, S. Ghai, P. Spensieri, E. Hlasny, Van der Kwast, Theodorus H, S.A. McCluskey, M.A. Haider, W. Kucharczyk and J. Trachtenberg, "Focal magnetic resonance guided focused ultrasound for prostate cancer: Initial North American experience," *Canadian Urological Association Journal* **6**, 283-286 (2012).
- 75 Y. Sinelnikov, T. Fjield and O. Sapozhnikov, "The mechanism of lesion formation by focused ultrasound ablation catheter for treatment of atrial fibrillation," *Acoust. Phys.* **55**, 647-656 (2009).
- 76 D. Melodelima, F. Prat, J. Fritsch, Y. Theillere and D. Cathignol, "Treatment of esophageal tumors using high intensity intraluminal ultrasound: first clinical results," *J. Transl. Med.* **6**, 28 (2008).
- 77 M. Pioche, C. Lafon, E. Constancier, A. Vignot, A. Birer, R. Gincul, V. Lepilliez, F. Prat, S. Roman, J.Y. Chapelon, J.C. Saurin and T. Ponchon, "High-intensity focused ultrasound liver destruction through the gastric wall under endoscopic ultrasound control: first experience in living pigs," *Endoscopy* **44 Suppl 2 UCTN**, E376-7 (2012).
- 78 D. Melodelima, R. Salomir, J. Chapelon, Y. Theillère, C. Moonen and D. Cathignol, "Intraluminal high intensity ultrasound treatment in the esophagus under fast MR temperature mapping: in vivo studies," *Magn. Reson. Med.* **54**, 975-982 (2005).
- 79 T. Li, T. Khokhlova, E. Maloney, Y. Wang, S. D'Andrea, F. Starr, N. Farr, K. Morrison, G. Keilman and J.H. Hwang, "Endoscopic high-intensity focused US: technical aspects and studies in an in vivo porcine model (with video)," *Gastrointest. Endosc.* **81**, 1243-1250 (2015).
- 80 R. Chopra, A. Colquhoun, M. Burtnyk, W.A. N'djin, I. Kobelevskiy, A. Boyes, K. Siddiqui, H. Foster, L. Sugar and M.A. Haider, "MR imaging-controlled transurethral ultrasound therapy for conformal treatment of prostate tissue: initial feasibility in humans," *Radiology* **265**, 303-313 (2012).
- 81 C. Diederich, R. Stafford, W. Nau, E. Burdette, R. Price and J. Hazle, "Transurethral ultrasound applicators with directional heating patterns for prostate thermal therapy: in vivo evaluation using magnetic resonance thermometry," *Med. Phys.* **31**, 405-413 (2004).

- 82 G. Sommer, K.B. Pauly, A. Holbrook, J. Plata, B. Daniel, D. Bouley, H. Gill, P. Prakash, V. Salgaonkar, P. Jones and C. Diederich, "Applicators for magnetic resonance-guided ultrasonic ablation of benign prostatic hyperplasia," *Invest. Radiol.* **48**, 387-394 (2013).
- 83 R. Chopra, M. Burtnyk, M.A. Haider and M.J. Bronskill, "Method for MRI-guided conformal thermal therapy of prostate with planar transurethral ultrasound heating applicators," *Phys.Med.Biol.* **50**, 4957 (2005).
- 84 A. Gelet, J. Chapelon, R. Bouvier, O. Rouviere, Y. Lasne, D. Lyonnet and J. Dubernard, "Transrectal high-intensity focused ultrasound: minimally invasive therapy of localized prostate cancer," *J. Endourol.* **14**, 519-528 (2000).
- 85 J. Chapelon, M. Ribault, A. Birer, F. Vernier, R. Souchon and A. Gelet, "Treatment of localised prostate cancer with transrectal high intensity focused ultrasound," *Eur. J. Ultrasound* **9**, 31-38 (1999).
- 86 T. Mabin, M. Sapoval, V. Cabane, J. Stemmett and M. Iyer, "First experience with endovascular ultrasound renal denervation for the treatment of resistant hypertension," *EuroIntervention* **8**, 57-61 (2012).
- 87 H. Nakagawa, M. Antz, T. Wong, B. Schmidt, S. Ernst, F. Ouyang, T. Vogtmann, R. Wu, K. Yokoyama and D. Lockwood, "Initial Experience Using a Forward Directed, High-Intensity Focused Ultrasound Balloon Catheter for Pulmonary Vein Antrum Isolation in Patients with Atrial Fibrillation," *J. Cardiovasc. Electrophysiol.* **18**, 136-144 (2007).
- 88 M. Lesh, C. Diederich, P. Guerra, Y. Goseki and P. Sparks, "An anatomic approach to prevention of atrial fibrillation: pulmonary vein isolation with through-the-balloon ultrasound ablation (TTB-USA)," *Thorac.Cardiovasc.Surg.* **47**, 347-351 (1999).
- 89 J.H. Wootton, I.J. Hsu and C.J. Diederich, "Endocervical ultrasound applicator for integrated hyperthermia and HDR brachytherapy in the treatment of locally advanced cervical carcinoma," *Med. Phys.* **38**, 598-611 (2011).
- 90 H.C. Klingler, M. Susani, R. Seip, J. Mauermann, N. Sanghvi and M.J. Marberger, "A novel approach to energy ablative therapy of small renal tumours: laparoscopic high-intensity focused ultrasound," *Eur. Urol.* **53**, 810-818 (2008).
- 91 D.L. Deardorff, C.J. Diederich and W.H. Nau, "Control of interstitial thermal coagulation: comparative evaluation of microwave and ultrasound applicators," *Med.Phys.* **28**, 104-117 (2001).

- 92 C.L. Brace, "Radiofrequency and microwave ablation of the liver, lung, kidney, and bone: what are the differences?" *Curr.Probl.Diagn.Radiol.* **38**, 135-143 (2009).
- 93 Y. Ni, S. Mulier, Y. Miao, L. Michel and G. Marchal, "A review of the general aspects of radiofrequency ablation," *Abdom.Imaging* **30**, 381-400 (2005).
- 94 B.D. De Senneville, C. Mougenot and C.T. Moonen, "Real-time adaptive methods for treatment of mobile organs by MRI-controlled high-intensity focused ultrasound," *Magn. Reson. Med.* **57**, 319-330 (2007).
- 95 J.A. Rooney and W.L. Nyborg, "Acoustic radiation pressure in a traveling plane wave," *American Journal of Physics* **40**, 1825-1830 (1972).
- 96 D. Dalecki, "Mechanical bioeffects of ultrasound," *Annu.Rev.Biomed.Eng.* **6**, 229-248 (2004).
- 97 B. Fahey, R. Nelson, D. Bradway, S. Hsu, D. Dumont and G. Trahey, "In vivo visualization of abdominal malignancies with acoustic radiation force elastography," *Phys. Med. Biol.* **53**, 279 (2007).
- 98 H.F. Stewart, "Ultrasonic measurement techniques and equipment output levels", in *Essentials of medical ultrasound* (Humana, Clifton, New Jersey, 1982), pp. 77-116.
- 99 W.D. O'Brien, "Ultrasound–biophysics mechanisms," *Prog.Biophys.Mol.Biol.* **93**, 212-255 (2007).
- 100 C. Chaussy and E. Schmiedt, "Extracorporeal shock wave lithotripsy (ESWL) for kidney stones. An alternative to surgery?" *Urol.Radiol.* **6**, 80-87 (1984).
- 101 Y. Liu, H. Miyoshi and M. Nakamura, "Encapsulated ultrasound microbubbles: therapeutic application in drug/gene delivery," *J.Controlled Release* **114**, 89-99 (2006).
- 102 K. Hynynen, N. McDannold, N. Vykhodtseva and F.A. Jolesz, "Noninvasive MR Imaging–guided Focal Opening of the Blood-Brain Barrier in Rabbits 1," *Radiology* **220**, 640-646 (2001).
- 103 J. Yuan, C. Mei, L.P. Panych, N.J. McDannold and B. Madore, "Towards fast and accurate temperature mapping with proton resonance frequency-based MR thermometry," *Quantitative imaging in medicine and surgery* **2**, 21-32 (2012).
- 104 V. Rieke and K. Butts Pauly, "MR thermometry," *J Magn Reson Imaging* **27**, 376-390 (2008).
- 105 B. Denis de Senneville, B. Quesson and C.T. Moonen, "Magnetic resonance temperature imaging," *International Journal of Hyperthermia* **21**, 515-531 (2005).

- 106 M. Lepetit-Coiffé, B. Quesson, O. Seror, E. Dumont, B. Le Bail, C.T. Moonen and H. Trillaud, "Real-time monitoring of radiofrequency ablation of rabbit liver by respiratory-gated quantitative temperature MRI," *Journal of Magnetic Resonance Imaging* **24**, 152-159 (2006).
- 107 S. Morikawa, T. Inubushi, Y. Kurumi, S. Naka, K. Sato, K. Demura, T. Tani and H.A. Haque, "Feasibility of respiratory triggering for MR-guided microwave ablation of liver tumors under general anesthesia," *Cardiovasc.Intervent.Radiol.* **27**, 370-373 (2004).
- 108 C. Weidensteiner, B. Quesson, B. Caire-Gana, N. Keroui, A. Rullier, H. Trillaud and C.T. Moonen, "Real-time MR temperature mapping of rabbit liver in vivo during thermal ablation," *Magnetic resonance in Medicine* **50**, 322-330 (2003).
- 109 K.K. Vigen, B.L. Daniel, J.M. Pauly and K. Butts, "Triggered, navigated, multi-baseline method for proton resonance frequency temperature mapping with respiratory motion," *Magn. Reson. Med.* **50**, 1003-1010 (2003).
- 110 V. Rieke, K.K. Vigen, G. Sommer, B.L. Daniel, J.M. Pauly and K. Butts, "Referenceless PRF shift thermometry," *Magnetic resonance in medicine* **51**, 1223-1231 (2004).
- 111 H.H. Pennes, "Analysis of tissue and arterial blood temperatures in the resting human forearm," *J. Appl. Physiol.* **1**, 93-122 (1948).
- 112 D. Haemmerich, A. Wright, D. Mahvi, F. Lee Jr and J. Webster, "Hepatic bipolar radiofrequency ablation creates coagulation zones close to blood vessels: a finite element study," *Med Biol Eng Comput* **41**, 317-323 (2003).
- 113 P. Prakash and C.J. Diederich, "Considerations for theoretical modelling of thermal ablation with catheter-based ultrasonic sources: Implications for treatment planning, monitoring and control," *Int. J. Hyperthermia* **28**, 69-86 (2012).
- 114 American Cancer Society, "Cancer Facts & Figures, 2013", (2013).
- 115 A. Stathis and M.J. Moore, "Advanced pancreatic carcinoma: current treatment and future challenges," *Nat. Rev. Clin. Oncol.* **7**, 163-172 (2010).
- 116 F.J. Brescia, "Palliative care in pancreatic cancer," *Cancer Control* **11**, 39-45 (2004).
- 117 M. Hameed, H. Hameed and M. Erdek, "Pain management in pancreatic cancer," *Cancers* **3**, 43-60 (2010).
- 118 Y. Zhou, "High-intensity focused ultrasound treatment for advanced pancreatic cancer," *Gastroenterol. Res. Pract.* **2014**, 1-11 (2014).

- 119 M. Anzidei, B.C. Marincola, M. Bezzi, G. Brachetti, F. Nudo, E. Cortesi, P. Berloco, C. Catalano and A. Napoli, "Magnetic resonance-guided high-intensity focused ultrasound treatment of locally advanced pancreatic adenocarcinoma: preliminary experience for pain palliation and local tumor control," *Invest. Radiol.* **49**, 759-765 (2014).
- 120 F. Wu, Z. Wang, H. Zhu, W. Chen, J. Zou, J. Bai, K. Li, C. Jin, F. Xie and H. Su, "Feasibility of US-guided high-intensity focused ultrasound treatment in patients with advanced pancreatic cancer: initial experience 1," *Radiology* **236**, 1034-1040 (2005).
- 121 J. Vidal-Jove, E. Perich and M.A. del Castillo, "Ultrasound guided high intensity focused ultrasound for malignant tumors: the Spanish experience of survival advantage in stage III and IV pancreatic cancer," *Ultrason. Sonochem.* **27**, 703-706 (2015).
- 122 R. Pezzilli, C. Ricci, C. Serra, R. Casadei, F. Monari, M. D'Ambra, R. Corinaldesi and F. Minni, "The problems of radiofrequency ablation as an approach for advanced unresectable ductal pancreatic carcinoma," *Cancers* **2**, 1419-1431 (2010).
- 123 R. Girelli, I. Frigerio, R. Salvia, E. Barbi, P. Tinazzi Martini and C. Bassi, "Feasibility and safety of radiofrequency ablation for locally advanced pancreatic cancer," *Br. J. Surg.* **97**, 220-225 (2010).
- 124 Z.A. Rasheed, W. Matsui and A. Maitra, "Pathology of pancreatic stroma in PDAC", in *Pancreatic Cancer and Tumor Microenvironment* (Transworld Research Network, Trivandrum (India), 2012).
- 125 R.D. Issels, L.H. Lindner, J. Verweij, P. Wust, P. Reichardt, B. Schem, S. Abdel-Rahman, S. Daugaard, C. Salat and C. Wendtner, "Neo-adjuvant chemotherapy alone or with regional hyperthermia for localised high-risk soft-tissue sarcoma: a randomised phase 3 multicentre study," *Lancet Oncol* **11**, 561-570 (2010).
- 126 K.E. Tschoep-Lechner, V. Milani, F. Berger, N. Dieterle, S. Abdel-Rahman, C. Salat and R. Issels, "Gemcitabine and cisplatin combined with regional hyperthermia as second-line treatment in patients with gemcitabine-refractory advanced pancreatic cancer," *Int J Hyperthermia* **29**, 8-16 (2013).
- 127 T. Ishikawa, S. Kokura, N. Sakamoto, T. Ando, E. Imamoto, T. Hattori, H. Oyamada, N. Yoshinami, M. Sakamoto and K. Kitagawa, "Phase II trial of combined regional hyperthermia and gemcitabine for locally advanced or metastatic pancreatic cancer," *Int J Hyperthermia* **28**, 597-604 (2012).

- 128 D. Needham and M.W. Dewhurst, "The development and testing of a new temperature-sensitive drug delivery system for the treatment of solid tumors," *Adv. Drug Deliv. Rev.* **53**, 285-305 (2001).
- 129 M.S. Adams, S.J. Scott, V.A. Salgaonkar, G. Sommer and C.J. Diederich, "Thermal therapy of pancreatic tumors using endoluminal ultrasound: parametric and patient-specific modeling," *Int. J. Hyperthermia* , (2016).
- 130 M.S. Adams, S.J. Scott, V.A. Salgaonkar, P.D. Jones, J.C. Plata-Camargo, G. Sommer and C.J. Diederich, in *SPIE BiOS*, (International Society for Optics and Photonics, 2015) pp. 93260F-93260F-8.
- 131 M.S. Adams, V.A. Salgaonkar, J. Plata-Camargo, P.D. Jones, A. Pascal-Tenorio, H. Chen, D.M. Bouley, G. Sommer, K.B. Pauly and C.J. Diederich, "Endoluminal ultrasound applicators for MR-guided thermal ablation of pancreatic tumors: Preliminary design and evaluation in a porcine pancreas model," *Med. Phys.* **43**, 4184-4197 (2016).
- 132 M.S. Adams, V.A. Salgaonkara, G. Sommerc and C.J. Diederich, in *Proc. of SPIE Vol*, 2017 pp. 100660I-1.
- 133 C. Lafon, Y. Theillere, F. Prat, A. Arefiev, J. Chapelon and D. Cathignol, "Development of an interstitial ultrasound applicator for endoscopic procedures: animal experimentation," *Ultrasound Med. Biol.* **26**, 669-675 (2000).
- 134 J.H. Hwang, N. Farr, K. Morrison, Y. Wang, T. Khokhlova, B. Ko, H. Jang and G. Keilman, "876 Development of an EUS-Guided High-Intensity Focused Ultrasound Endoscope," *Gastrointest. Endosc.* **73**, AB155 (2011).
- 135 P. Prakash, V.A. Salgaonkar and C.J. Diederich, "Modelling of endoluminal and interstitial ultrasound hyperthermia and thermal ablation: Applications for device design, feedback control and treatment planning," *Int J Hyperthermia* **29**, 296-307 (2013).
- 136 X. Chen, C.J. Diederich, J.H. Wootton, J. Pouliot and I. Hsu, "Optimisation-based thermal treatment planning for catheter-based ultrasound hyperthermia," *Int J Hyperthermia* **26**, 39-55 (2010).
- 137 S.J. Scott, V. Salgaonkar, P. Prakash, E.C. Burdette and C.J. Diederich, "Interstitial ultrasound ablation of vertebral and paraspinal tumours: Parametric and patient-specific simulations," *Int J Hyperthermia* **30**, 228-244 (2014).

- 138 J.H. Wootton, P. Prakash, I.J. Hsu and C.J. Diederich, "Implant strategies for endocervical and interstitial ultrasound hyperthermia adjunct to HDR brachytherapy for the treatment of cervical cancer," *Phys.Med.Biol.* **56**, 3967 (2011).
- 139 M. Burtnyk, R. Chopra and M.J. Bronskill, "Quantitative analysis of 3-D conformal MRI-guided transurethral ultrasound therapy of the prostate: Theoretical simulations," *Int J Hyperthermia* **25**, 116-131 (2009).
- 140 M. Burtnyk, R. Chopra and M. Bronskill, "Simulation study on the heating of the surrounding anatomy during transurethral ultrasound prostate therapy: A 3D theoretical analysis of patient safety," *Med.Phys.* **37**, 2862-2875 (2010).
- 141 S. Varadarajulu, S. Banerjee, B.A. Barth, D.J. Desilets, V. Kaul, S.R. Kethu, M.C. Pedrosa, P.R. Pfau, J.L. Tokar and A. Wang, "GI endoscopes," *Gastrointest. Endosc.* **74**, 1-6. e6 (2011).
- 142 P. Prakash, V.A. Salgaonkar, S.J. Scott, P. Jones, D. Hensley, A. Holbrook, J. Plata, G. Sommer and C.J. Diederich, "MR guided thermal therapy of pancreatic tumors with endoluminal, intraluminal and interstitial catheter-based ultrasound devices: Preliminary theoretical and experimental investigations," *Proc SPIE*, 85840V-85840V-10 (2013).
- 143 Francis A. Duck, *Physical properties of tissues: a comprehensive reference book*, (Academic press, 2013).
- 144 P. Hasgall, E. Neufeld and M. Gosselin, IT'IS Database for thermal and electromagnetic parameters of biological tissues. Version 2.4, July 30th, 2013 , (2013).
- 145 S. Kersting, R. Konopke, F. Kersting, A. Volk, M. Distler, H. Bergert, H. Saeger, R. Grützmann and A. Bunk, "Quantitative perfusion analysis of transabdominal contrast-enhanced ultrasonography of pancreatic masses and carcinomas," *Gastroenterology* **137**, 1903-1911 (2009).
- 146 C.B. Caldwell and J.J. Ricotta, "Changes in visceral blood flow with elevated intraabdominal pressure," *J Surg Res* **43**, 14-20 (1987).
- 147 L. Delrue, P. Blanckaert, D. Mertens, S. Van Meerbeeck, W. Ceelen and P. Duyck, "Tissue perfusion in pathologies of the pancreas: assessment using 128-slice computed tomography," *Abdom.Imaging* **37**, 595-601 (2012).
- 148 S. Kandel, C. Kloeters, H. Meyer, P. Hein, A. Hilbig and P. Rogalla, "Whole-organ perfusion of the pancreas using dynamic volume CT in patients with primary pancreas carcinoma: acquisition technique, post-processing and initial results," *Eur.Radiol.* **19**, 2641-2646 (2009).

- 149 M. O'Donnell, J. Mimbs and J. Miller, "The relationship between collagen and ultrasonic attenuation in myocardial tissue," *J.Acoust.Soc.Am.* **65**, 512-517 (1979).
- 150 T. Imamura, H. Iguchi, T. Manabe, G. Ohshio, T. Yoshimura, Z. Wang, H. Suwa, S. Ishigami and M. Imamura, "Quantitative analysis of collagen and collagen subtypes I, III, and V in human pancreatic cancer, tumor-associated chronic pancreatitis, and alcoholic chronic pancreatitis." *Pancreas* **11**, 357-364 (1995).
- 151 N. Smith, N. Merrilees, K. Hynynen and M. Dahleh, "Control system for an MRI compatible intracavitary ultrasound array for thermal treatment of prostate disease," *Int J Hyperthermia* **17**, 271-282 (2001).
- 152 N. McDannold, K. Hynynen, D. Wolf, G. Wolf and F. Jolesz, "MRI evaluation of thermal ablation of tumors with focused ultrasound," *J Magn Reson Imaging* **8**, 91-100 (1998).
- 153 G. Masselli, A. Picarelli, M. Di Tola, V. Libanori, G. Donato, E. Poletini, A. Piermattei, P. Palumbo, A. Pittalis and A. Saponara, "Celiac disease: evaluation with dynamic contrast-enhanced MR imaging," *Radiology* **256**, 783-790 (2010).
- 154 J.P. Jones and M. Behrens, "Invivo measurement of frequency dependent attenuation in normal liver, pancreas, and spleen," *Ultrason.Imaging* **3**, 205-206 (1981).
- 155 V. Arienti, C. Califano, G. Brusco, L. Boriani, F. Biagi, M. Giulia Sama, S. Sottili, A. Domanico, G.R. Corazza and G. Gasbarrini, "Doppler ultrasonographic evaluation of splanchnic blood flow in coeliac disease," *Gut* **39**, 369-373 (1996).
- 156 M.D. Perišić, D. Čulafić and M. Kerkez, "Specificity of splenic blood flow in liver cirrhosis," *Rom.J.Intern.Med.* **43**, 141-151 (2005).
- 157 G.H. Hübner, N. Steudel, G. Kleber, C. Behrmann, E. Lotterer and W.E. Fleig, "Hepatic arterial blood flow velocities: assessment by transcutaneous and intravascular Doppler sonography," *J.Hepatol.* **32**, 893-899 (2000).
- 158 J. Chato, "Heat transfer to blood vessels," *J Biomech Eng* **102**, 110-118 (1980).
- 159 I.T. Gabe, J.H. Gault, J. Ross Jr, D.T. Mason, C.J. Mills, J.P. Schillingford and E. Braunwald, "Measurement of instantaneous blood flow velocity and pressure in conscious man with a catheter-tip velocity probe," *Circulation* **40**, 603-614 (1969).
- 160 K. Nylund, T. Hausken, S. Ødegaard, G. Eide and O. Gilja, "Gastrointestinal wall thickness measured with transabdominal ultrasonography and its relationship to demographic factors in healthy subjects," *Ultraschall Med.* **33**, E225 (2012).

- 161 I. Zuber-Jerger, A. Muller, F. Kullmann, C.M. Gelbmann, E. Endlicher, U. Muller-Ladner and M. Fleck, "Gastrointestinal manifestation of systemic sclerosis--thickening of the upper gastrointestinal wall detected by endoscopic ultrasound is a valid sign," *Rheumatology* **49**, 368-372 (2010).
- 162 S. Pichardo and K. Hynynen, "New design for an endoesophageal sector-based array for the treatment of atrial fibrillation: a parametric simulation study," *IEEE Trans Ultrason Ferroelectr Freq Control* **56**, 600-612 (2009).
- 163 J. Werner, E. Park, H. Lee, D. Francischelli and N.B. Smith, "Feasibility of in vivo transesophageal cardiac ablation using a phased ultrasound array," *Ultrasound Med.Biol.* **36**, 752-760 (2010).
- 164 R.S. Date, J. Biggins, I. Paterson, J. Denton, R.F. McMahon and A.K. Siriwardena, "Development and validation of an experimental model for the assessment of radiofrequency ablation of pancreatic parenchyma," *Pancreas* **30**, 266-271 (2005).
- 165 D. Li, S. Zhou, S. Qiu and S. Qiao, "Thermodamage, thermosensitivity and thermotolerance of normal swine oesophagus," *Int J Hyperthermia* **3**, 143-151 (1987).
- 166 M.S. Bhutani and J.C. Deutsch, EUS Pathology with Digital Anatomy Correlation: A Text and Atlas, (PMPH-USA, 2009).
- 167 A.B. Ross, C.J. Diederich, W.H. Nau, V. Rieke, R.K. Butts, G. Sommer, H. Gill and D.M. Bouley, "Curvilinear transurethral ultrasound applicator for selective prostate thermal therapy," *Med. Phys.* **32**, 1555-1565 (2005).
- 168 D. Arora, D. Cooley, T. Perry, M. Skliar and R.B. Roemer, "Direct thermal dose control of constrained focused ultrasound treatments: phantom and in vivo evaluation," *Phys Med Biol* **50**, 1919 (2005).
- 169 M.A. Lewis, R.M. Staruch and R. Chopra, "Thermometry and ablation monitoring with ultrasound," *Int. J. Hyperthermia* **31**, 163-181 (2015).
- 170 N.J. McDannold and F.A. Jolesz, "Magnetic resonance image-guided thermal ablations," *Topics Magn. Res. Imaging* **11**, 191-202 (2000).
- 171 B.D. De Senneville, C. Mougnot, B. Quesson, I. Dragonu, N. Grenier and C.T. Moonen, "MR thermometry for monitoring tumor ablation," *Eur. Radiol.* **17**, 2401-2410 (2007).

- 172 J.G. Fortner, D.S. Klimstra, R.T. Senie and B.J. Maclean, "Tumor size is the primary prognosticator for pancreatic cancer after regional pancreatectomy," *Ann. Surg.* **223**, 147-153 (1996).
- 173 S. Eroglu, B. Gimi, B. Roman, G. Friedman and R.L. Magin, "NMR spiral surface microcoils: design, fabrication, and imaging," *Concepts Magn. Reson. B* **17**, 1-10 (2003).
- 174 C.L. Dumoulin and R.D. Darrow, U.S. Patent No. 6,289,233 (11 September 2001).
- 175 C.L. Dumoulin, R.P. Mallozzi, R.D. Darrow and E.J. Schmidt, "Phase-field dithering for active catheter tracking," *Magn. Reson. Med.* **63**, 1398-1403 (2010).
- 176 S. Roujol, M. Ries, B. Quesson, C. Moonen and B. Denis de Senneville, "Real-time MR-thermometry and dosimetry for interventional guidance on abdominal organs," *Magn. Reson. Med.* **63**, 1080-1087 (2010).
- 177 R.L. King, Y. Liu, S. Maruvada, B.A. Herman, K.A. Wear and G.R. Harris, "Development and characterization of a tissue-mimicking material for high-intensity focused ultrasound," *IEEE Trans. Ultrason. Ferroelectr. Freq. Control* **58**, (2011).
- 178 S. Elayaperumal, J.C. Plata, A.B. Holbrook, Y. Park, K.B. Pauly, B.L. Daniel and M.R. Cutkosky, "Autonomous real-time interventional scan plane control with a 3-D shape-sensing needle," *IEEE Trans. Med. Imaging* **33**, 2128-2139 (2014).
- 179 J. Ferrer, W.E. Scott 3rd, B.P. Weegman, T.M. Suszynski, D.E. Sutherland, B.J. Hering and K.K. Papas, "Pig pancreas anatomy: implications for pancreas procurement, preservation, and islet isolation," *Transplantation* **86**, 1503-1510 (2008).
- 180 D.K. Bhasin, S.S. Rana and V.S. Chandail, "The pancreas and respiration: oblivious to the obvious," *J. Pancreas* **7**, 578-583 (2006).
- 181 C. Weidensteiner, B. Quesson, B. Caire-Gana, N. Kerioui, A. Rullier, H. Trillaud and C.T. Moonen, "Real-time MR temperature mapping of rabbit liver in vivo during thermal ablation," *Magn. Reson. Med.* **50**, 322-330 (2003).
- 182 S. Morikawa, T. Inubushi, Y. Kurumi, S. Naka, K. Sato, K. Demura, T. Tani and H.A. Haque, "Feasibility of respiratory triggering for MR-guided microwave ablation of liver tumors under general anesthesia," *Cardiovasc. Intervent. Radiol.* **27**, 370-373 (2004).
- 183 L. Marti-Bonmati, M. Graells and C. Ronchera-Oms, "Reduction of peristaltic artifacts on magnetic resonance imaging of the abdomen: a comparative evaluation of three drugs," *Abdom. Imaging* **21**, 309-313 (1996).

- 184 R. Salomir, F.C. Vimeux, J.A. de Zwart, N. Grenier and C.T. Moonen, "Hyperthermia by MR-guided focused ultrasound: Accurate temperature control based on fast MRI and a physical model of local energy deposition and heat conduction," *Magn. Reson. Med.* **43**, 342-347 (2000).
- 185 A. Vanne and K. Hynynen, "MRI feedback temperature control for focused ultrasound surgery," *Phys. Med. Biol.* **48**, 31 (2002).
- 186 E. Delabrousse, R. Salomir, A. Birer, C. Paquet, F. Mithieux, J. Chapelon, F. Cotton and C. Lafon, "Automatic temperature control for MR-guided interstitial ultrasound ablation in liver using a percutaneous applicator: Ex vivo and in vivo initial studies," *Magn. Reson. Med.* **63**, 667-679 (2010).
- 187 Y.J. Yoon and P. Benkeser, "Ultrasonic phased arrays with variable geometric focusing for hyperthermia applications," *IEEE Trans. Ultrason. Ferroelectr. Freq. Control* **39**, 273-278 (1992).
- 188 X. Fan and K. Hynynen, "The effects of curved tissue layers on the power deposition patterns of therapeutic ultrasound beams," *Med. Phys.* **21**, 25-34 (1994).
- 189 E.G. Moros, X. Fan and W.L. Straube, "Ultrasound power deposition model for the chest wall," *Ultrasound Med. Biol.* **25**, 1275-1287 (1999).
- 190 G. Knollman, J. Bellin and J. Weaver, "Variable-Focus Liquid-Filled Hydroacoustic Lens," *J. Acoust. Soc. Am.* **49**, 253-261 (1971).
- 191 D.L. Deardorff and C.J. Diederich, "Ultrasound applicators with internal water-cooling for high-powered interstitial thermal therapy," *IEEE Trans. Biomed. Eng.* **47**, 1356-1365 (2000).
- 192 M.A. Saab, "Applications of high-pressure balloons in the medical device industry," *Medical Device & Diagnostic Industry Magazine*, 86-94 (2000).
- 193 E.T. Roche, A. Fabozzo, Y. Lee, P. Polygerinos, I. Friehs, L. Schuster, W. Whyte, A.M. Casar Berazaluce, A. Bueno, N. Lang, M.J. Pereira, E. Feins, S. Wasserman, E.D. O'Cearbhaill, N.V. Vasilyev, D.J. Mooney, J.M. Karp, P.J. Del Nido and C.J. Walsh, "A light-reflecting balloon catheter for atraumatic tissue defect repair," *Sci. Transl. Med.* **7**, 306ra149 (2015).
- 194 F.A. Chipperfield and S.A. Dunkerton, "Welding and joining techniques for polymeric medical devices." *Welding and Cutting* **56**, 208-209 (2004).
- 195 D. Pullen, S. Tavakoli, D. Pullen and S. Dunkerton, "A review of adhesive bonding techniques for joining medical materials," *Assem. Autom.* **25**, 100-105 (2005).

- 196 A. Ali, D.H. Plettenburg and P. Breedveld, "Steerable Catheters in Cardiology: Classifying Steerability and Assessing Future Challenges," *IEEE Transactions on Biomedical Engineering* **63**, 679-693 (2016).
- 197 C.A. Cain and S. Umemura, "Concentric-ring and sector-vortex phased-array applicators for ultrasound hyperthermia," *IEEE Trans.Microwave Theory Tech.* **34**, 542-551 (1986).
- 198 J. Chapelon, P. Faure, M. Plantier, D. Cathignol, R. Souchon, F. Gorry and A. Gelet, in ULTRASONICS SYMPOSIUM, (INSTITUTE OF ELECTRICAL & ELECTRONICS ENGINEERS INC, 1993) pp. 1211-1211.
- 199 T. Fjield, X. Fan and K. Hynynen, "A parametric study of the concentric-ring transducer design for MRI guided ultrasound surgery," *J.Acoust.Soc.Am.* **100**, 1220-1230 (1996).
- 200 W. MathWorld, Parabola, (2015).
- 201 S. Umemura and C. Cain, "The sector-vortex phased array: acoustic field synthesis for hyperthermia," *IEEE Trans.Ultrason.Ferroelectr.Freq.Control* **36**, 249-257 (1989).
- 202 T. Fjield and K. Hynynen, "The combined concentric-ring and sector-vortex phased array for MRI guided ultrasound surgery," *IEEE Trans.Ultrason.Ferroelectr.Freq.Control* **44**, 1157-1167 (1997).

Appendix A

MR-compatible endoscopic articulation assembly

A.1 Introduction

In envisioning an endoluminal ultrasound applicator that would be navigated into the upper GI tract and precisely positioned to target specific sites in the pancreas, there are clear requirements for high positional accuracy and controlled manipulation of the device tip where ultrasound is emitted, particularly due to the abundance of sensitive anatomy in and around the pancreas. For the practical endoluminal applicator designs used in the majority of the experimental evaluations within this research project (see Chapter 3), positional capabilities were relatively limited to whole body translation and rotation of the entire catheter assembly. While adequate for navigating the assembly through the esophagus into the stomach and orienting it towards pancreatic tissue, the limited positional controls are unsuitable for precise applicator placement and targeting of specific tissue sites while the ensuring safety of nearby sensitive tissues.

Commercial endoscopes integrate articulation controls to provide precise 4-way steering of the device tip.¹⁴¹ Steering can be accomplished using a wide variety of physical, thermal, magnetic or electrical actuation methods, though using pull-wires that are attached to articulating rings or segments at the device tip is most common.¹⁹⁶ While ultrasound applicators have been attached onto existing endoscopes in order to utilize their imaging guidance and positional capabilities⁷⁹, the vast majority of endoscopes contain magnetic components, which are not MR-compatible, and hence cannot be used in an interventional MR procedure. As such, there is a need to develop an endoluminal ultrasound applicator with endoscopic articulation capabilities that is completely MR-compatible. In addition to improving the positional control of the applicator in the stomach for precise spatial localization and targeting, articulation could also improve coupling between the applicator and luminal wall, which could enhance luminal sparing by providing optimal heat transfer between the wall and the circulating cooling water.

Hence, this section introduces a preliminary design for a MR-compatible endoluminal applicator with endoscopic articulation capabilities. The design is intended to be very cost-effective, simple, and modular, predominantly consisting of 3D printed parts and standard off-the-shelf components. Initial fabricated prototypes are also presented.

A.2 Design

A.2.1 Overview

Figure A.1 shows a CAD schematic of the complete applicator assembly. The articulation is provided by four parallel pull-wires that run inside the length of the catheter body, attaching to the distal tip of the articulation rings segment and to pulley assemblies within the control handle. Each pull wire controls deflection of the tip along a principal direction: up, down, left, or right. The ultrasound applicator fixture is attached to the distal tip of the catheter assembly, and the

corresponding power cables and flow lines are routed through the articulation rings, catheter body, and control handle to the proximal connectors.

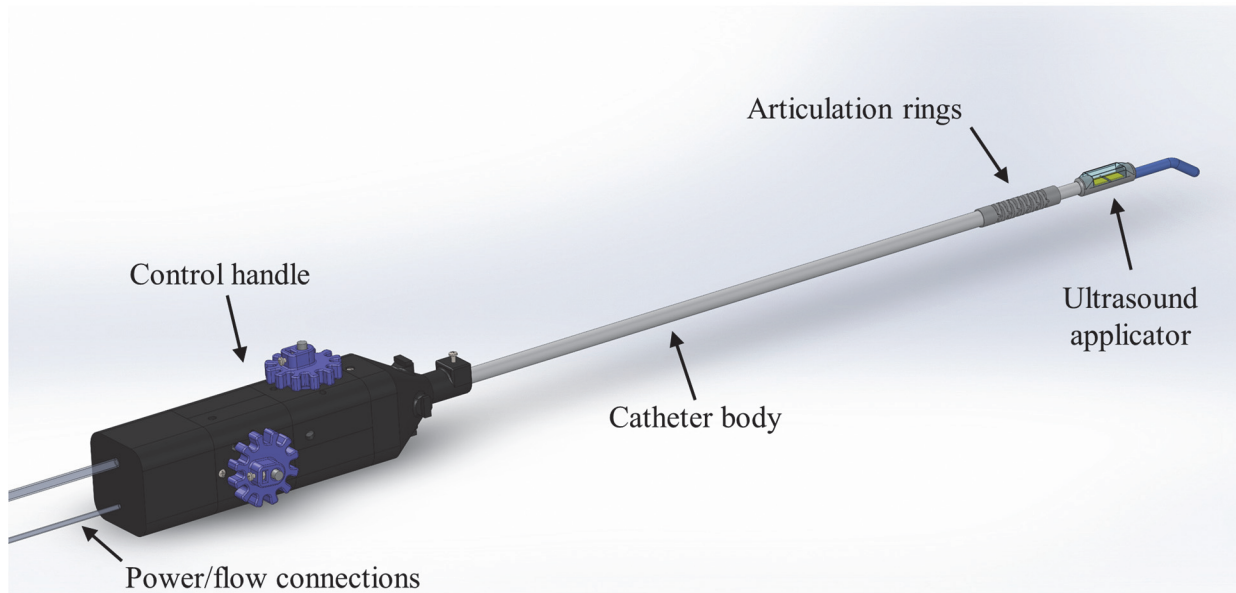


Figure A.1 CAD schematic of the MR-compatible endoluminal ultrasound applicator with articulated steering capabilities.

A.2.2 Control handle

The control handle housing is modular, consisting of four compartments and six 3D printed parts (Zortrax M200, Zortrax), as shown in Figure A.2. The distal adapter contains an embedded set screw to attach to the catheter body, and has four T-shaped parts with a hole at the bottom that each route a pull-wire. By adjusting the length of these parts protruding into the housing cavity, these parts serve as tensioners to adjust the tension of each pull-wire independently. The next two proximal compartments contain two orthogonal pulley subassemblies that control tip articulation along the left-right directions and along the up-down directions, respectively. The last compartment, the proximal adapter, contains open interior space for slack in the flow lines and power cabling, matching networks, and ports for flow/power connections. The flow tubes and power lines from the ultrasound applicator are routed through an enclosed channel along the

interior wall of the control housing, originating in the distal adapter and terminating at the junction to the proximal adapter. The pull-wires are routed through the center of the housing to their respective pulley subassembly. Thin rectangular prisms protrude from the interior walls of the housing assembly, each containing holes at set depths which are used to uniquely route each pull-wire, ensuring proper alignment to the corresponding terminating pulley and mitigating any potential tangles or interleaves between the wires. The assembly can be assembled and disassembled modularly, permitting easy assembly and adjustment, with compartments attached to each other via plastic screws/nuts.

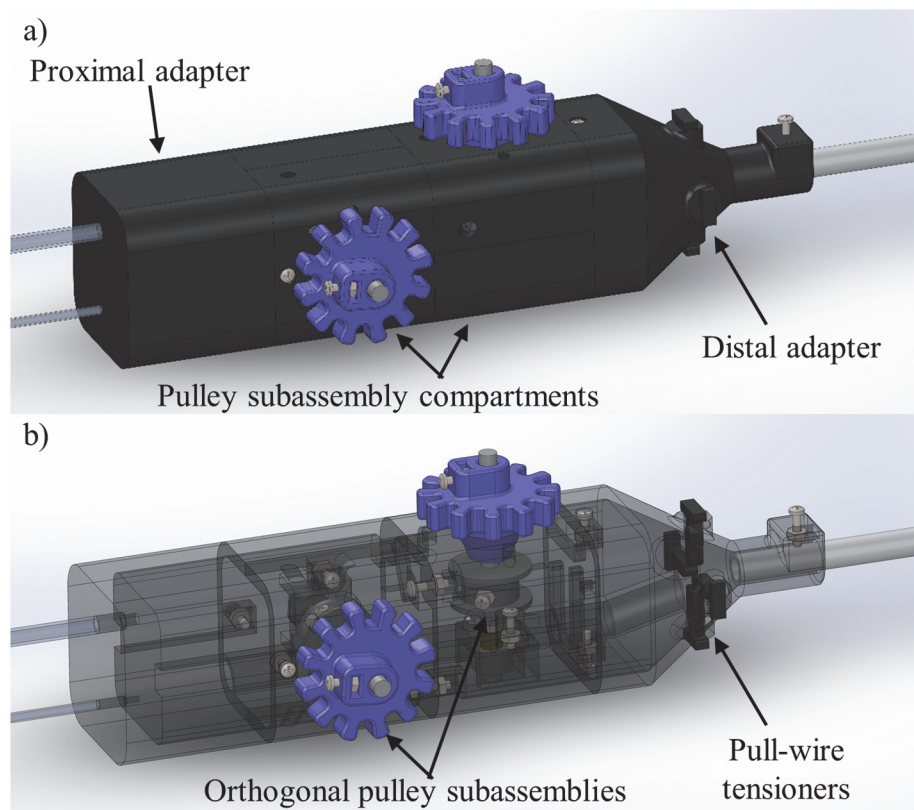


Figure A.2 Control handle assembly, containing four modular compartments that appropriately route power/flow lines from the ultrasound applicator to external connectors and pull-wires to their respective pulley assembly. Housing body is shown in (a) opaque and (c) transparent display states.

A.2.3 Pulley subassembly

Two orthogonally-aligned pulley assemblies control tip articulation along the left-right and up-down directions. Each assembly, as shown in Figure A.3, consists of an aluminum rod inserted through the housing assembly, centered in a peg-insert on the posterior interior. An end-stop is attached to the bottom of the rod, which in combination with the corral embedded in the housing fixture, limits vertical displacement of the rod to a set amount. The corral contains a press-fit brass bearing, to center the rod, and above it the pulley is fixed to the middle portion of the rod. At the top of the rod, outside the housing assembly, the knob is affixed. Pull-wires are routed through opposite flanges on the pulley and attached to screws, which can be tightened or loosened individually to adjust wire tension. As the assembly is rotated, one of the pull-wires undergoes tension while the opposite wire is slackened, causing bending of the articulation rings along the direction of the wire under tension. To lock the position, the entire rod assembly can be pushed into the housing, creating a press-fit between the bottom of the knob and the opening in the housing which prevents rotation until the knob is pulled out. The pulley, knob, and end-stop are all 3D printed (Zortrax M200, Zortrax) and affixed to the rod through brass set screws.

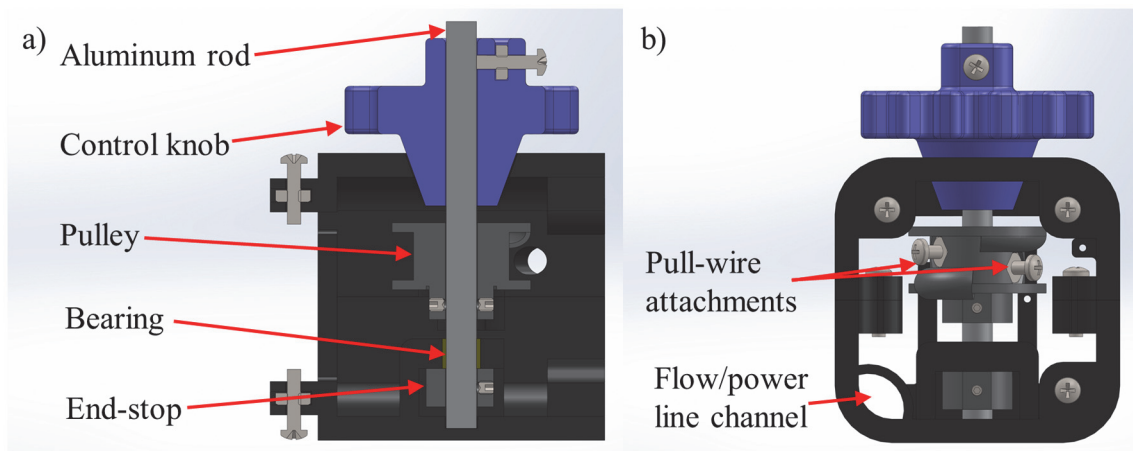


Figure A.3 Pulley subassembly that controls pull-wire tension and tip articulation. (a) Cross-sectional view of the subassembly as inserted into the housing compartment, and (b) view from the proximal aspect of the compartment

A.2.4 Articulation rings

The articulation segment is composed of 3D printed (Form 1+, Formlabs) rings that are stacked together, with each successive ring rotated 90 degrees relative to its neighbors, as shown in Figure A.4. They permit bending along the left/right (Figure A.2 (b)), with concurrent bending up/down along the orthogonal axis to achieve full omnidirectional motion. As shown in Figure A.2 (c), each ring has two lumens along the interior to contain pull wires, and a central lumen of 44 mm² surface area for power/flow line routing from the ultrasound applicator. Each ring has insertion tabs and notches to attach to the adjacent ring, and there are proximal and distal adapter components which connect to the main catheter tubing body. The overall diameter of the articulation ring assembly is 12 mm OD, and a thin silicone tube covers the assembly to make it water-tight.

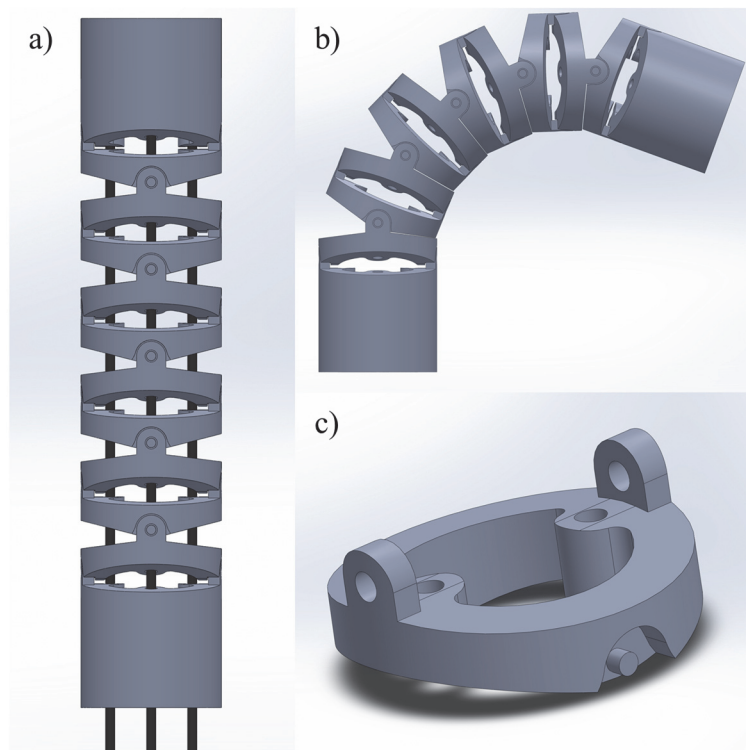


Figure A.4 (a) Omnidirectional articulation assembly, consisting of stacked interleaved ring segments with four parallel pull-wires routed through lumens along the inner surface of each ring. The wires are fixed to the distal adapter component. When tension is applied to one of the pull wires, the opposite wire slackens, permitting bending along a direction, as shown in (b). An individual ring segment is illustrated in (c).

A.3 Fabricated prototypes

Figure A.5 shows a complete prototype assembly, featuring an ultrasound applicator with two curvilinear transducers along the length of the device (each 9.3 mm x 11.4 mm, 25.1 mm ROC, 3.14 MHz). The catheter body consisted of custom-made multi-lumen silicone tubing (12 mm OD), with a large central lumen that contained flow/power lines and four small peripheral lumens which routed each of the pull-wires. MR compatibility of the complete assembly was verified in a 3T GE Discovery MRI scanner, and the device was able to be inserted orally down the esophagus in an anesthetized porcine under MR guidance, as shown in Figure A.6.

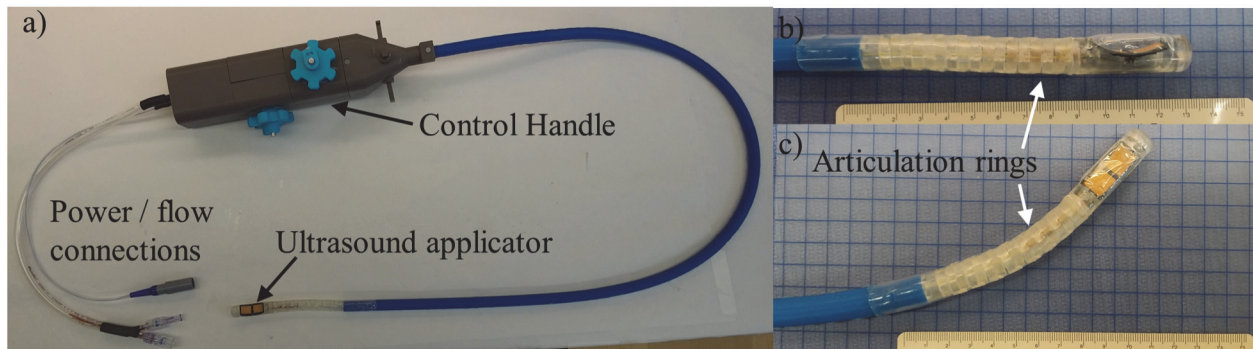


Figure A.5 (a) Prototype endoluminal ultrasound applicator with endoscopic tip articulation capabilities. (b) Distal tip of the assembly, highlighting the ultrasound applicator and articulation ring segment in neutral and (c) bent states.



Figure A.6 T2w MR image illustrating delivery of the prototype assembly (red arrow) through the porcine esophagus *in vivo*.

An improved design iteration for the articulation ring segments is shown in Figure A.7, as based off the design description in Figure A.4. These rings have larger internal diameters to more easily accommodate the power/flow lines and an adjusted surface curvature to permit a tighter bending radius of curvature, as shown in Figure A.7 (b).

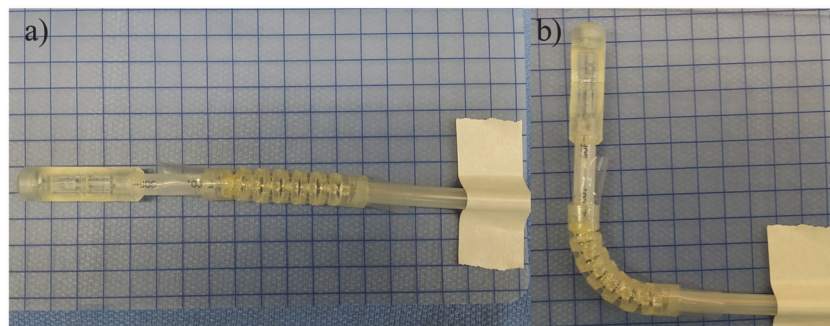


Figure A.7 (a) Prototype endoscopic tip articulation assembly with improved ring design and (b) tighter bending capabilities.

A.4 Discussion

In general, the capability to precisely spatially-localize and steer energy emissions of an endoluminal ultrasound applicator is critical for effective therapy delivery and mitigating complications. For thermal therapy applications in the pancreas, safety concerns are particularly high due to the close proximity of sensitive tissues, such as the pancreatic duct, major vasculature, bowel, and normal pancreatic parenchyma. Thermal damage to these tissues could result in pancreatic juice leakage and pseudocyst formation, hemorrhage, gastric fistulas, and/or pancreatitis. While image-guided methods, including the MR and MRTI-based guidance presented in Chapter 3, could serve as a vital tool for ensuring energy is delivered to the desired targets, the applicator itself must be capable of reaching the ideal positions for delivering the treatment. Integrating catheter steering and tip articulation mechanisms within the endoluminal ultrasound applicator could potentially fulfill this need.

A design for a MR-compatible steerable endoluminal ultrasound applicator has been presented. The design is low cost, with parts primarily 3D printed from cheap plastic or resin-based materials, and the mechanisms for articulation are simple, allowing for quick and easy assembly. A prototype assembly was fabricated, verified to be MR-compatible, and orally passed down the porcine esophagus *in vivo*. A prototype with an improved tip bending radius of curvature has also been fabricated, and should more easily accommodate passage through tortuous channels. Further evaluations of complete prototype assemblies in animal models are necessary to motivate further design changes and to establish benefits of the articulation capabilities in terms of positioning the applicator to treat specific sites and optimally coupling to the luminal wall. This technology could be applied for the practical applicator configurations presented in Chapter 3, as well as the more complex assembly configurations presented in Chapter 4 and Appendix B.

Appendix B

Preliminary modeling analysis of alternative deployable ultrasound applicator assemblies for enhanced volumetric or selective energy localization

B.1 Introduction

As alluded to in the discussion section of Chapter 4, many additional applicator assembly designs can be conceived that incorporate deployable components in order to augment the effective acoustic aperture and enhance therapeutic potential while still retaining a small-profile during delivery into the body. This section introduces design schemes and preliminary theoretical analyses of promising alternative configurations to the end-fire and side-fire applicator designs presented in Chapter 4. In contrast to the initial assemblies, these new designs do not contain fluid lens compartments. Select configurations of each proposed design were analyzed by adapting the acoustic and/or biothermal modeling methodology introduced in Chapter 4.

B.2 Volumetric end-fire/side-fire deployable assemblies

By simply removing the fluid lens compartment for the end-fire and side-fire designs presented in Chapter 4; or equivalently, replacing the perfluorocarbon lens fluid solution contained therein with water, focusing capabilities can be substituted for a more volumetric, but still collimated and directional emission of acoustic energy, as shown in Figure B.1. For the end-fire, this expanded configuration would approximate a large planar disk transducer with outer diameter equal to the expanded diameter of the conical reflector and a central dead-zone equal to the diameter of the tubular transducer source. In contrast to the selective and localized heating capabilities of the end-fire/side-fire designs that integrates a convex fluid lens, these design alternatives could be suitable for more volumetric tissue exposure and temperature elevation.

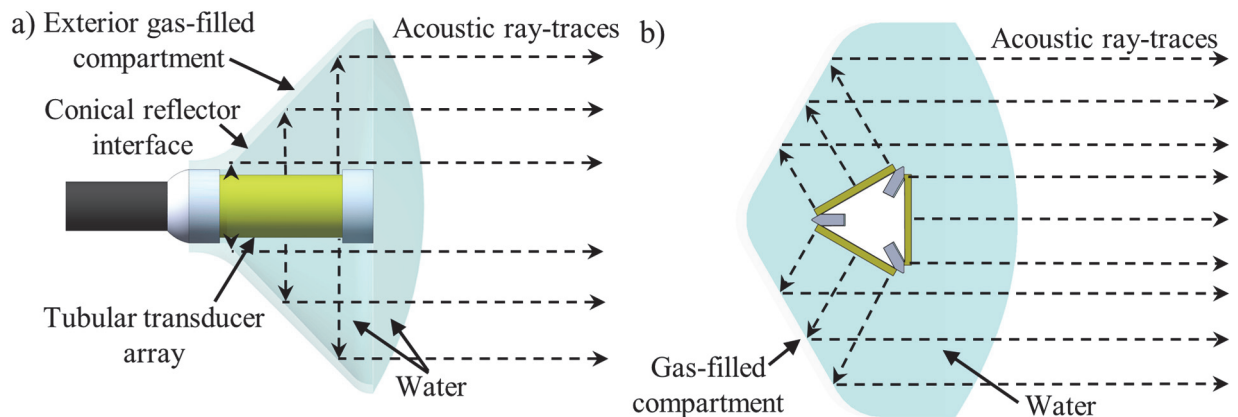


Figure B.1 Schematic of the deployable (a) end-fire and (b) side-fire (central transverse cross-section shown) ultrasound applicator assemblies with no distal fluid lens compartment. As depicted by the ray-traces for each case, acoustic energy is reflected off the interface between the interior water compartment and the exterior gas-filled compartment. Reflected acoustic energy is collimated either out the distal tip, or adjacent to the applicator fixture, for the end-fire and side-fire designs, respectively.

Two select configurations of the end-fire design were analyzed using acoustic and biothermal modeling: a small configuration (1.5 MHz, 6 mm OD x 12 mm height tubular transducer, 30 mm expanded balloon diameter), and a larger configuration (1.5 MHz, 10 mm OD x 20 mm height tubular transducer, 50 mm expanded balloon diameter). Only a single configuration for the side-

fire configuration (1.5 MHz, 12 mm fixture diameter, 10 x 30 mm transducer width x height, ~40 mm expanded balloon diameter), which approximately matched the collapsed diameter of the larger end-fire configuration, was analyzed. Acoustic propagation through the expanded assemblies was modeled using the method of secondary sources, similarly to the assemblies in Chapter 4 with the difference of substituting perfluorocarbon lens fluid with water in the distal compartment. Using the simulated acoustic intensity distributions as input, biothermal simulations for endoluminal heating of pancreatic tissue, using the 3D generic model geometry shown in Figure 4.1, were performed. Due to the volumetric nature of heating, applied powers and target temperatures were chosen as suitable for hyperthermia treatments (40-45 °C). A convective heat flux boundary condition at the interface between the distal applicator balloon and the inner stomach wall was modeled to account for cooling effects of water (25 °C) circulation through the balloon. For each configuration, a steady state temperature distribution was generated using a constant input intensity that corresponded to a maximum tissue temperature of 45 °C.

Simulated hyperthermic temperature distributions in the central longitudinal plane for the two end-fire configurations are illustrated in Fig. 2. The smaller configuration (30 mm expanded balloon - Figure B.2 (a)) could maintain approximately 20.1 cm³ of pancreatic tissue between 40 °C ≤ T ≤ 45 °C, with the corresponding diameter and depth extent of the 40 °C contour being 2.9 cm and 4.1 cm, respectively. The larger configuration (50 mm expanded balloon - Figure B.2 (b)) could maintain approximately 64.3 cm³ of pancreatic tissue between 40 °C ≤ T ≤ 45 °C, with the corresponding diameter and depth extent of the 40 °C contour being 5.0 cm and 4.2 cm, respectively.

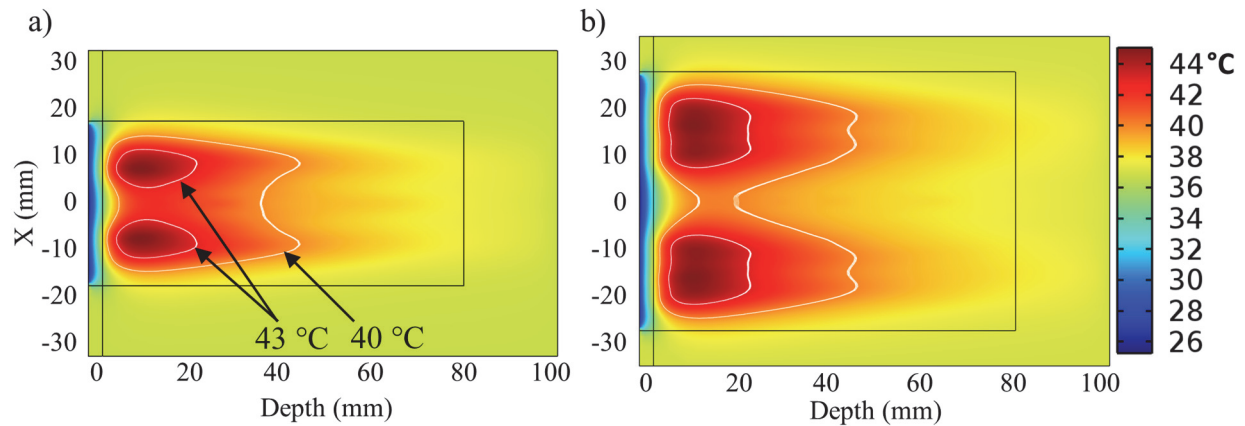


Figure B.2 Simulated endoluminal hyperthermic temperature distributions in pancreatic tissue for end-fire applicator assemblies without focusing fluid lens compartments. Central longitudinal 2D slices of the 3D tissue block model are shown for (a) small (1.5 MHz, 6 mm OD x 12 mm height tubular transducer, 30 mm expanded balloon diameter) and (b) large (1.5 MHz, 10 mm OD x 20 mm height tubular transducer, 50 mm expanded balloon diameter) assembly configurations. Maximum tissue temperature for the steady-state temperature solution did not exceed 45 °C, and 40/43 °C contours are shown in white, as labeled.

The simulated hyperthermic temperature distributions in the central transverse and sagittal planes for the side-fire configuration is shown in Figure B.3. 28.5 cm³ of tissue was elevated between 40-45 °C, and the extent of the 40 °C contour was 3.4 cm x 3.1 cm x 4.5 cm in the X, Y, and Z (depth) dimensions.

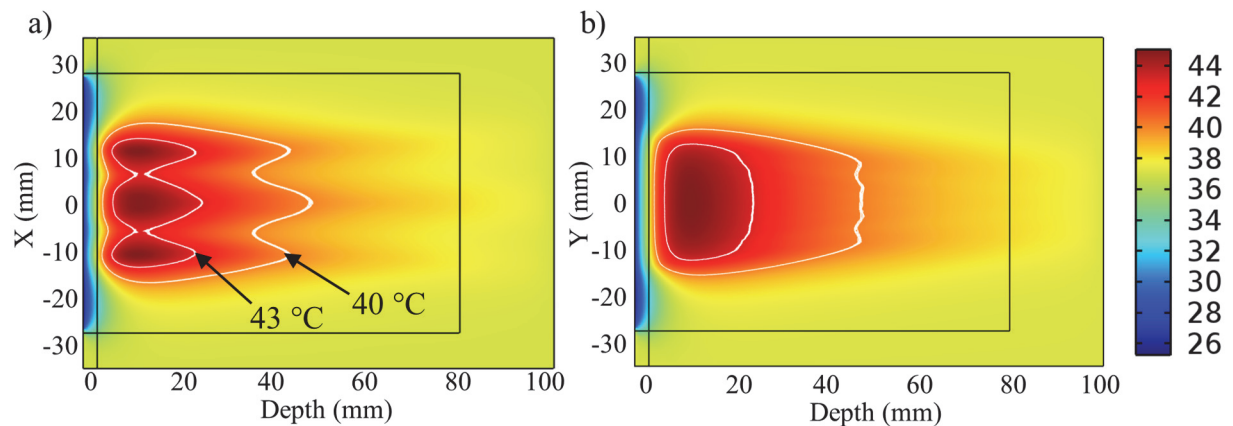


Figure B.3 Simulated endoluminal hyperthermic temperature distributions in pancreatic tissue in the central (a) transverse and (b) sagittal 2D planes for the side-fire applicator assembly (1.5 MHz, 12 mm fixture diameter, ~10 x 30 mm transducer, ~40 mm expanded balloon diameter) without a focusing fluid lens compartment. Maximum tissue temperature for the steady-state temperature solution did not exceed 45 °C, and 40/43 °C contours are shown in white, as labeled.

These preliminary biothermal simulations indicate that both the end-fire and side-fire deployable applicator assembly designs are capable of elevating large volumes of tissue to hyperthermic temperature ranges for a single, static applicator placement. The volumes of tissue maintained at 40-45 °C for the larger end-fire and side-fire configurations were much larger compared to static placements of more conventional applicators designs, as investigated in simulation studies presented in Chapter 2 (Figure 2.8). The heating extent along the transverse (X-dimension) for the two end-fire assemblies were closely delimited by the diameter of the expanded reflector balloons. However, there was some variation in the uniformity of the temperature across the transverse diameter, with lower values in the central region due to the acoustic dead-zone at the central portion of the applicator assembly. As can be seen by differences between the smaller and larger configurations, increasing the transducer diameter resulted in greater temperature discrepancies between the central and peripheral regions of the heated zone. Uniformity could potentially be filled by adding a planar disk transducer onto the tip of the applicator assembly, or by using a conical reflector balloon geometry with a marginally lower conical angle ($< 45^\circ$ relative to the long axis) so that the reflected acoustic waves converge slightly. The side-fire configuration displays better temperature uniformity; however, the spatial extent of tissue at hyperthermic temperatures is reduced compared to the larger end-fire configuration, despite both designs having similar collapsed profiles. This is likely due to the difference in how acoustic energy is dispersed across the reflector surfaces for the end-fire and side-fire designs: energy emitted by the tubular transducers is dispersed across the entire conical interface for the end-fire design, independent of the tubular transducer radius; whereas the dispersion of energy across the reflector surface for the side-fire is limited, and varies as a function of the transducer width (fixture size) and how the transducer stage is centered within the multi-compartment

balloon. Whereas for the end-fire the height of the tubular transducer is constrained by the expanded balloon diameter (using a larger balloon diameter requires a longer tube to cover the reflector surface), both the transducer width (i.e., fixture diameter) and length for the side-fire design need to increase in order to augment the effective therapeutic aperture. As a result, increasing the spatial extent of heating would necessitate a larger overall profile when the side-fire assembly is in its collapsed state, which could limit device delivery and accessibility.

B.3 End-fire with 1D phased array and conical/paraboloid reflector

As briefly discussed in Chapter 1, focusing of ultrasonic waves can be achieved using arrays of transducer elements that are independently phased to electronically steer the beam. A modification to the end-fire design presented in Chapter 4 was explored in which the fluid lens was removed and the tubular transducer array was converted into a one-dimensional phased array, with ring-segment sub-elements positioned along the length of the array, as shown in Figure B.4 (a). By integrating the phased-array of tubular transducers with the reflector balloon, this arrangement is envisioned to mimic a concentric ring transducer array¹⁹⁷⁻¹⁹⁹, which is capable of electronic steering of the beam in depth along the central longitudinal axis. Focusing performance of the conventional concentric ring transducer array depends on a variety of parameters, including the number of independent rings, the center-to-center ring spacing, and the inherent geometric focus of the array.¹⁹⁹ As such, analogous properties for the proposed deployable assembly were hypothesized to influence focal capabilities.

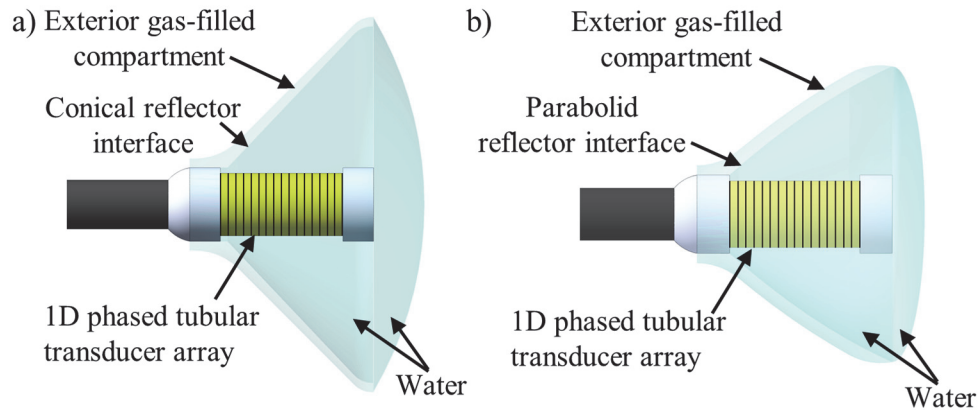


Figure B.4 Design schema for end-fire deployable assemblies with (a) conical and (b) paraboloid reflector balloon geometries and a tubular transducer phased-array source that can produce electronic focusing at variable depths along the central longitudinal axis beyond the distal tip of the assembly.

Two reflector geometries were investigated in combination with the tubular transducer phased-array. In combination with the conical reflector geometry, as used in previous end-fire assembly configurations, the deployed assembly mimics a flat concentric ring array with no geometric focus. The second reflector geometry has a paraboloid geometry, as seen in Figure 4 (b). Figure B.5 shows that the 2D parabolic profile of the reflector is revolved around the central device axis to form the 3D paraboloid geometry, and creates a natural geometric focus for the waves emitted radially by the tubular transducer array. By tailoring the profile of the parabola, this geometric focal depth can be set, and as the desired focal depth increases to infinity, the geometry converges to a conical profile. Hence, in combination with the paraboloid balloon reflector geometry, the deployed assembly is representative of a concentric ring array that has a convex, geometrically-focused surface.

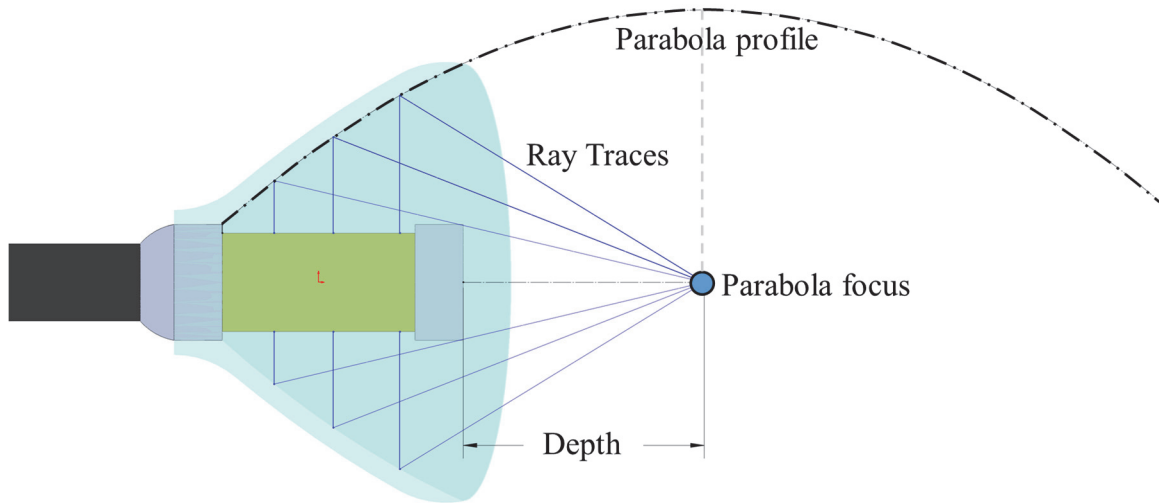


Figure B.5 Cross-sectional view of the deployable end-fire assembly with a paraboloid balloon reflector. The profile of the 2D parabola that defines the reflector interface is depicted, and corresponds to a specific focal depth according to the geometric convergence of acoustic ray traces as radially emitted by the tubular transducer source.

Acoustic propagation through the deployed balloon assembly was modeled using the method of secondary sources, which requires discretization of the tubular transducer geometry as well as the conical/paraboloid surface into simple “point” sources. Whereas the conical reflector surface is relatively trivial to discretize into regularly-spaced simple sources of known center coordinates and orientation (as described by the unit normal vector of the surface at the center coordinate) due to its simple geometry, the same for the paraboloid reflector is more involved due to its more complex geometry. This problem can be resolved by first considering the 2D parabola that defines the cross-sectional profile of the reflector, as seen in Figure B.5. The equation of the parabola can be uniquely determined using the coordinates of the most proximal point of the parabola (as constrained by the applicator layout) as well as the target focal depth. The coordinates of points that are equidistant along the parabolic curve can be determined using the parametrized arc length equation and the corresponding parametric equations of the parabola.²⁰⁰ The unit normal vector at each of those points is then determined using the derivative of the tangent vector equation.

Lastly, these coordinates and vectors can be revolved around the longitudinal central device axis in order to generate the full 3D paraboloid surface.

To validate that the paraboloid geometries were generated accurately for a desired focal depth, deployable assemblies were modeled using a non-phased tubular transducer centered within paraboloid reflector balloons of varying focal depths. The output acoustic intensity distributions were simulated, as shown in Figure B.6, as the paraboloid geometry was varied to adjust the focal depth.

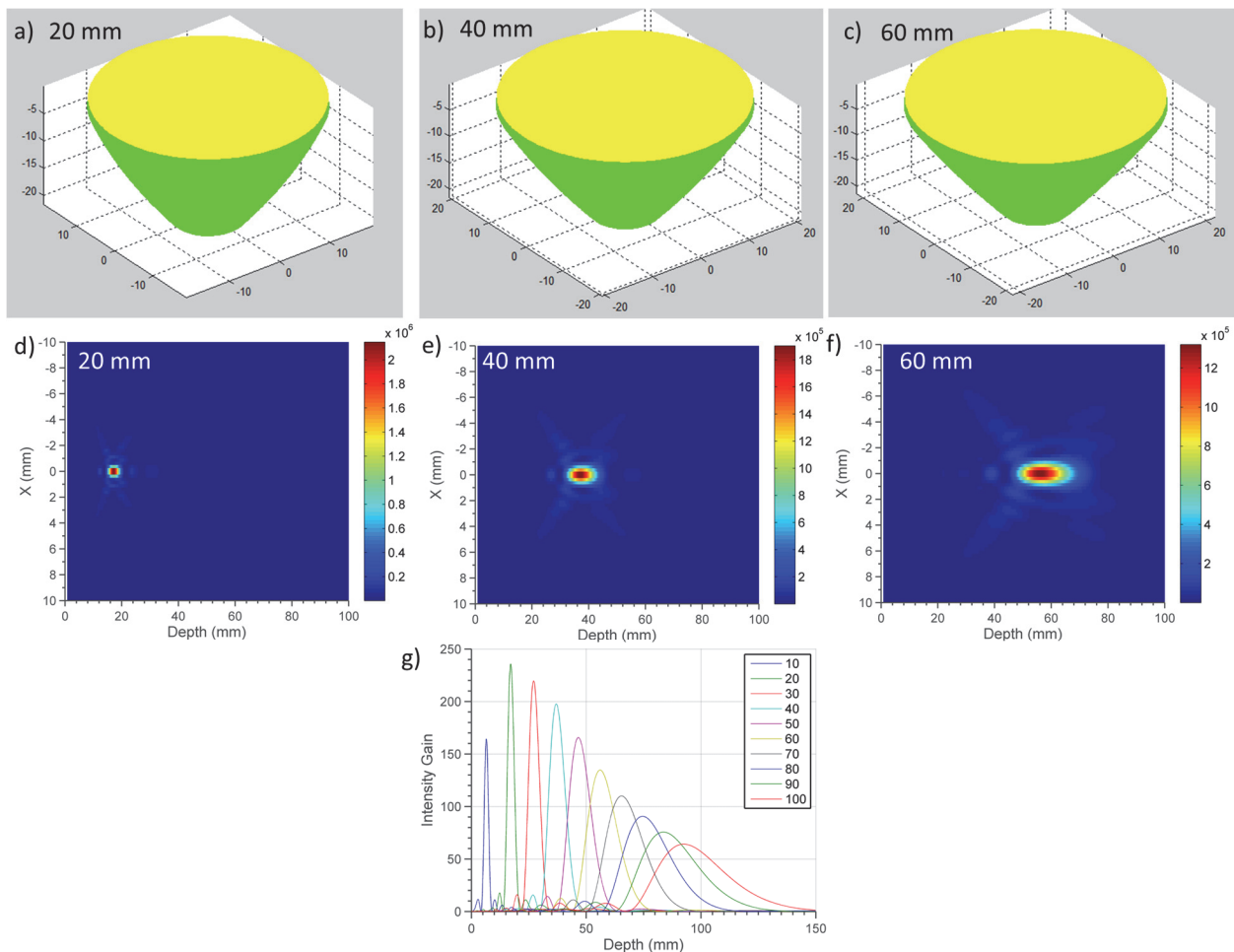


Figure B.6 (a)-(c) Paraboloid reflector geometries (green) of varying geometric focal depths of 20, 40, or 60 mm, respectively. Using a non-phased tubular transducer source centered in each of the paraboloid reflector geometries, the (d)-(f) corresponding longitudinal acoustic intensity distributions (units of W/m²) confirm that the paraboloid geometry create focal distributions at the appropriate depth. (g) The central axial intensity distribution is shown as the paraboloid reflector geometry is varied for focal depths of 10-100 mm.

For electronic steering and focusing using the 1D tubular transducer phased array, the appropriate phasing of each sub-element was determined by first calculating the total path length between the central coordinate of each sub-element, the corresponding reflector surface (assuming perfectly radial transmission of the tubular transducer source), and the desired focal depth.¹⁹⁹ The phase of each sub-element was calculated as the modulus of the total path-length by the acoustic wavelength, converted to radians. As the transducer array was discretized into simple sources much smaller ($\sim\lambda/16$ spacing) than the size of the individual ring segment sub-elements of the phased array, all simple sources within the bounds of an individual sub-element were assigned the same phase value.

Simulations were performed to assess the influence of the ring-segment size, or equivalently, the number of ring-segments in the phased array transducers, on the electronic focusing capabilities. Figure B.7 shows simulation results using a deployable assembly consisting of a conical balloon (50 mm OD) and a tubular phased-array (1.5 MHz, 10 mm OD x 19.5 mm height) with electronic phasing applied for a 30 mm focal depth, as the length of the ring-segment sub-elements was varied between 9.75 mm to 0.65 mm (equivalently, 9.75λ to 0.65λ). This corresponds to an increasing number of sub-element ring-segments, or channels, from 2 to 30. It is clear that the quality of focusing and focal gain increases as the length of each ring-segment decreases, and that there is negligible focusing capabilities and prominent grating lobes above ring-segment lengths of 2.44 mm (2.44λ).

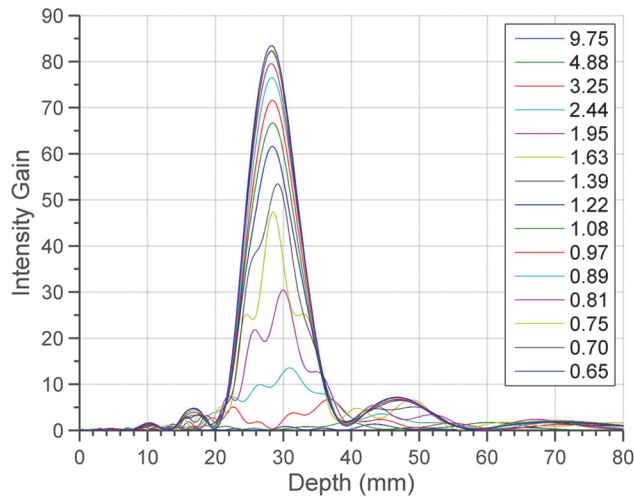


Figure B.7 Central axial intensity gain profile for a deployable applicator assembly consisting of a conical balloon reflector (50 mm OD) and a tubular phased-array (1.5 MHz, 10 mm OD x 19.5 mm height) with electronic phasing applied for a 30 mm focal depth, as the length of the ring-segment sub-elements was varied between 9.75 mm to 0.65 mm, corresponding to 2 and 30 total individual channels, respectively. The corresponding number of channels increases by 2 with each successively smaller segment.

Additional simulations were performed to compare deployable applicator configurations using a conical balloon reflector geometry against those with paraboloid reflector geometries, for three distinct paraboloid geometries corresponding to focal depths of 25, 40, and 55 mm. Each assembly configuration was modeled with the same tubular transducer phased-array (1.5 MHz, 10 mm OD x 19.5 mm height, 16 channels of 1.22 mm long ring-segments). Appropriate phasing was simulated to investigate focusing capabilities across a 1-7 cm range of depths. The central axial intensity gain profiles for each configuration are shown in Figure B.8.

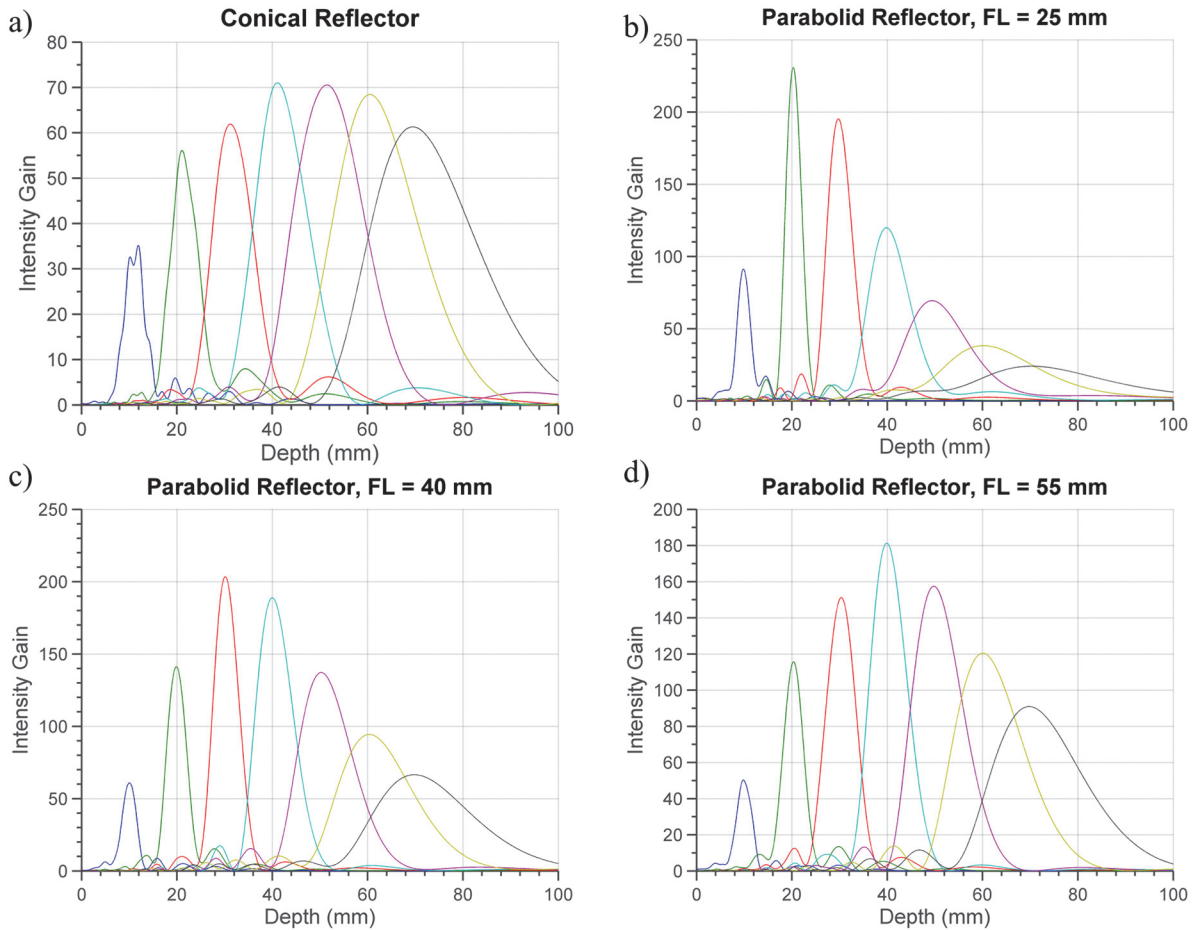


Figure B.8 Central axial intensity gain profiles for deployable applicator assemblies with a tubular transducer phased-array (1.5 MHz, 10 mm OD x 19.5 mm height, 16 channels of 1.22 mm long ring-segments) and a (a) conical reflector balloon or a (b)-(d) paraboloid reflector balloon with geometric focal depths of (b) 25 mm, (c) 40 mm, or (d) 55 mm.

As shown in Figure B.8, the assemblies with the paraboloid reflector are capable of much greater focal gain as compared to the conical reflector. Furthermore, the magnitude of focal gain across depth is a function of the paraboloid geometry. For each of the paraboloid geometries, maximum focal gain is close to the geometric focus, and there is greater variation between intensity profiles at successive focal depths as compared to the conical reflector configuration. As such, this simulated behavior confirms that the configuration with a conical reflector behaves similarly to a

flat concentric ring array, whereas the paraboloid reflector configurations behave akin to spherically-curved concentric ring array.

These preliminary theoretical investigations illustrate that utilizing phased arrays with deployable balloon reflectors could be a promising means of augmenting the effective therapeutic aperture of catheter-based ultrasound devices with dynamic control over the target depth. One advantage over utilizing phased-arrays and electronic steering to focus, over the fluid-lens based focusing proposed in Chapter 4, is that the electronic phasing has the capability for more robust and faster beamforming, requiring no mechanical or moving parts. Further, there would be less attenuation-based losses in the balloon media (i.e., water), and no losses from reflection at material interfaces with the lens fluid. The phased array design would also accommodate simpler balloon designs made of purely non-compliant PET or nylon materials, by forgoing the composite balloon design that accommodates a distensible distal membrane needed for fluid lens focal adjustment. A significant drawback to the phased array design is the significant cost and engineering complexity associated with the phased transducer array, as well as the necessary driving electronics. These costs would scale with the number of sub-elements composing the phased-array.

More extensive theoretical and experimental investigations are needed to comprehensively assess the utility of the phased-array deployable assembly design. Future efforts could also investigate designs that incorporate sectoring of the transducer array along the angular extent, alone or in combination with sectoring along the tube length. Angular-sectored arrays, in combination with the conical or paraboloid reflector balloon geometries, could emulate sector vortex transducer arrays, which are capable of generating annular-shaped foci.^{197,201} The combined angular-sectored and longitudinally-sectored phased array would thereby emulate a combined concentric-ring sector vortex array, with potential for more complex beamforming and generation


of annular focal patterns at selective target depths.²⁰² Linear planar phased arrays could also be incorporated into the side-fire design, opening the possibility for full beam steering across each dimension.

Publishing Agreement

It is the policy of the University to encourage the distribution of all theses, dissertations, and manuscripts. Copies of all UCSF theses, dissertations, and manuscripts will be routed to the library via the Graduate Division. The library will make all theses, dissertations, and manuscripts accessible to the public and will preserve these to the best of their abilities, in perpetuity.

Please sign the following statement:

I hereby grant permission to the Graduate Division of the University of California, San Francisco to release copies of my thesis, dissertation, or manuscript to the Campus Library to provide access and preservation, in whole or in part, in perpetuity.



Author Signature



Date